



**Steel Founders' Society of America
Research Report No. 94A**

**Fatigue and Fracture Toughness
Of Five Carbon or Low Alloy
Cast Steels at Room
Or Low Climate Temperature**

Published by the
Carbon and Low Alloy Steel Technical Research Committee
Steel Founders' Society of America

DR. JOHN M. SVOBODA
Technical and Research Director

OCTOBER, 1982

**Fatigue and Fracture Toughness of Five Carbon
or Low Alloy Cast Steels at Room
or Low Climatic Temperatures
By: Ralph L Stephens***

Table of Contents

Chapter	Page
Preface	i
1 Introduction and Material Characterization	
1.1 Introduction	1
1.2 Materials Selection and Characterization.....	2
1.2.1 Materials	2
1.2.2 Pouring, Heat Treatment and Microstructure	2
1.2.3 Hardness	4
1.2.4 Monotonic Tensile Properties.	5
1.2.5 Charpy V Notch Impact (CVN)	7
1.3 Summary..	8
References	8
2 Cyclic Stress-Strain and Low Cycle Fatigue	
2.1 Cyclic Stress-Strain Behavior	9
2.2 Low Cycle Fatigue.....	13
2.2.1 Test Procedures	13
2.2.2 Test Results.	13
2.3 Discussion of Results.....	18
2.3.1 Cyclic Strain Hardening and Softening	18
2.3.2 Fatigue Life.	18
2.4 Summary and Conclusions..	21
References	22
3 Constant Amplitude Fatigue Crack Growth	
3.1 Experimental Procedures.	23
3.2 Test Results	24
3.3 Macro and Micro Fractography.	29
3.3.1 Macro.....	29
3.3.2 Scanning Electron Microscopy	31
3.4 Discussion of Results,	31
3.5 Summary and Conclusions..	34
References	34
4 Variable Amplitude Fatigue Crack Initiation, Growth and Fracture	
4.1 Introduction	36
4.2 Experimental Procedures.	37
4.3 Test Results	38
4.4 Macro and Micro Fractography	45
4.4.1 Macro	45
4.4.2 Scanning Electron Microscopy (SEM)	45
4.5 Discussion of Results	49
4.6 Summary and Conclusions	50
References	50

Chapter	Page
5 Plane Stress Fracture Toughness, R-Curve	
5.1 Experimental Procedures and Results.....	51
5.1.1 Introduction.....	51
5.1.2 Experimental Procedures	51
5.1.3 Results	52
Macrofractography	55
Microfractography (SEM)	55
5.2 Discussion of Results.....	55
5.3 Summary and Conclusions.....	58
References	58
6 Plane Strain Fracture Toughness Using the J-Integral	
6.1 Introduction	59
6.2 Test Procedures and Results.....	59
6.3 Test Data Reduction.....	60
6.4 Discussion of Results.....	63
6.4.1 J_{Ic} , J_c , K_{Ic} , K_c	63
6.4.2 Correlation Between K_{Ic} and Upper Shelf CVN Energy.....	64
6.4.3 Valid J_{Ic} Determination in the CVN Transition Temperature Region.....	64
6.5 Summary and Conclusions.....	65
References	65
Appendix	
A Background on Low Cycle Fatigue, ϵ -N.....	66
B Fundamentals of LEFM for Application to Fatigue Crack Growth and Fracture	70
C Background on Fatigue Crack Growth, da/dN - ΔK	79
D Low Temperature Fatigue Behavior of Steels -A Review.....	85

© By Steel Founders' Society of America, 1982

Cast Metals Federation Building
455 State St., Des Plaines, Illinois 60016

Printed in the United States of America

PREFACE

This is the final report on the three year SFSA research project 111, Fatigue and Fracture Toughness of Five Carbon or Low Alloy Steels at Room and Low Climatic Temperatures. The report includes six chapters and four Appendices. Each chapter was written to stand alone with the background information of Chapter 1. Thus a modular type format was used in the organization of this report which differs somewhat from other SFSA Research Reports. Since the research is aimed principally at the needs of the practicing design/test/research engineer, foundrymen may find much of the material out of their field. To circumvent this difference in background and experience, appendices have been included at the back of the report which provide the fundamentals and descriptions of:

- A. Low Cycle Fatigue
- B. Linear Elastic Fracture Mechanics (LEFM)
- C. Fatigue Crack Growth Using LEFM Concepts

These descriptions have been excerpted from the Metal Fatigue in Engineering by H.O. Fuchs and R.I. Stephens. The book was published by Wiley Interscience, New York in June, 1980. These appendices are also worthwhile reading for those engineers not thoroughly familiar with low cycle fatigue and LEFM concepts.

The report is incomplete from the standpoint that a seventh chapter dealing with analytical fatigue life calculations for the variable amplitude tests of Chapter 4 has not been included. This work is part of Mr. S.G. Lee's Ph.D. dissertation and his work will not be completed until summer, 1982. The report is also incomplete from the standpoint that a complete integration of Chapters 2-6 has not been included. Thus each chapter principally stands as a separate entity and can essentially be published in this manner. Professor Stephens decided not to write the integrating chapter at this time since an extension of the low cycle fatigue behavior to 2×10^7 reversals and an extension of fatigue crack growth rates to threshold levels is currently in progress. Both these extensions involve room temperature and -50°F (-45°F). When the extension is completed, a much more meaningful integration/correlation of this report will be made. Thus additional chapters to this report will include fatigue life calculations, extension of low cycle fatigue to 2×10^7 reversals, threshold and near threshold fatigue crack growth behavior, and a chapter tying together all the results. This addition will be completed by December 1982 and issued as a separate research report.

The report has only a single author, yet many people were directly and indirectly involved with the research. Essentially all of the individual research was accomplished by graduate students working on advanced degrees at the University of Iowa under the direction of Prof. Stephens. To understand how broad the research was, graduate student theses in Chemical and Materials Engineering, Civil Engineering, and Mechanical Engineering were written from this project. Three Master of Science degrees and two Ph.D. degrees were or will be earned from this research project. Two additional graduate students worked on the project as part of their research assistantship duties. Graduate students that participated in this work are: J. Chung, A. Fatemi, H. Lee, G. Njus, C. Vaca and C. Wang.

Prof. Stephens, his students and his staff are to be commended on a major contribution to the understanding of the behavior of cast steels. The Carbon and Low Alloy Technical Research Committee wishes to express its appreciation on behalf of the Society for this fine work.

Dr. John Svoboda
Technical and Research Director

by direction of the
Carbon and Low Alloy
Technical Research Committee

R. C. Maxton, Chairman

D. C. Harsch
P. Harvey
E. J. Lenar
R. P. Pritchard
W. Scott
E. E. Weber
R. Young

Chapter 1

Introduction and Material Characterization

1.1 Introduction

Design engineers must make decisions concerning component material selection and size. These decisions have been made with and without adequate rational. The SAE Fatigue Design and Evaluation Committee along with ASTM E-9 and E-24 committees have attempted to formulate, verify and promote rational criteria for design against fatigue and fracture. Design philosophies based upon low cycle fatigue strain versus life behavior, $\epsilon_a - N_f$, crack propagation, $da/dN - \Delta K$, and fracture toughness, K_{Ic} , K_{IIc} , J_{Ic} , have emerged as being sound and successful. These design philosophies will grow with even greater emphasis in the future. The US government has already required usage of fracture toughness and fatigue crack propagation concepts in design and inspection in aerospace structures, nuclear pressure vessels, and bridge design. Room temperature crack propagation data and fracture toughness data have been accumulated in the Damage Tolerant Design Handbook (1) to aid in design decisions. SAE has accumulated room temperature low cycle fatigue data in publication J1099 (2) for this same purpose and is attempting to expand this publication. ASTM has prepared recommended practices for obtaining low cycle fatigue data, fatigue crack propagation data, and fracture toughness. Additional committee work is going on to improve these practices and extend them to more complex and newer ideas. Thus both SAE and ASTM along with other professional engineering societies are well aware of the need for rational fatigue and fracture design which includes usage of known material properties, testing, and inspection.

The steel fatigue material properties available to design engineers through SAE J1099 and the Damage Tolerant Design Handbook are essentially for wrought steels at room temperature. Little cast steel low cycle fatigue, crack propagation, and fracture toughness data are available. Very little low temperature fatigue and fracture toughness behavior exists for either wrought or cast steels. Low temperature fatigue behavior is often con-

sidered to be better than room temperature behavior. This is true in many constant amplitude tests involving various types of specimens. However, sufficient constant amplitude tests also dispute this, particularly in steels below their nil ductility transition regions (3,4). This transition region under fatigue may or may not coincide with impact transition regions. Under real-life spectrum loads, substantial interaction and sequence effects occur and constant amplitude test data may not provide adequate fatigue life prediction information. For example, the lower fracture toughness and ductility at low temperatures can be very detrimental. Residual compressive and tensile stresses formed from service loading, which greatly affect fatigue behavior, will be different at room and low temperatures. Thus both room and low temperature fatigue behavior of cast steels under both constant amplitude and representative variable amplitude loading is badly needed by design engineers.

The objectives of this research are to provide the design engineer with the above needed fatigue and fracture toughness material properties for five common carbon or low alloy cast steels at both room temperature and low climatic temperature. Both macro and microscopic fractography are used to aid in better understanding this mechanical behavior. In addition, total fatigue life predictions for variable amplitude loading, developed principally for wrought steels, are extended to cast steels at both room and low temperatures. The research/material properties obtained can be broken down as follows:

1. Microstructure
2. Monotonic tensile stress-strain behavior, $\sigma - \epsilon$
3. Cyclic stress-strain behavior, $\sigma' - \epsilon'$
4. Low cycle fatigue behavior

$$\frac{\Delta \epsilon}{2} = \frac{\sigma_f}{E} (2N_f)^b + \epsilon_f' (2N_f)^c$$

5. Fatigue crack propagation behavior

$$\frac{da}{dN} = A (\Delta K)^n$$

6. Variable amplitude loading using the SAE transmission history and a modified transmission history with a keyhole specimen for both crack initiation, propagation and final fracture.

7. Plane stress fracture toughness, R-curve

8. $J_{Ic} \rightarrow K_{Ic}$ and CVN correlations

9. Macro and microscopic (SEM) fractography and analysis

10. Total fatigue life predictions of cast steels.

The principal low temperature chosen was -50°F (-45°C) since this is a representative low climatic temperature found in the U.S.A. A few tests were run on one steel at -30°F (-34°C) before the -50°F (-45°C test temperature was finalized. In addition, a few variable amplitude loading tests were run at -75°F (-60°C) and -30°F (-34°C) to determine additional low temperature influence on fatigue behavior.

1.2 Material Selection and Characterization

1.2.1 Materials

About ten major companies from the ground vehicle industry, along with the SFSA Carbon and Low Alloy Research Committee, provided input to the selection of five commonly used carbon or low alloy cast steels. Five different cast steels rather than different heat treatments of the same cast steel were chosen in order to provide more diverse representative material properties for the engineering profession. The five cast steels chosen were:

SAE 0030: normalized and tempered (NT)

SAE 0050A: normalized and tempered (NT)

C-Mn: normalized, quenched and tempered (NQT)

Mn-Mo: normalized, quenched and tempered (NQT)

AISI 8630: normalized, quenched and tempered (NQT)

Their room temperature ultimate tensile strengths and yield strengths ranged from 72-166 ksi (500-1150 MPa) and 44-143 ksi (300-1000 MPa) respectively. Brinell hardness varied from 137 to 305 and both ferritic-pearlitic and tempered martensitic microstructures were involved. Thus, the five cast steels investigated include a wide range of representative carbon and low alloy cast steels used in the ground vehicle industries and in other industries.

1.1.2 Pouring, Heat Treatment and Microstructure

Approximately twenty individual casting blocks were poured from a single melt for each of the five cast steels at different companies. The 0030 and 8630 steels were poured by Pelton Casteel Inc., Milwaukee, Wisconsin, the C-Mn and Mn-Mo was poured by Evans/Racine Steel Castings, Racine, Wisconsin and the 0050A steel was poured by Sterling Steel Casting Co., East St. Louis, Illinois. The cast blocks were heavily risered for proper soundness. The 0030 steel was cast as blocks 4.5 in (115 mm) x 4 in (102 mm) x 3 in (76 mm) while the other four steels were cast as blocks 18.5 in (470 mm) long with a trapezoidal cross-section about 5.5 in (140 mm) high and thickness of 1.7 in (43 mm) and 2.7 in (69 mm). The heat treatment of the five cast steels is given in Table 1.1 and the final chemical composition, % by weight, is given in Table 1.2. The medium carbon 0030 steel and the high carbon 0050A steel were both normalized and tempered (NT) resulting in a ferritic-pearlitic microstructure while the low-alloy C-Mn, Mn-Mo and 8630 steels were normalized, austenitized, water quenched, and tempered (NQT) resulting in a tempered martensitic microstructure. Final microstructures for the five cast steels are shown in Figure 1.1. These microphotographs were taken at 500 x magnification. The etchant was 3% Nital solution. The ASTM grain size for the 0030 steel is 8 to 9 which is quite a fine grain size. For 0050A steel the ASTM grain size is also 8 to 9. The microstructure of 0030 steel has approximately 75 percent ferrite and 25 percent pearlite. The 0050A steel with its higher carbon content has approximately 20 percent ferrite and 80 percent pearlite.

Table 1.1. Cast Steel Heat Treatment

0030			
Normalize	30 min.	at	1650°F (900°C)
Temper	90 min.	at	1250°F (677°C)
0050A			
Normalize	4 hrs.	at	1650°F (900°C)
Temper	4 hrs.	at	1200°F (650°C)
C-Mn			
Normalize	3 hrs.	at	1650°F (900°C)
Austenitize	1 hr.	at	1650°F (900°C)
Water quench			
2nd Austenitize*	1 hr.	at	1650°F (900°C)
Water quench			
Temper	2½ hrs.	at	1150°F (620°C)

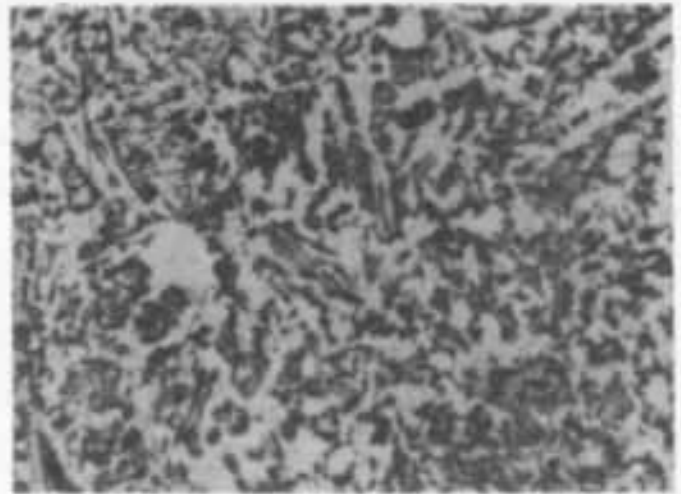
(continued)

Table 1.1. Cast Steel Heat Treatment (cont.)

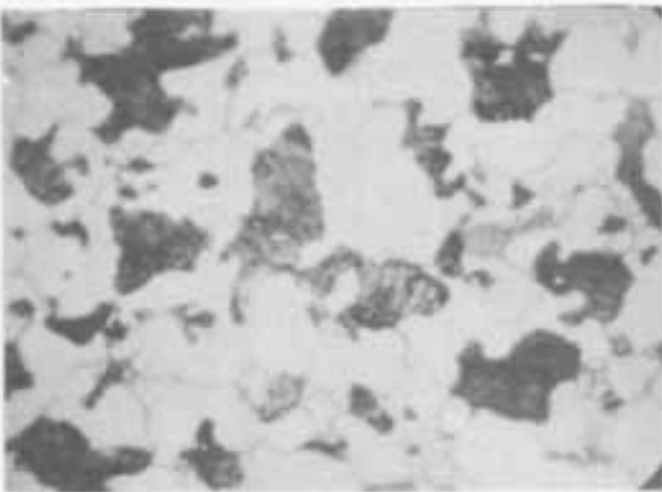
Mn-Mo			
Normalize	3 hrs.	at	1650°F (900°C)
Austenitize	1 hr.	at	1650°F (900°C)
Water quench			
+ Temper	2½ hrs.	at	1025°F (552°C)
+ Temper	2½ hrs.	at	1120°F (604°C)
+ Temper	2½ hrs.	at	1200°F (650°C)
+ Temper	2½ hrs.	at	1260°F (682°C)

8630			
Normalize		at	1650°F (900°C)
Austenitize		at	1625°F (885°C)
Water quench			
Temper	1½ hrs.	at	950°F (510°C)

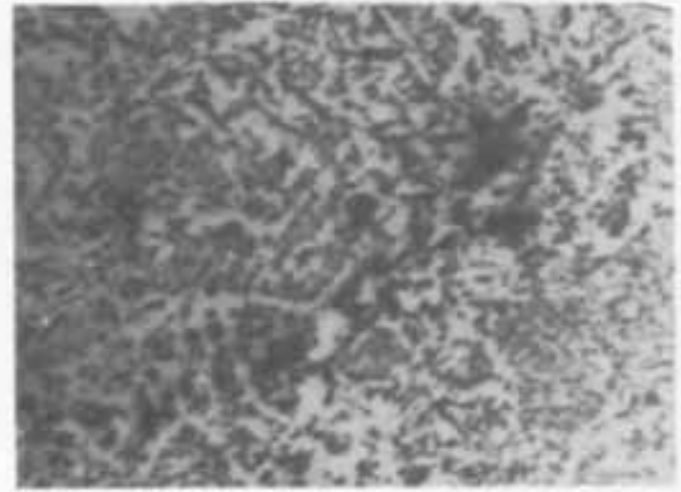
*to assume complete austenitization
 +to avoid overtempering blocks were tempered in successive stages.



C-Mn



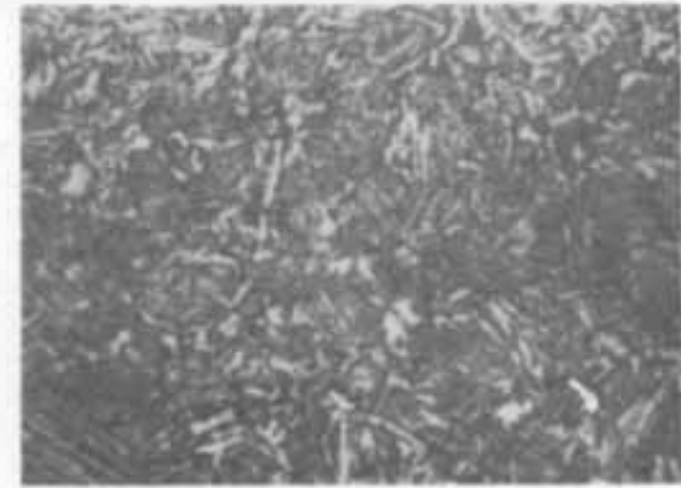
0030



Mn-Mo



0050A



8630

Figure 1.1. Cast steel microstructures, 500x.

Table 1.2. Cast Steel Chemistry - % by Wt.

	C	Mn	Si	S	P	Cr	Ni	Mo	Al	Cu	Ti	V
0030	.24	.71	.44	.026	.015	.10	.10	.08	.06	.05	.013	
0050A	.49	.93	.61	.023	.024	.11	.08	.04	.08	.07		.012
C-Mn	.23	1.25	.39	.028	.036	.10	.09	.04	.02			
Mn-Mo	.34	1.32	.40	.035	.024	.11	.11	.22	.06			
8630	.30	.84	.53	.022	.021	.51	.61	.17	.08	.020		.01

All five cast steels contained the usual inclusions and porosity. These were readily found in the scanning electron microscope (SEM) while examining the various fatigue and fracture surfaces. It was later found, however, that the 8630 steel percent reduction in area, as determined from a monotonic tensile test, was unusually low at room temperature. Low cycle fatigue tests at room temperature with 8630 steel also produced unreasonably poor results at the larger strain amplitudes. All other 8630 tests had very reasonable and consistent results. SEM fractographic analysis of these few tests at both room and low temperature revealed 20 to 30 percent micro shrinkage in room temperature specimens. These tests are to be repeated with specimens taken from blocks which do not contain this unreasonable localized micro shrinkage.

The principal inclusions found in the steels were MnS. The chemical composition of these major inclusions were verified using an electron microprobe. Other inclusion chemistries were also

determined, however these were much smaller in both size and proportion of inclusions. It was concluded from the above examinations that, except for some localized regions in the 8630 steel blocks, the five cast steels had typical and representative chemical compositions and microstructure.

1.2.3 Hardness

Rectangular blocks were cut from the cast blocks for each steel and hardness measurements were made on three orthogonal planes (Table 1.3) with both the Rockwell B and Brinell hardness testers. The Rockwell B tests were used to obtain a range of hardness from top to bottom and across the section. As many as 15-40 Rockwell B readings were taken in a given direction. The range of values is shown in Table 1.3 for the five cast steels. Occasionally a very low reading occurred in the 0030 and 0050A steel, but duplicate tests taken adjacent to these low values fell within the ranges given in Table 1.3. Thus, these low readings were omitted since the very small size of the Rockwell B ball contributes to larger hardness scatter in cast steels compared to Brinell hardness results.

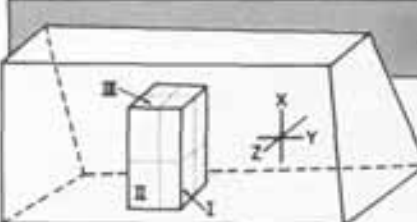


Table 1.3. Cast Steel Hardness Summary

	0030		0050A		C-Mn		Mn-Mo		8630	
	BHN	R _b								
Face I	135		191		176		206			
x direction		75-85		90-98		95-98		102.5-106	307	-
z direction		77-83		88-98		96-97		103-104.5	315	-
Face II	140		193		177		207			
x direction		78-83		88-100		95-98		100.5-104	302	-
y direction		78-84		93-98		95-97		102-103	302	-
Face III	137		191		170		204			
y direction		77-83		97-99		94-96		103-104	302	-
z direction		81-84		98-100		94-97		102-103	302	-
	BHN _{AVE} = 137		BHN _{AVE} = 192		BHN _{AVE} = 174		BHN _{AVE} = 206		BHN _{AVE} = 305	
	R _{bAVE} = 79		R _{bAVE} = 97		R _{bAVE} = 96		R _{bAVE} = 102			

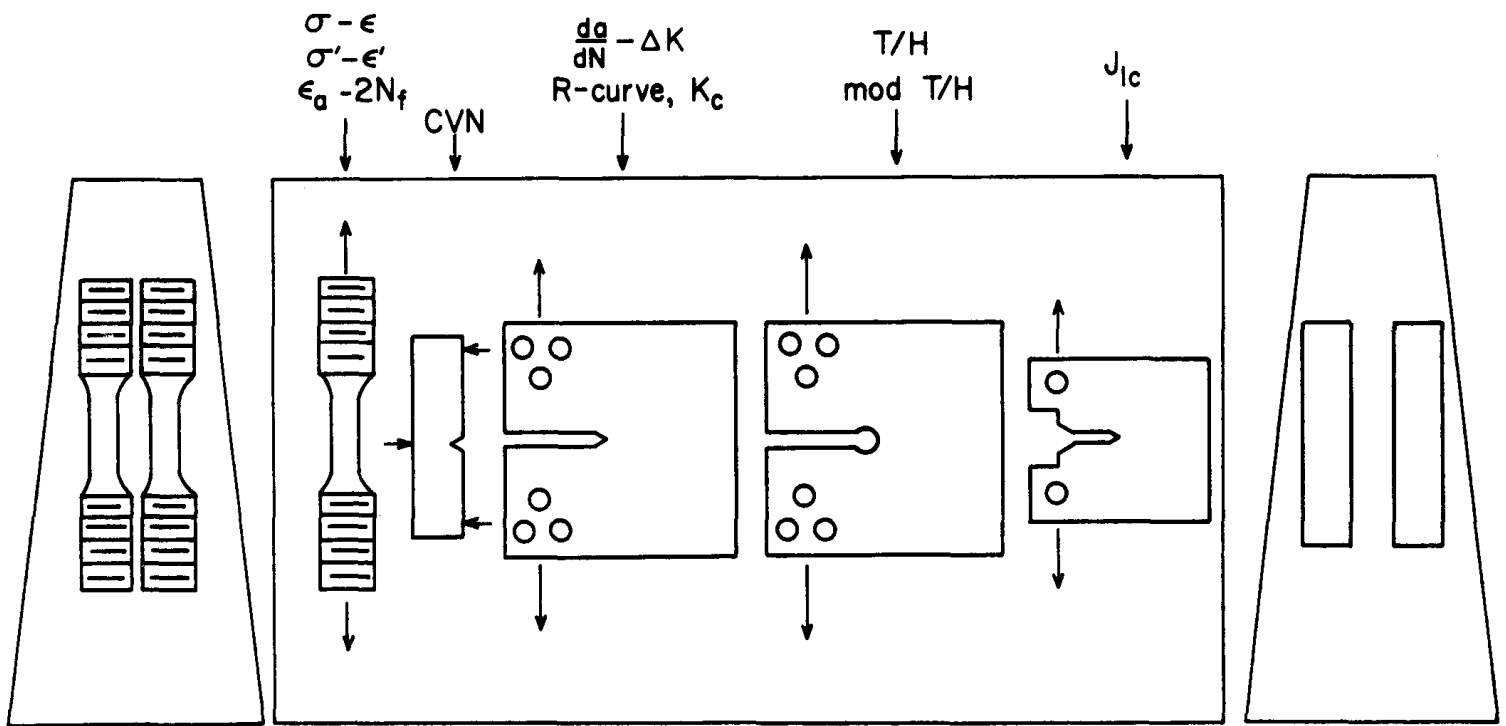


Figure 1.2. Test specimens orientation within a block.

Three to eight Brinell hardness readings were obtained for each of the three orthogonal faces using a 3000 kg loading for 8630 steel and three readings per face were made using a 1500 kg loading for the other four steels. These results are given in Table 1.3. The average Rockwell B and Brinell hardness values for each steel are also given in Table 1.3. The average Brinell hardness values were 137, 192, 174, 206 and 305 for 0030, 0050A, C-Mn, Mn-Mo and 8630 cast steel respectively.

In general, the Rockwell B and Brinell tests indicated hardness variation was not significant for a given steel.

1.2.4 Monotonic Tensile Properties

Test specimen orientations for the trapezoidal cross-section blocks are shown in Figure 1.2. The top, bottom and middle longitudinal portions of the blocks were not used for test specimens due to possible different flow characteristics during pouring. Specimens were taken randomly along the length of the blocks. All specimens were aligned such that the plane of maximum normal stress (and plane of crack propagation) was the same for all tests. The 0030 steel, which was cast as rectangular blocks, also had all specimens aligned with the maximum normal stress on the same plane. The tensile specimens and low cycle fatigue specimens were identical with detailed dimensions shown in Figure 1.3. The nominal diameter was 1/4 in (6.3 mm) and the gage length was 0.5 in (12.7 mm). These specimens contained a polished surface with all final polishing scratches in the longitudinal direction. Tensile tests were performed with a 20 kip (89 kN) MTS electrohydraulic test system in ram displacement control. All grips were loose before starting the test to assume axial alignment. The low temperature tests were performed in an automated CO₂ cold temperature chamber. Autographic strain readings were only obtained up to about 1.5 percent strain due to the limits of the extensometer. Loads, however, were recorded to fracture. The strain rate in the elastic and initial yield region was about .0007 sec⁻¹. At the higher

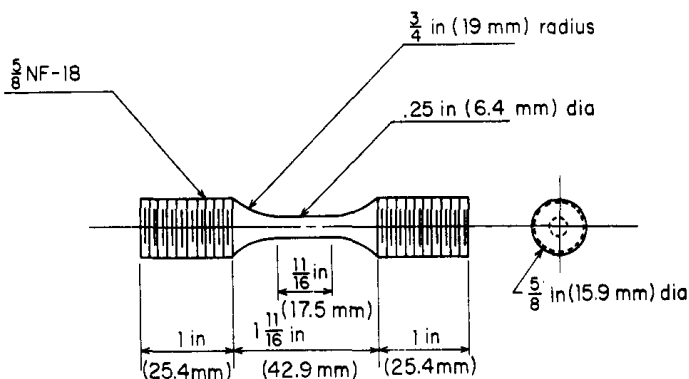


Figure 1.3. Uniaxial tensile and low cycle fatigue specimen.

Table 1.4. Cast steel monotonic tensile stress-strain properties

Material	S _u ksi/MPa	.2% S _y ksi/MPa	S _{yp} ksi/MPa	σ _f ksi/MPa	% RA	ε _f	E Mpsi/GPa	Specimen Number
Room Temperature								
0030*	72/496	44/303	52/358	109/750	46	.62	30/207	-
0050A	114.2/788	60.8/419	62/427	125.4/864	17.5	.192	30.3/209	A1
	114/785	60.1/414	60.1/414	124.7/859	19.7	.219		A2
C-Mn	83.2/573	57.5/396	60.6/418	100.2/690	27.5	.322	30.2/209	C1
	85.9/592	59/407	65.2/449	104/717	29.6	.351		C2
Mn-Mo	101.9/702	79.5/548	77.5/534	106.6/735	30.6	.365	30.6/211	M1
	102/702	77.6/535	79.6/548	110.6/762	32.0	.386		M2
8630	166.3/1146	141.4/974	-	182.1/1255	23	.261	30/207	28
	166/1144	145.4/1002	-	187/1288	35	.43		34
-50°F (-45°C)								
0030	78.7/542	47.4/327	56/386	92/634	31.7	.381	30.3/209	S1L
	78.5/541	45.3/312	52/358	88.7/611	28.4	.334		S2L
0050A	121/834	64.2/442	69.4/478	131/903	13.3	.143	30.3/209	A1L
	121/834	62.1/428	64.2/442	137/944	18.4	.203		A2L
C-Mn	89.8/619	61.6/424	67/462	100.6/693	22.8	.259	30.2/209	C1L
	87.8/605	72.9/502	75.5/620	83.6/576	14.0	.15		C3L
Mn-Mo	108/744	81.5/562	83/572	119.2/821	26.1	.302	30.5/210	M1L
	111/765	81.5/562	84.5/582	130.3/898	34.0	.416		M2L
8630	175.7/1211	149.6/1031	-	182/1254	25.9	.299	31.1/214	29
	166.6/1148	141.3/974	-	182/1254	30.3	.361		31.2/215

*Average values only.

strains, the strain rate was increased by a factor of 3 to about .002 sec⁻¹. Total test time per specimen took up to about eight minutes or less. Two specimens were tested for each steel at both room temperature and -50°F (-45°C). A third 8630 steel specimen was tested at each temperature to be sure the low percent reduction in area was not due to experimental error. The tensile test results of each specimen are shown in Table 1.4 and the average values are shown in Table 1.5. Both American/British units and SI units are included in the Tables. S_u is the ultimate tensile strength, S_y is the 0.2% offset yield strength, and S_{yp} is the upper yield point stress, σ_f is the true fracture stress calculated from the final fracture load divided by the area at fracture and ε_f is the true fracture strain calculated from

$$\epsilon_f = \ln\left(\frac{1}{1-RA}\right) \quad (1.1)$$

where RA is the reduction of the cross-sectional area at fracture. E is Young's modulus of elasticity.

Very little scatter occurred for a given material and test temperature. Typical stress-strain curves in the yield region for each of the five steels at room temperature and -50°C (-45°C) are shown in Figure 1.4.

Tables 1.4 and 1.5 and Figure 1.4 indicate that -50°F (-45°C) had essentially no effect on Young's modulus but increased the yield strengths by about 5 percent (15 Percent for C-Mn) and increased the ultimate strength by approximately 5-10 percent for all of the cast steels. The reduction in area at -50°F (-45°C) decreased 34% for 0030, 15% for 0050A, 36% for C-Mn, and 4% for Mn-Mo, and 8630 steel. The true fracture stress at -50°F (-45°C) decreased for 0030, C-Mn and 8630 steels but increased for 0050A and Mn-Mo steels.

Strain rate influence on the monotonic tensile yield properties were obtained from the first 1/4 cycle of the low cycle fatigue tests. In these tests, the strain rate was set at 0.01 sec⁻¹ which took bet-

Table 1.5. Cast Steel Average Monotonic Tensile Stress-Strain properties.

Material	S _U ksi/MPa	.2% S _y ksi/MPa	S _{yp} ksi/MPa	σ _f ksi/MPa	% RA	ε _f	Mpsi/GPa
Room Temperature							
0030*	72/496	44/303	52/358	109/750	46	.62	30/207
050A	114/787	60/415	61/421	126/866	19	.21	30.3/209
C-Mn	85/583	58/402	63/434	102/703	26	.34	30.2/209
Mn-Mo	102/702	79/542	79/542	109/749	31	.37	30.6/211
8630	166/1144	143/985	-	184/1268	29	.35	30/207
-50°F (-45°C)							
0030	79/542	46/320	54/372	90/622	30	.36	30.3/209
0050A	121/834	63/436	67/450	134/924	16	.17	30.3/209
C-Mn	89/612	67/464	71/492	92/634	18	.21	30.2/209
Mn-Mo	110/758	81/562	84/579	125/861	30	.36	30.5/210
8630	171/1178	145/999	-	182/1254	28	.33	31/214

*Obtained from reference 5.

ween 0.5 and 1.5 seconds to yielding. This rate is about 15 times faster than the normal monotonic tensile tests. The increase in the upper yield point stress ranged from zero to eight percent while the .2% yield strength and Young's modulus were essentially unaffected.

1.2.5 Charpy V Notch Impact (CVN)

Standard 10 mm x 10 mm Charpy V notch

specimens were tested with a standard pendulum impact test machine from -100°F (-73°C) to +250°F (121°C). Two specimens were tested at about ten different temperatures within this range for each of the five cast steels. The CVN energy versus temperature results are shown in Figure 1.5. Superimposed on the five curves are four vertical lines which represent the four test temperatures involved in this research. The principal temperatures of room and -50°F (-45°C) plus the additional temperatures of -30°F (-34°C) and -75°F (-60°C) are indicated.

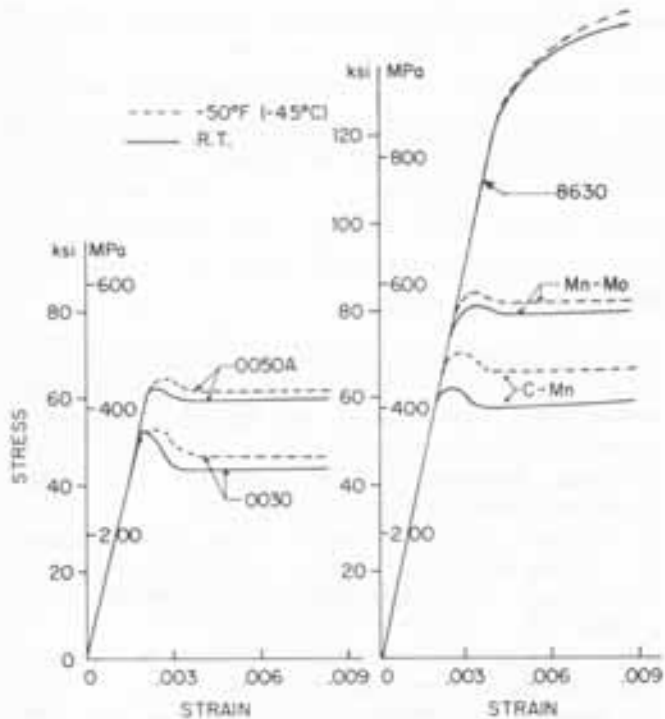


Figure 1.4. Monotonic tensile behavior in the yield region, room temperature and -50°F (-45°C).

The upper shelf region was found to be below 250°F (121°C) for all steels except 0050A. The lower shelf region was above -100°F (-73°C) for the 0030, 0050A and 8630 cast steels. The lower shelf region for C-Mn and Mn-Mo occurs at a temperature less than -100°F (-73°C). Room temperature is in the upper shelf region for C-Mn and Mn-Mo steels, is in the upper transition region for 0030 and 8630 steels, and is in the lower transition region for 0050A steel. The three low test temperatures are in the lower transition region for C-Mn, Mn-Mo and 8630 steels and essentially in the lower shelf region of 0050A, however, exists up to about 25°F (-4 °C) which is well above the three low temperature test conditions. The data for lateral contraction and percent crystalline fracture are consistent with respect to energy values given in Figure 1.5.

The smooth monotonic tensile specimens tested at -50°F (-45°C) do not show the sensitivity to temperature as do the notched impact Charpy V notch specimens, which is quite usual.

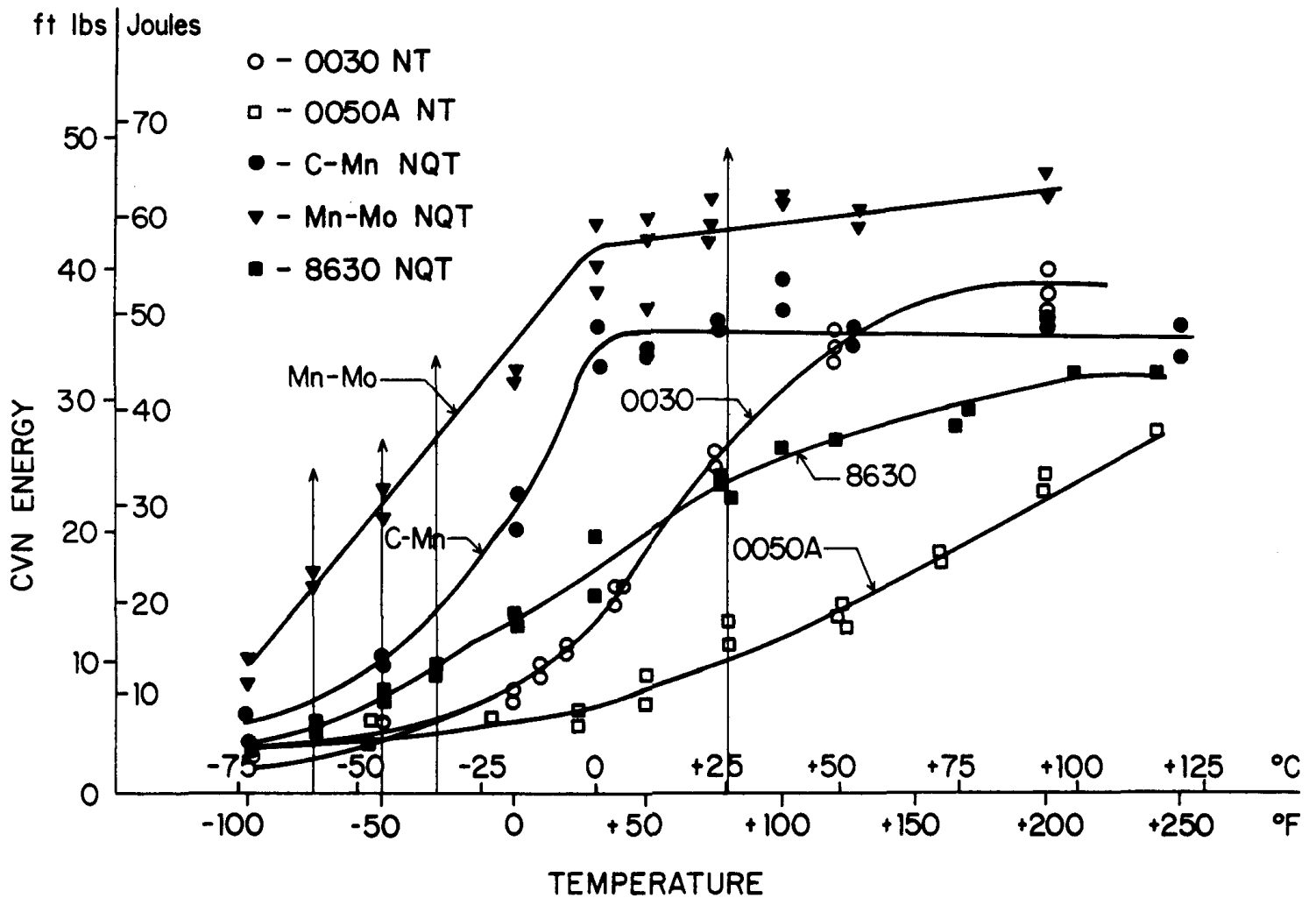


Figure 1.5. Charpy V notch behavior.

1.3 Summary

The five carbon or low alloy cast steels contained representative microstructures, hardness, tensile properties and CVN behavior. However, the percent RA in 8630 was outside usual limits due to localized microshrinkage. BHN values ranged from 137 to 306. The averaged room temperature ultimate strengths were 72 (496), 114 (787), 85 (583), 102 (702), and 166 (1144 MPa) for 0030, 0050A, C-Mn, Mn-Mo, and 8630 cast steels respectively. Tensile ultimate and yield strength at -50°F (-45°C) were increased between 5-15 percent for all steels compared to room temperature values. Ductility, as measured by percent RA, decreased in all steels at -50°F (-45°C). A strain rate increase by a factor of 15 had essentially no effect on the 2% yield strength and Young's modulus but increased the upper yield point from zero to eight percent. The -50°F (-45°C) temperature occurs in the lower CVN transition region for C-Mn, Mn-Mo and 8630

steels and in the lower shelf region for 0030 and 0050A steels.

Chapter 1 References

1. Damage Tolerant Design Handbook, A Completion of Fracture and Crack Growth Data for High Strength Alloys, MCIC-HB-01, Metals and Ceramics Information Center. Battelle, Columbus. Ohio.
2. "Technical Report on Fatigue Properties", SAE J1099, Society of Automotive Engineers, Feb. 1975.
3. R.I. Stephens, J.H. Chung and G. Glinka, "Low Temperature Fatigue Behavior of Steels - A Review", paper No. 790517, April, 1979, SAE Transactions, Vol. 88, 1980, p. 1892.
4. H.O. Fuchs and R.I. Stephens, Metal Fatigue in Engineering, Wiley Interscience, New York, 1980.
5. R.I. Stephens, G. Mauritzson, P.H. Benner and D.R. Galiart, "Fatigue and Fracture Roughness of SAE 0030 Cast Steel and Comparison with SAE 1020 Wrought Steel", J. of Steel Castings Research, No.83, July, 1978, p. 1.

Cyclic Stress-Strain and Low Cycle Fatigue

2.1 Cyclic Stress-Strain Behavior

The cyclic stress-strain curve provides a measure of the steady-state cyclic deformation resistance of a material. It may be quite similar or substantially different from the monotonic stress-strain curve. It is obtained by connecting the tips of stable true stress-strain hysteresis loops from either companion test specimens or from a single specimen subjected to incremental strain, or multiple steps. Both the companion specimen method and the incremental step method were used in this research to obtain cyclic stress-strain curves for the five cast steels, 0030, 0050A, C-Mn, Mn-Mo and 8630, at room temperature and -50°F (-45°C). The companion specimen cyclic stress-strain curves were obtained from strain controlled low cycle fatigue tests using the stress amplitude, and the total, elastic and plastic strain amplitude components at half-life. Approximately ten specimens were used per test condition.

The test specimen used for obtaining the cyclic stress-strain properties and the low cycle fatigue behavior is shown in Figure 2.1. Specimens were polished with decreasing grades of emery cloth from 0 to 000. Final polishing scratches were in the longitudinal direction. A 20 kip (89 kN) closed-loop electrohydraulic test system using strain control was used for the tests. Specimens were mounted in

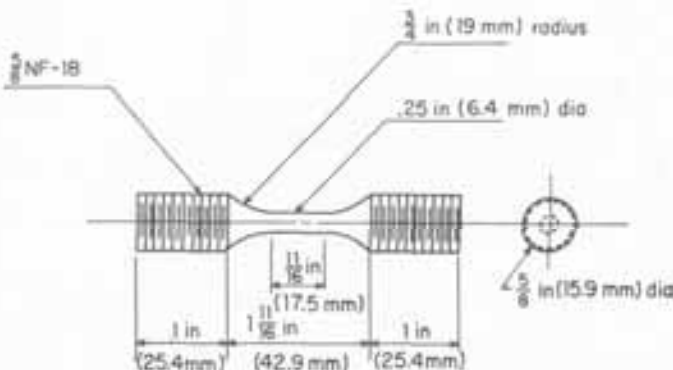


Figure 2.1. Low cycle fatigue specimen.

an axially aligned Wood's metal grippina system which eliminates bending stresses during final specimen locking. An automated CO₂ temperature chamber was used for the low temperature tests.

Strain input history and corresponding typical load response for the incremental step test is shown in Figure 2.2. Each strain block contained 79 reversals with the magnitude ranging from zero to 0.012 strain. A constant strain rate, $\dot{\epsilon}$, equal to 0.01 per second was used for the incremental step tests. Hysteresis loops from the second and third blocks were recorded on an X-Y recorder during the test. Typical load-strain hysteresis loops are shown in Figure 2.3 for C-Mn cast steel at room temperature and -50°F (-45°C). Cyclic stress-strain curves were obtained by drawing a curve through the tips of these hysteresis loops. This was usually through the decreasing portion of the second block.

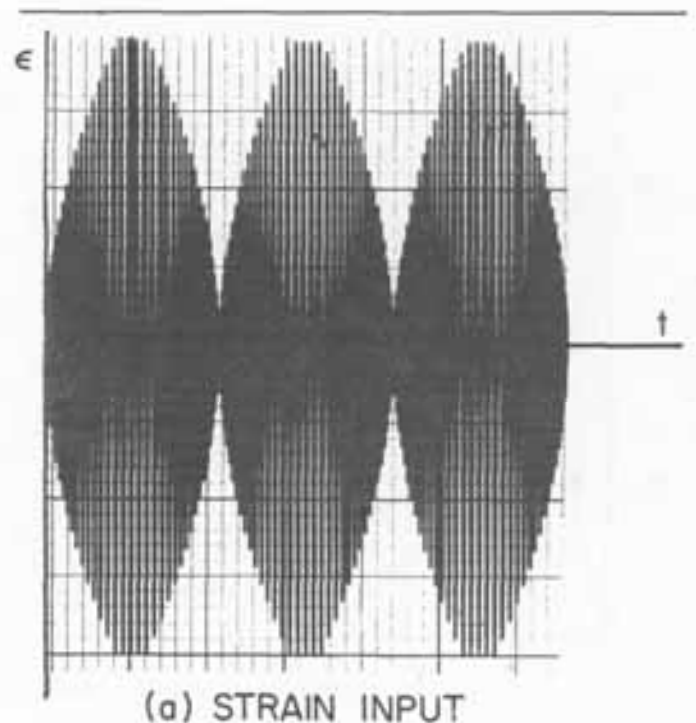


Figure 2.2(a). Incremental step test record.

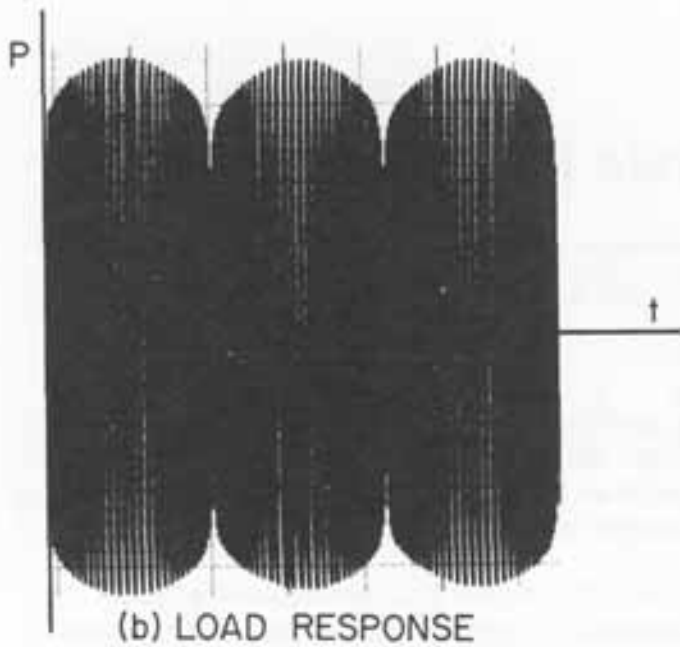


Figure 2.2(b). Incremental step test record.

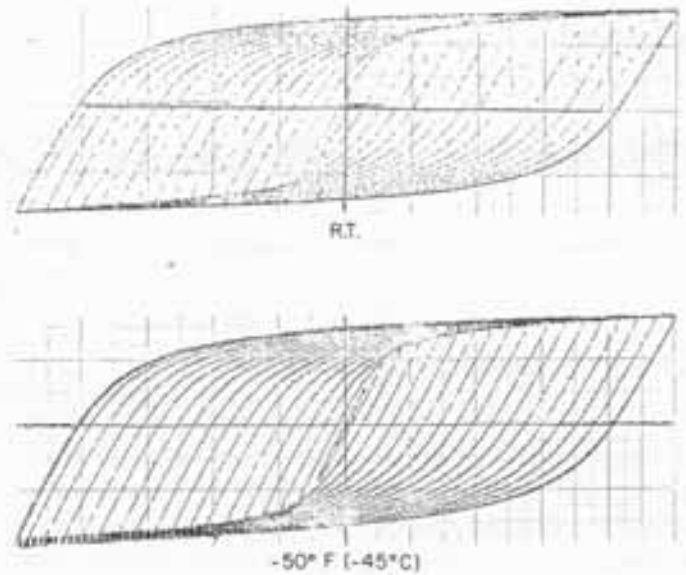


Figure 2.3. Incremental step hysteresis loops, C-Mn steel.

Cyclic stress-strain curves using the incremental step method and the companion specimen method are shown superimposed on monotonic stress-strain curves in Figures 2.4 to 2.8 for both room temperature (R.T.) and -50°F (-45°C). The solid curves are the monotonic stress-strain curves taken from Figure 1.4 while the two different dashed lines represent the cyclic stress-strain behavior. For all

five cast steels at both temperatures, the cyclic stress-strain curves are initially identical to monotonic curves and then become nonlinear at stresses or strains of about 20 to 50 percent below that for the monotonic curves. The monotonic upper yield point stress found in four of the five cast steels was eliminated under the cyclic conditions (8630 has a continuous monotonic stress-strain

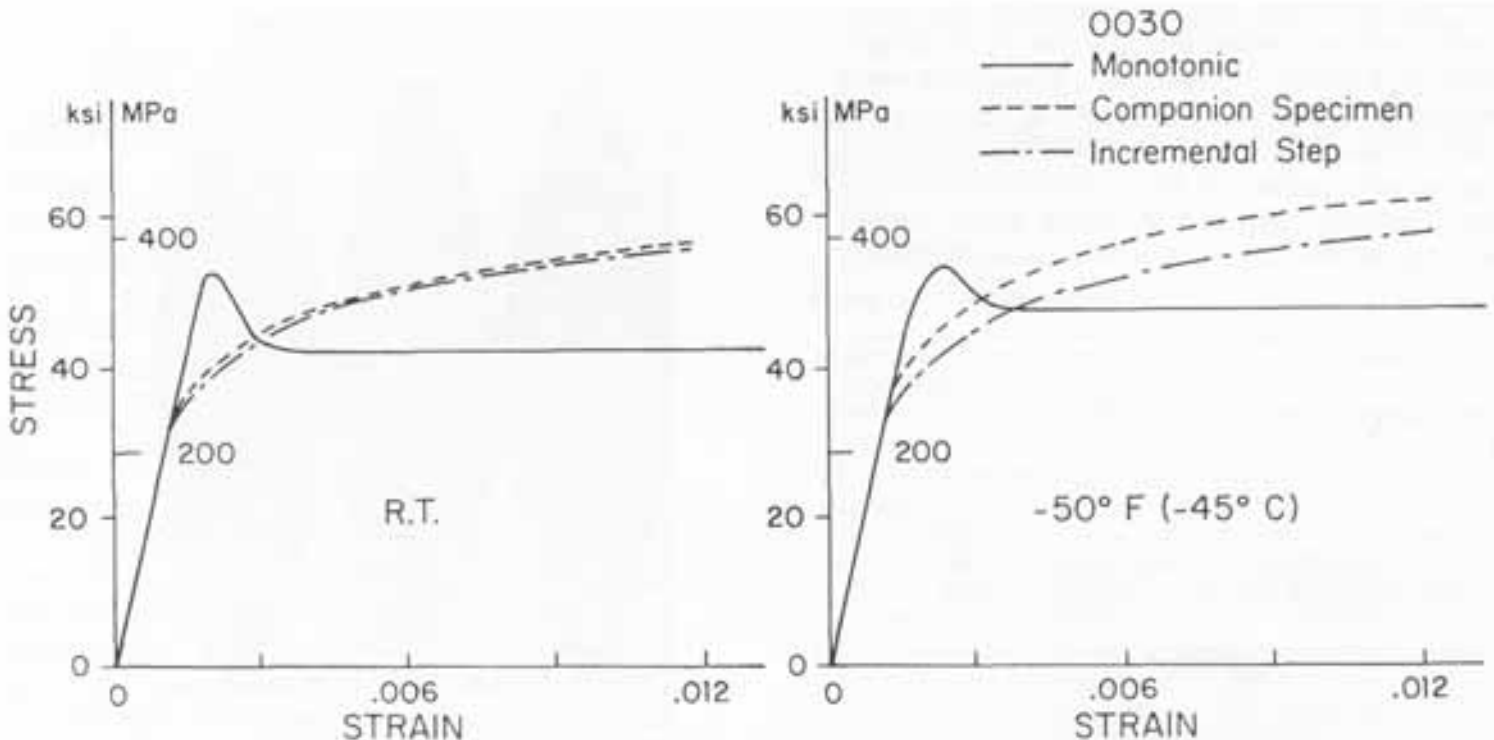


Figure 2.4. Monotonic and cyclic stress-strain behavior, 0030 cast steel.

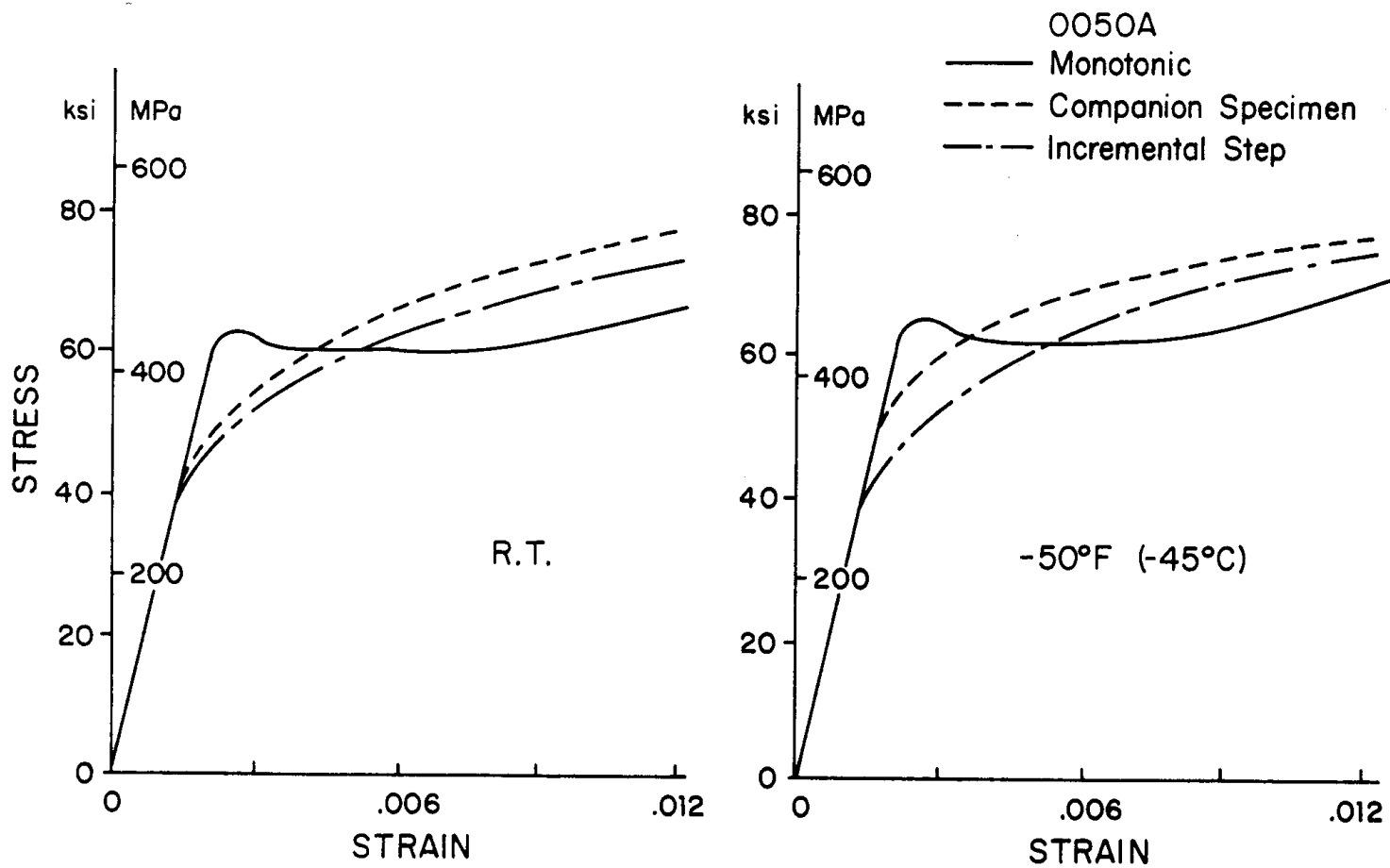


Figure 2.5. Monotonic and cyclic stress-strain behavior, 0050A cast steel.

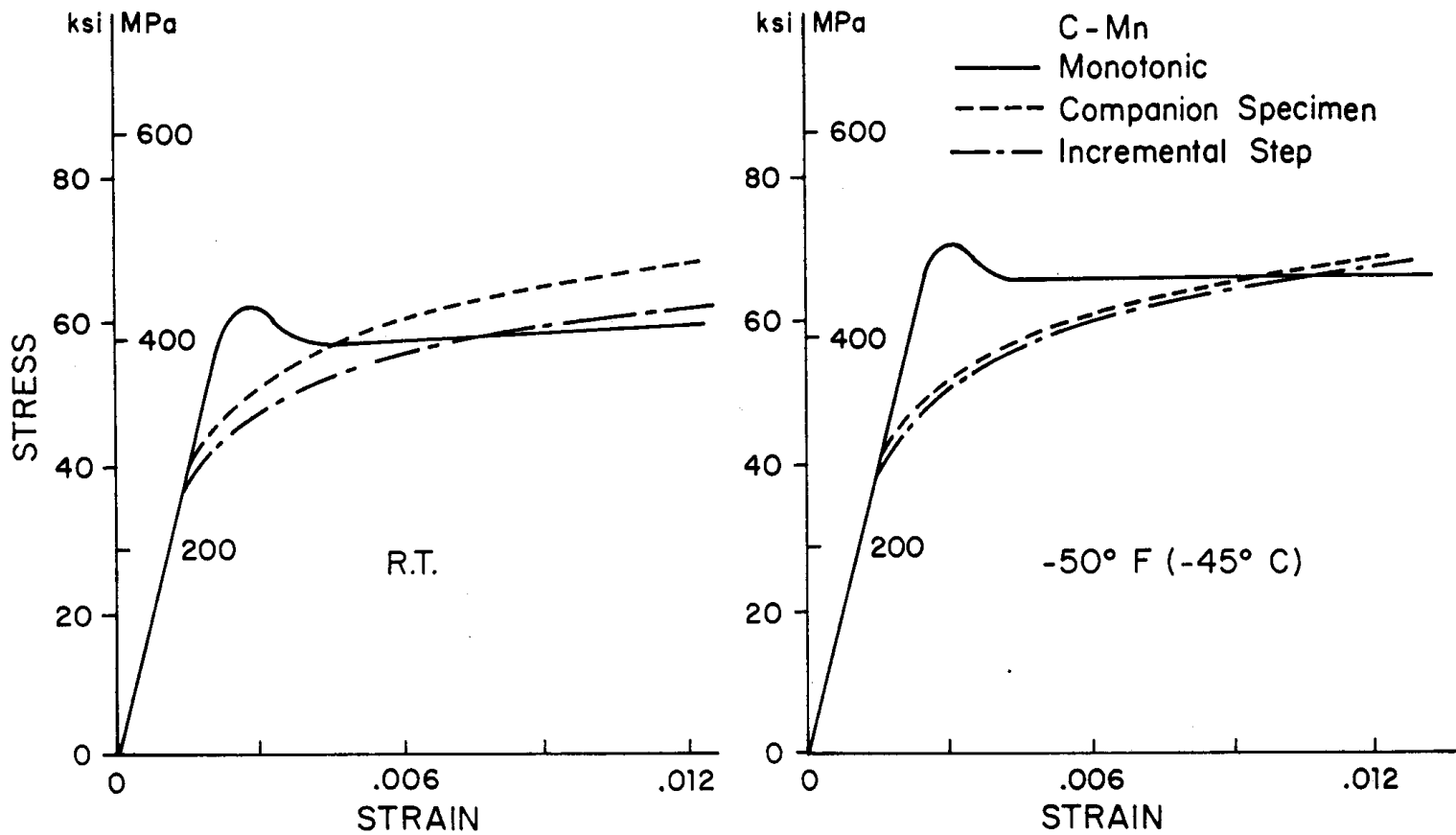


Figure 2.6. Monotonic and cyclic stress-strain behavior, C-Mn cast steel.

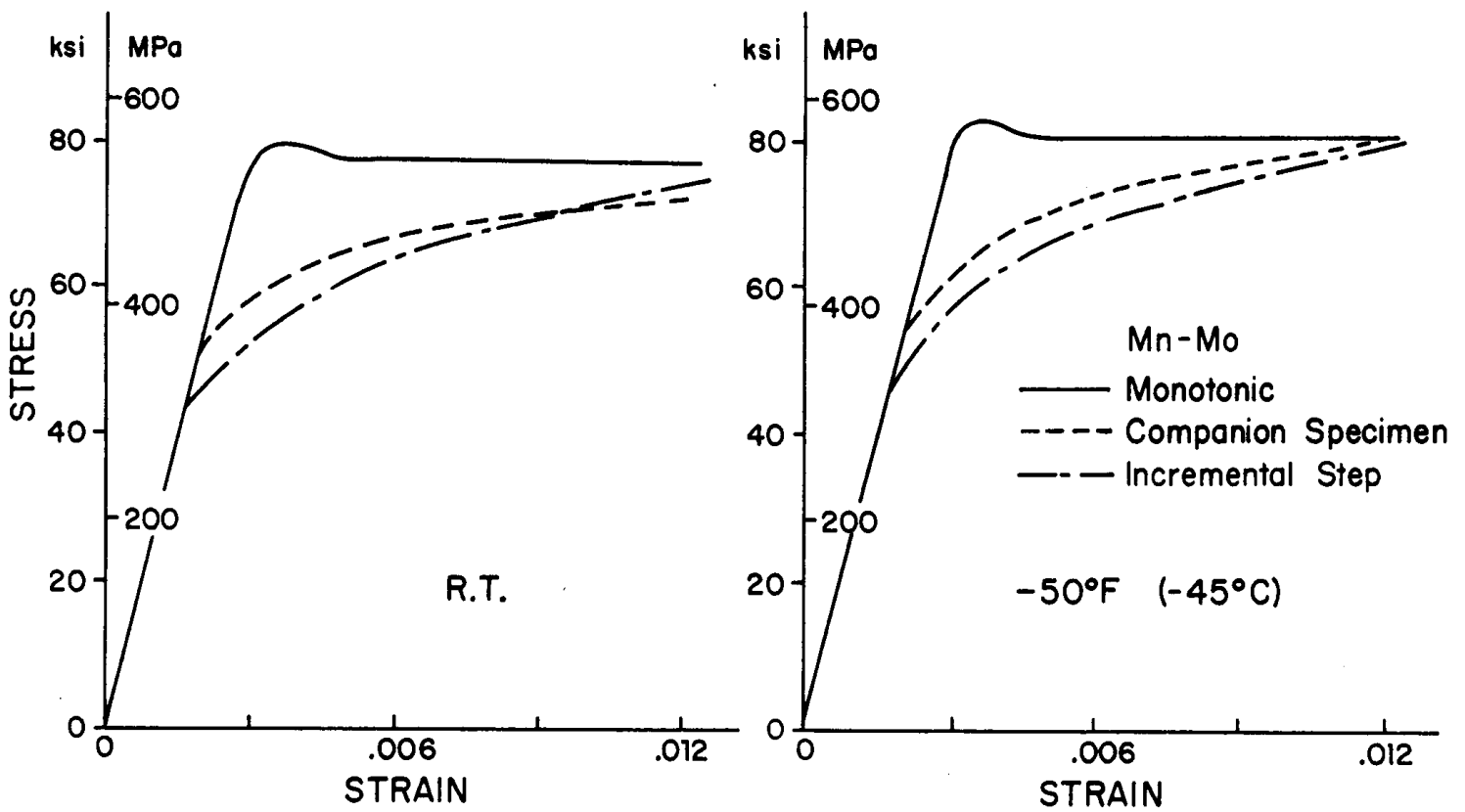


Figure 2.7. Monotonic and cyclic stress-strain behavior, Mn-Mo cast steel.

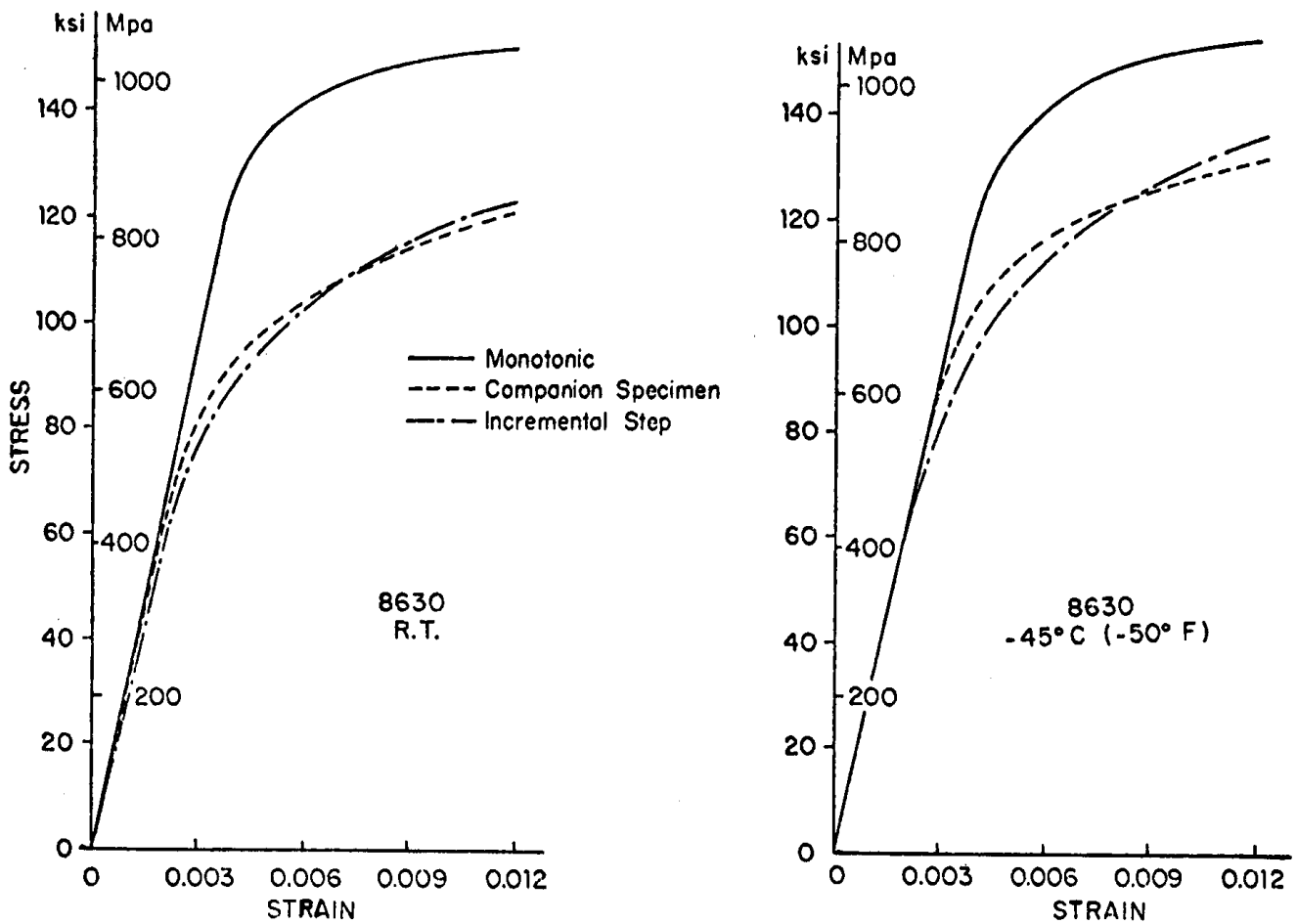


Figure 2.8. Monotonic and cyclic stress-strain behavior, 8630 cast steel.

curve). At larger strains the cyclic curves intersect or converge with the monotonic curves for these four steels. Thus these four cast steels cyclic strain soften at the smaller strain levels and then cyclic strain harden at the larger strain levels. For 8630 steel, the cyclic curves were always equal to or below the monotonic curve as shown in Figure 2.8. This steel, thus, only has cyclic strain softening.

In the inelastic region for both room and low temperature, the companion specimen cyclic stress-strain curves were slightly higher than those for the incremental step tests, except for one case (Mn-Mo at R.T.) where the two curves intersect at about 0.01 strain. The difference in stresses between the two cyclic curves was less than 10 ksi (70 MPa) for a given strain which is less than about twenty percent. Others have shown negligible to substantial differences in cyclic stress-strain curves using the two test techniques with other materials (1 -3).

The cyclic stress-strain curves using companion specimens were raised from about one to fifteen percent at -50°F (-45°C) compared to room temperature except for 8630 steel where the curve was lowered about two percent. Similar behavior existed with the incremental step tests except that 0050A also showed a slightly lower cyclic stress-strain curve at the low temperature. The increase in the cyclic stress-strain curves at low temperature for most of the tests was consistent with similar monotonic yield and ultimate strength increases at -50°F (-45°C). The three slight decreases at low temperature could be due to normal experimental accuracy, or with 8630, greater microshrinkage and brittleness that was found in room temperature axial test specimens only.

The equations for the cyclic stress-strain curves were determined using a least root mean square computer analysis. The equations based upon both elastic and plastic strain components include:

$$\epsilon = \epsilon_e + \epsilon_p \quad (2.1)$$

$$= \frac{\sigma}{E} + \left(\frac{\sigma}{K'} \right)^{1/n'} \quad (2.2)$$

or

$$\epsilon_a = \frac{\Delta\epsilon}{2} = \frac{\Delta\epsilon_e}{2} + \frac{\Delta\epsilon_p}{2} \quad (2.3)$$

$$= \frac{\sigma_a}{E} + \left(\frac{\sigma_a}{K'} \right)^{1/n'} \quad (2.4)$$

-where σ or σ_a is the stress or stress amplitude respectively

E = Young's modulus

K = cyclic strength coefficient

n' = cyclic strain hardening exponent

Values of n' and K' are given in Table 2.1 for the five cast steels at room and low temperature for both the companion specimen and incremental step methods. The 0.2% cyclic yield strengths, S'y, were obtained from Figures 2.4 to 2.8 and these values are also included in Table 2.1. Low Temperature cyclic yield strengths had less than ten percent difference than at room temperature. Seven out of ten values were higher at the low temperature.

2.2 Low Cycle Fatigue

2.2.1 Test Procedures

All low cycle fatigue tests were obtained with a 20 kip (89 kN) closed-loop electrohydraulic test system using Wood's metal grips. Tests at -50°F (-45°C) were obtained in an automated CO₂ temperature chamber. Strains were measured and controlled using a 1/2 in (12.7 mm) extensionmeter affixed to the specimen of Figure 2.1 through scotch tape and clamped by small springs. Tests were conducted in strain control except for two specimens with strain amplitudes of .0013 and .0015. At these strain levels the plastic strain is negligible and thus load control and strain control techniques produce essentially the same results. Between 10 and 12 specimens were tested for each of the five cast steels at both room temperature and -50°F (-45°C). Constant amplitude strain amplitudes varied from .0013 to .015 which gave fatigue lines from 10² to 10⁶ reversals. Tests were run until complete specimen fracture.

A constant strain rate, $\dot{\epsilon}$, of 0.01 per second (.02 to .8 Hz) was used for tests conducted with strain amplitudes greater than .0025. At lower strain amplitudes, frequencies between 1 and 20 Hz were used depending upon the strain amplitudes. Tests were started in tension and the first ten hysteresis loops were plotted using an X-Y recorder for most tests. During the tests, hysteresis loops were plotted periodically on the X-Y recorder. In addition, loads and strains were monitored with strip chart recorders and the measurement amplitude panel.

2.2.2 Test Results

Typical hysteresis loops are shown in Figure 2.9 for 0030 cast steel at -50°F (-45°C). The first ten hysteresis loops, which show initial cyclic hardening, are shown in Figure 2.9 (a). A stable hysteresis loop at about half life is shown in Figure 2.9 (b) while a series of hysteresis loops obtained during the final fracture stage is shown in Figure 2.9 (c).

Table 2.1. Cast Steel Cyclic Stress-Strain Properties

Material	n'		K'		S _y	
	Companion Specimen Method	Incremental Step Method	Companion Specimen Method ksi/MPa	Incremental Step Method ksi/MPa	Companion Specimen Method ksi/MPa	Incremental Step Method ksi/MPa
Room Temperature						
0030	.136	.130	107/738	103/710	47/324	46/317
0050A	.171	.174	169/1165	167/1151	58/400	55/379
C-Mn	.141	.136	130/896	116/800	54/372	48 /331
Mn-Mo	.096	.153	114/786	151/1041	62/427	56/386
8630	.122	.195	218/1502	329/2267	99/682	96/661
-50°F (-45°C)						
0030	.116	.135	106/731	107/738	52/359	46/317
0050A	.117	.179	131/903	166/1145	61/421	51/352
C-Mn	.139	.132	130/896	125/862	55/379	52/359
Mn-Mo	.105	.146	132/910	157/1083	68/469	60/414
8630	.095	.197	208/1433	369/2542	116/799	109/751

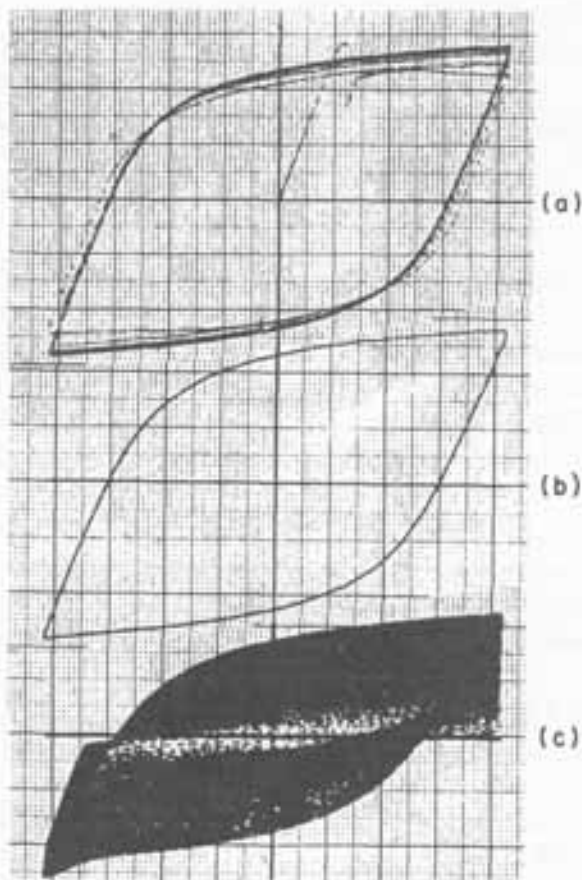


Figure 2.9. Low cycle fatigue hysteresis loops, 0030 cast steel, -50°F (-45°C).

Excluding specific initial cyclic softening or hardening, the behavior in Figure 2.9 was typical of all tests. Approximate half-life stable hysteresis loops were used to obtain elastic and plastic strain and stress amplitudes. With Young's modulus, E, obtained from the slope of the first quarter cycle, the elastic strain amplitude was calculated from

$$\frac{\Delta \epsilon_e}{2} = \frac{\Delta \sigma}{2E} \quad (2.5)$$

and the plastic strain amplitude was calculated as

$$\frac{\Delta \epsilon_p}{2} = \frac{\Delta \epsilon}{2} - \frac{\Delta \epsilon_e}{2} \quad (2.6)$$

$$= \frac{\Delta \epsilon}{2} - \frac{\Delta \sigma}{2E} \quad (2.7)$$

where $\Delta \epsilon/2$ is the known controlled total strain amplitude. These elastic, plastic and total strain amplitudes were plotted versus number of applied reversals to fracture, $2N_f$, on log-log coordinates in Figures 2.10 to 2.14 for each of the five cast steels at room temperature and -50°F (-45°C). The elastic

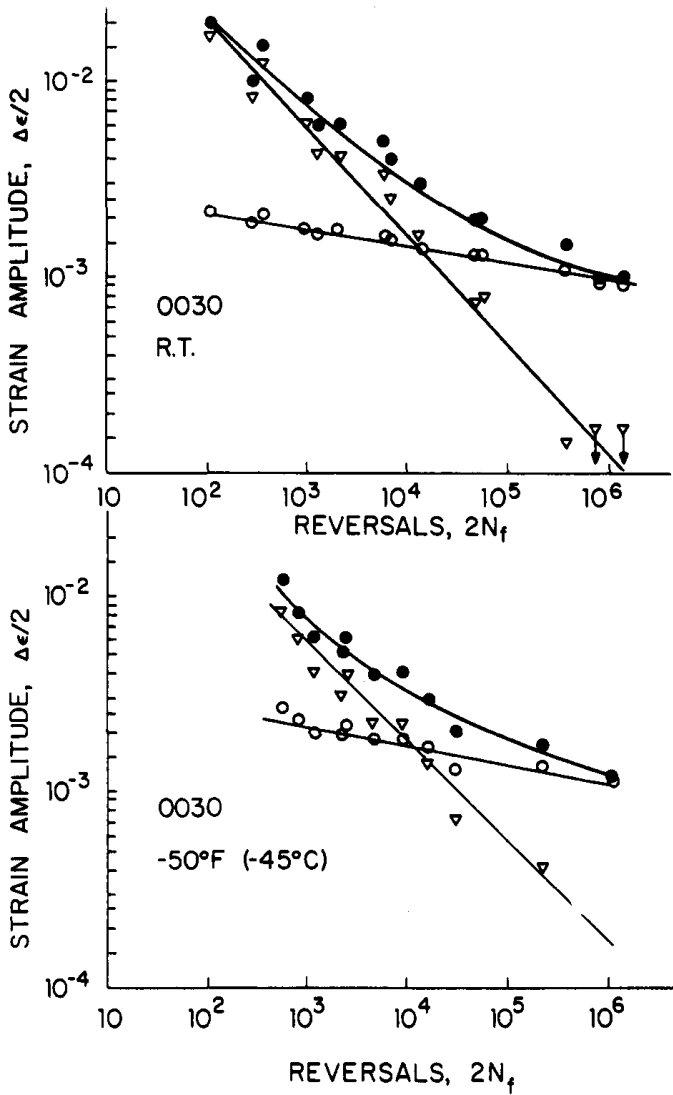


Figure 2.10. Low cycle fatigue behavior for 0030 cast steel.

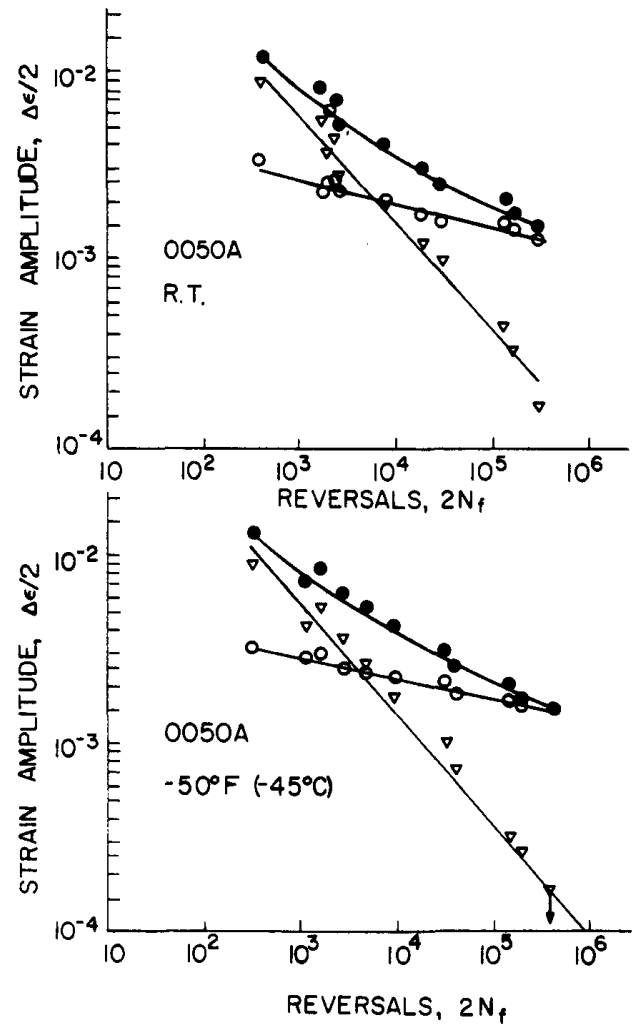


Figure 2.11. Low cycle fatigue behavior for 0050A cast steel.

and plastic components can be represented by straight line relationships such that

$$\frac{\Delta \epsilon}{2} = \frac{\Delta \epsilon_e}{2} + \frac{\Delta \epsilon_p}{2} \quad (2.8)$$

$$= \frac{\sigma_f'}{E} (2N_f)^b + \epsilon_f' (2N_f)^c \quad (2.9)$$

where σ_f' is the fatigue strength coefficient
 b is the fatigue strength exponent
 ϵ_f' is the fatigue ductility coefficient
 c is the fatigue ductility exponent
 E is Young's modulus
 $2N_f$ is the number of reversals to failure
 σ_f' , ϵ_f' , b and c were obtained with a least root mean square computer analysis.

At long life, five of the plastic strain amplitude, $\Delta \epsilon_p / 2$, versus $2N_f$ curves show open triangles with

a vertical arrow pointing down. These data points represent plastic strain amplitudes with magnitudes less than 0.0001. They are negligible at long lives and thus were deliberately excluded in the plastic strain-life equations. The include them in the analysis would cause substantial unrealistic bias in the plastic strain amplitude model at intermediate or short lives.

The low cycle fatigue material properties are given in Table 2.2 along with average values of S_u and S_y obtained from monotonic tensile tests. Both room temperature and -50°F (-45°C) properties are listed.

A fractographic study using a scanning electron microscope (SEM) was performed on different low cycle fatigue specimens subjected to high and low strain amplitudes. Since the low cycle fatigue tests were performed in strain control, substantial crack growth existed before final fracture which occurred only after substantial load decrease. Many of the

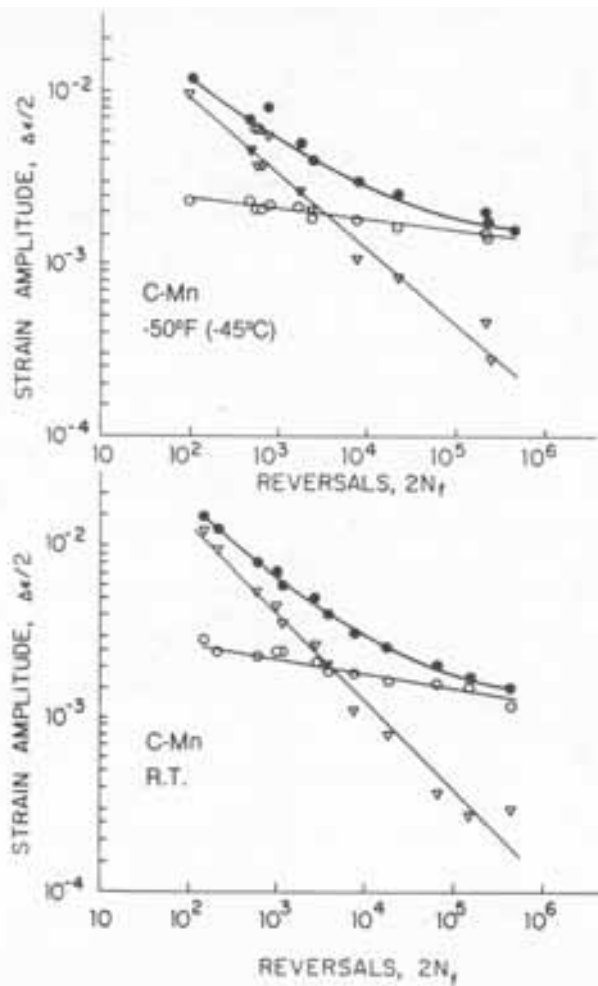


Figure 2.12. Low cycle fatigue behavior for C-Mn cast steel.

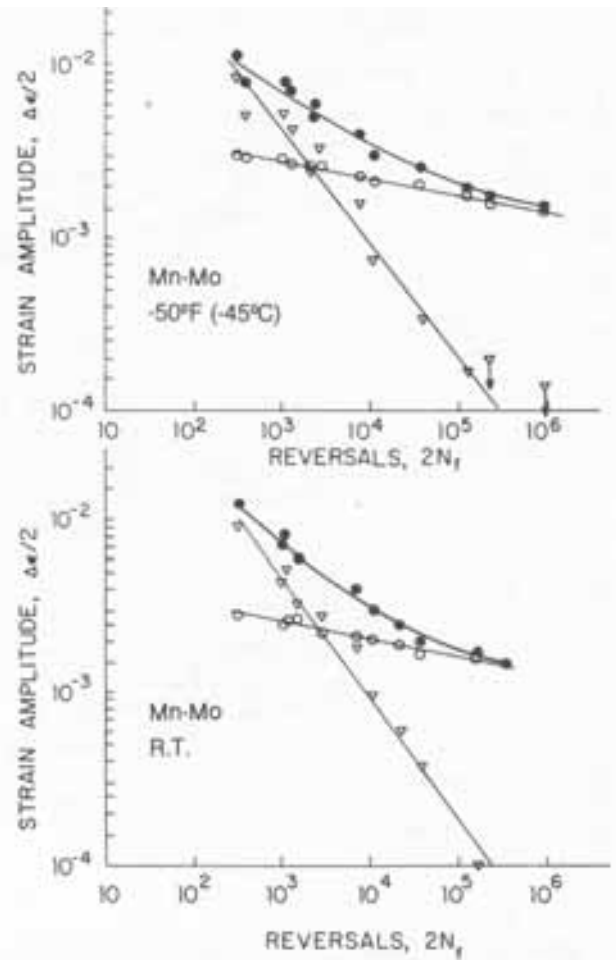


Figure 2.13. Low cycle fatigue behavior for Mn-Mo cast steel.

Table 2.2. Cast Steel Monotonic and Low Cycle Fatigue Properties.

Material	S_u ksi (MPa)	S_y ksi (MPa)	ϵ_f/c_f	σ_f/c_f ksi (MPa)/ksi (MPa)	b	c	S_u/S_y
Room Temperature							
0030	72 (496)	44 (303)	.62/.28	109 (752)/95 (655)	-.083	-.552	1.6
0050A	114 (786)	61 (421)	.21/.30	126 (869)/194 (1338)	-.127	-.569	1.9
C-Mn	85 (586)	58 (400)	.34/.15	102 (703)/126 (869)	-.101	-.514	1.5
Mn-Mo	102 (703)	79(545)	.38/.78	109 (752)/162 (1117)	-.101	-.729	1.3
8630	166 (1144)	143 (985)	.35/.42	184 (1268)/281 (1936)	-.121	-.693	1.2
-50°F (-45°C)							
0030	79 (544)	46 (317)	.36/.18	90 (621)/121 (834)	-.089	-.506	1.7
0050A	121 (834)	63 (434)	.17/.32	134 (924)/186 (1282)	-.111	-.582	1.9
C-Mn	89 (614)	67 (462)	.26/.07	92 (634)/104 (717)	-.067	-.439	1.3
Mn-Mo	110 (758)	82 (565)	.36/.47	125 (862)/159 (1096)	-.090	-.671	1.3
8630	171 (1178)	145 (999)	.33/.35	182 (1254)/259 (1785)	-.099	-.659	1.2

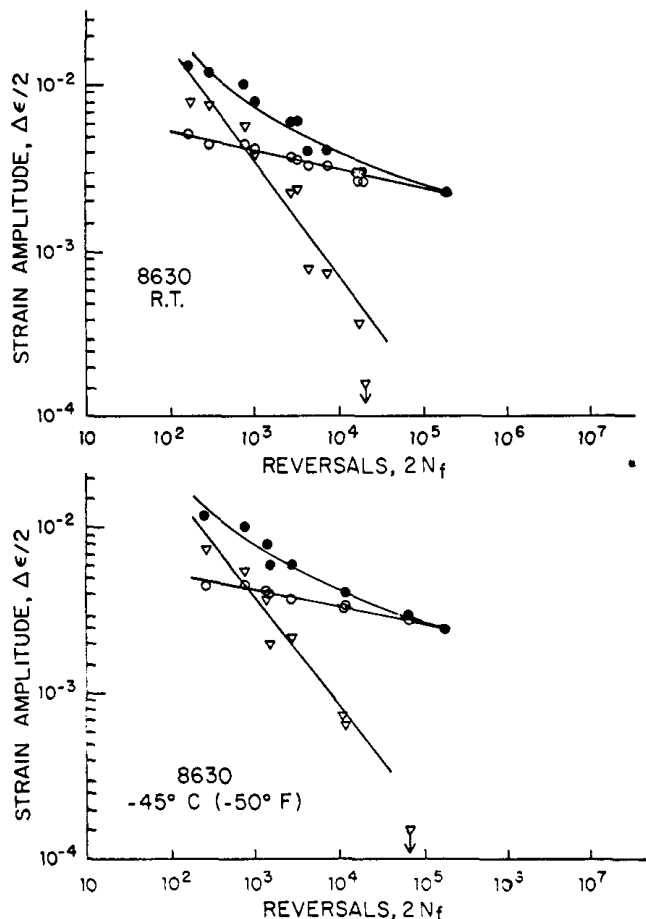


Figure 2.14. Low cycle fatigue behavior for 8630 cast steel.

fracture surfaces contained severe rubbing damage and rough surface due to compression loads and therefore the extent of the fractographic study was reduced. Multi-crack initiation sites were often observed on specimens tested at the low strain amplitudes while crack origins were less clearly identifiable at the high strain amplitude. Cracks initiated at or near the surface, often involving inclusions or porosity.

Hysteresis loops like those shown in Figure 2.9 can provide an overall idea of the type of cyclic hardening and softening that occurs in low cycle fatigue tests. More detailed behavior, however, can be understood by plotting the stress amplitude or maximum tensile stress as a function of the applied cycles for given tests. Semi-log plots of maximum tensile stress versus applied cycles are shown in Figures 2.15-2.19 for both room temperature and -50°F (-45°C). The room temperature data for 0030 steel was not obtained. Three to five representative curves are shown for each cast steel and temperature condition. These were chosen with strains varying from smaller amplitudes and hence

longer low cycle fatigue life, to larger amplitudes and hence shorter low cycle fatigue life. The strain amplitude is labeled on each curve. If no data points are shown on a given curve, this indicates the curve was obtained from a continuous plot of load versus time (and hence cycles). Data points indicate periodic readings which were obtained either from hysteresis loops or from the measurement amplitude panel. It is seen from these figures that both cyclic hardening and softening occurred in the cast steels.

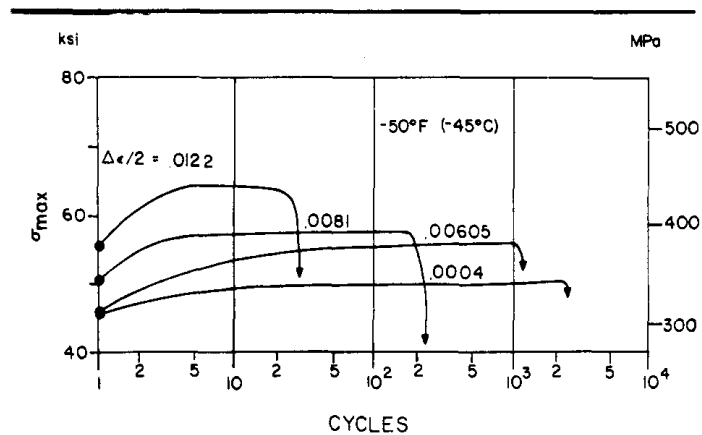


Figure 2.15. Maximum tensile stress versus applied cycles for 0030 cast steel.

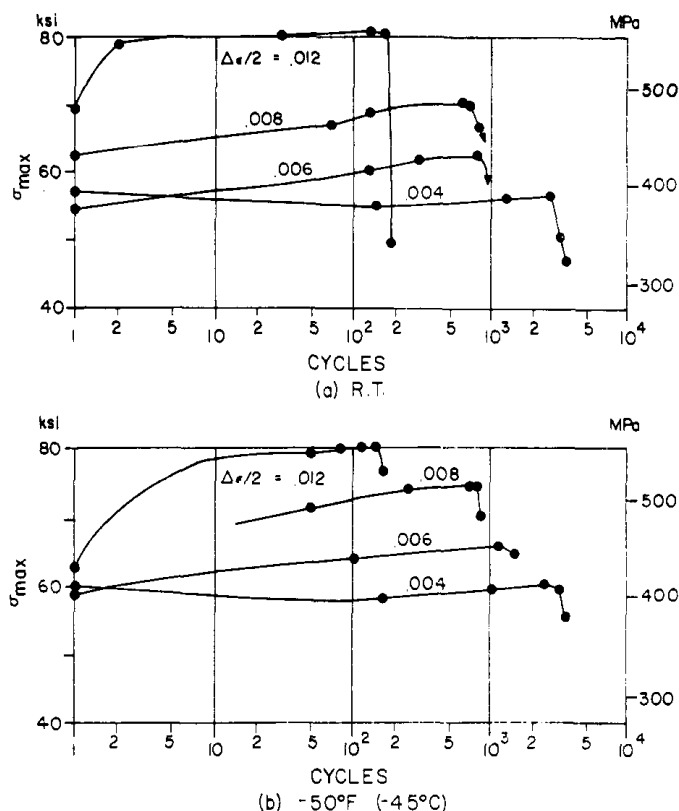


Figure 2.16. Maximum tensile stress versus applied cycles for 0050A cast steel.

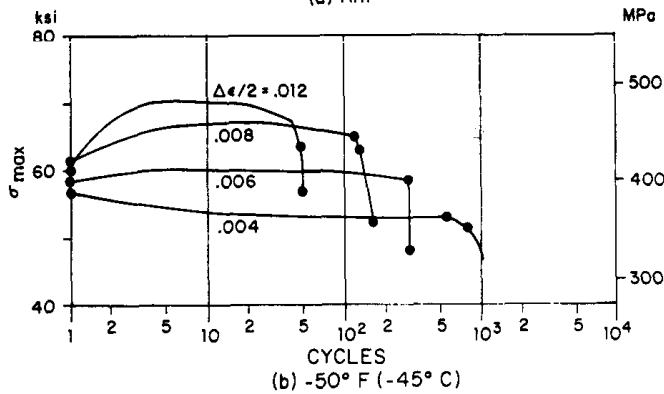
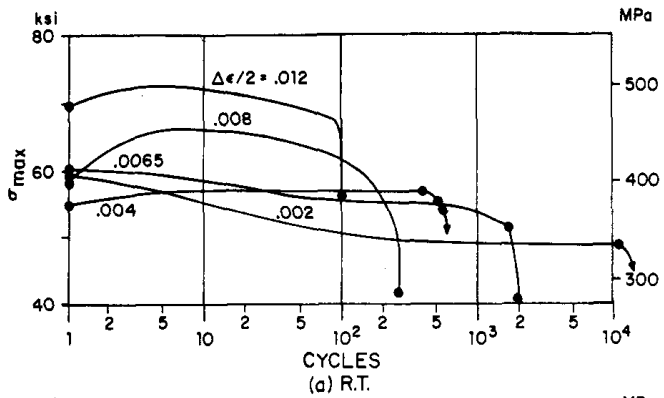


Figure 2.17. Maximum tensile stress versus applied cycles for C-Mn cast steel.

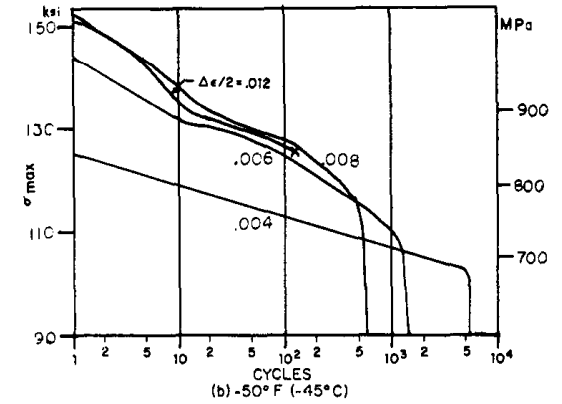
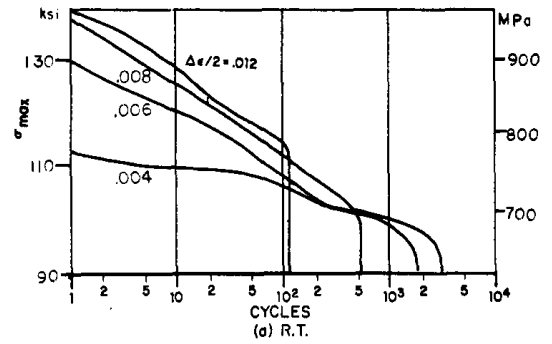


Figure 2.19. Maximum tensile stress versus applied cycles for 8630 cast steel.

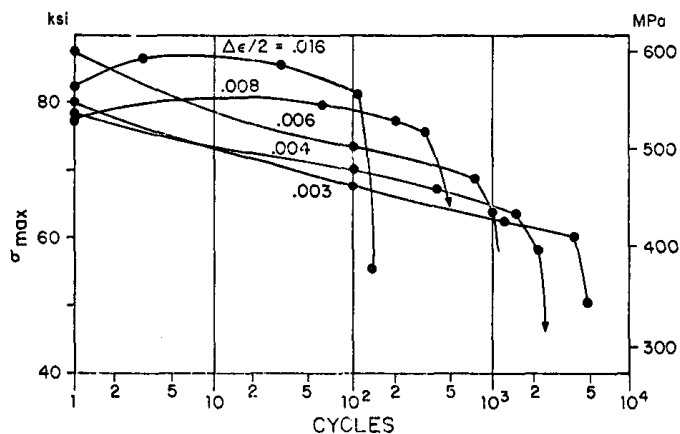
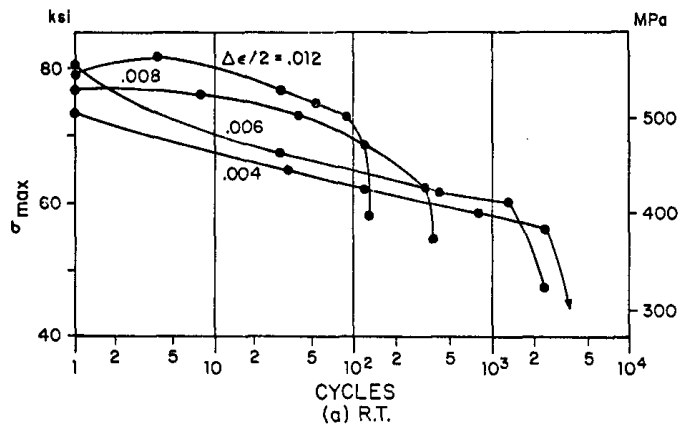


Figure 2.18. Maximum tensile stress versus applied cycles for Mn-Mo cast steel.

2.3 Discussion of Results

2.3.1 Cycle Strain Hardening and Softening

SAE J1099 report (4) lists room temperature monotonic, cyclic and low cycle fatigue properties for more than sixty wrought steels. None of these properties, however, are given for cast steels. The cyclic stress-strain exponent n' for the wrought steels varies from .05 to .36, however, more than 90 percent of these steels have n' between .1 and .2. Values of n' for the five cast steels from this research, using either the incremental step or companion specimen methods at both room and low temperature varied from .095 to .179. Thus the cyclic strain hardening exponent for the five cast steels falls very reasonably into the common range for wrought steels. Figures 2.4 to 2.7 indicate that the upper yield point stress in the cast steels is lost under room or low temperature cyclic stress-strain conditions. This same behavior has been shown to exist at room temperature for wrought steels (1,2). Also shown in Figures 2.4 to 2.7 is that the cyclic stress-strain curve falls below the monotonic stress-strain at smaller strains and intersects or converges with the monotonic curve at strains less than .012 for both temperatures. Thus these four low to medium strength cast steels (0030, 0050A,

C-Mn and Mn-Mo) have cyclic strain softening at smaller strains and cyclic strain hardening at larger strains. Again, this same type of behavior exists with low and medium strength wrought steels that exhibit a monotonic upper yield point stress. The higher strength 8630 cast steel showed cyclic softening for all inelastic strain conditions, which is also consistent for higher strength wrought steels.

At -50°F (-45°C) both monotonic yield strength and ultimate strength increased for all five cast steels within about ten percent compared to room temperature. The cyclic yield strength increased within this same value for seven out of ten tests. The 8630 cast steel which showed decreases, had substantially greater micro shrinkage in the room temperature tests which could explain this different behavior. The mixed behavior with 0050A could be due to normal experimental accuracy. Thus it appears reasonable to expect similar small cyclic and monotonic strength increases at low climatic temperatures relative to room temperature for similar cast steels.

The room and low temperature cyclic stress changes that occurred in the five cast steels under strain-controlled low cycle fatigue testing shown in Figure 2.15 to 2.19 compare reasonably with behavior usually found for room temperature wrought steels. Since the abscissa is a log scale, half-life is substantially skewed to the right for a given curve. Half-life is usually, or often considered, as a steady-state condition representative of stress-strain response for most of the total fatigue life; many exceptions, however, certainly exist (5). The five cast steels at both room temperature and -50°F (-45°C) completely satisfy the above wrought steel findings. For 0030, 0050A and C-Mn cast steels, half-life values of σ_{max} do represent majority life steady-state conditions. For Mn-Mo and 8630 steels, continuous cyclic softening existed from start to fracture. All curves show a drastic decrease in σ_{max} somewhat before final fracture. This drop is due to fatigue crack growth. In many cases, σ_{max} decreased to almost zero before final fracture as in Figure 2.9 (c). Some researchers terminate low cycle fatigue tests when σ_{max} drops twenty percent. These cast steel tests, however, were run to fracture. The difference in life to a twenty percent drop in σ_{max} and total fracture ranged from about 15 to 50 percent for all five cast steels at both temperatures. This difference depended upon $\Delta\varepsilon/2$, material and temperature and is the same kind of difference that can occur in wrought steels.

An analysis of Figures 2.4 to 2.8 indicates cyclic

strain hardening occurred for 0030 and 0050A, cyclic softening occurred for Mn-Mo and 8630, and mixed cyclic softening and hardening occurred for C-Mn steel. Manson et al. (6) found that when the ratio of S_u/S_y from a monotonic tensile test was greater than 1.4, the material had cyclic strain hardening; when the ratio was less than 1.2 cyclic strain softening existed. For ratios between 1.2 and 1.4 they showed it was difficult to predict cyclic changes. Their research involved essentially wrought minerals. The ratio of S_u/S_y for the five cast steels at room temperature and -50 °F (-45 °C) are shown in Table 2.2. The following existed for the five cast steels at the two temperatures:

$$\begin{aligned} S_u/S_y < 1.5; & \text{cyclic strain hardening} \\ S_u/S_y \leq 1.3; & \text{cyclic strain softening} \\ 1.3 < S_u/S_y \leq 1.5; & \text{mixed cyclic strain hardening and softening} \end{aligned}$$

Thus the five cast steels fall close to the behavior reported by Manson et al. but the ratios were increased by approximately 0.1.

2.3.2 Fatigue Life

The low cycle fatigue curves of Figures 2.10 to 2.14 do not conveniently show the effect of temperature on fatigue behavior nor the comparison of the five steels at a given temperature. The total strain-life curves have been superimposed in Figure 2.20 for proper comparison of temperature influence. The solid curves in Figure 2.20 represent room temperature behavior and the dashed curves are for -50°F (-45°C). Since these are log-log plots, differences between curves are less evident. No specific shape trend is noted for the five cast steels except at longer fatigue lives ($>5 \times 10^5$ reversals), the lower temperature strain amplitudes are between zero and 30 percent higher than at room temperature. Thus at longer fatigue lives the fatigue resistance of smooth axial specimens at -50°F (-45°C) is similar to or better than that at room temperature. At the shorter lives, mixed results exist such that in some cases the low temperature was beneficial, detrimental, or had negligible influence. Very little low cycle fatigue information is available in the literature and that which is available, has shown the same trends given in Figure 2.20 (7-10).

The large decrease in short life fatigue resistance at low temperature for C-Mn steel is in agreement with the larger number of inclusions and porosity found in the low temperature fracture surfaces. For 8630 steel, the large difference can be attributed to the large percentage of micro shrinkage found in

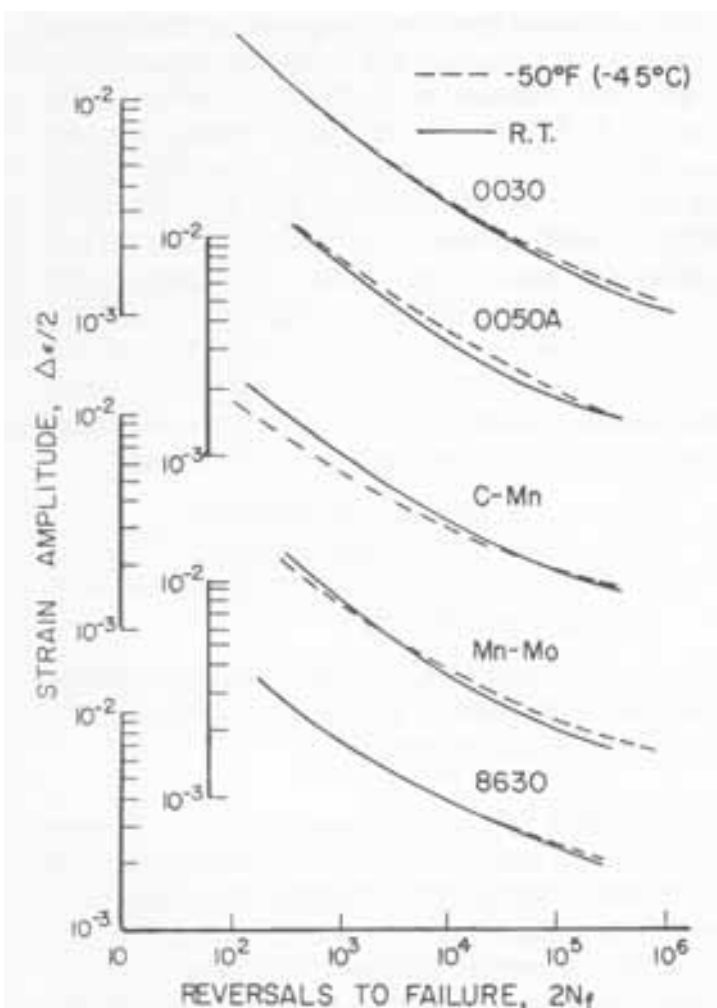


Figure 2.20. Comparison of low cycle fatigue behavior at room temperature and -50°F (-45°C).

the room temperature specimens. The micro shrinkage problem is also the cause of the very unusual room temperature strain-life curves in Figure 2.14. The 8630 room temperature low cycle fatigue, cyclic and monotonic tests will be repeated with specimens taken from blocks which do not contain unreasonable microshrinkage.

The room temperature and low temperature total strain-life curves have been superimposed in Figure 2.21 (a) and Figure 2.21 (b) respectively, where it is seen that at each temperature, four of the five steels are reasonably banded together. At room temperature 8630 steel is quite separate and at -50°F (45°C) C-Mn steel is quite separate. These differences can be attributed to microshrinkage, inclusions and porosity as indicated previously. At fatigue lives greater than about 5×10^5 reversals, the plastic strain component is negligible and thus total strain amplitudes here are essentially elastic. These strain amplitudes can be converted to stress amplitudes with Young's modulus. Values of the alternating stresses at 10^6 reversals are given:

	Room Temperature ksi (MPa)	-50°F (-45°C) ksi (MPa)
0030	30 (208)	31 (214)
0050A	33.5 (231)	40 (276)
C-Mn	31 (214)	41 (283)
Mn-Mo	40 (276)	45 (310)
8630	53.7 (370)	66 (455)

8630 steel has the largest values and 0030 steel the smallest. The difference at room temperature is 79 percent which is quite significant. These differences are somewhat disguised on log-log plots. The magnitudes of these alternating stresses range from 30 to 46 percent of the ultimate tensile strength. Extension of the low cycle fatigue data to 2×10^7 reversals is currently being obtained which will provide a comparison of fatigue limits. At shorter fatigue lives much less difference exists for the banded steels. Thus the major low cycle fatigue differences, for most of the cast steels, occur at greater than 10^5 reversals.

The low cycle fatigue material properties, σ'_f , ϵ'_f , b and c provided in Table 2.2 and the cyclic stress-strain material properties n' , K' and S'_y provided in Table 2.1 can be used for these five cast steels in

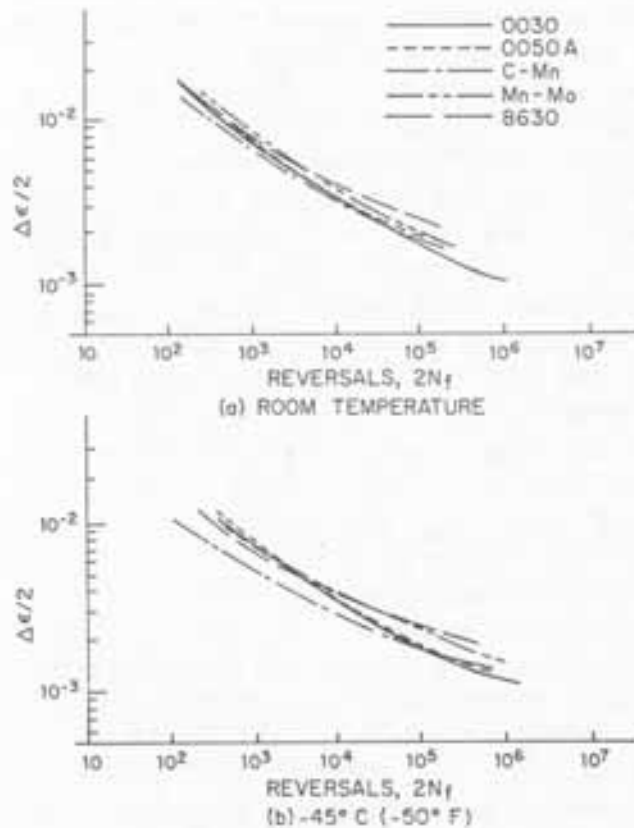


Figure 2.21. Comparison of low cycle fatigue behavior for five cast steels.

fatigue design situations where notch strain or notch stress analysis is applicable. These material properties all fall within values published in J1099 for wrought steels at room temperature. In J1099, b ranges from .06 to .15 while for the five cast steels, b ranges from .067 to .141. In J1099, c ranges from -.39 to .77 while for the five cast steels, c ranges from .376 to .729. In J1099, no correlation exists between ϵ_f and ϵ'_f nor σ_f and σ'_f . This is also the case for the five cast steels. Thus it appears that low cycle fatigue procedures developed principally for wrought materials are equally applicable to cast steels.

2.4 Summary and Conclusions

1) Cyclic stress-strain behavior and low cycle fatigue behavior from 10 to 10^6 reversals was obtained for five cast steels at room temperature and -50°F (-45°C).

2) The monotonic upper yield point stress found in low and medium strength cast steels was lost under cyclic stress-strain conditions at both room and low temperature. For these conditions, the cast steels exhibited cyclic strain softening at small strains and cyclic strain hardening at larger strains. The higher strength 8630 cast steel exhibited only cyclic strain softening. The companion specimen method cyclic stress-strain curves were always slightly higher than the incremental step cyclic stress strain curves. These differences ranged almost zero to 20 percent. The above cyclic stress-strain behavior for the five cast steels is similar to that found in the literature for wrought steels.

3) Cyclic strain hardening was found for cast steels with $S_u/S_y > 1.5$, cyclic strain softening for $S_u/S_y \leq 1.3$ and mixed cyclic softening and hardening for S_u/S_y equal to or less than 1.5 and greater than 1.3. These values are about 0.1 higher than values found by Manson et al. for principally wrought materials.

4) The cyclic stress-strain curves and the cyclic yield strength at -50°F (-45°C) increased an average of about 10 percent compared to room temperature results except for 8630 steel which had substantial microshrinkage in the room temperature specimens. The increases were similar to increases found in S_y and S_u from monotonic tests.

5) Half-life steady state hysteresis loops were

representative of most low cycle fatigue life for only 0030, 0050A and C-Mn cast steels. Mn-Mo and 8630 cast steels had continuous cyclic softening from the beginning of the test to fracture.

6) The fatigue life to fracture for the five cast steels ranged from 15 to 50 percent longer than fatigue life to a drop in the maximum tensile stress of 20 percent. This was a function of strain amplitude, material and temperature.

7) Values of plastic strain amplitude less than 0.0001 were excluded from least root mean square calculations since they would unrealistically bias the log log linear plastic strain model at intermediate or short lives, and they realistically have no influence at longer lives. This practice is recommended for other low cycle fatigue data analyses.

8) Low cycle fatigue behavior at -50°F (-45°C) was equal to or better than at room temperature for lives greater than 5×10^5 reversals; however, mixed behavior existed at shorter lives. The fatigue strengths at 10^6 reversals were from zero to 30 percent better at -50°F (-45°C). Mixed low cycle fatigue behavior at low temperatures has also been reported in the literature for wrought steels.

9) Values of low cycle fatigue material properties for the five cast steels were within the ranges found in SAE report J1099 for wrought steels.

10) Fatigue cracks initiated from the surface and at regions containing porosity and inclusions. Multi cracks were often initiated in specimens subjected to smaller strain amplitudes.

11) The poor fatigue resistance at larger strain amplitudes for 8630 cast steel is attributed to excess microshrinkage in the room temperature specimens. These tests will be repeated with specimens taken from blocks containing usual microshrinkage.

12) The room temperature fatigue strengths of the five cast steels at 10^6 reversals ranged from 30 ksi (208 MPa) for 0030 steel to 53.7 ksi (370 MPa) for 8630 steel. The five steel room temperature fatigue strengths were within 30 to 40 percent of the ultimate tensile strength. This range was 32 to 46 percent at -50°F (-45°C).

13) Low cycle fatigue concepts, which were principally developed and proven with wrought steels, are applicable to these five cast steels and would appear to be quite realistically applicable for additional cast steels.

Chapter 2 References

1. R.W. Landgraf, "The Resistance of Metals to Cyclic Deformation", in Achievement of High Fatigue Resistance In Metals and Alloys, ASTM STP 467, 1970, p. 3.
2. R.W. Landgraf, "Cyclic Stress-Strain Response in Commercial Alloys", Proceedings of Symposium, Work Hardening in Tension and Fatigue, Cincinnati, Ohio, Nov., 1975, AIME, p. 240.
3. C.E. Jaske, H. Mindlin and J.S. Perrin, "Development of Elevated Temperature Fatigue Design Information for Type 316 Stainless Steel", Institute of Mechanical Engineers, Conference Publication 3, 1973, p. 163.1.
4. "Technical Report on Fatigue Properties", SAE J1099, Feb., 1975.
5. H.O. Fuchs and R.I. Stephens, Metal Fatigue in Engineering, Wiley Interscience, New York, 1980.
6. R.W. Smith, M.W. Hirsberg and S.S. Manson, "Fatigue Behavior of Materials Under Strain Cycling in the Low and Intermediate Life Range", NASA TND-1574, April, 1963.
7. R.I. Stephens, J.H. Chung and G. Glinka, "Low Temperature Fatigue Behavior of Steels-A Review", Paper No. 790517, April, 1979, SAE Transactions, Vol. 88, 1980, p. 1892.
8. A.J. Nachtigall, "Strain-Cycling Fatigue Behavior of Ten Structural Metals Tested in Liquid Helium (4K), in Liquid Nitrogen (78K) and in Ambient Air (300K)", NASA TN D-7532, Feb., 1974.
9. J. Polak and M. Klesnil, "The Dynamics of Cyclic Plastic Deformation and Fatigue Life of Low Carbon Steel at Low Temperature", Materials Science Engineering, Vol. 26, No. 2, Dec. 1976, p. 157.
10. M. Kikukawa, M. Jono, T. Kamato and T. Nakomo, "Low Cycle Fatigue Properties of Steels at Low Temperatures", Proceedings, 73th Japan Congress on Materials Research, 1970, p. 69.

Constant Amplitude Fatigue Crack Growth

3.1 Experimental Procedures

Constant load amplitude fatigue crack growth tests were conducted with the five cast steels at room temperature (R.T.) and at either -50°F (-45°C) or -30°F (-34°C). The 0030 cast steel was tested at -30°F (-34°C) while the other four steels were tested at -50°F (-45°C). All tests were run using a 20 kip (89 kN) closed-loop electrohydraulic test system in load control. Low temperature tests were performed in an automated CO_2 chamber. Compact type (CT) chevron specimens were cut from the blocks as shown previously in Figure 1.2. Actual specimen dimensions are shown in Figure 3.1. Specimen thickness was 0.324 in (8.2 mm) and width, w , was 2.55 in (64.8 mm) for all the cast steels while two values of specimen height, $2H$, were used. Initial tests using 0030 cast steel had $H/w = 0.49$ while the other four cast steels were tested with $H/w = 0.60$. The three hole configuration was used in connection with a monoball gripping system which allows only axial ram loading for both tension and compression loads. Tests were originally planned with the load ratio R (equal to P_{\min}/P_{\max}) set at essentially zero and -1 . However extreme difficulties occurred in monitoring the 0030 cast steel crack tip with $R = -1$ at the low temperature. The $R = -1$ value was therefore abandoned and final R ratios of essentially zero and $+1/2$ were chosen for the other four cast steels. The minimum load for $R \approx 0$ was always set at 50 lbs (220 N) rather than zero in order to avoid any compression and possible chattering between the specimen and grips. Therefore actual $R \approx 0$ values varied from 0.015 to 0.04.

Fatigue crack growth tests were performed according to ASTM Standard Test for Constant-Load-Amplitude Fatigue Crack Growth Rates above 10^{-8} m/cycle (E647-78T). Precracking was performed using a load-shedding technique with a few single compression loads following each load-shed to minimize crack growth retardation. Two to four load-shed steps were made for most tests. The final precracking was done at the same load level used in the actual test. Precrack extension from the

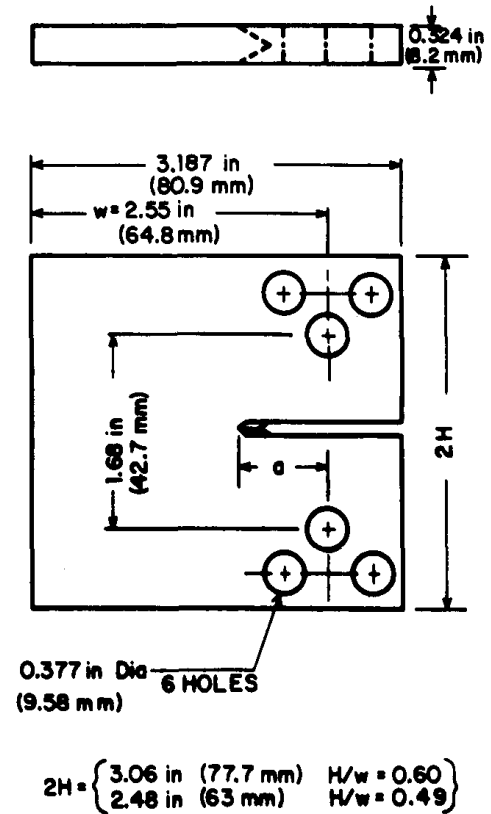


Figure 3.1. Constant amplitude fatigue crack growth test specimen.

chevron notch was at least 0.1 in (2.5 mm) to avoid any transient effects. Initial crack lengths were thus between 0.85 in (21.6 mm) and 0.87 in (22 mm) for actual data taking. Specimens were polished with decreasing grades of emery paper on one side only for proper observation of the crack tip region. Cracks were monitored using a 33 x magnification traveling telescope and stroboscopic illumination with a least reading of 0.01 mm (.0004 in). At low temperature tests, cracks were monitored through the glass window in the temperature chamber. Most crack growth data were taken with crack extension increments bet-

ween 0.25 mm (0.01 in) and 0.75 mm (0.03 in). Loads were applied with a sine wave between 10 and 40 Hz depending on crack length and load range magnitude. Between two and four test specimens were run for each test condition with different initial stress intensity factor ranges, ΔK_i , in order to obtain overlapping crack growth rates between 2×10^{-7} and 10^{-4} in/cycle (5×10^{-9} and 2.5×10^{-4} m/cycle). This region generally covers the straight-line portion of the log-log sigmoidal-shaped da/dN versus ΔK curve, and can be represented mathematically by the Paris equation (1).

$$\frac{da}{dN} = A (\Delta K)^n \quad (3.1)$$

where

a = crack length as measured from the center load line

N = applied cycles,

da/dN = crack growth rate,

ΔK = positive stress intensity factor range equal to $K_{max} - K_{min}$ for tensile loading and $K_{max} - 0$ when compression is involved, and

n and A = material constants for the particular test conditions used.

Values of da/dN and ΔK were obtained by reducing the a versus N data for a given test specimen using a second order incremental polynomial as suggested in ASTM standard E647. The stress intensity factor K or ΔK for the two compact specimens (2,3) are

for $H/w = 0.6$

$$K = \left[\frac{P}{B\sqrt{w}} \right] \frac{(2 + \frac{a}{w})}{(1 - \frac{a}{w})^{3/2}} \left[.886 + 4.64 \left(\frac{a}{w} \right) - 13.32 \left(\frac{a}{w} \right)^2 + 14.72 \left(\frac{a}{w} \right)^3 - 5.6 \left(\frac{a}{w} \right)^4 \right] \quad (3.2)$$

for $H/w = 0.49$

$$K = \left[\frac{P\sqrt{a}}{Bw} \right] \left[30.96 - 195.9 \left(\frac{a}{w} \right) + 730.6 \left(\frac{a}{w} \right)^2 - 1186.2 \left(\frac{a}{w} \right)^3 + 754.6 \left(\frac{a}{w} \right)^4 \right] \quad (3.3)$$

where P is the applied load, B the specimen thickness and w the specimen width. For ΔK calculations, P is replaced by ΔP .

3.2 Test Results

Representative a versus N data are shown in Figure 3.2. These data are for Mn-Mo cast steel which were obtained under the same initial crack lengths and under the same initial stress intensity factor range of 19 ksi [$\sqrt{\text{in}}$ (20.9 MPa $\sqrt{\text{m}}$)]. Data at room temperature and -50°F (-45°C) are shown for both $R \approx 0$ and $1/2$. These representative data indicate very reasonable continuity in the a versus N data. Similar behavior existed in all the cast steels under constant amplitude loading for both $R \approx 0$ and $1/2$ at both room and low temperatures. As mentioned in Chapter 1, however, large scatter existed in the 0030 cast steel tested at low temperature with $R = -1$ due to difficulties in locating the precise crack tip.

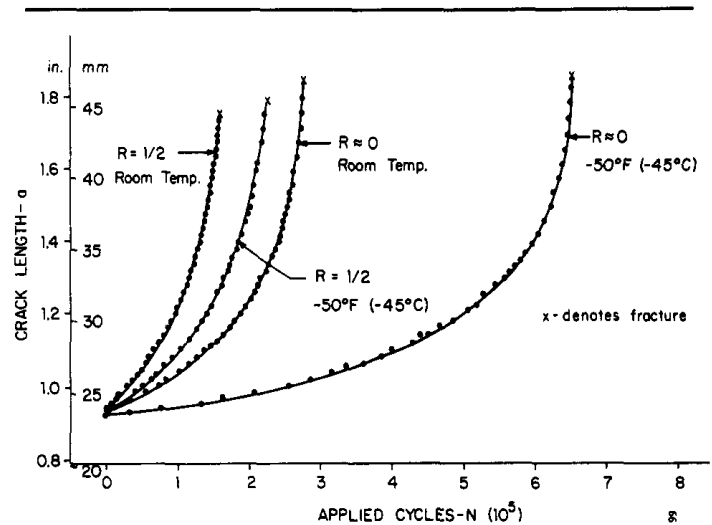


Figure 3.2. Typical constant amplitude fatigue crack growth at room and low temperature, Mn-Mo cast steel.

From Figure 3.2 it is seen that fatigue crack growth life is longer at -50°F (-45°C) than at room temperature for a given R ratio. The increase was about 20 percent for the two $R = 1/2$ tests and 135 percent for the two $R \approx 0$ tests. Similarly, increases in fatigue crack growth life occurred with the other four cast steels at low temperature for a given R ratio. The increase in fatigue life is due to slower fatigue crack growth rates at the low temperature

during approximately the first two-thirds or so, of the total crack growth. At longer crack lengths, and hence higher stress intensity factor ranges, the crack growth rates, da/dN , appear to be somewhat equivalent. This implies that da/dN versus ΔK data for different test conditions will tend to converge at the higher stress intensity factor ranges.

The da/dN versus ΔK data for the five cast steels, two test temperatures, and two R ratios have been plotted on log-log scales in Figures 3.3 to 3.12. All data points have been shown as obtained from the second order incremental polynomial computer procedure. Each figure is for a given R ratio and steel and thus gives a comparison of room and low temperature constant amplitude fatigue crack growth behavior. In each figure, the solid circles represent room temperature (R.T.) and the open circles represent -50°F (-45°C) except for the 0030 cast steel where the low temperature is -30°F (-34°C). Each set of data points represent two to four different test specimens which were tested with different initial stress intensity factor ranges in order to obtain the desired range of crack growth rates. A greater range was usually obtained specifically for the $R \approx 0$ conditions.

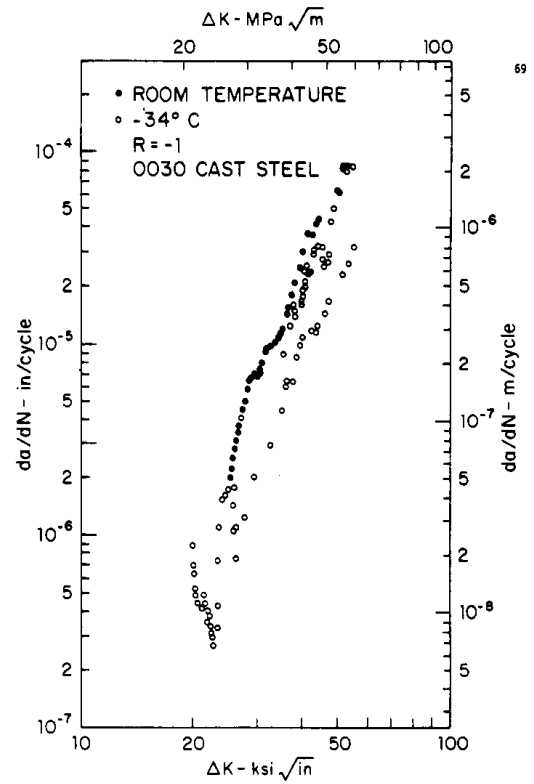


Figure 3.4. Constant amplitude fatigue crack growth behavior.

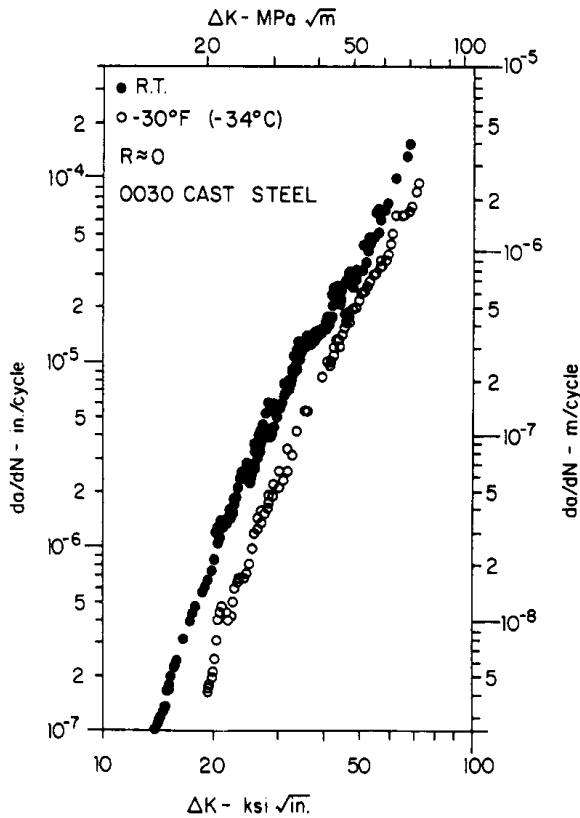


Figure 3.3. Constant amplitude fatigue crack growth behavior.

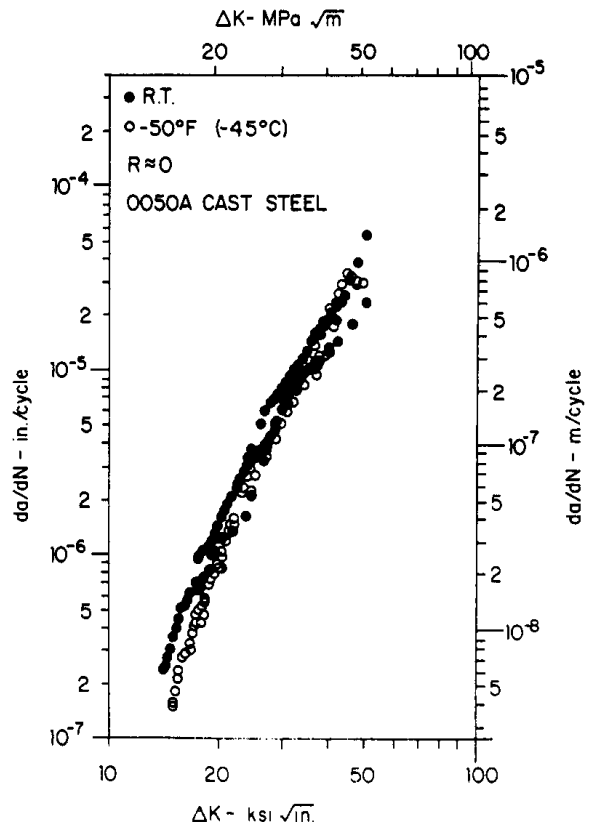


Figure 3.5. Constant amplitude fatigue crack growth behavior.

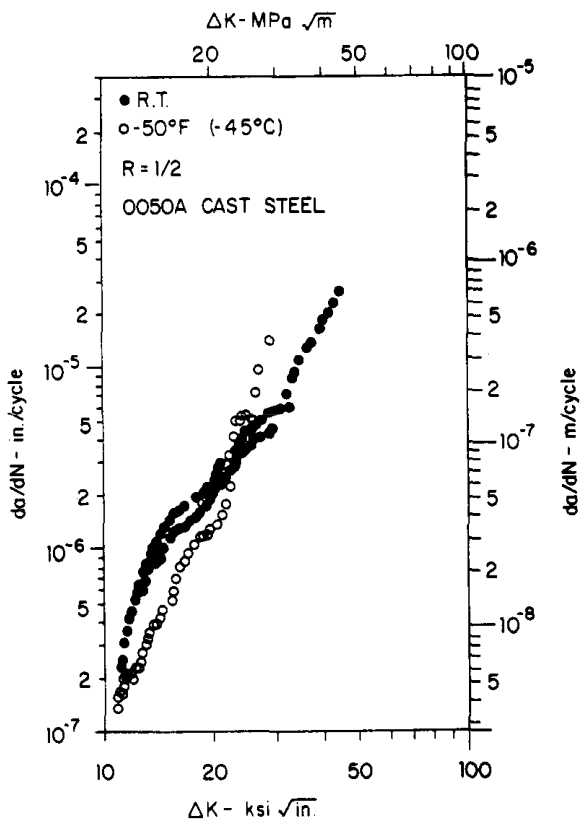


Figure 3.6. Constant amplitude fatigue crack growth behavior.

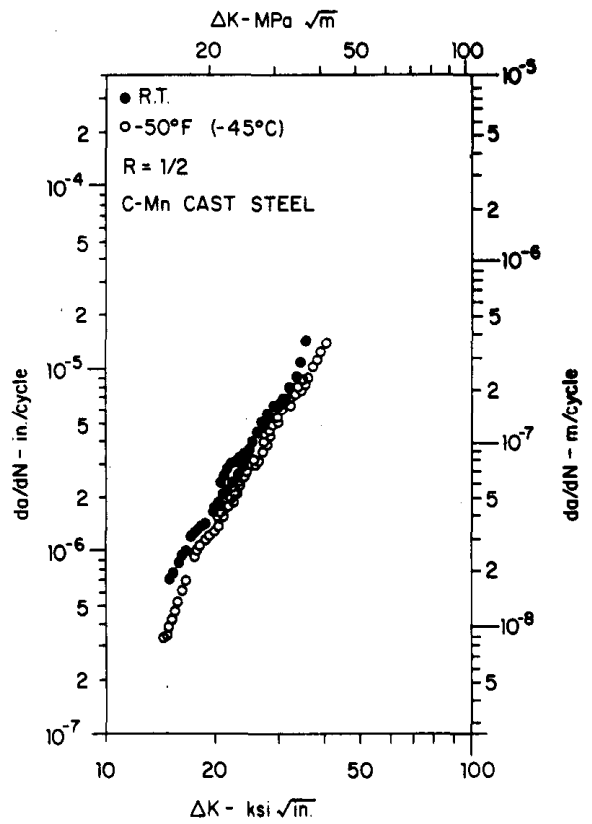


Figure 3.8. Constant amplitude fatigue crack growth behavior.

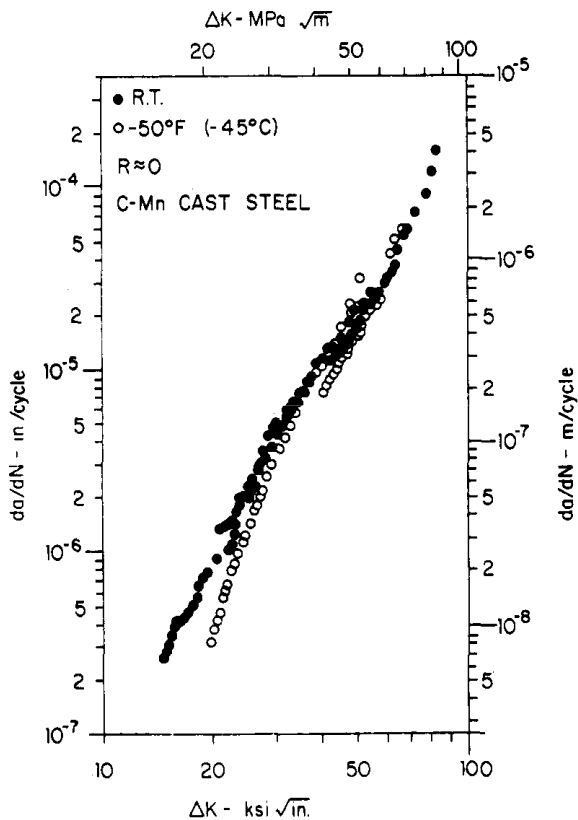


Figure 3.7. Constant amplitude fatigue crack growth behavior.

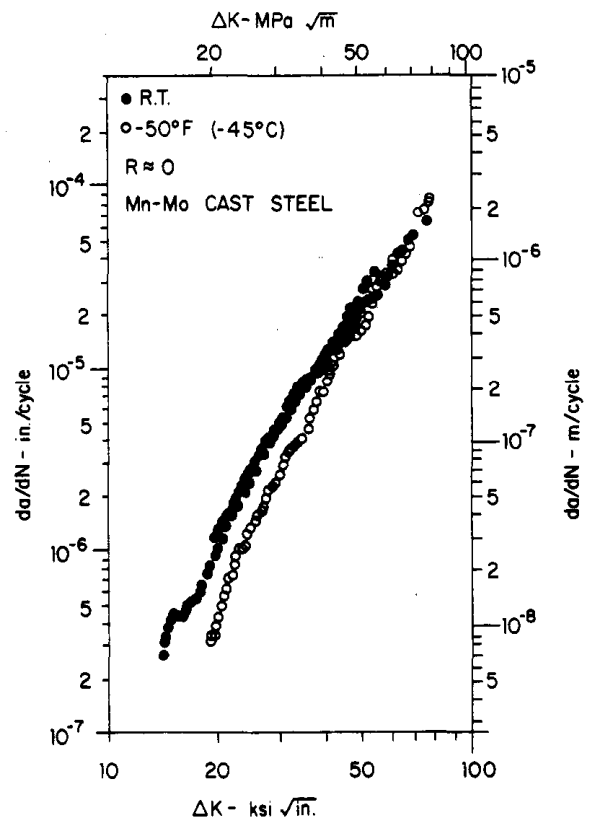


Figure 3.9. Constant amplitude fatigue crack growth behavior.

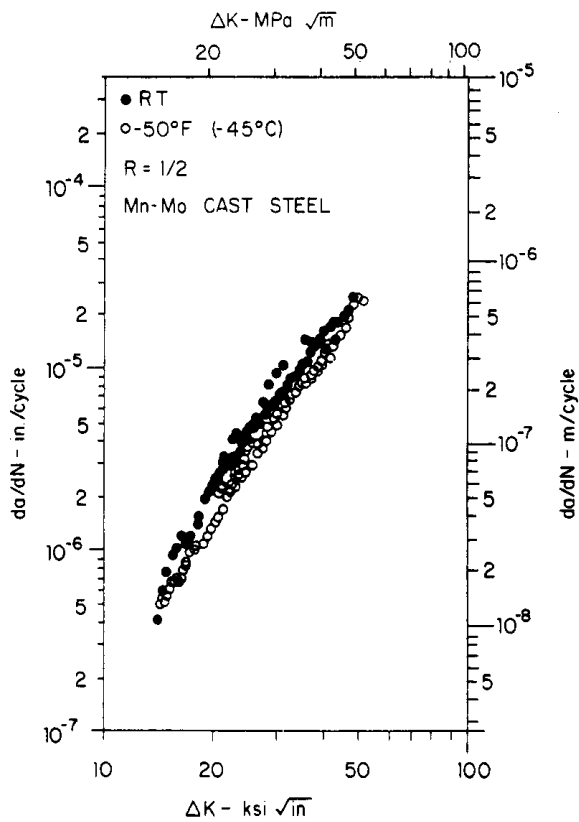


Figure 3.10. Constant amplitude fatigue crack growth behavior.

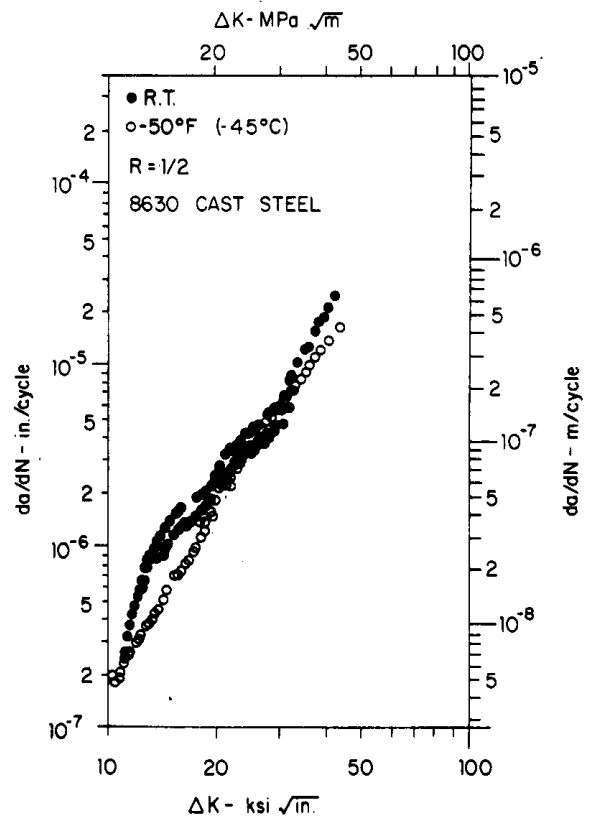


Figure 3.12. Constant amplitude fatigue crack growth behavior.

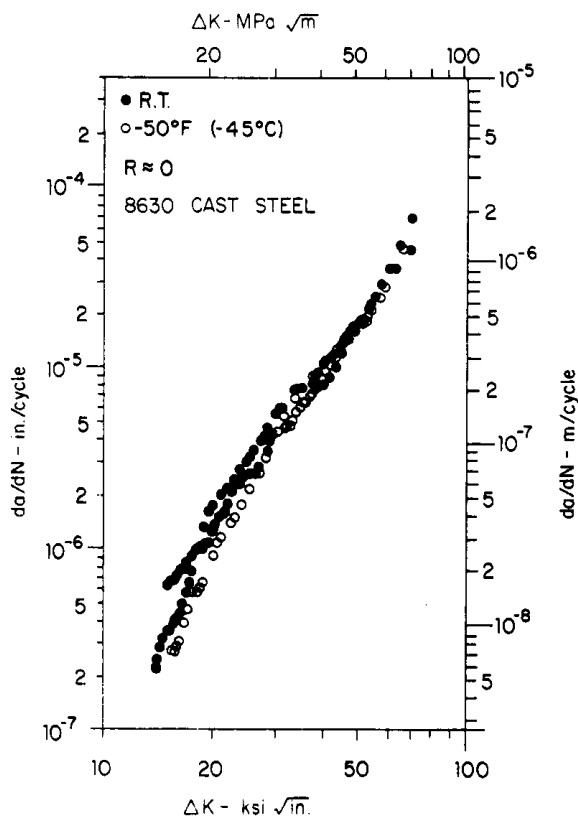


Figure 3.11. Constant amplitude fatigue crack growth behavior.

Most of the data show scatter similar to that found in the literature for multiple testing of wrought steels. In general, scatter can be attributed to inherent scatter, material heterogeneity, different plastic zone sizes, multiple specimens, experimental accuracy, and operator error. As mentioned previously, the $R = -1$ rests with 0030 steel at low temperature (Figure 3.4 open circles) involved substantial difficulties in locating the crack tip. These data have only been included on a semi-quantitative basis and no attempt was made to reduce these data to a mathematical expression. Somewhat greater scatter occurred in the 0050A and 8630 cast steels at room temperature than for the other materials and test conditions. This appears to be primarily due to multiple specimen usage, since some banding of data is evident. These data, however, are still quantitatively reliable.

For the five cast steels and two R ratios, the low temperature caused a decrease in fatigue crack growth rates at the lower ΔK values by a factor ranging from about 1.2 to 3. For $R = 1/2$ this range was only between about 1 and 2. At the higher ΔK values the room and low temperature data tend to converge and in some cases actually crossover. Since very little fatigue crack growth life is involved

at the high ΔK values, the most common practical region is the lower ΔK values where the low temperature had either small or definite beneficial effects.

Since most of the data fall within a reasonable log-log linear scatter band, the Paris equation (1)

$$\frac{da}{dN} = A (\Delta K)^n \quad (3.1)$$

was used to quantify the data. A composite least root mean square computer calculation was made for each material condition using the multiple specimen results for that condition. Values of A and n are given in Table 3.1. Both American/British units and SI units are given where da/dN is in in/cycle (m/cycle) and ΔK is in ksi $\sqrt{\text{in}}$ (MPa $\sqrt{\text{m}}$). These values represent reasonable crack growth values which can be used in design situations. Here it is seen that for 18 test conditions, the coefficient A ranged within about two order of magnitude and n varied from 2.67 to 4.72 or a factor of about 1.8. Material comparisons based only on A or n, however, should not be made because the two values are interdependent.

The Paris equations taken from Table 3.1 have been superimposed in composite form in Figures 3.13 to 3.15 for better comparison of different

variables. The curves have been drawn only in the range where experimental data existed, that is, no extrapolation is shown. Figure 3.13 shows the comparison between room temperature (R.T.) and low temperature with $R \approx 0$ for the five different steels, while Figure 3.14 shows the same conditions for $R = 1/2$. A shift in the abscissa is indicated for each material for ease of viewing; however, the curves are still log-log plots. In Figures 3.13 and 3.14 the beneficial effect of the lower temperature at low ΔK values and the convergence or crossing at high ΔK values is evident.

Figure 3.15 is a composite plot of the 18 different conditions, again, separated on the basis of material. It is seen that the influence of increased mean tensile stress ($R = 1/2$ compared to $R \approx 0$) is determined for both room temperature and low temperature conditions. Factors of 1.5 to 3 increases in da/dN for a given ΔK occurred for materials and temperatures as R was increased from zero to 1/2. Mn-Mo results at -50°F (-45°C), however, did tend to converge at high ΔK values. For a given cast steel, the crack growth rates for the two temperatures and two R ratios as shown in Figure 3.15 were always within a factor of 4 or less for all ΔK values. The maximum differences again occurred at the lower ΔK values.

Table 3.1. Least Square Constant Amplitude Fatigue Crack Growth Constants for $da/dN = A(\Delta K)^n$.						
Material	R = 0			R = 1/2		
	A (in./cycle) (ksi $\sqrt{\text{in.}}$)	A (m/cycle) (MPa $\sqrt{\text{m}}$)	n	A (in./cycle) (ksi $\sqrt{\text{in.}}$)	A (m/cycle) (MPa $\sqrt{\text{m}}$)	n
Room Temperature						
0030	$.198 \times 10^{-12}$	3.34×10^{-14}	4.33	-	-	-
0050A	1.19×10^{-11}	2.24×10^{-13}	3.88	1.08×10^{-10}	1.99×10^{-12}	3.40
C-Mn	4.18×10^{-11}	7.74×10^{-13}	3.35	1.25×10^{-10}	2.34×10^{-12}	3.21
Mn-Mo	5.99×10^{-11}	1.12×10^{-12}	3.28	3.7×10^{-10}	7.15×10^{-12}	2.89
8630	1.42×10^{-10}	2.63×10^{-12}	3.03	7.55×10^{-10}	1.39×10^{-11}	2.67
-50 °F (-45 °C)						
0030*	2.14×10^{-13}	3.48×10^{-15}	4.72	-	-	-
0050A	1.08×10^{-12}	1.79×10^{-14}	4.53	4.94×10^{-12}	8.36×10^{-14}	4.30
C-Mn	3.11×10^{-12}	5.4×10^{-14}	4.01	3.49×10^{-11}	6.36×10^{-13}	3.52
Mn-Mo	5.52×10^{-12}	9.76×10^{-14}	3.84	1.64×10^{-10}	3.13×10^{-12}	3.04
8630	3.45×10^{-11}	6.38×10^{-13}	3.38	1.05×10^{-10}	1.97×10^{-12}	3.22

* -30°F (-34°C) for 0030 steel

3.3 Macro and Microfractography

3.3.1 Macro

Macroscopic fractographs at approximately 2x magnification are shown in Figure 3.16 for each of the five steels under constant amplitude loading with $R \approx 0$ at both room and low temperature. Both the fatigue crack growth regions and the final fracture regions are shown. In all cases the fatigue crack grew from the chevron notch (bottom of photos) toward the top. The macro fractographic appearance for both $R \approx 0$ and $1/2$ were quite similar for a given material and temperature. No beach marks were evident in any specimens due to the constant amplitude loading. In all tests, an appreciable mode I flat fatigue crack growth region existed, with longer fatigue crack growth regions occurring at the smaller load ranges. In many cases the smooth fatigue region became rougher at longer crack lengths and thus at higher stress intensity factor ranges, but still remained essentially mode I fatigue cracks. Additional specific macroscopic characteristics evident in Figure 3.16 for each steel follows:

0030

The major difference in the room and low temperature fatigue crack growth region was the rougher surface at -30°F (-34°C) compared with that at room temperature. The final fracture region showed substantial ductility at room temperature as indicated by appreciable necking and shear lips. At -30°F (-34°C) little necking or shear lips existed and much of the final fracture region contained bright shiny brittle fracture.

0050A

The fatigue crack growth regions at both room temperature and -50°F (-45°C) were very similar. They were both very flat and smooth. At -50°F (-45°C) some fatigue crack jumping and arrest occurred at the longer crack lengths and two specimens. This occurred in regions with very high stress intensity factor ranges and very high nominal crack growth rates. The final fracture region at room temperature contained very little necking or shear lips and none existed at -50°F (-45°C). At the low temperature, the final fracture region was a completely flat, bright and shiny brittle fracture. At room temperature, the final fracture region contained a few beach-mark like markings within bright shiny brittle regions. Thus at both temperatures, final brittle fracture existed.

C-Mn

The fatigue crack growth regions for both room temperature and -50°F (-45°C) were initially very

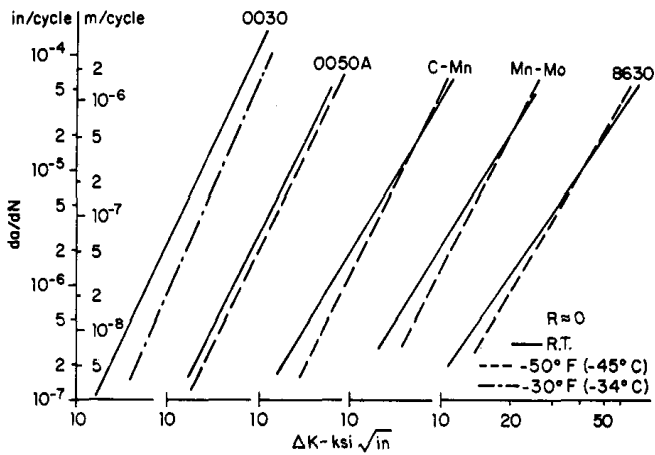


Figure 3.13. Composite da/dN versus ΔK for $R \approx 0$, room and low temperature.

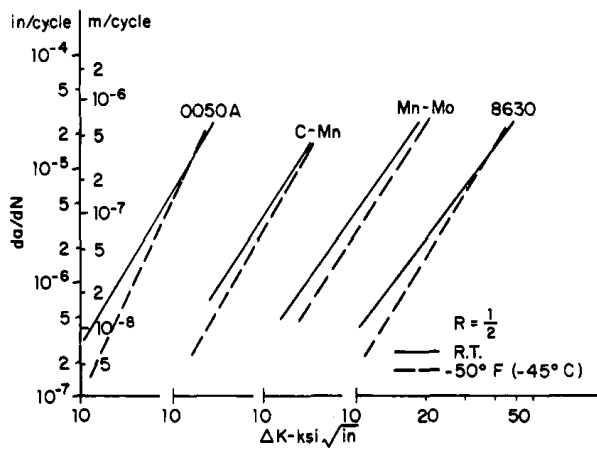


Figure 3.14. Composite da/dN versus ΔK for $R = 1/2$, room and low temperature.

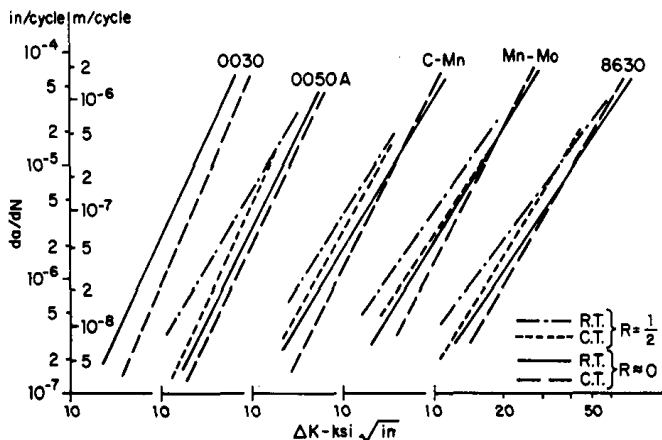
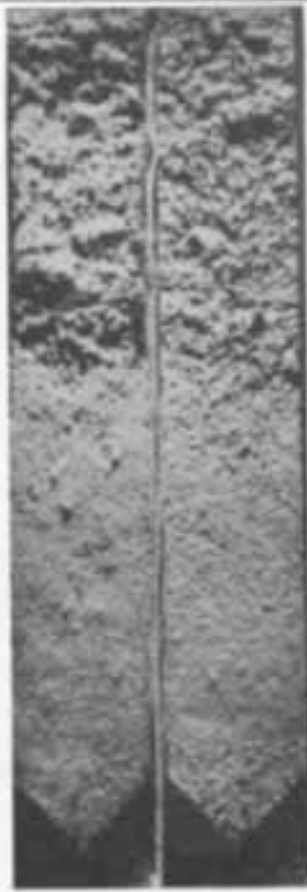


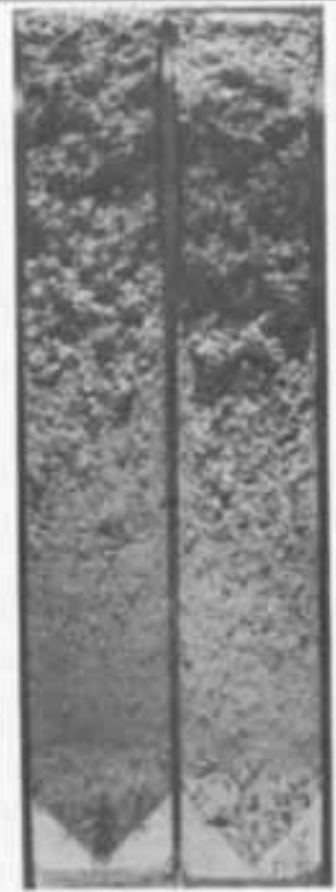
Figure 3.15. Composite da/dN versus ΔK for $R \approx 0$ and $1/2$, room and low temperature.



R.T. -30°F (-34°C)
0030



R.T. -50°F (-45°C)
0050A



R.T. -50°F (-45°C)
C-Mn



R.T. -50°F (-45°C)
Mn-Mo



R.T. -50°F (-45°C)
8630

Figure 3.16. Macroscopic fracture surfaces for constant amplitude loading for $R = 0$, room and low temperature.

smooth and flat with little differences between the two temperatures. Surface roughness increased at the longer fatigue crack lengths. Appreciable necking occurred in the final fracture region at both room and low temperature without substantial shear lips. A few bright shiny regions existed within the final fracture region at -50°F (-45°C), but essentially the material behaved in a very ductile manner at final fracture for both room and low temperature.

Mn-Mo

The fatigue crack growth regions for both room temperature and -50°F (-45°C) were initially smooth and flat with increased roughness at longer crack lengths. Appreciable necking with some shear lips occurred in the final fracture region at both temperatures. Thus, ductile final fracture existed at both room temperatures and -50°F (-45°C).

8630

The similar fatigue crack growth regions at both room temperature and -50°F (-45°C) were very smooth and flat with some roughness occurring at longer fatigue crack lengths. Reasonable necking occurred at room temperature in the final fracture region but none occurred at -50°F (-45°C). A twenty percent or more shear lip region existed at room temperature with less than one percent at the low temperature. No bright shiny brittle fracture regions existed at either temperature. The final fracture, however, went from appreciable slant or mixed-mode fracture at room temperature to mode I at low temperature.

3.3.2 Scanning Electron Microscopy (SEM)

Representative SEM fractographs ($1500\times$ - $3000\times$) for the five cast steels taken in the constant amplitude fatigue crack growth regions with $R \approx 0$ at both room and low temperature are shown in Figure 3.17. In all cases the specimen fracture surface was mounted normal to the SEM electron beam with nominal fatigue crack growth direction going from the bottom to the top in each fractograph. The 0030, C-Mn and Mn-Mo cast steels were also examined using $R = 1/2$. Little differences in the microfracture surfaces existed between these $R \approx 0$ and $R = 1/2$ tests.

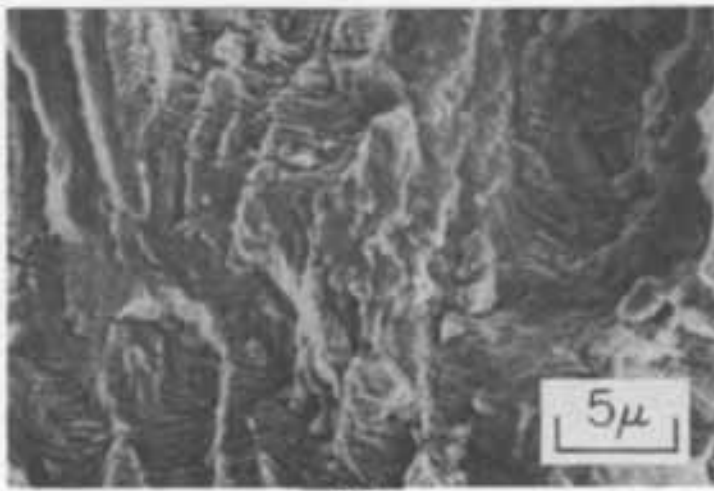
Fatigue striation bandings were readily found in the ferritic-pearlitic 0030 cast steel at both room temperature and -30°F (-34°C) as shown in Figure 3.17 (a). These bands were often well defined and were randomly distributed throughout the fatigue crack growth region. Striation banding also occurred in the ferritic-pearlitic 0050A cast steel at both room temperature and -50°F (-45°C) but were much

more difficult to locate and less clearly defined as shown in Figure 3.17 (b). For the tempered martensitic C-Mn, Mn-Mo and 8630 cast steels, very few distinct striations could be found. Some did exist, but in general the surfaces contained more of a ductile failure mode or quasi-striation surface as shown in Figure 3.17 (c-d). In all five steels the SEM analysis revealed ductile type transcrystalline fatigue crack growth behavior, at both room and low temperature. However, some mixed ductile and cleavage regions become evident in 0050A steel at -50°F (-45°C) at the longer crack lengths. Secondary micro-cracking, voids and inclusions were common in all conditions and increased with increased crack length and at the low temperature. In general, however, for each cast steel the fatigue crack growth mechanisms, as observed with the SEM from several hundred to several thousand magnification, were essentially the same at both room and low temperature. No brittle micro fatigue crack growth behavior was observed at either room or low temperature except for 0050A at -50°F (-45°C) with longer crack lengths approaching final fracture.

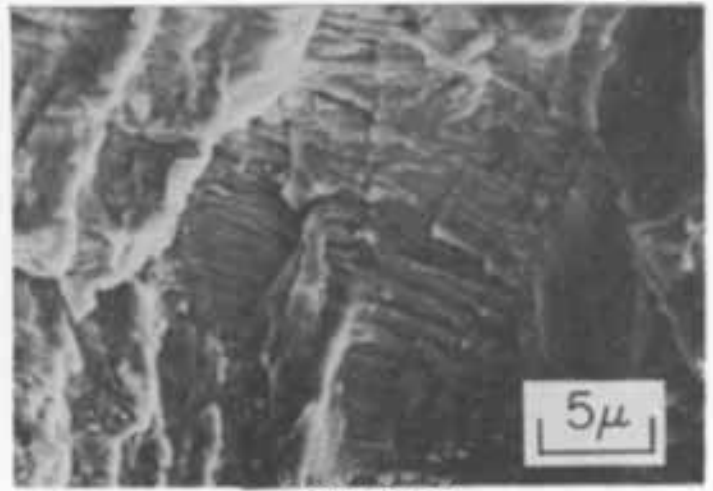
3.4 Discussion of Results

Barsom (4) has evaluated the Paris equation at room temperature with $R \approx 0$ for a wide variety of wrought steels and has found that many ferritic-pearlitic steels fall within a scatter band of about two. He has also found a similar scatter band width for martensitic wrought steels and has suggested that conservative upper bound values could be used in design if actual data could not be obtained. Superposition of these conservative values on the room temperature $R \approx 0$ da/dN versus ΔK data, or on the Paris equations, for the five cast steels, indicates the cast steels have lower crack growth rates by factors ranging from two to five at lower ΔK values and convergence or crossover at the higher ΔK values. Thus it appears that these five cast steels fall into a category equal to or better than similar wrought steels when compared using the Paris equation at room temperature. The values of A and n given in Table 3.1 for the five cast steels can be used in engineering design when the Paris equation is applicable.

A comparison of the five different cast steels for a given R ratio and temperature indicate that the constant amplitude fatigue crack growth rates vary by a factor of three or less. This does not mean that fatigue lives will vary by a factor of three, since many of the da/dN versus ΔK curves tend to con-

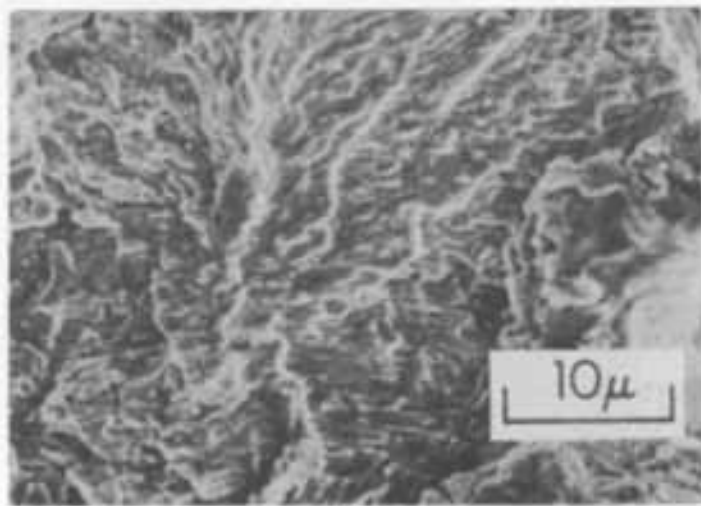


R.T.

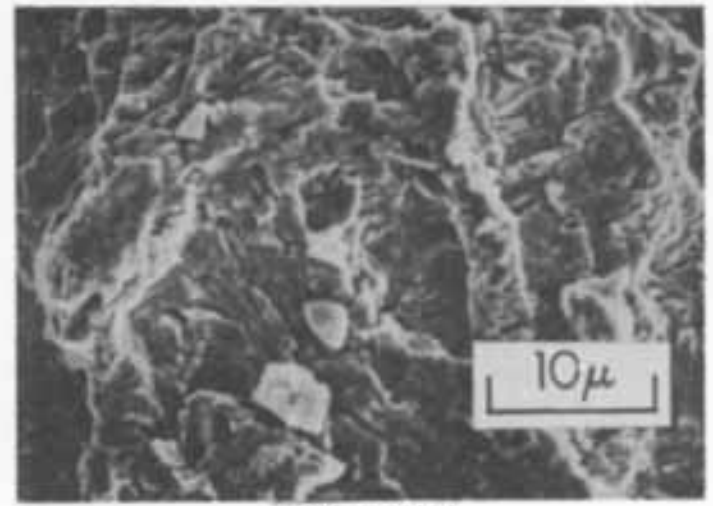


-30°F (-34°C)

(a) 0030

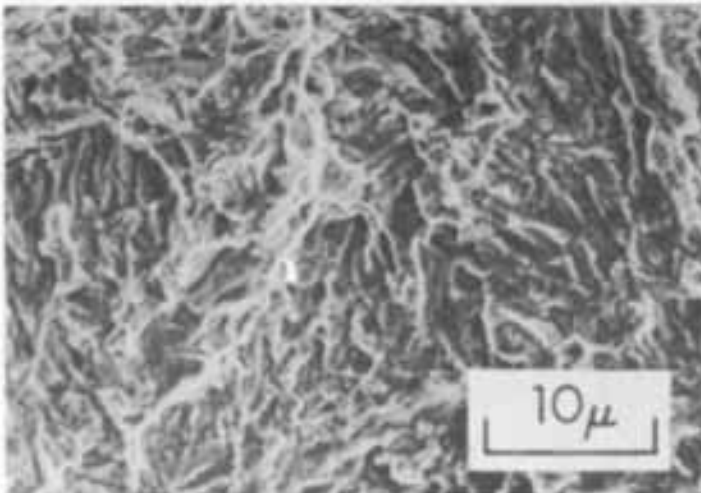


R.T.

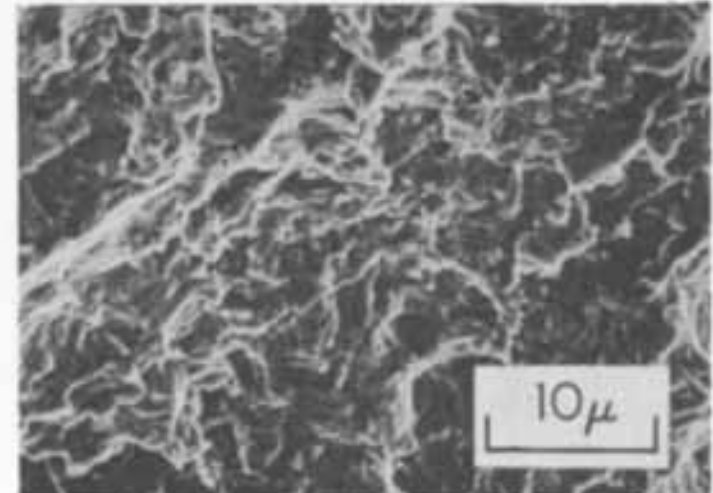


-50°F (-45°C)

(b) 0050A



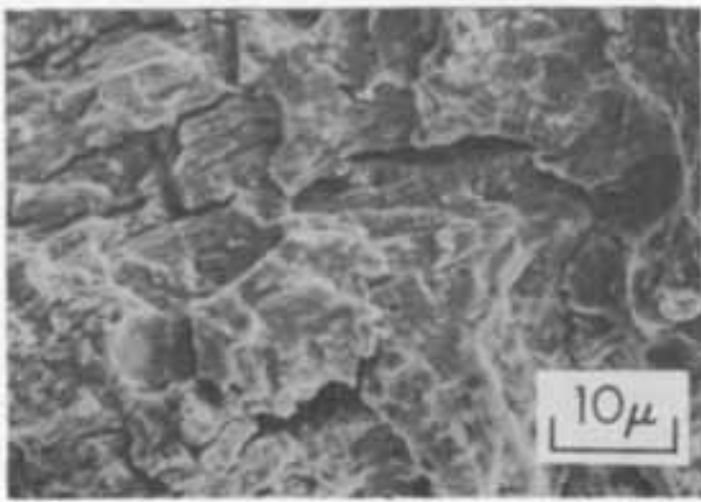
R.T.



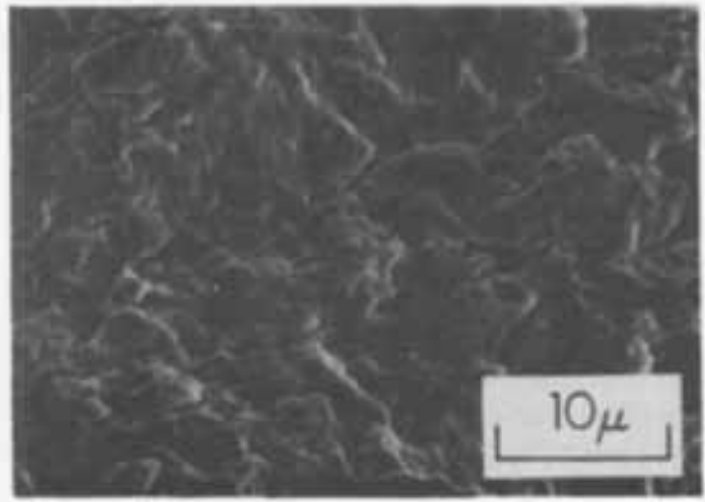
-50°F (-45°C)

(c) C-Mn

Figure 3.17. SEM fractographs from constant amplitude fatigue crack growth regions, room and low temperature.

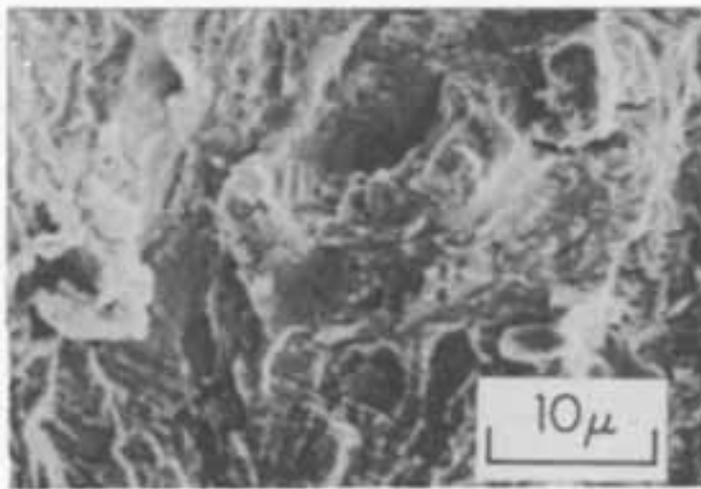


R.T.

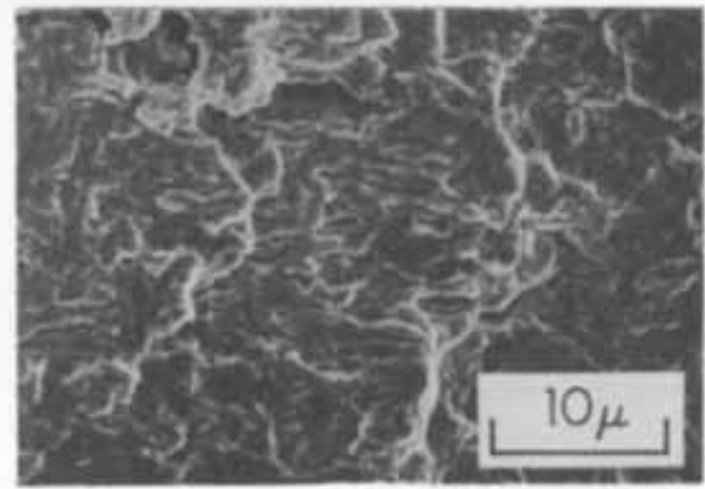


-50°F (-45°C)

(d) Mn-Mo



R.T.



-50°F (-45°C)

(e) 8630

Figure 3.17 (continued). SEM fractographs from constant amplitude fatigue crack growth regions, room and low temperature.

verge and even crossover. An average extreme difference of a factor of two is more reasonable for a given condition. The only exception to this is the very low crack growth rates at -30°F (-34°C) with $R \approx 0$ for 0030 cast steel. This condition was lower than others by a factor of three. Thus the kind of variation in constant amplitude fatigue crack growth behavior found between the five different cast steels is similar to that found in wrought steels.

The influence of mean stress was such that crack growth rates with $R = 1/2$ were within 1.5 to 3 times higher than for $R \approx 0$ for a given test condition. It has often been cited (based on wrought products primarily) that in the log-log linear region, mean stress influence on da/dN is small (5-7). This research, however, indicates slightly greater influence

than that found primarily with wrought products.

Fatigue crack growth rates at low temperatures were always less than those at room temperature except for a few data points at very high ΔK values where fatigue life is quite small. The beneficial behavior occurred despite the fact that 0030 and 0050A steels at low temperature were operating in the CVN lower shelf region and that C-Mn, Mn-Mo and 8630 were operating in the middle to lower CVN transition regions. Others have reported similar behavior for wrought steels as summarized in reference 8. Thus it appears that for cast steels, a transition from beneficial constant amplitude fatigue crack growth behavior to detrimental behavior will not occur until low temperatures are sufficiently into the lower shelf CVN region.

The SEM analysis indicated that fatigue crack growth mechanisms can involve ductile striations or ductile failure while final fracture can be entirely by cleavage. This was seen principally with the 0030, 0050A and 8630 steels at low temperatures. The SEM also indicated little difference in the fatigue crack growth topology at room and low temperatures. These similar fractographic results contribute to the understanding of why the low temperatures were beneficial to the constant amplitude fatigue crack growth behavior.

Microscopic striation spacings were measured in the 0030 cast steel at room temperature and compared with macroscopic crack growth rates. Many difficulties existed in measuring the striations due to various orientations, banding randomness and the too often ill-defined striations. The striation spacing turned out to be essentially statistically constant at all crack lengths and hence independent of stress intensity factor range. Thus a realistic comparison of crack extension per cycle could not be correlated with striations.

3.5 Summary and Conclusions

1) Constant amplitude fatigue crack growth behavior was obtained for five commonly used cast steels at both room temperature and -50°F (-45°C) or -30°F (-34°C) for crack growth rates above 2×10^{-7} in/cycle (5×10^{-9} m/cycle). The data were analysed using the Paris equation, $da/dN = A(\Delta K)^n$; values of A and n were determined using a least root mean square analysis. These values can be used in design decisions when the Paris equation is applicable.

2) All fatigue cracks were flat mode I type cracks for all five cast steels at both room and low temperature. da/dN versus ΔK scatter with $R \approx 0$ or $1/2$ for multiple specimens was similar to that found in the literature for wrought steels.

3) Crack growth rates, da/dN , at low temperature, -50°F (-45°C) or -30°F (-34°C) were less than room temperature rates at lower ΔK values by a factor of 1.2 to 3 for all five cast steels with $R \approx 0$. This reduction factor was from 1 to 2 with $R = 1/2$. At higher ΔK values room temperature and low temperature data tended to converge or even crossover.

4) Crack growth rates da/dN for $R = 1/2$ tests were 1.5 to 3 times higher than for $R \approx 0$ tests for both room and low temperatures. This increase was slightly higher than what is often suggested in the literature for principally wrought steels.

5) Ductile type transcrystalline fatigue crack growth occurred for all five cast steels at both room and low temperature. Fatigue striations were evident in the ferritic-pearlitic 0030 and 0050A cast steels at both room and low temperatures. Fewer striations, however were found in the 0050A steel. Some mixed ductile/cleavage also was evident in 0050A at long crack lengths at -50°F (-45°C). Very few striations were found in the martensitic C-Mn, Mn-Mo and 8630 cast steels at room and low temperatures where fatigue crack growth was by ductile failure. Secondary microcracking, voids and inclusions were evident in all five cast steels at both room and low temperatures. These increased in number at longer crack lengths. Striation spacing measurements made on 0030 cast steel at room temperature were essentially independent of ΔK , and thus no correlation could be made with macroscopic crack growth rates.

6) Ductile type fatigue crack growth behavior existed in low temperatures even though these temperatures were in the lower shelf CVN region for 0030 and 0050A cast steel, in the lower transition CVN region for C-Mn and 8630 cast steel and in the middle transition CVN region for Mn-Mo cast steel. Thus CVN impact ductile-brittle transitions do not predict possible ductile-brittle transitions in constant amplitude fatigue crack growth behavior in these five cast steels.

7) Final fracture areas showed ductile dimples at room temperature except for 0050A steel which was cleavage fracture. At the low temperatures, only C-Mn and Mn-Mo exhibited ductile dimples while 0030, 0050A and 8630 steel showed cleavage fracture.

8) The fatigue crack growth rates for the five cast steels at lower ΔK values were 2 to 5 times lower than conservative equations proposed by Barsom for principally wrought steels. At higher ΔK values Barsom's equations and the cast steel data converge or even crossover. Thus, fatigue crack growth rates for the five cast steels appear to be equivalent to, or perhaps even slightly better, than wrought steels.

Chapter 3 References

1. P.C. Paris and F. Erdogan, "A Critical Analysis of Crack Propagation Laws", Trans. ASME, Journal of Basic Engineering, Vol. 85, No. 4, 1963, p. 528.
2. "Standard Test Method for Plane-Strain Fracture Toughness of Metallic Materials", Annual Book of ASTM Standards, Part 10, E399, 1981.
3. E.T. Wessel, "State of the Art of the WOL Specimen for K_{Ic} Fracture Toughness Testing", Engineering Fracture

Mechanics, Vol. 1, No. 1, June, 1968, p. 77.

4. J.M. Barsom, "Fatigue-Crack Propagation in Steels of Various Yield Strengths", Trans-ASME, Journal of Engineering Industry, Series B, No. 4, Nov., 1971, p. 1190.
5. S.T. Rolfe, and J.M. Barsom, Fracture and Fatigue Control in Structures-Applications of Fracture Mechanics, Prentice-Hall, Englewood Cliffs, New Jersey, 1977.
6. R.W. Hertzberg, Deformation and Fracture Mechanics of

Engineering Materials, John Wiley and Sons, New York, 1976.

7. H.O. Fuchs and R.I. Stephens, Metal Fatigue in Engineering, Wiley Interscience, New York, 1980.
8. R.I. Stephens, J.H. Chung and G. Glinka, "Low Temperature Fatigue Behavior of Steels - A Review", paper No. 790517, April 1979, SAE Transactions, Vo. 88, 1980, p. 1892.

Chapter 4

Variable Amplitude Fatigue Crack Initiation, Growth and Fracture

4.1 Introduction

Constant amplitude stress-life, strain-life, and crack growth rate properties have contributed much to the understanding of fatigue behavior and to materials selection and life predictions. However, misconceptions and incorrect design decisions may be made based upon constant amplitude fatigue behavior, which does not provide information on sequential and interaction effects with variable loading. For example, tensile overloads may prolong fatigue life by inducing residual compressive stresses at a notch root or at a crack-tip region (increasing crack-tip closure) while compressive overloads may shorten fatigue life by inducing residual tensile stresses at a notch root or at a crack-tip region (decreasing crack-tip closure). A more realistic comparison of material or component fatigue behavior is thus determined, not from constant amplitude tests, but from load or

strain histories that closely duplicate or simulate actual service history and environment. The SAE Fatigue Design and Evaluation Committee previously selected three representative service spectra indicative of real-life loading that were used for comparative fatigue testing and fatigue life predictions (1). One such spectrum is the transmission history shown in Figure 4.1 (a) which will be referred to as T/H. This history has predominantly tensile loadings along with significant compressive loads. The T/H spectrum has been modified at the University of Iowa by eliminating all compressive loadings. This modified history is referred to as mod T/H and is shown in Figure 4.1 (b).

T/H and mod T/H load range histograms obtained by rainflow counting are shown in Figure 4.2. A total of 1710 load reversals make up one T/H

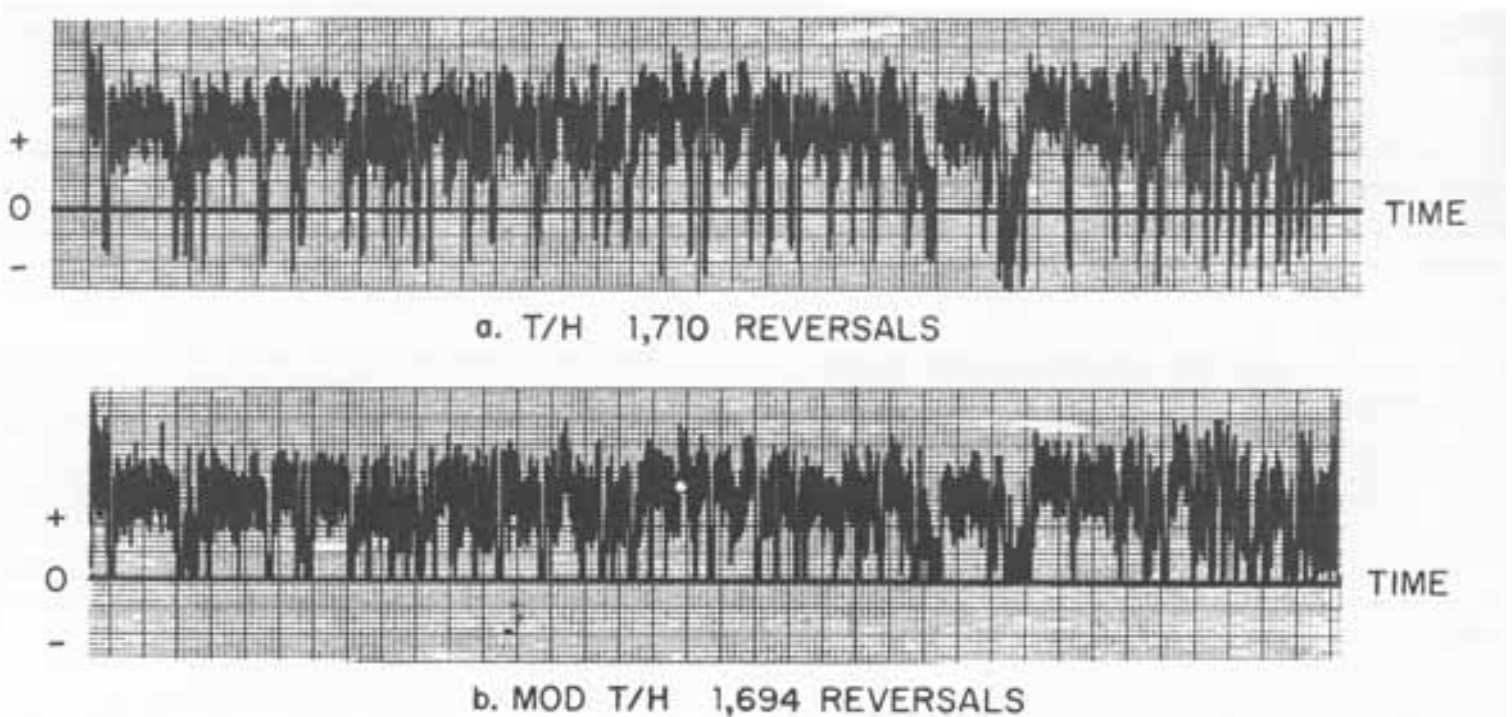


Figure 4.1. Variable amplitude load spectra T/H and mod T/H.

history block. The mod T/H has only 1694 reversals per block because 16 reversals were removed by eliminating the compressive loads. Most of the load ranges for both histories are of relatively small magnitude. Elimination of the compression eliminated some of the highest ranges and shifted the magnitude of some of the smaller ranges as shown in Figure 4.2. These two histories were used for all variable amplitude tests with the five cast steels at room and low temperatures in conjunction with a keyhole compact specimen for better simulation of real-life conditions.

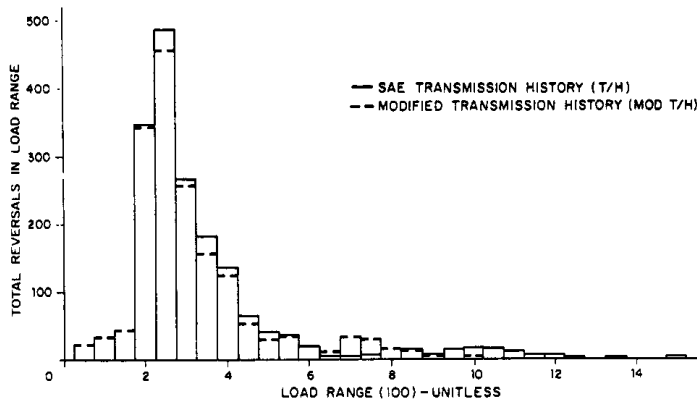


Figure 4.2. Load spectra range histograms for T/H and mod T/H.

4.2 Experimental Procedures

A keyhole specimen with 0.324 in (8.2 mm) thickness was used in conjunction with the T/H and mod T/H histories. This specimen is shown in Figure 4.3. The specimen has the same overall dimensions as the compact specimen used for constant amplitude fatigue crack growth tests; however, a 3/16 in (4.76 mm) diameter as drilled keyhole notch has replaced the chevron starter notch. The keyhole notch was left in the as-drilled condition without additional reaming or polishing to better simulate actual component field conditions. A theoretical elastic stress concentration factor of $K_t = 4$ was determined using several different finite element models and programs with $H/w = 0.6$. The value of $H/w = 0.6$ was used for all tests except for some of the early tests with the 0030 cast steel which had H/w equal to 0.49. The test specimens were polished on one surface in order to better monitor fatigue crack initiation and growth. Polishing scratches were perpendicular to the direction of crack growth.

Variable amplitude fatigue tests using either the

T/H or mod T/H histories were run under load control at 12 Hz using an automated profiler in conjunction with the 20 kip (89 kN) closed-loop electrohydraulic test system. The block history was repeated until specimen fracture. Low temperature tests were conducted in the automated CO₂ chamber from -30°F (-34°C) to -75°F (-60°C). Fatigue crack initiation and crack growth were monitored with a 33x traveling telescope. Crack growth increments between about 0.01 in (0.25 mm) and 0.1 in (2.5 mm) were monitored until specimen fracture. About fifteen percent of the room temperature tests also had an electropotential monitoring system to better aid in detecting crack initiation at the notch. Fatigue crack initiation was quantitatively defined as the first visible surface crack length of $\Delta a = 0.01$ in (0.25 mm) which could be observed emanating from the keyhole notch with the optical telescope. The electropotential system, however, always indicated cracks had initiated at the notch interior shortly prior to the observation on the surface. The number of blocks involved in this difference was small and therefore the chosen criteria for crack initiation appears quite reasonable from an engineering point of view. A crack length Δa measured from the notch equal to 0.1 in (2.5 mm) was also specifically monitored since this value was previously selected by the SAE Fatigue Design and Evaluation Committee as a

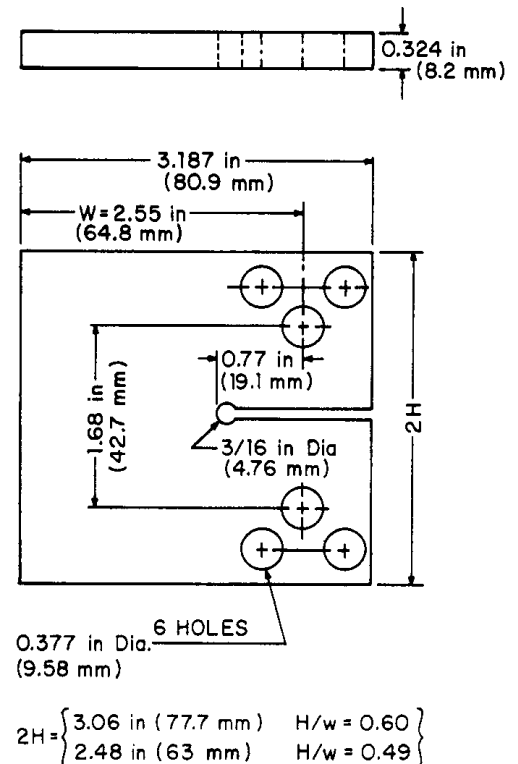


Figure 4.3. Keyhole notch specimen.

limiting value of crack initiation used with notch strain analysis prediction methods (1). This value is also a reasonable crack length where linear elastic fracture mechanics (LEFM) analysis becomes quite applicable. Most multiple initiated interior cracks had also coalesced into one major crack at this point.

The T/H and mod T/H block histories begin and end with zero load. The first and last load in each block has the same peak value P_{max} . Three peak load levels were chosen for the T/H history and two of these peak load levels were chosen for the mod T/H history for each of the five cast steels. The load choices provided reasonable test time per specimen and produced fatigue lives from 54 to 1,940 blocks which was equivalent to about 9×10^4 to 3.3×10^6 reversals. Tests lasted from 1 hour to 1.5 days. Tests were duplicated for all test conditions except for two.

The compact specimen is predominantly a bend specimen with a small axial contribution. Nominal elastic stresses σ_{nom} at the keyhole notch can be calculated from

$$\sigma_{nom} = \frac{P}{A} + \frac{Mc}{I} \quad (4.1)$$

where P is the applied load, A is the net section area, M is the bending moment, c is the distance from the neutral axis to the keyhole notch, and I is the net section moment of inertia. Values of peak σ_{nom} for the three different peak load levels were 57 ksi (393 MPa), 46 ksi (314 MPa), and 40 ksi (275 MPa). Since K_t at the notch is 4, all specimens were subjected to localized plasticity at the keyhole notch on the first loading.

The above three peak σ_{nom} levels were used at room temperature and -50°F (-45°C) [-30°F (-34°C) for 0030 steel] with the T/H history. The two higher values were used for the mod T/H tests at room temperature and -50°F (-45°C) [-30°F (-34°C) for 0030 steel]. In order to better study the influence of different reasonable low climatic temperatures, tests were also run in duplicate using the T/H history with peak σ_{nom} equal to 46 ksi (314 MPa) at either -30°F (-34°C), -50°F (-45°C) and -75°F (-60°C).

4.3 Test Results

The variable amplitude test results using the keyhole compact specimens with the T/H and mod T/H load spectra are shown in Tables 4.1 and 4.2 respectively. In Table 4.1 for T/H, there are five major column divisions representing, first the peak σ_{nom} values and then the four different

temperature results. For a given temperature, four sub-columns are shown giving applied blocks to three different life criteria and then the crack extension Δa_f at fracture. N_1 represents the number of applied blocks to crack initiation defined as $\Delta a = 0.01$ in (0.25 mm), N_2 represents the number of applied blocks to $\Delta a = 0.1$ in (2.5 mm) and N_f represents the number of applied blocks to final fracture as measured on a test specimen. The rows are organized for specific values of peak σ_{nom} for the five different cast steels. The same format is used in Table 4.2 for the mod T/H except only room temperature and one low temperature is involved. These tables, involving the five cast steels, can be analyzed to determine the effects of several parameters such as:

- 1) the effect of peak σ_{nom} on the three life criteria.
- 2) the effect of different temperatures on the three life criteria.
- 3) the effect of temperature on the final crack length which is related to fracture toughness.
- 4) the effect of removing the compression loads at two temperatures.

The above can also be used to rank the five cast steels relative to each other for different behavior criteria.

In order to aid in analyzing the data in Tables 4.1 and 4.2, S-N type log-log plots of peak σ_{nom} versus number of applied blocks to $\Delta a = 0.01$ in (.25 mm), N_1 , to $\Delta a = 0.1$ in (2.5 mm), N_2 , and to final fracture, N_f , have been drawn in Figures 4.4 to 4.8 for the five cast steels. Each figure, which is for a given steel, has (a) room temperature data and (b) -50°F (-45°C) data [-30°F (-34°C) for 030]. The solid data points and curves are for the T/H spectrum and the open data points are for the mod T/H spectrum. Circles represent N_1 , squares represent N_2 and triangles represent blocks to final fracture (N_f). All curves shown in Figures 4.4 to 4.8 have been drawn as straight lines through the approximate average of the data for a given life criteria. This was done as an approximation not to claim a log-log linear relationship, but for reasonable aid in viewing the overall test results.

As given in Tables 4.1 and 4.2, final crack length at fracture for all test conditions ranged from 0.08 in (2 mm) for 0050A steel at -75°F (-60°C) which is a very brittle condition to 1.14 in (29 mm) for 8630 steel at room temperature which indicates excellent fracture toughness. The crack lengths at fracture depended upon material, peak σ_{nom} and temperature. Removing the compression portion of the loading had no influence on Δa_f for a given peak

Table 4.1. T/H History Blocks to Three Crack Length Criteria

Peak Nominal Stress ksi (MPa)	Room Temperature				-30°F (-34°C)				-50°F (-45°C)				-75°F (-60°C)			
	N ₁	N ₂	N _f	Δa_f in (mm)	N ₁	N ₂	N _f	Δa_f in (mm)	N ₁	N ₂	N _f	Δa_f in (mm)	N ₁	N ₂	N _f	Δa_f in (mm)
0030																
57 (393)	40	65	97	-	51	91	149	.63 (16)								
	18	39	54	-	37	63	96	.51 (13)								
46 (314)	79	102	169	-	89	163	254	.71 (18)	80	144	219	.51 (13)	88	117	186	.4 (10)
	67	77	141	.79 (20)	130	186	304	.63 (16)	68	145	248	.51 (13)	78	120	158	.24 (6)
40 (275)	124	156	313	-	149	185	351	.83 (21)								
	80	134	270	-	155	187	364	.83 (21)								
0050A																
57 (393)	13	58	113	.59 (15)					73	91	98	.28 (7)				
	28	76	125	.71 (18)					89	97	99	.12 (3)				
46 (314)	103	155	297	.83 (21)	101	190	289	.55 (14)	55	130	212	.24 (6)	142	-	153	.08 (2)
	100	236	399	.75 (19)	155	188	281	.43 (11)	100	168	271	.35 (9)	156	172	172	.12 (3)
40 (275)	233	433	656	.83 (21)					265	303	379	.51 (13)				
	212	235	445	.79 (20)					214	250	419	.35 (9)				
C-Mn																
57 (393)	31	54	108	.75 (19)					30	80	169	.75 (19)				
	31	63	114	.71 (18)					32	82	179	.71 (18)				
46 (314)	105	141	285	.83 (21)	72	222	489	.87 (22)	139	287	606	.91 (23)	175	210	412	.83 (21)
	92	147	288	.79 (20)	152	251	530	.94 (24)	91	190	640	.79 (20)	166	229	468	.87 (22)
40 (275)	78	259	606	.83 (21)					158	361	746	.83 (21)				
	100	205	668	.94 (24)					167	315	751	.91 (23)				
Mn-Mo																
57 (393)	38	116	262	.87 (22)					19	108	259	.87 (22)				
	28	86	224	.87 (22)					91	292	292	.91 (23)				
46 (314)	100	197	635	.91 (23)	133	531	799	.83 (21)	306	368	629	.94 (24)	256	323	506	.67 (17)
	209	295	551	.94 (24)	150	316	621	.87 (22)	252	350	-	-	373	442	684	.79 (20)
40 (275)	287	482	795	.94 (24)					224	793	1313	.94 (24)				
	243	398	758	.98 (25)												
8630																
57 (393)	125	170	308	.94 (24)					110	221	394	.63 (16)				
	116	185	352	.94 (24)					217	253	360	.51 (13)				
46 (314)	250	338	532	1.14 (29)	479	559	959	.94 (24)	696	741	946	.75 (19)	758	830	1050	.75 (19)
	258	340	597	1.10 (28)	393	447	744	.79 (20)	390	438	705	.79 (20)	585	635	870	.55 (15)
40 (275)	495	746	1283	1.10 (28)					760	1261	1940	.75 (18)				
	696	1020	1497	1.02 (26)												

nom and temperature. The macro fatigue cracks grew essentially perpendicular to the applied load in almost all cases. A general deviation from this plane was usually with \pm five degrees. For a given test specimen, only one predominant surface crack grew past $\Delta a \approx 0.1$ in (2.5 mm); however, as many as 1 to 4 surface cracks initiated from the keyhole notch. These multiple small cracks either became nonpropagating cracks or coalesced with the

predominant crack.

From both the Tables and Figures 4.4 to 4.8, very little scatter for the three life criteria existed in the duplicate tests (triplicate for 0030 for some tests) for all five cast steels. Scatter of life to fracture for duplicate tests was between a factor of 1 and 2. Most of this scatter, however, was less than a factor of 1.5. Greater scatter ranging from a factor of 1

Table 4.2. Mod T/H History Blocks to Three Crack Length Criteria								
Peak Nominal Stress ksi (MPa)	Room Temperature				Low Temperature*			
	N ₁	N ₂	N _f	Δa_f in (mm)	N ₁	N ₂	N _f	Δa_f in (mm)
0030*								
46 (393)	180	273	346	- -	200	283	437	.55 (14)
	247	355	453	.67 (17)	367	462	674	.63 (16)
	113	193	340	.71 (18)				
40 (275)	373	522	751	- -	639	716	968	.75 (19)
	322	388	567	.71 (18)	517	637	925	.71 (18)
		298	447					
0050A								
57 (393)	109	224	307	.51 (13)	218	346	347	.12 (3)
	123	190	286	.55 (14)	194	200	211	.20 (5)
46 (314)	424	595	760	.79 (20)	620	676	722	.20 (5)
	339	605	873	.75 (19)	731	803	897	.39 (10)
C-Mn								
57 (393)	175	235	331	.71 (18)	221	302	492	.75 (19)
	100	224	328	.71 (18)	229	328	449	.71 (18)
46 (314)	430	491	641	.79 (20)	735	783	1011	.79 (20)
	395	530	798	.79 (20)	1105	1270	1583	.79 (20)
Mn-Mo								
57 (393)	170	263	409	.83 (21)	278	423	615	.83 (21)
	174	341	526	.83 (21)	306	355	523	.83 (21)
46 (314)	429	762	1103	.91 (23)	661	730	1056	.94 (24)
	501	646	957	.91 (23)	1346	1406	1713	.94 (24)
8630								
57 (393)	420	482	648	.94 (24)	616	640	739	.40 (10)
	490	566	709	.94 (24)	620	690	874	.64 (16)
46 (314)	1310	1412	1718	.98 (25)	2262	2392	2746	.75 (19)
	615	736	1159	1.06 (27)				

*-30°F (-34°C) for 0030

-50°F (-45°C) for 0050A, C-Mn, Mn-Mo and 8630.

to about 4 occurred for crack initiation, $\Delta a = 0.01$ in (.25 mm), which can be attributed to the as-drilled keyhole notch surface roughness variation, multiple interior cracks, and the exact decision as to when a surface crack was visible. Most of the scatter for crack initiation, however, was less than a factor of 2.

The number of blocks within the three life criteria regions for a given specimen and test condition ranged from 15 to 75 percent of total life for crack initiation, 5 to 50 percent to grow the crack to $\Delta a = 0.1$ in (2.5 mm), and followed by 20 to 70 percent to grow the crack to fracture [excluding 0050A at -50°F (-45°C) or lower]. Thus all three regions, in general, significantly contributed to the total life of

the five cast steels except where substantial brittleness occurred in the 0050A steel at lower temperatures. This implies the importance of including both crack initiation, growth of short cracks from notches, and growth of longer cracks in a total fatigue life prediction procedure.

The magnitude of the peak σ_{nom} had the greatest influence on all three life criteria. Following this influence was the effect of removing the compression from the block history. The mod T/H data (dashed lines and open data points in Figures 4.4 to 4.8) have substantially increased blocks to all three criteria for a given peak σ_{nom} for both room and low temperature. The greatest influence of removing the compression loads was with crack initia-

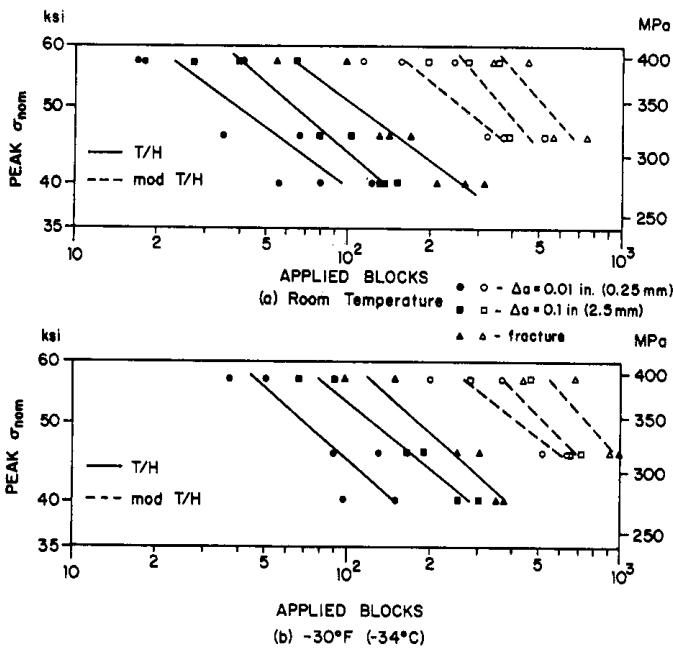


Figure 4.4. Peak σ_{nom} versus three life criteria, 0030 cast steel.

tion, $\Delta a = 0.01$ in (0.25 mm), where average increases in fatigue life ranged from factors of 3 to 9. For the short crack growth region in the presence of the keyhole notch, N_2-N_1 , average increases in life ranged from factors of essentially 1 to 4, while for long crack growth life from N_2 to N_f , factors ranged from essentially 1 to 3. Thus for both room and low temperature variable amplitude spectra, the compression loadings in general were

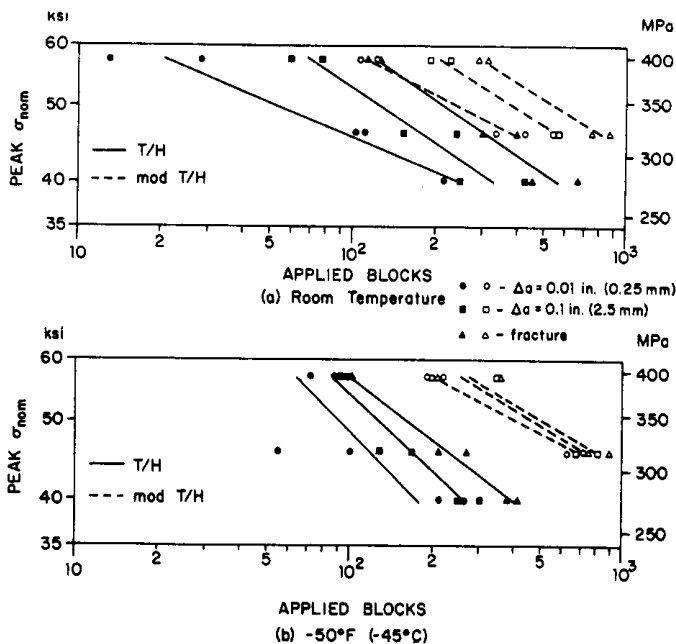


Figure 4.5. Peak σ_{nom} versus three life criteria, 0050A cast steel.

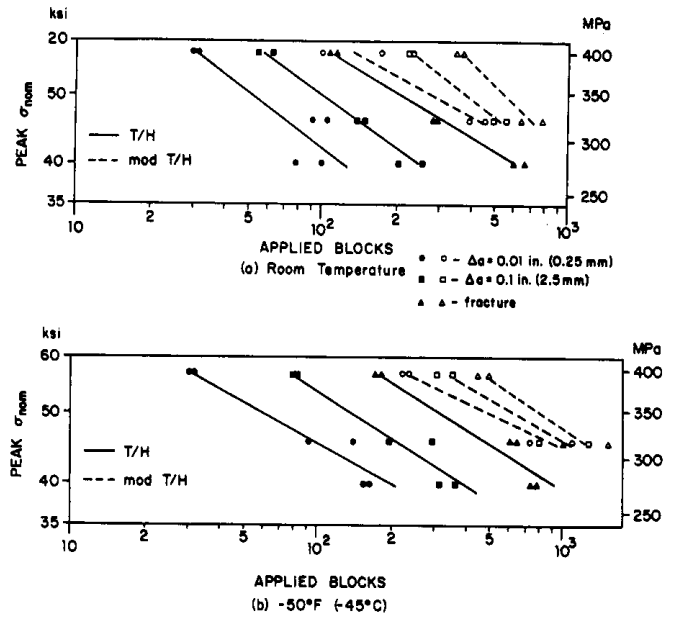


Figure 4.6. Peak σ_{nom} versus three life criteria, C-Mn cast steel.

significantly detrimental to fatigue crack initiation life and somewhat detrimental to fatigue crack growth life.

Comparing the data in Tables 4.1 and 4.2 and in Figures 4.4 to 4.8 it can be determined that, except for 0050A steel, all the average low temperature fatigue lives for the three life criteria were equal to or better than at room temperature. The increase in

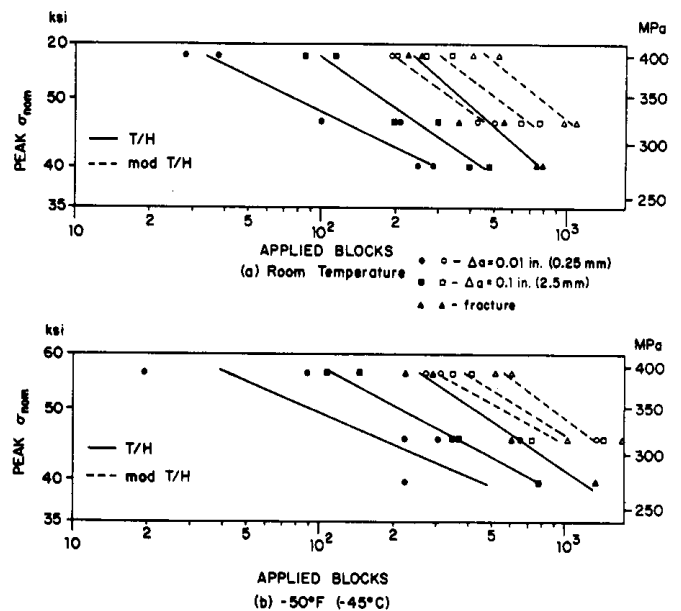


Figure 4.7. Peak σ_{nom} versus three life criteria, Mn-Mo cast steel.

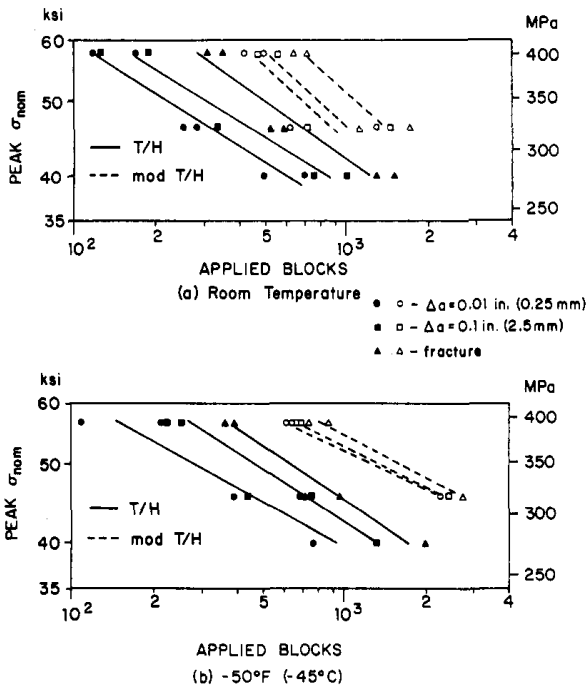


Figure 4.8. Peak σ_{nom} versus three life criteria, 8630 cast steel.

blocks to crack initiation (open data points) and blocks to fracture (solid data points) are plotted versus test temperature for all five cast steels. Straight line segments have been drawn from one test temperature to another through the average of the data as shown. This figure clearly shows the small scatter for a given test condition and the influence of the four test temperatures with each of the five cast steels. It is seen that as the temperature was lowered from room temperature to -75°F (-60°C), the average fatigue crack initiation life for all five cast steels was essentially equal to or better than that at room temperature by a factor of 2.5. The greater increases occurred in Mn-Mo and 8630 steel at the lower temperatures. Total life to fracture at low temperature was also essentially equal to or better than at room temperature by less than a factor of 2.5 except for 0050A steel. This steel showed a continuous drop in total fatigue life as the temperature was lowered from room temperature to -75°F (-60°C). Thus even though the lower temperatures were not detrimental to fatigue crack initiation life, in 0050A steel they were quite detrimental to total fatigue life.

crack initiation life and in total life was generally less than a factor of 2.5. In order to obtain a better visualization of the influence of lower temperatures on variable amplitude fatigue crack initiation, growth and total life, the extended low temperature data for peak σ_{nom} equal to 46 ksi (314 MPa) with the T/H spectrum is plotted in Figure 4.9. Here

Average fatigue crack growth life can be determined from Figure 4.9 for each of the test conditions by subtracting the average applied blocks to crack initiation from the average applied blocks to fracture. These subtractions are plotted in Figure 4.10 where it is evident that, except for 0050A steel, the crack growth life tends to first increase

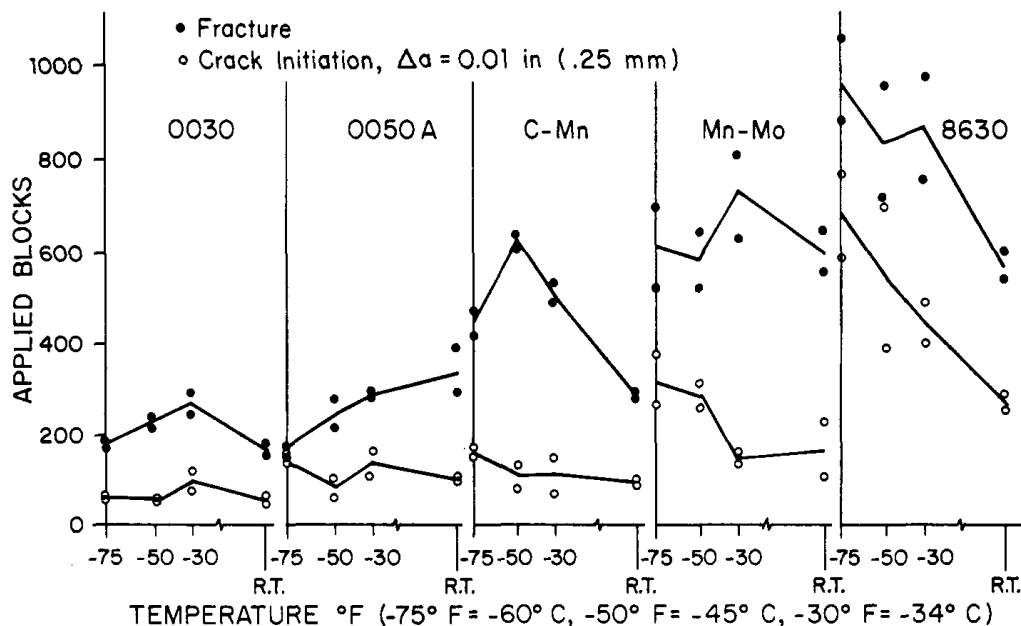


Figure 4.9. Average fatigue life to crack initiation, N_1 , and fracture, N_f , with T/H loading, peak $\sigma_{nom} = 46$ ksi (314 MPa).

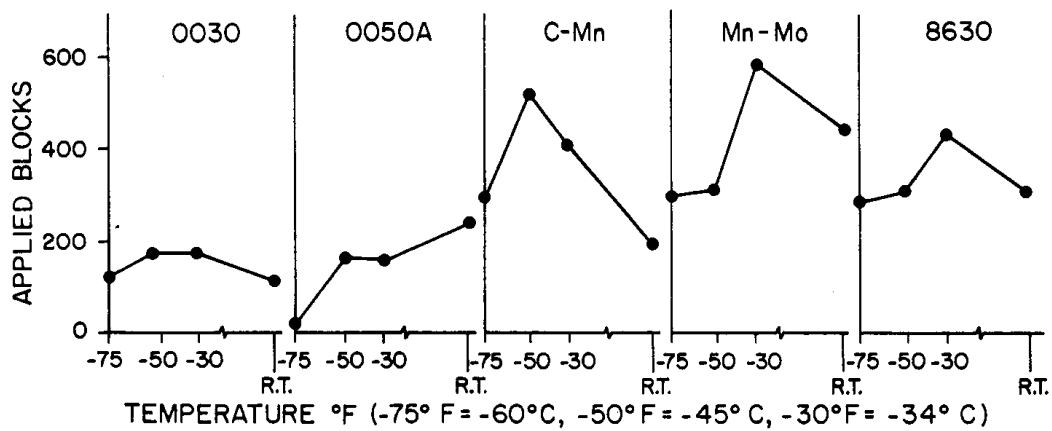


Figure 4.10. Average fatigue crack growth life, $N_f - N_1$, with T/H loading, peak $\sigma_{nom} = 46$ ksi (314 MPa).

as the temperature is lowered, reaches a maximum, and then decreases. For 0050A steel the crack growth life decreased at all lower test temperatures. The maximum fatigue crack growth life at the lower temperatures for the four steels was between 1.3 and 2.5 times greater than at room temperature. However, at -75°F (-60°C) only C-Mn had better fatigue crack growth life than at room temperature.

Fatigue crack extension from the keyhole notch, Δa is plotted versus applied blocks for the four different test temperatures with the T/H loading and peak σ_{nom} equal to 46 ksi (314 MPa) in Figure 4.11 for the five cast steels. Only crack extension up to

about .4 in (10 mm) is shown since the rates become quite high and with substantial similarity beyond this length. More than half of the curves in Figure 4.11 are somewhat sigmoidal in shape, in that the crack growth rate starts out high for short cracks, then decreases as the crack grows one or two mm from the keyhole notch and then increases until fracture. The change in curvature at short crack lengths is due to the interaction of the local plastic zone at the notch with the crack tip. It is seen that the fatigue crack growth rates at the different temperatures indicate the trends found in Figure 4.10. As the temperature is decreased for a given steel, fatigue crack growth rates are lower,

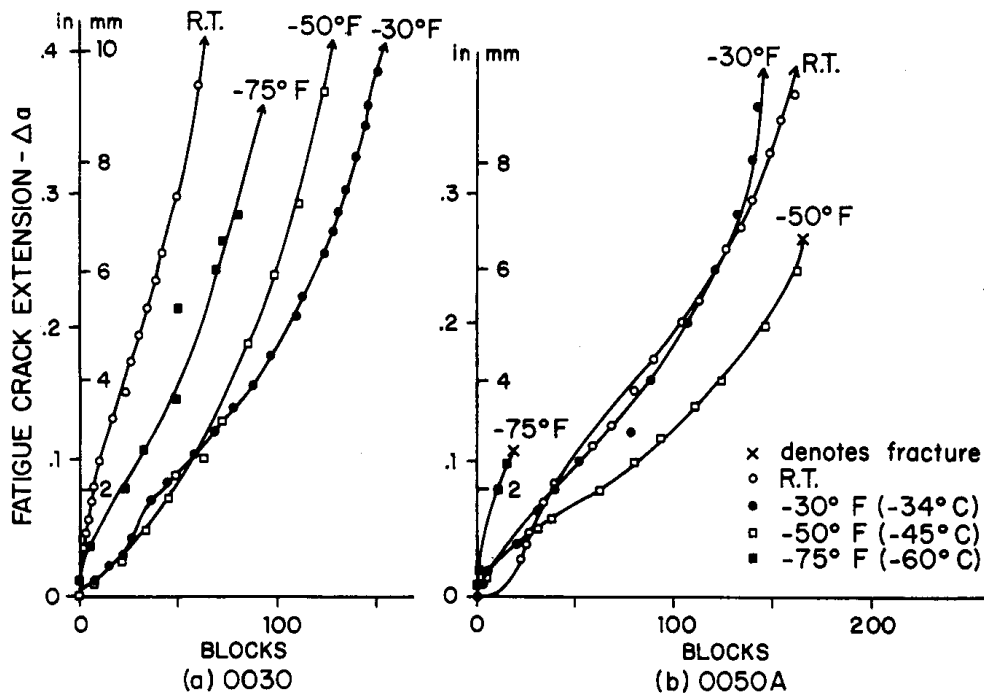


Figure 4.11. Fatigue crack extension versus applied blocks.

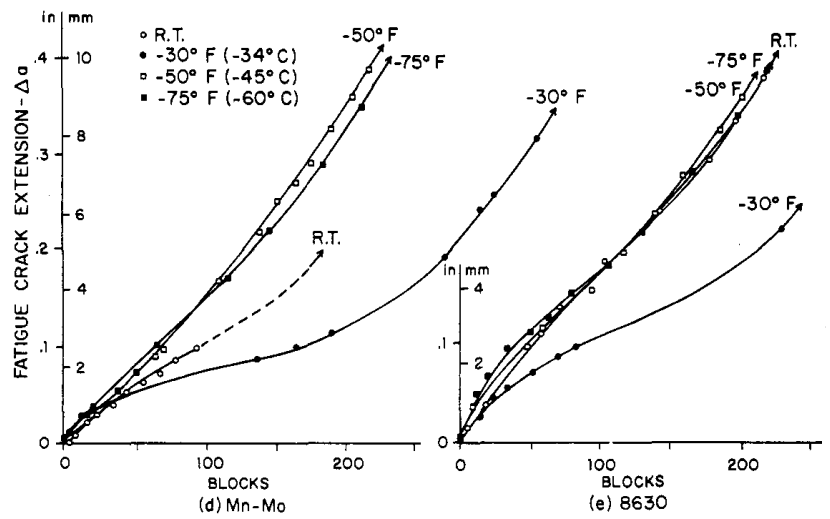
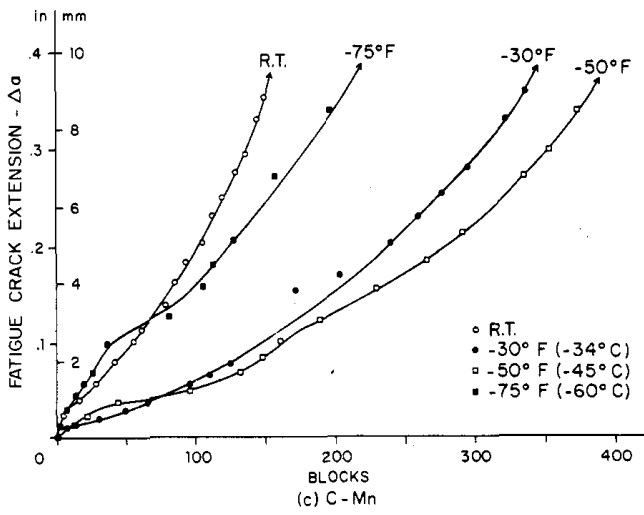


Figure 4.11 (continued). Fatigue crack extension versus applied blocks.

but as the temperature is decreased even further, the rates revert to higher values which approach or surpass those at room temperature. Thus the increases in fatigue crack growth rates as the temperature was lowered contributed to the poor lower temperature fatigue crack growth life. In addition, the crack lengths at final fracture for 0050A at the two lowest temperatures are shown to be very short.

Final crack lengths at fracture, Δa_f , for all five

steels for the test conditions in Figure 4.9 to 4.11 are plotted in Figure 4.12. Here it is evident for 0030, 0050A, and 8630 steel that crack lengths at fracture decreased as the temperature was lowered. For 0030 and 0050A the decrease was very large. Thus shorter crack lengths at fracture, and hence, lower fracture toughness at the lower temperatures also contributed to the eventual lower fatigue crack growth life at the lower temperatures.

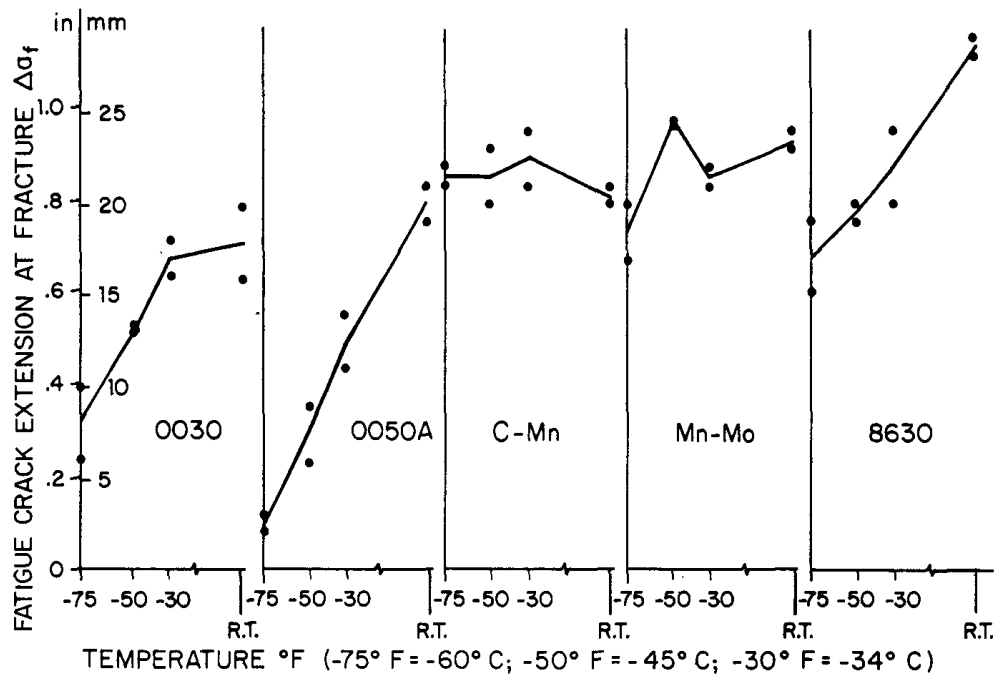


Figure 4.12. Average fatigue crack extension at fracture with T/H loading, peak $\sigma_{nom} = 46$ ksi (314 MPa).

4.4 Macro and Micro Fractography

4.4.1 Macro

Macroscopic fractographs at approximately 2x magnification are shown in Figure 4.13 for each of the five cast steels for the T/H spectrum with peak σ_{nom} equal to 46 ksi (314 MPa) at the four test temperatures. The fatigue crack initiation, crack growth, and final fracture regions are shown. In all cases the fatigue crack initiated from the keyhole notch (bottom of photos) and grew toward the top of the photos. Despite the variable amplitude loading, no beach marks are evident in any of the specimens. In all tests, mode I fatigue crack growth existed. Initiation and coalescence of multiple interior cracks at the keyhole notch is evident in most specimens. The roughness in the fatigue crack growth region varies from material to material and also at the four different test temperatures. The roughness was greater at the higher values of peak σ_{nom} and at the longer crack lengths. In some cases it was difficult to distinguish the end of the fatigue crack growth region due to the roughness. The mod T/H spectrum, however, caused much less roughness due to the elimination of the compression loads. In all steels, except 0050A, the variable amplitude fatigue crack growth regions were rougher than constant amplitude fatigue regions due to higher peak stresses, variable amplitudes, and compression. Additional specific macroscopic characteristics evident in Figure 4.13 for each steel follow:

0030

The greatest roughness occurred in this steel compared to the others. This increased at the lower temperatures. The final fracture region showed substantial ductility and necking at room temperature and essentially brittle fracture at the three lower temperatures.

0050A

The fatigue crack growth regions were quite smooth at all four temperatures. The decrease in crack length at fracture as the temperature decreased is quite evident. A substantial jump in the fatigue crack region just prior to fracture is evident at -50°F (-45°C). These jumps near final fracture occurred in several specimens at low temperatures. The final fracture region at room temperature contained only a slight amount of necking and shear lips. However, at the lower temperatures, no necking or shear lips existed and the fracture regions were completely flat, bright and shiny brittle fractures. Thus at all temperatures, final brittle fracture existed.

C-Mn

The fatigue crack growth region size and roughness were essentially independent of test temperature. Necking with slight shear lips exist in the final fracture region at all four temperatures. These are less at -75°F (-60°C) with some brittleness mixed in the primarily ductile fracture. The final fractures were completely ductile at the other three temperatures.

Mn-Mo

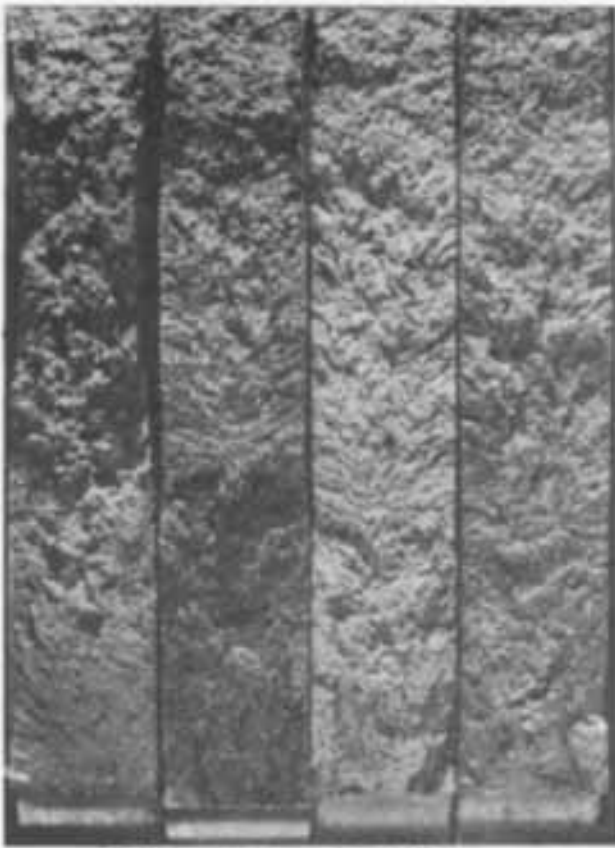
The fatigue crack growth region size and roughness were similar at all temperatures except -75°F (-60°C). The shorter fatigue crack length at fracture for -75°F (-60°C) is evident. Appreciable necking exists for all temperatures except -75°F (-60°C). Shear lip size decreased as the temperature was lowered. However, final fracture areas were still ductile at all temperatures.

8630

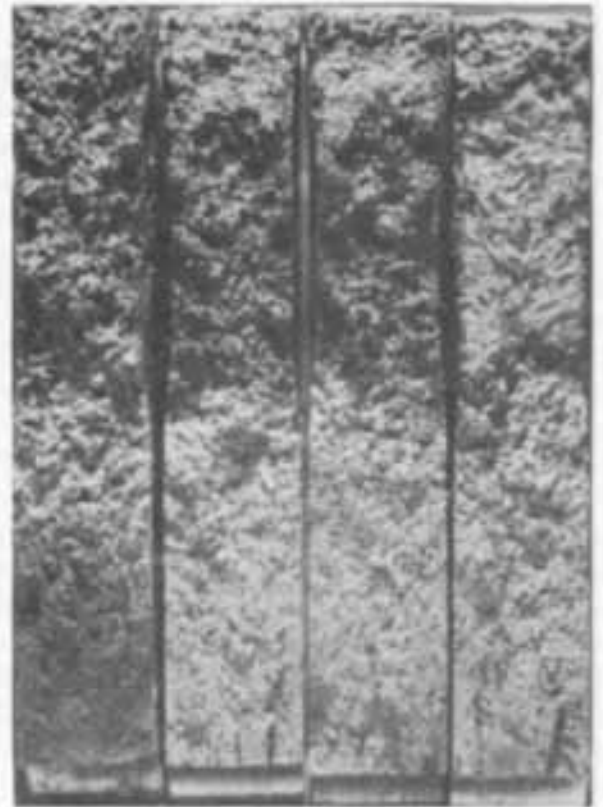
Less roughness occurred in the fatigue crack growth region at the lower temperatures. The decrease in final crack length at fracture for the lower temperatures is evident. At -75°F (-60°C) a substantial jump in the fatigue crack region just prior to fracture is seen. These jumps near final fracture occurred in several specimens at the low temperatures. The final fracture region has appreciable shear lips at room temperature and -30°F (-34°C) with only small shear lips at -50°F (-45°C) and no shear lips at -75°F (-60°C). No bright shiny brittle fracture regions existed at any of the four test temperatures. The final fractures, however, went from appreciable slant or mixed-mode fracture at room temperature to mode I at the two lower temperatures.

4.4.2 Scanning Electron Microscopy (SEM)

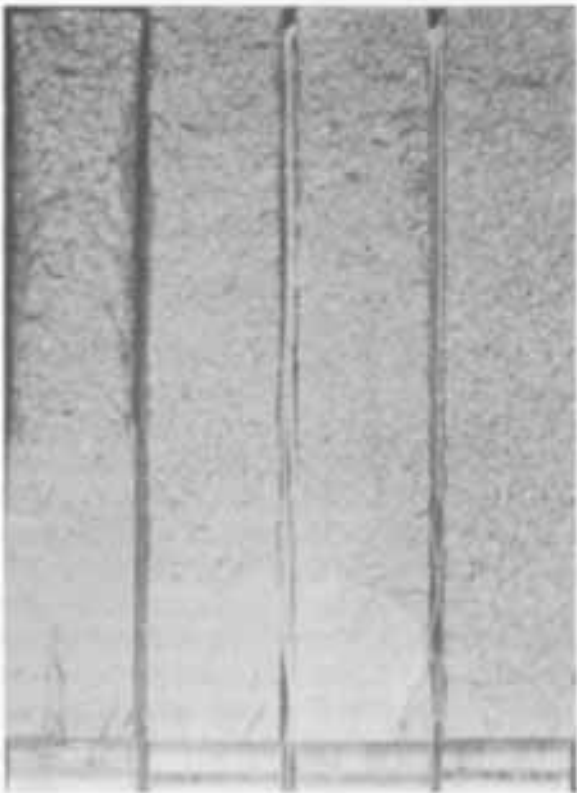
Both T/H and mod T/H specimen fracture surfaces from the different test temperatures were examined with the SEM from 50x to 3500x magnification. The fracture surfaces were mounted normal to the SEM electron beam. Two to four independent fatigue crack initiation sites were found for the different test specimens. These sites were usually from the as-drilled keyhole notch scratches; however, some were formed at inclusions or porosity directly adjacent to the notch edge. The fatigue crack growth regions were much more irregular than for constant amplitude loading and striations were fewer, more poorly defined and more difficult to locate. They were often flatter due to crack closure and rubbing between the two crack surfaces. Both the T/H and mod T/H fracture surfaces



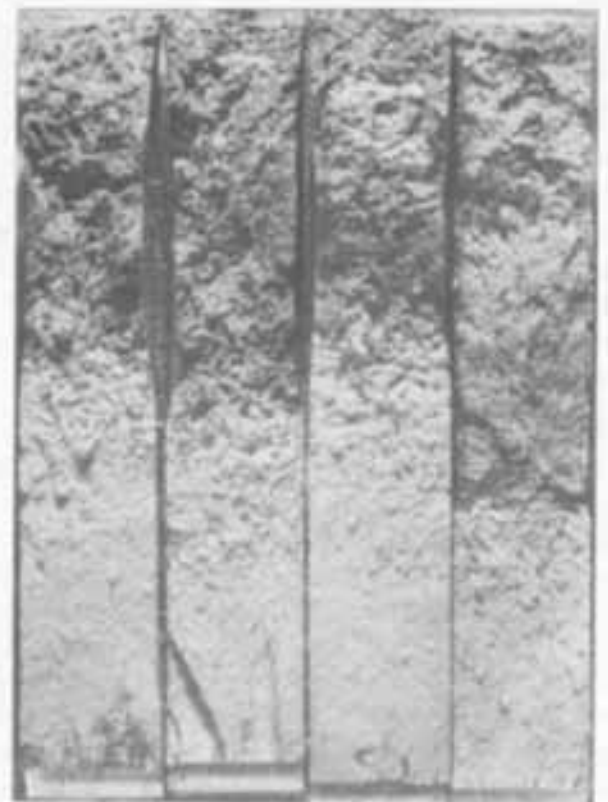
R.T. -30°F -50°F -75°F
-34°C -45°C -60°C
0030



R.T. -30°F -50°F -75°F
-34°C -45°C -60°C
C-Mn



R.T. -30°F -50°F -75°F
-34°C -45°C -60°C
0050A



R.T. -30°F -50°F -75°F
-34°C -45°C -60°C
Mn-Mo

Figure 4.13. Macroscopic fracture surfaces for T/H tests, peak $\sigma_{nom} = 46$ ksi (314 MPa), room and low temperature.



R.T. -30°F -50°F -75°F
 -34°C -45°C -60°C
 8630

Figure 4.13 (continued). Macroscopic fracture surfaces for T/H tests, peak $\sigma_{nom} = 46$ ksi (314 MPa), room and low temperature.

were similar, but slightly less rubbing and crack closure existed in the mod T/H spectrum. Substantial numbers of inclusions, porosity, and secondary cracks existed on the fracture surfaces at all temperatures. These increased in numbers at the longer crack lengths.

Typical SEM fractographs taken in the T/H fatigue crack growth region with magnification between 1000x and 3000x are shown in Figure 4.14 for each of the five steels at room temperature and -50°F (-45°C). Fatigue cracks grew from top to bottom in the photographs. The fatigue crack growth morphology did not change significantly at any of the test temperatures except near impending final fracture for a few of the very low temperature tests. In general the fatigue crack growth behavior from room temperature to -75°F (-60°C) was transcrystalline and ductile, with and without striations. Just prior to impending fracture, a few mixed cleavage facets were found dispersed within the ductile fatigue matrix at lower temperatures. These regions, however, contribute very little to the overall fatigue crack growth life or total life of an individual test.

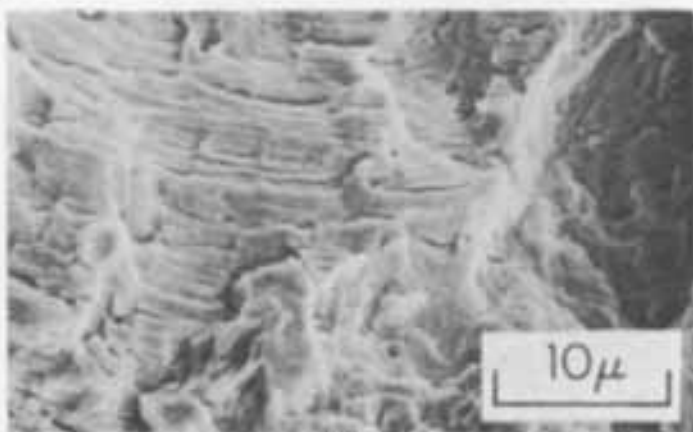
The final fracture region was usually quite distinct from the fatigue region. Final fractures ranged from 100 percent ductile dimples to 100 percent cleavage. Mixed modes also existed. Specific microscopic characteristics for each steel follows:

0030

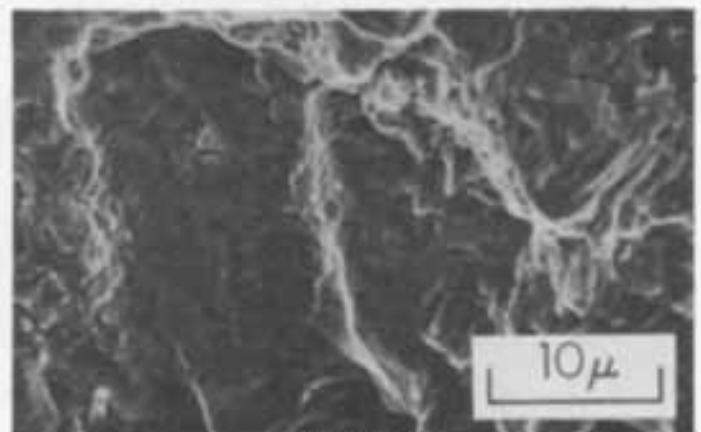
The greatest number of striations with the variable amplitude histories occurred in 0030 steel at room temperature as shown in Figure 4.14 (a). The more flattened regions are shown at -50°F (-45°C). Some mixed cleavage facets and ductile fatigue occurred at all three low temperatures just prior to fracture. The final fracture region was ductile dimples at room temperature, mostly cleavage at -30°F (-34°C) and all cleavage at the two lowest temperatures.

0050A

Striations were very scarce under all temperature



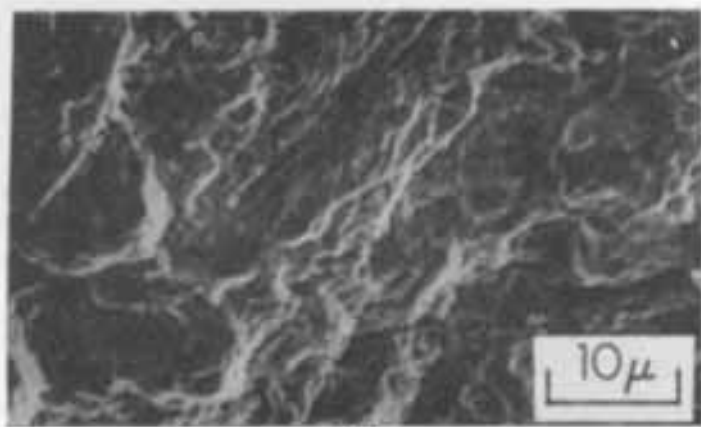
R.T.



-30°F (-34°C)

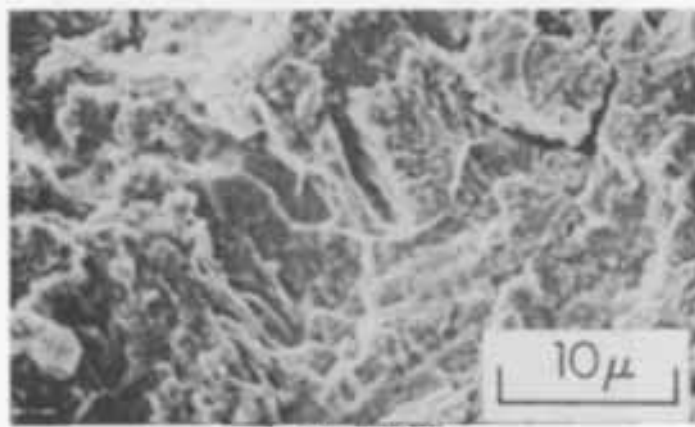
(a) 0030

Figure 4.14. SEM fractographs for T/H tests, peak $\sigma_{nom} = 46$ ksi (314 MPa), room and -50°F (-45°C).

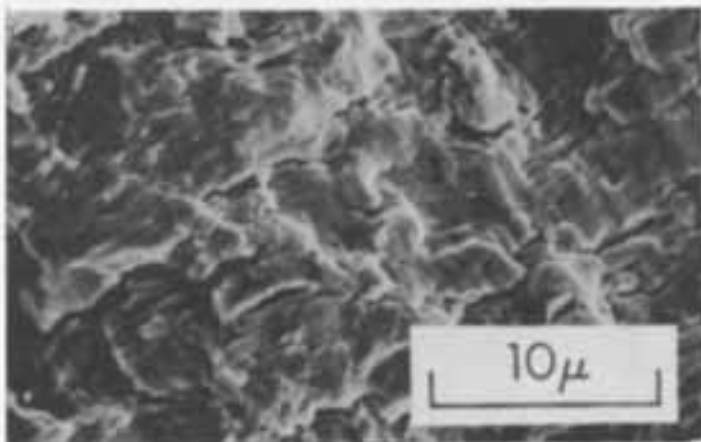


R.T.

(b) 0050A

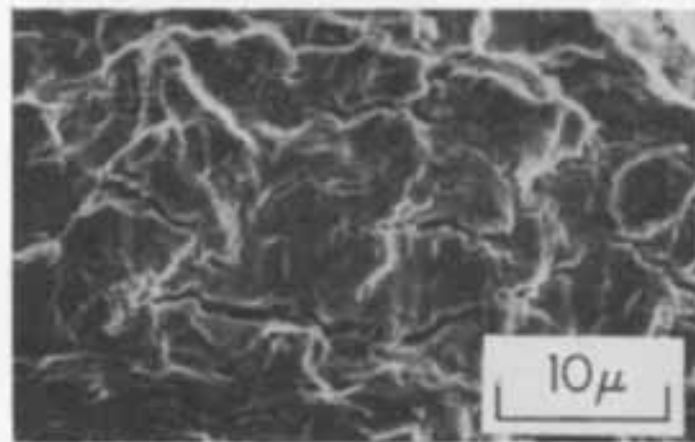


-50°F (-45°C)

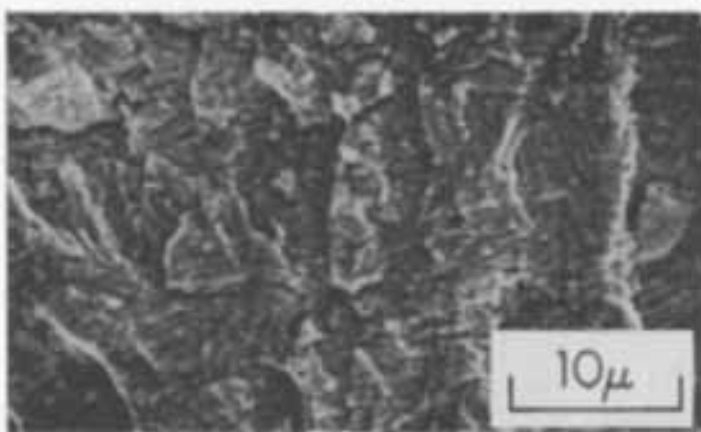


R.T.

(c) C-Mn

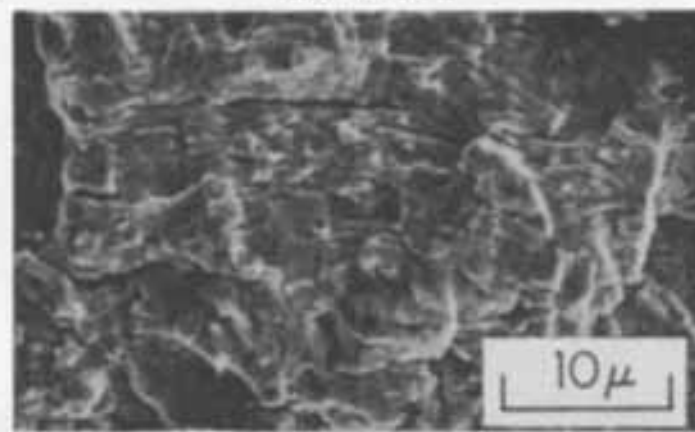


-50°F (-45°C)

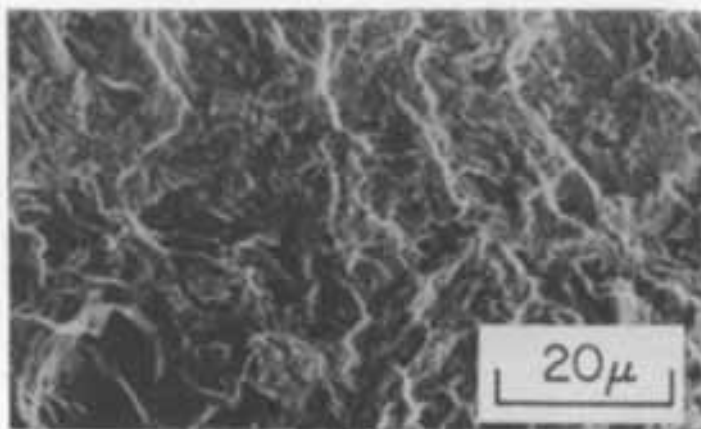


R.T.

(d) Mn-Mo

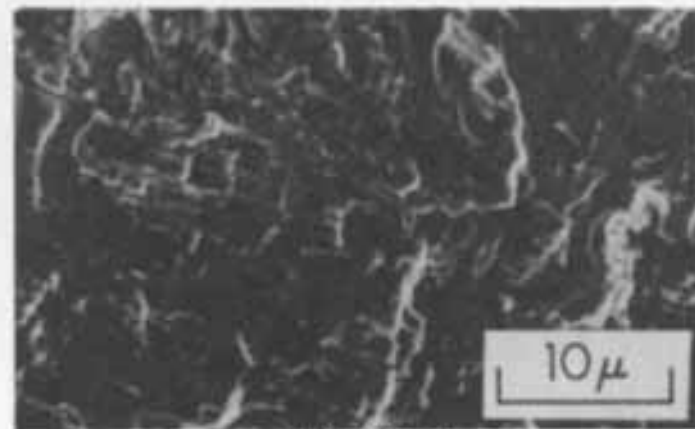


-50°F (-45°C)



R.T.

(e) 8830



-50°F (-45°C)

Figure 4.14 (continued). SEM fractographs for T/H tests, peak $\sigma_{nom} = 46$ ksi (314 MPa), room and -50°F (-45°C).

conditions, however. Fatigue crack growth was still ductile as shown in Figure 4.14 (b). Some mixed cleavage facets and ductile fatigue occurred at the two lowest temperatures just prior to fracture. The final fracture region was cleavage at all temperatures.

C-Mn and Mn-Mo

Fatigue crack growth was ductile at all temperatures with very few striations which were usually flattened as shown in Figure 4.14 (c) and 4.14 (d). Some mixed cleavage facets and ductile fatigue occurred only at -75°F (-60°C) just prior to fracture. Final fracture regions had ductile dimples at all test temperatures, however, some cleavage also became evident at -50°F (-45°C) and somewhat more evident at -75°F (-60°C).

8630

Fatigue crack growth was ductile as shown in Figure 4.14 (e) at all temperatures with only a few striations present. At room temperature the final fracture region was all ductile dimples while at -30°F (-34°C) mixed dimple and cleavage existed. At the two lowest temperatures, final fractures were completely by cleavage.

4.5 Discussion of Results

The low temperature tests were performed in the lower shelf CVN energy region for 0030 and 0050A steels, the lower transition to lower shelf region for C-Mn and 8630 steels, and in the mid or lower transition region for Mn-Mo steel as shown in Figure 1.5. However, under variable amplitude conditions, fatigue crack initiation life at the three low temperatures was always approximately equal to or better than at room temperature by less than a factor of 2.5. Since -50°F (-45°C) was determined to be a reasonable low climatic temperature involved with most ground vehicles in the USA, it appears that these five cast steels should perform adequately in components based upon only fatigue crack initiation. However, 0050A, in particular, had extremely poor fatigue crack growth life at low temperatures due to higher crack growth rates and lower fracture toughness. This cast steel would not be desirable for use at low climatic temperatures.

Fatigue crack growth life and rates for the other four cast steels under variable amplitude loading were better at -30°F (-34°C) than at room temperature as shown in Figures 4.10 and 4.11; but this behavior tended to reverse as the temperature was lowered to -50°F (-45°C) or -75°F (-60°C). Decreases in fracture toughness at the lower

temperatures partially contributed to the lower fatigue crack growth life. The reversal in fatigue crack growth rates has previously been shown for constant amplitude loading (2-5). This reversal in crack growth rates occurs at temperatures below the beginning of the lower shelf CVN region for both constant and variable amplitude loading. Thus it appears from the above, that steels with NDT values or lower shelf CVN regions below operating temperatures should have fatigue resistance equal to or better than that at room temperature. Additional research, however, is needed to reinforce this idea, particularly under variable amplitude impact loadings.

The macroscopic fatigue crack growth behavior was not really clarified with the SEM fractographic analysis, since the general microscopic fracture surfaces were generally quite similar and ductile at all test temperatures. Some exceptions occurred just prior to impending fracture with the formation of dispersed cleavage facets. Negligible fatigue life, however, exists here under any microscopic mechanisms.

The influence of compression on fatigue crack growth behavior has been somewhat controversial. It has often been claimed that non-overload compressive stresses should have little influence on fatigue crack growth, since the crack will be closed during small compressive loadings. This research has shown that by eliminating the compressive loads (mod T/H) fatigue crack growth life increased by factors between 1 and 4. This increase is not necessarily negligible. Thus it appears that compressive loadings can have an influence on variable amplitude fatigue crack growth behavior. However, the major influence is in crack initiation where life increases between 3 and 9 occurred in this research.

The selection or comparison of cast steels based on fatigue resistance is an important engineering decision. The five cast steels subjected to the T/H and mod T/H spectra can be compared on the basis of fatigue crack initiation life, N_1 , crack growth life, $N_f - N_1$, or total fatigue life N_f at the different temperatures. This complete comparison can be made from Tables 4.1 and 4.2 and from the S-N type diagrams of Figures 4.4 to 4.8. However, Figures 4.9 to 4.10 which agree completely with the general behavior under all values of peak σ_{nom} , can provide the same general information with much greater ease. From Figure 4.9 it is seen for both room and low temperatures that 8630 has the best fatigue resistance based on variable

amplitude fatigue crack initiation life and total life. Mn-Mo steel is ranked second for these conditions. Crack initiation life for the other three steels were essentially equivalent. 0030 and 0050A, the ferritic-pearlitic steels, in general have the lower total fatigue life resistance. Crack growth life is shown in Figure 4.10 where it is seen that the martensitic steels C-Mn, Mn-Mo and 8630 in general have the greater fatigue crack growth resistance at the various temperatures.

4.6 Summary and Conclusions

1) The five cast steels were subjected to two variable amplitude load histories at room temperature and three different low climatic test temperatures using an as-drilled keyhole notch compact specimen. Three criteria were specifically monitored namely: crack initiation defined by the first visible surface crack Δa equal to 0.01 in (0.25 mm), Δa equal to 0.1 in (2.5 mm) and final fracture. Multiple cracks initiated at the keyhole notch and these usually coalesced into one mode I fatigue crack at Δa approximately equal to 0.1 in (2.5 mm). The T/H history had 1710 reversals and included both tension and compression loads. This history was modified by truncating the compression loads (mod T/H, 1694 reversals).

2) Fatigue life within all three criteria was significant at all test temperatures. Thus, total fatigue life predictions of notched components should include crack initiation, growth of short cracks under the influence of the notch plastic zone and growth of longer crack lengths away from the notch influence.

3) Eliminating the compression at the four temperatures increased fatigue crack initiation life by factors of 3 to 9, increased short crack growth life by factors of 1 to 4, and increased long crack growth life by factors of 1 to 3. Thus compression loads had greater influence on crack initiation, but the influence on crack growth was also significant.

4) Except for 0050A cast steel, all the average low temperature fatigue lives for the three life criteria were equal to or better than at room temperature. The increase in crack initiation life was within a factor of 2.5 as was the total fatigue life to fracture. Crack growth life, however, tended to increase as the temperature was lowered and then this trend

reversed. This reversal was due to increased crack growth rates and decreased fracture toughness. 0050A steel, however, had a continuous decrease in fatigue crack growth life for lower temperatures.

5) SEM analysis indicated that fatigue crack growth was ductile with and without observable striations at all temperatures. Final fracture region morphology depended upon both material and temperature. Final fracture surfaces ranged from 100 percent ductile dimples to 100 percent cleavage. Thus fatigue crack growth mechanisms were independent of final fracture mechanisms.

6) Ductile fatigue mechanisms can exist at temperatures within the lower shelf CVN energy regions. It appears that if operating temperatures are above lower shelf CVN regions, then fatigue crack initiation life and fatigue crack growth life should be equivalent to or better than at room temperature.

7) In general, the three martensitic cast steels 8630, Mn-Mo and C-Mn had better fatigue resistance with the variable amplitude loading spectra at the four test temperatures than the ferritic-pearlitic 0030 and 0050A cast steels.

8) 0030, C-Mn, Mn-Mo and 8630 cast steels are suitable for low climatic temperature conditions (0050A is excluded). This can only be stated for the non-welded condition since weldments were not considered.

Chapter 4 References

1. R.M. Wetzel, Editor, Fatigue Under Complex Loading, SAE, 1977.
2. R.I. Stephens, J.H. Chung and G. Glinka, "Low Temperature Fatigue Behavior of Steels - A Review", paper No. 790517, April, 1979. SAE Transactions, Vol. 88, 1980, p. 1892.
3. W.W. Gerberich and N.R. Moody, "A Review of Fatigue Fracture Topology Effects on Threshold and Kinetic Mechanisms", Symposium on Fatigue Mechanisms, J.T. Fong, Editor, ASTM STP 675, 1979, p. 451.
4. T. Kawasaki, T. Yokobori, Y. Sawaki, S. Nakanishi, and H. Izumi, "Fatigue and Fracture Toughness and Fatigue Crack Propagation in 5.5% Ni Steel at Low Temperature", 1977 ICF-4 Vol. 3, Waterloo, Canada, June, 1977, p. 857.
5. R.L. Tobler and R.P. Reed, "Fatigue Crack Growth Resistance of Structural Alloys at Cryogenic Temperature", paper presented at the Cryogenic Engineering Conference/ International Cryogenic Materials Conference; University of Boulder, Colorado, August, 1977.

Plane Stress Fracture Toughness, R-Curve

5.1 Experimental Procedures and Results

5.1.1 Introduction

Fracture toughness of a material depends on the volume of material plastically deformed prior to fracture. Since this volume depends on the specimen thickness, it follows that the fracture toughness will vary with the thickness. For thick specimens, large normal stresses exist in the through thickness (transverse) direction which will restrict plastic deformation. Fracture toughness for this condition is referred to as plane strain fracture toughness denoted by K_{Ic} . For thinner specimens however, the degree of plastic constraint acting at the crack tip is much smaller than for thick specimens and the material exhibits a higher fracture toughness. This condition is referred to as plane stress fracture toughness, and is denoted by K_{Ic} in the literature. K_{Ic} is usually more difficult to obtain than K_{Ic} due mainly to the complexity of the elastic-plastic behavior at the tip of the crack. In addition, with rising load conditions, the material experiences slow stable crack extension prior to fracture, which makes it difficult to determine the maximum stress intensity factor level at crack instability because this crack length is uncertain. Thus, plane stress fracture toughness testing has not developed nearly to the extent of plane strain fracture toughness testing. Currently the R-curve analysis is applicable for determining K_{Ic} for intermediate strength materials (1) where the plastic-zone size, r_y , is small relative to the specimen dimensions, where:

$$r_y = \frac{1}{2\pi} \left(\frac{K}{S_y} \right)^2 \quad (5.1)$$

An R-curve is a continuous record of toughness development in terms of crack growth resistance, K_{R} , plotted against crack extension in the material as a crack is driven under a continuously increasing stress intensity factor, K (1). During slow-stable fracturing, the developing crack growth resistance, K_{R} , is equal to the applied stress intensity factor K . The R-curve analysis was used in this research in

an attempt to obtain and compare the plane stress fracture toughness, K_{Ic} for the five cast steels at room and low temperature.

5.1.2 Experimental Procedures

The R-curve tests were performed in accordance with the ASTM Standard Recommended Practice for R-Curve Determination E561 (1) using compact specimens as shown in Figure 5.1. H/w was 0.49 for the 0030 cast steel and 0.60 for the 0050A, C-Mn, Mn-Mo and 8630 cast steels. These were the same specimen dimensions used for the constant amplitude fatigue crack growth experiments. Specimens were cut from the blocks as shown in

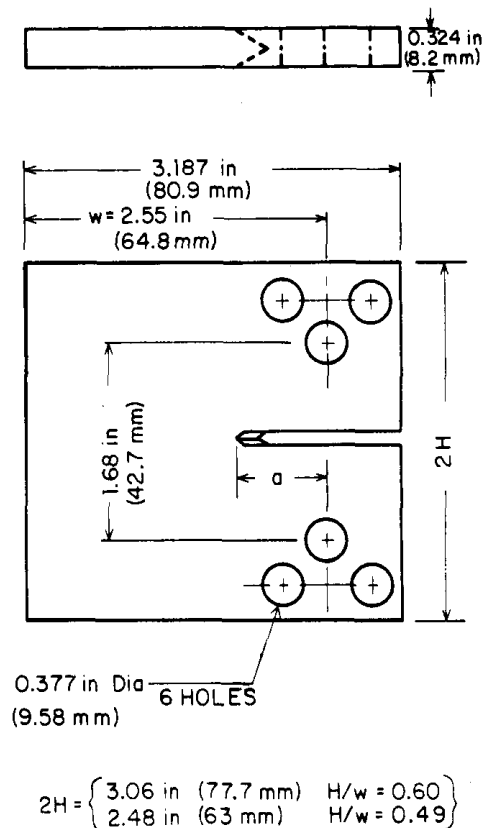


Figure 5.1. R-curve test specimen.

Figure 1.2. The chevron specimens were precracked with $R \approx 0$ using constant amplitude loading with several decreasing step levels. Total fatigue precracked length was about .25 in (6.5 mm) for all specimens which increased the total initial crack length, a_0 , to 1 in (25.4 mm). The initial a/w ratio was approximately 0.4.

The R-curve tests were conducted in load control using a ramp function with the 20 kip (89 kN) electrohydraulic closed loop test system. Duplicate tests were run for each material at both room temperature and low temperature. For the 0030 cast steel, the low temperature was -30°F (-34°C) and for the other four steels -50°F (-45°C) was used. Low temperature tests were performed in the CO_2 automated temperature chamber. Between 8 and 38 increasing load steps were made for each R-curve test. Crack extension measurements were made at each load increment with a 33 x traveling telescope. The hold time at each load increment was three or more minutes. The tests were performed until unstable crack growth occurred which led to final fracture.

5.1.3 Results

The applicable stress intensity factor for the compact specimen is (1,2):

for $B/w = .6$

$$K = \frac{P}{B\sqrt{w}} \frac{2 + (\frac{a}{w})}{1 - (\frac{a}{w})^{3/2}} \left[.886 + 4.64 \left(\frac{a}{w}\right) - 13.32 \left(\frac{a}{w}\right)^2 + 14.72 \left(\frac{a}{w}\right)^3 - 5.6 \left(\frac{a}{w}\right)^4 \right] \quad (5.2)$$

for $B/w = .49$

$$K = \left[\frac{P\sqrt{a}}{Bw} \right] \left[30.96 - 195.8 \left(\frac{a}{w}\right) + 730.6 \left(\frac{a}{w}\right)^2 - 1186.3 \left(\frac{a}{w}\right)^3 + 754.6 \left(\frac{a}{w}\right)^4 \right] \quad (5.3)$$

where

a = crack length or plastic zone corrected crack length

w = specimen width

B = specimen thickness

P = applied load

The plastic zone corrected crack length is

$$\text{where } a = a_0 + \Delta a + r_y \quad (5.4)$$

a_0 = starting crack length

Δa = physical crack extension during testing

r_y = plastic zone correction, eq. 5.1.

To have a valid plane stress fracture toughness test, the uncracked ligament should satisfy the following:

$$w - a \geq 8 r_y \quad (5.5)$$

Value of r_y near unstable crack extension for the five cast steels at room temperature ranged from 0.3 to 0.7 in (8 to 18 mm) and at low temperature r_y ranged from 0.1 to 0.7 in (2.5 to 18 mm). Equation 5.5 was satisfied only with the 8630 cast steel at -50°F (-45°C). The assumption of small localized plasticity was completely unrealistic with the other nine test conditions. This invalidates quantitative calculations of plane stress fracture toughness K_{IC} . R-curves, however, were established with K_R equal to K without a plastic zone correction. K versus the measured crack extension, Δa , during testing are shown in Figures 5.2 to 5.6 for the five cast steels in both room and low temperatures. The complete data for the duplicate tests at each condition are included in the figures. Each curve represents data from one specimen. The solid data points and solid

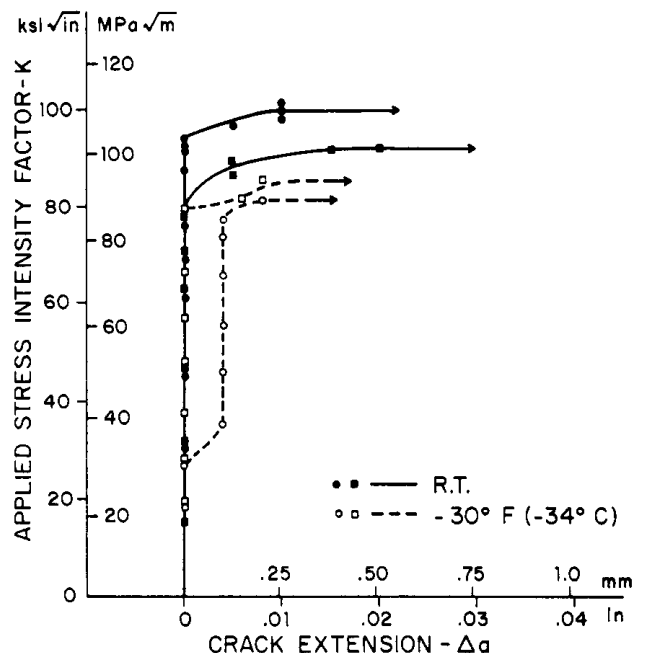


Figure 5.2. R-curve for 0030 cast steel.

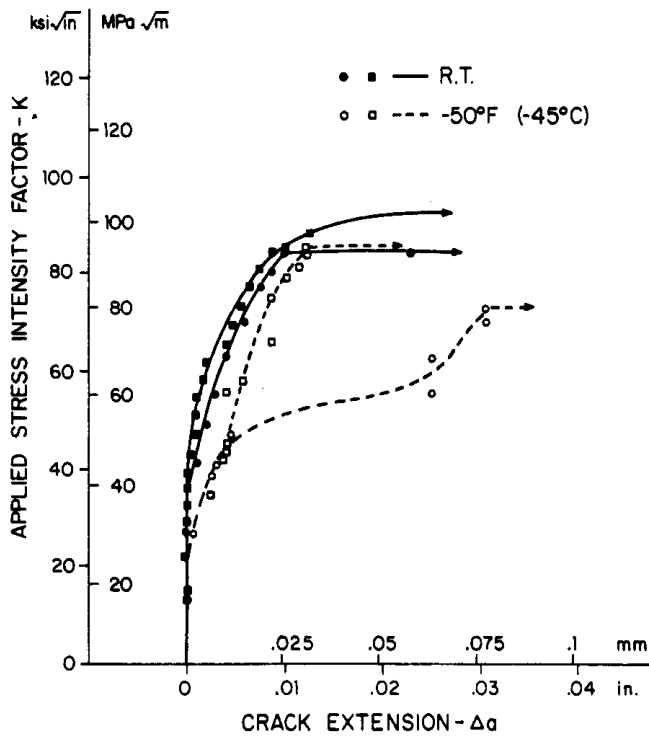


Figure 5.3. R-curve for 0050A cast steel.

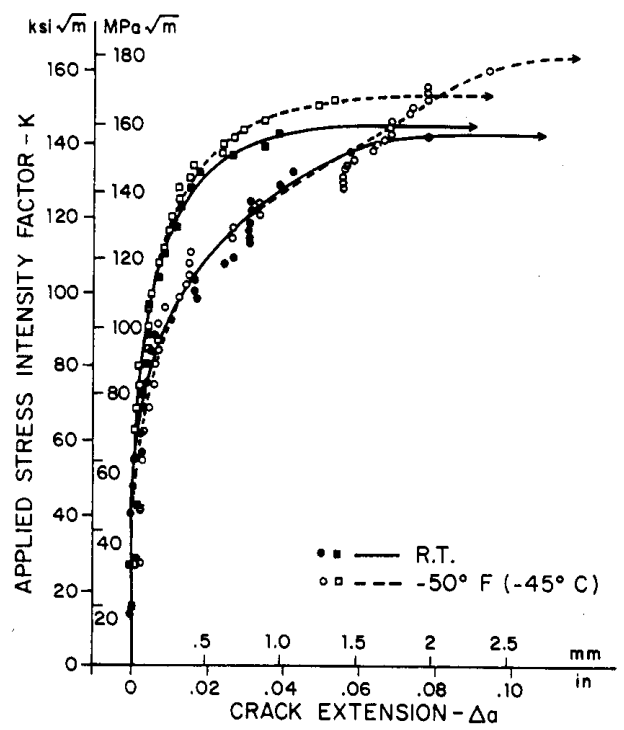


Figure 5.5. R-curve for Mn-Mo cast steel.

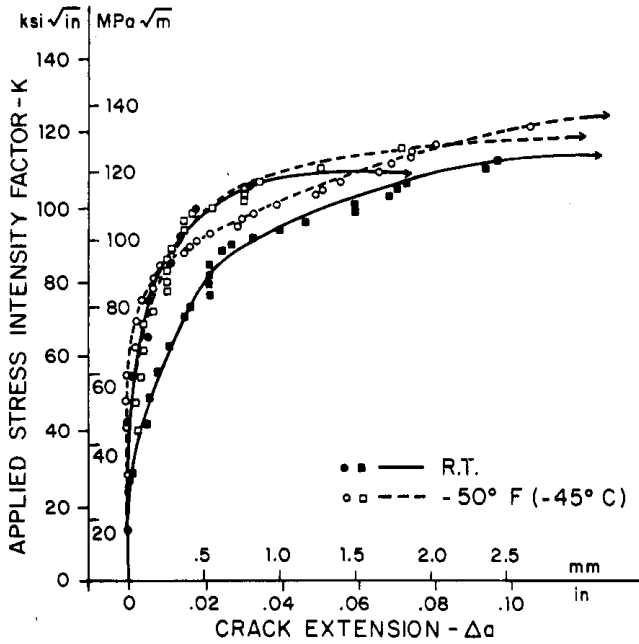


Figure 5.4. R-curve for C-Mn cast steel.

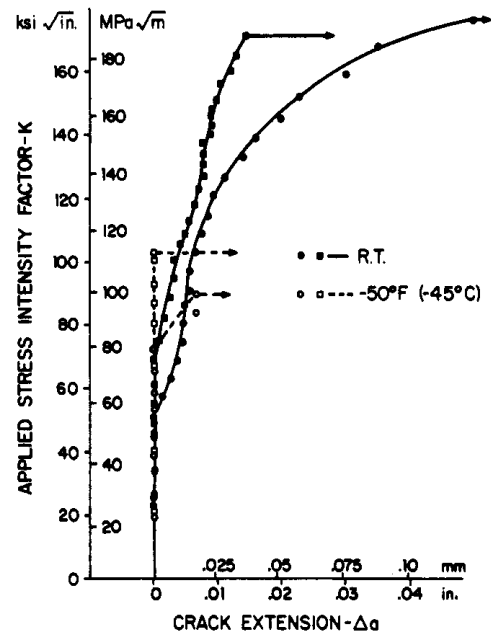
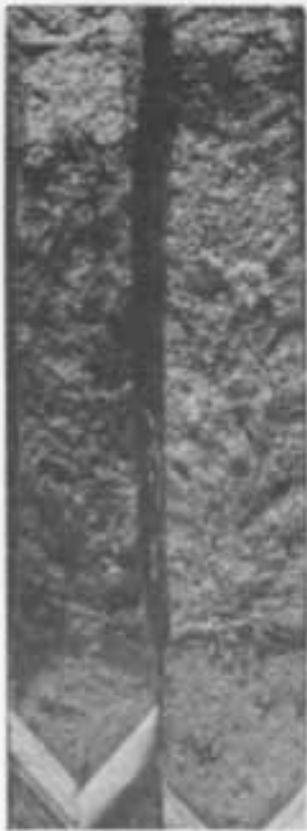


Figure 5.6. R-curve for 8630 cast steel.

curves represent room temperature (R.T.) behavior and the open data points and dashed curves represent low temperature behavior. Scatter for duplicate tests was quite small with respect to K at crack instability. Greater scatter, however, can be seen during stable crack growth for a few tests due to the very limited crack extension in all tests before fracture and to the crack measurement dif-

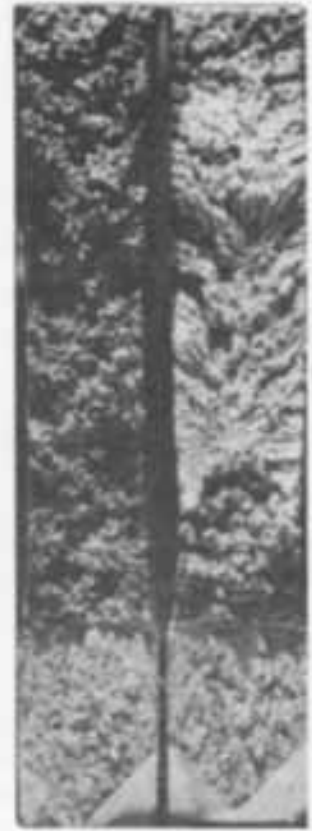
ficulties with the large plastic zones. Total stable surface crack extension varied from essentially zero to 0.1 in. (2.5 mm). The C-Mn and Mn-Mo steels had the greatest stable crack extension and hence the abscissa for these two steels (Figure 5.4 and 5.5) is twice that for the other three steels. The limited stable crack extension is due principally to the load control test procedure.



R.T. -30°F (-34°C)
0030



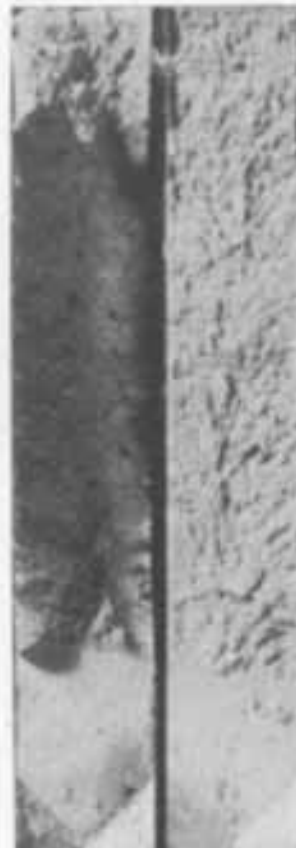
R.T. -50°F (-45°C)
0050A



R.T. -50°F (-45°C)
C-Mn



R.T. -50°F (-45°C)
Mn-Mo



R.T. -50°F (-45°C)
8630

Figure 5.7. Macroscopic fracture surfaces for R-curve tests, room and low temperature.

Macrofractography

Macrophotographs of the fracture surfaces for the five cast steels at both room and low temperatures are shown in Figure 5.7. at approximately 2 X magnification. The smooth precrack fatigue region is evident on all specimens. The room temperature fracture surface for a given material is to the left of each photo set. The photos indicate the following for the fracture region:

0030: substantial roughness, necking and ductility at room temperature while a bright shiny flat brittle type fracture existed at -30°F (-34°C).

0050A: bright shiny flat brittle type fracture at both room and low temperature with essentially no necking. An approximate 2 percent shear lip existed at room temperature.

C-Mn: Appreciable roughness, necking and ductility at both temperatures. Some shear lip existed at room temperature. At low temperature, a slow stable crack extension and tunneling region is noticeable along with chevron type patterns.

Mn-Mo: 100 percent shear (slant) fracture at both temperatures with appreciable necking and roughness. A stable crack extension and tunneling region is seen at the low temperature.

8630: 100 percent shear (slant) fracture at room temperature without necking. At the low temperature only a two percent shear lip existed with the remaining region showing a flat shiny brittle type fracture.

Microfractography (SEM)

SEM fractographs for the five steels at both room

and low temperatures are shown in Figure 5.8. Magnification varied from 200 x to 780 x. The fracture surfaces were perpendicular to the electron beam. The fracture mode varied from essentially 100 percent dimpled rupture to 100 percent cleavage. Mixed dimples and cleavage were also found in some tests. Inclusions and voids were evident in the fracture surface as would be expected. The interface between the fatigue precrack region and the fracture region was always evident. A summary of the fracture mechanisms is given below:

Material	Room Temperature	Low Temperature *
0030	dimples	cleavage
0050A	cleavage plus a few dimples	cleavage
C-Mn	dimples	dimples and cleavage
Mn-Mo	dimples	dimples
8630	dimples	cleavage

*-30°F (-34°C) for 0030, for others -50°F (-45°C)

5.2 Discussion of Results

Based upon both macro and microscopic fractographic analysis of the R-curve test specimens, the 0050A steel behaved in a brittle manner at room temperature and low temperature while the other four cast steels had ductile behavior at room temperature. This ductile type behavior included appreciable macroscopic necking and/or 100 percent shear (slant) type fracture and microscopic ductile dimples. The 0050A brittle fracture was flat on the macro scale and cleavage at the micro

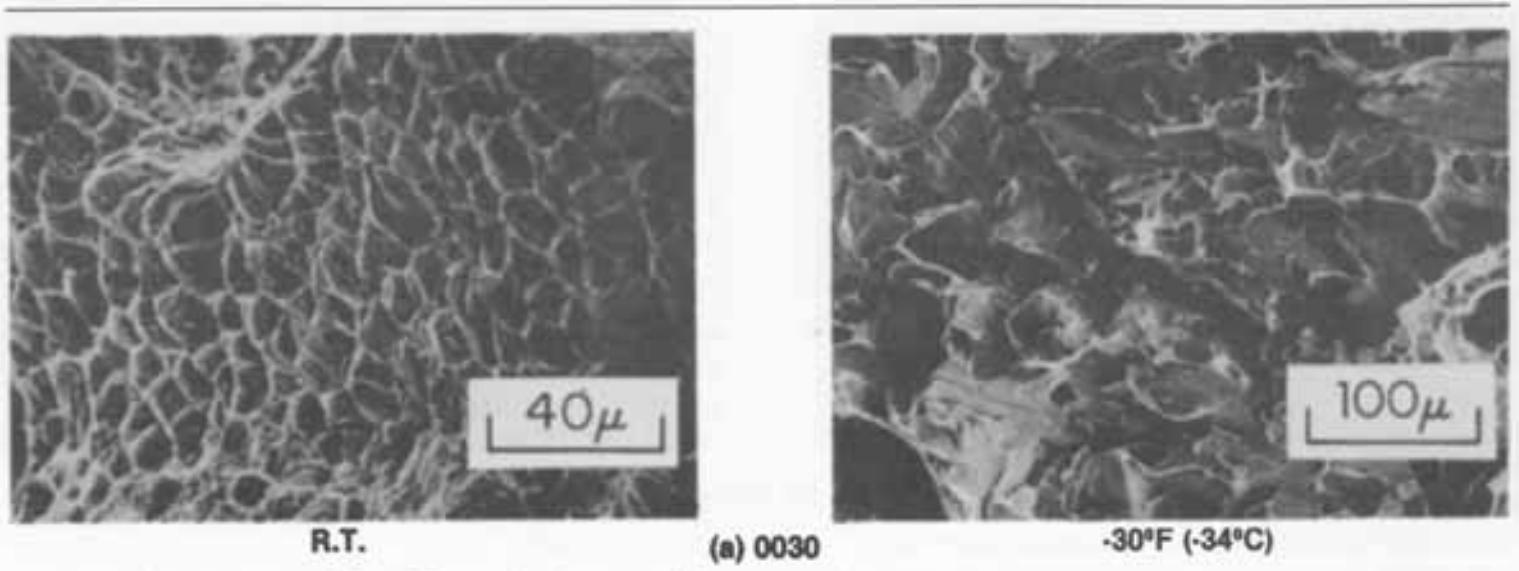
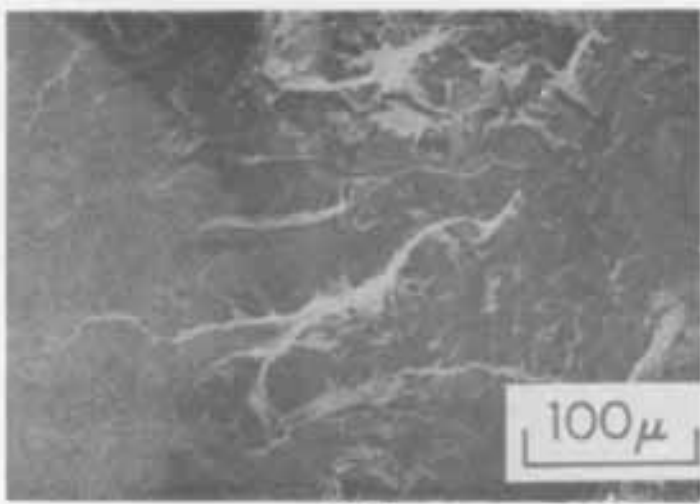
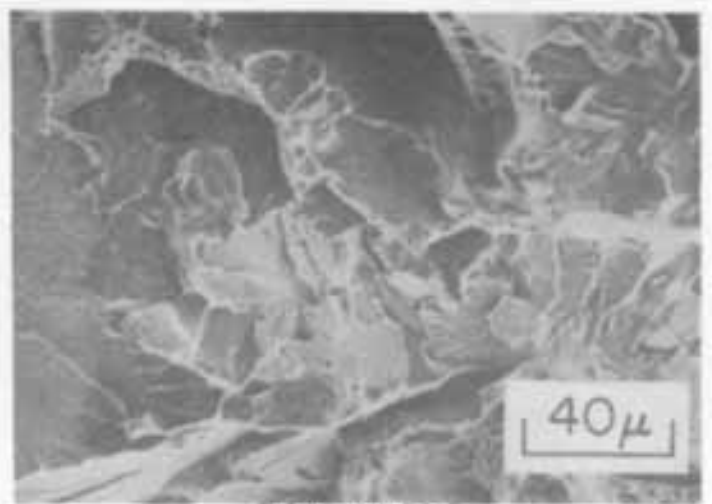


Figure 5.8. SEM fractographs from R-curve tests, room and low temperature.

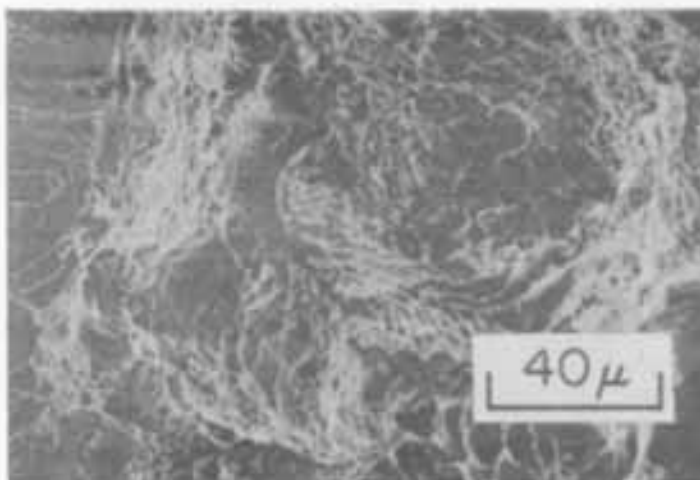


R.T.

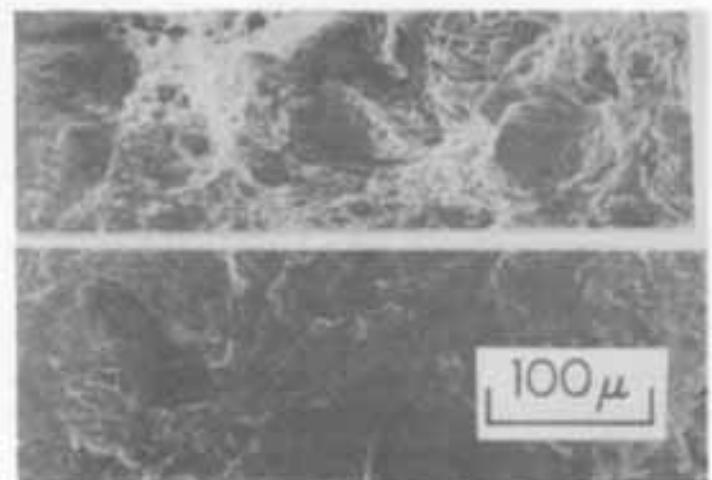


-50°F (-45°C)

(b) 0050A

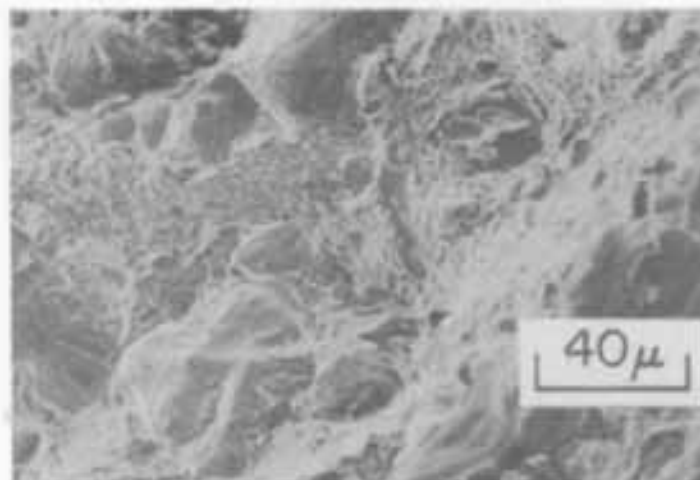


R.T.

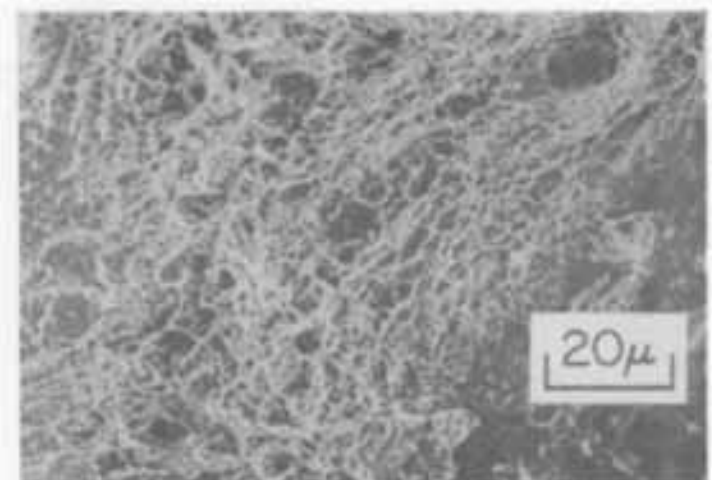


-50°F (-45°C)

(c) C-Mn



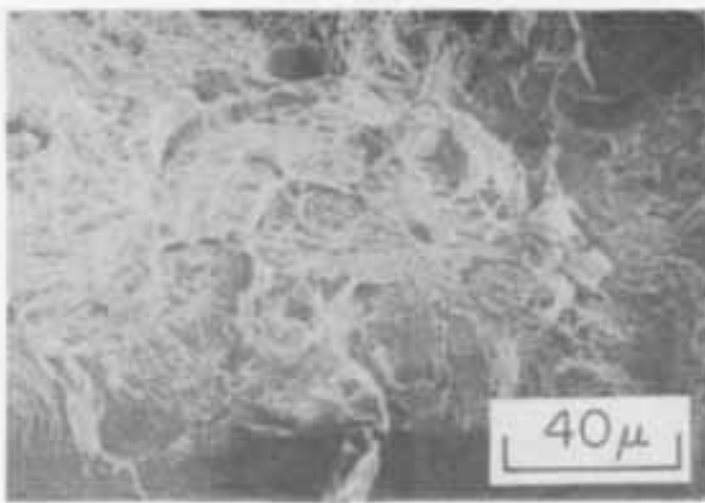
R.T.



-50°F (-45°C)

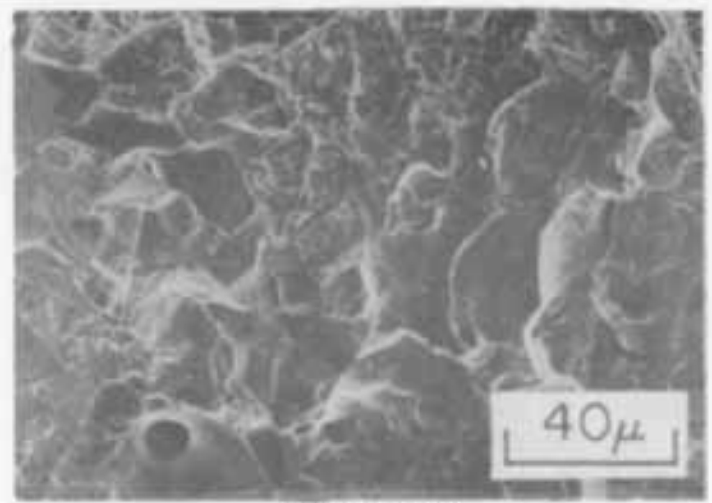
(d) Mn-Mo

Figure 5.8 (continued). SEM fractographs from R-curve tests, room and low temperature.



R.T.

(e) 8630



-50°F (-45°C)

Figure 5.8 (continued). SEM fractographs from R-curve tests, room and low temperature.

scale. The smooth specimen room temperature monotonic tensile behavior of 0050A steel resulted in 19 percent reduction in area which indicates reasonable ductility. Room temperature was in the lower transition region of the Charpy V notch energy versus temperature curve for the 0050A steel. Thus the fracture behavior of 0050A steel at room temperature was much more sensitive to notches/strain-rate and cracks than were the other four cast steels.

At -50 °F (-45 °C) [-30 °F (-34 °C) for 0030 steel] only the C-Mn and Mn-Mo cast steels retained a ductile type fracture region in the R-curve tests. This was exemplified by appreciable necking and/or 100 percent shear (slant) fracture at the macro level and ductile dimples at the micro level. These two materials exhibited only a small decrease in ductility in the monotonic tensile test as measured by % RA when the temperature was dropped from room temperature to -50°F (-45 °C). The low temperature R-curve brittle fracture of 0030, 0050A and 8630 cast steels involved flat shiny macrofracture and cleavage at the micro level. The change in ductility, as measured by % RA, in the monotonic tensile test was not sufficient to anticipate this low temperature R-curve brittle behavior.

The above mixed R-curve behavior can be somewhat anticipated from the Charpy V notch behavior. As seen from Figure 1.5, the low temperature R-curve tests were in the lower shelf region for 0030 and 0050A, the lower transition region for C-Mn and 8630 and the middle transition region for Mn-Mo. Thus, brittle behavior of the cracked R-curve specimens could be somewhat anticipated for four of the five steels. However, only

three materials behaved in a brittle manner in the R-curve tests.

The R-curves of Figures 5.2 to 5.6 do not completely indicate the effect of temperature on plane stress fracture toughness due to the extensive plasticity at the crack tip. Nor do they adequately compare different material behavior due to the large differences in plasticity in each condition. The values for K in these figures were based upon linear elastic fracture mechanics without plastic zone corrections. These corrections, however, were too large to use in an elastic model. The figures, however, can be used on a semi-quantitative basis since K is principally proportioned only to the applied load P due to the very limited crack extension during the R-curve test. Here it is seen that the average K value at unstable crack growth at the low temperature was reduced about 15 percent for the ferritic-pearlitic 0030 and 0050A steels, was increased about 10 percent for the martensitic C-Mn and Mn-Mo steels and was decreased about 50 percent for the martensitic 8630 steel.

In order to have a better comparison of the fracture toughness for the five cast steels at the two test temperatures, a quantitative “elastic” fracture toughness, K_{e} , can be determined for these small specimens using equations 5.2 or 5.3 with the maximum applied load and the initial crack length. K_{e} is directly related to the residual static strength of the precracked specimens. It gives a quantitative comparison of how these specifically cracked specimens behaved in the presence of appreciable crack tip plasticity (note 8630 at low temperature had only small crack tip plasticity). Values of K_{e} are

Table 5.1. Elastic Fracture Toughness, K_{Ic}

Material	Individual Tests		Average	
	Room Temp. ksi√In (MPa√m)	-50 °F (-45 °C) ksi√In (MPa√m)	Room Temp. ksi√In (MPa√m)	-50 °F (-45 °C) ksi√In (MPa√m)
0030	92 (101) 94 (103)	*85 (93) 90 (99)	93 (102)	*87 (96)
0050A	91 (100) 86 (95)	73 (80) 85 (94)	88 (97)	79 (87)
C-Mn	94 (103) 96 (105)	100 (110) 100 (110)	95 (104)	100 (110)
Mn-Mo	120 (132) 127 (140)	132 (145) 135 (148)	123 (136)	133 (146)
8630	169 (186) 168 (185)	90 (99) 103 (113)	168 (185)	96 (106)

*-30°F (-34°C)

given in Table 5.1 for individual tests along with average values. Scatter in K_{Ic} for the duplicate tests are less than 15 percent which is very reasonable. It is seen that K_{Ic} values provide essentially the same behavior pattern as found from comparing K values in Figure 5.2 to 5.6 at instabilities. This is due to the small crack extension prior to the instabilities. Based upon K_{Ic} , and hence load carrying capacity in the presence of the crack, the low temperature was slightly detrimental (<10%) for 0030 and 0050A steels, slightly beneficial (< 10%) for C-Mn and Mn-Mo, and substantially detrimental (43%) for 8630 steel.

A comparison of K_{Ic} values for either temperature with the fracture surfaces (both macro and micro) of the R-curve tests, Charpy V notch values, tensile yield or ultimate strengths and % RA could not be made in general. A qualitative correlation is somewhat- reasonable for the C-Mn and Mn-Mo steels, but is quite unreasonable for the other three steels. Thus, it is not practical at this point to relate the plane stress fracture toughness behavior of these five cast steels to the simple tensile test or Charpy V notch test. Perhaps a better correlation would exist if valid plane stress fracture toughness, K_{Ic} , values had been obtained. This would require significantly larger specimens for all materials except the 8630 steel.

A reasonable correlation did exist, however, between the macrofracture surface appearance, indicated by necking, slant or flat fracture, and the microfracture surface appearance indicated by ductile dimples or cleavage. This correlation,

however, is usually expected.

On the basis of residual static strength in the presence of substantial plasticity, as indicated by K_{Ic} , 8630 was the best cast steel at room temperature followed by Mn-Mo, while the other three cast steels were quite similar but with substantially lower values. At low temperature, Mn-Mo was the best, while the four other cast steels were reasonably similar but with substantially lower values.

5.3 Summary and Conclusions

- 1) Due to insufficient specimen size and excess plasticity, the plane stress fracture toughness K_{Ic} could not be obtained. K_{Ic} , an elastic fracture toughness which is related to residual static strength was determined and used for comparison purposes.
- 2) Values of K_{Ic} at low temperature relative to room temperature were reduced slightly (<10%) for 0030 and 0050A cast steels, increased slightly (<10%) for C-Mn and Mn-Mo cast steels, and substantially decreased (43%) for 8630 cast steel.
- 3) K_{Ic} was the highest for 8630 at room temperature while Mn-Mo had the highest K_{Ic} at low temperature.
- 4) SEM analysis revealed fracture surfaces contained from essentially 100% ductile dimples to 100% cleavage plus some mixed-mode behavior. 0050A had essentially all cleavage at both temperatures while C-Mn and Mn-Mo had primarily ductile dimples at both temperatures. 0030 and 8630 had ductile dimples at room temperature and cleavage at low temperature.
- 5) No correlation for K_{Ic} , at a given temperature, could be made with tensile yield or ultimate strengths, percent reduction in area nor Charpy V notch behavior.
- 6) C-Mn and Mn-Mo cast steels had the least low temperature crack sensitivity while 8630 cast steel was the most sensitive to cracks at low temperature.

Chapter 5 References

1. "Standard Recommended Practice for R-Curve Determination", Annual Book of ASTM Standards, part 10, E561.
2. E.T. Wessel, "State of the Art of the WOL Specimen for K_{Ic} Fracture Toughness Testing", Engineering Fracture Mechanics, Vol. 1, No. 1, 1968, p. 77.

Plane Strain Fracture Toughness Using the J-Integral

6.1 Introduction

Plane strain fracture toughness K_{Ic} could be obtained for the five cast steels, 0030, 0050A, C-Mn, Mn-Mo and 8630 at room and low temperature using test methods described in ASTM standard E399 (1). However, four of these steels exhibited appreciable ductility and low yield strengths in smooth specimen monotonic tensile tests which could require specimen thickness and crack length for valid K_{Ic} values to range from approximately 2 in (50 mm) to 20 in (500 mm). The larger dimensions are completely unreasonable for cost effective testing. The path independent J-integral can be used to estimate fracture toughness characteristics of materials exhibiting appreciable elastic-plastic conditions without such large specimens. The J-integral is a means of extending fracture mechanics concepts from linear-elastic behavior to elastic-plastic behavior (2). For linear-elastic behavior, the J-integral is identical to G , the strain energy release rate per unit crack extension, which is directly related to the stress intensity factor K . Thus linear-elastic fracture criteria based upon K_{Ic} , G_{Ic} or J_{Ic} are identical. For mode I linear-elastic plane strain conditions,

$$J_{Ic} = G_{Ic} = \frac{K_{Ic}^2}{E} (1-\nu^2) \quad (6.1)$$

where E is Young's modulus and ν is Poisson's ratio. Since J_{Ic} characterizes the toughness of materials at or near the onset of crack extension from a pre-existing sharp crack, it may be used as a conservative estimate of K_{Ic} on specimens that contain appreciable ductility but lack sufficient thickness to be tested for K_{Ic} according to ASTM E399 requirements. Thus ASTM standard E813 (3) was used in an attempt to establish J_{Ic} values for the five cast steels at room temperature and -50°F (-45°C). These values were then to be converted to conservative values of plane strain fracture toughness K_{Ic} using equation 6.1. As will be seen, J_{Ic} was obtained for four of the five cast steels at room temperature and only two of the five cast steels at -50°F (-45°C), due to brittle or cleavage fracture in

four of the test conditions.

6.2 Test Procedures and Results

J_{Ic} tests using the multiple specimen procedures described in ASTM standard E813 (3) were conducted at both room temperature and -50°F (-45°C) with a 20 kip (89 kN) closed-loop electrohydraulic test system. Low temperature tests were conducted in an automated CO_2 cold temperature chamber. Load line displacement was measured with a 1/2 in (12.7 mm) clip gage at room temperature and with a 1/4 in (6.35 mm) clip gage at -50°F (-45°C). This resulted in a different specimen configuration at the region where the clip gages were attached. The low temperature tests were performed with compact specimens as shown in Figure 6.1 with knife edges glued to the specimen to hold the clip gage. Room temperature tests were performed with compact specimens containing an integrally machined knife edge for holding the load-line displacement clip gage. Other than this all specimens had the same nominal dimensions. Specimen thickness was 1 in (25.4 mm). A sharp chevron starter notch was machined to aid in providing a proper fatigue crack tip contour. In order to

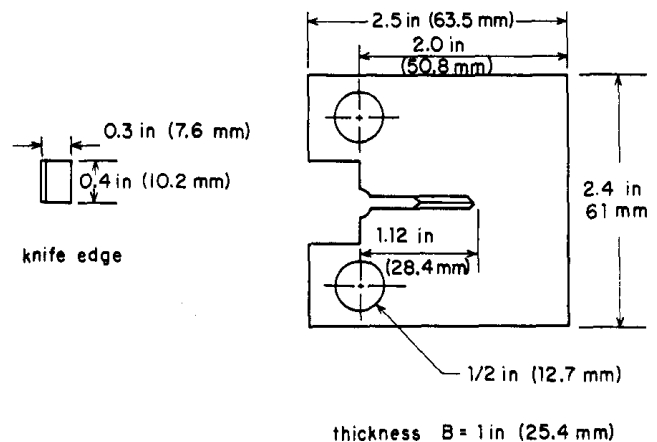


Figure 6.1. J_{Ic} , J_c test specimen.

minimize friction between the specimen, pins and the grips, molybdenum disulfide dry film lubricant spray was applied. Fatigue precracking was done at room temperature at 25 Hz with the load ratio $R = P_{min}/P_{max} \approx 0$. Typical fatigue precracks can be seen in Figure 6.2 as the first dark area emanating from the chevron starter notch. Fatigue crack tip contours and precracking procedures satisfied ASTM E813 standard. Final test crack lengths ranged from 1.2 to 1.3 in (30.5 to 33 mm) which resulted in a/w ratios ranging from .6 to .65.

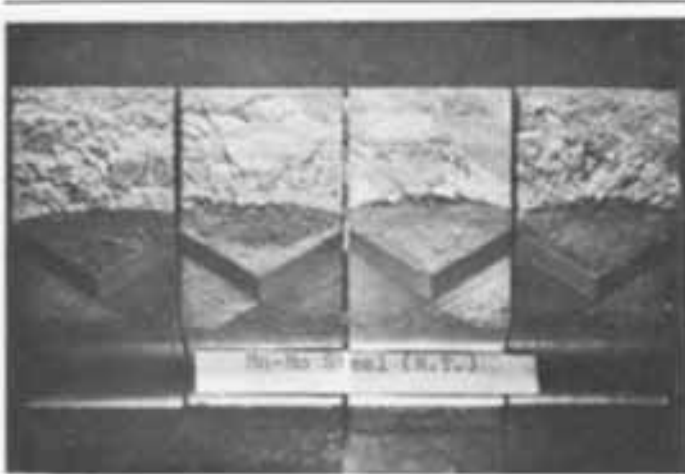


Figure 6.2. J_{IC} specimen fracture surfaces for Mn-Mo cast steel at room temperature.

During each J-integral test, both applied load and load line displacement were plotted simultaneously on an x-y recorder to obtain total applied work. Specimens were tested in displacement control at a rate of .03 in/min (.76 mm/min). For J_{IC} determination, specimens were unloaded at different specific load line displacements based upon initial estimates or on a previous test experience as suggested in ASTM E813. A set of four typical load versus load line displacement curves is shown in Figure 6.3. Immediately following unloading, specimens were oxidized in a furnace at 700°F (370°C) for approximately 20 minutes to heat-tint the pre-fatigue crack region and the test crack extension region. After heat-tinting, the specimens were submerged in liquid nitrogen for 10 minutes and then put back in the test machine and fractured in a brittle manner. Figure 6.2 shows a set of four fractured surfaces of Mn-Mo cast steel tested at room temperature to different load-line displacement levels. These specimen displacements increased from left to right as .049 in (1.24 mm), .052 in (1.33 mm), .060 in (1.52 mm) and .080 in (2.1 mm). Each specimen shows the contoured fatigue crack region followed by the darker stable crack

extension region formed during J_{IC} testing. Different amounts of stable crack growth can be seen on each specimen due to unloading at different displacement levels. Fatigue crack growth and J_{IC} test crack extension was measured using a 33x traveling microscope. The behavior shown in Figure 6.2 is typical of that obtained for valid J_{IC} tests.

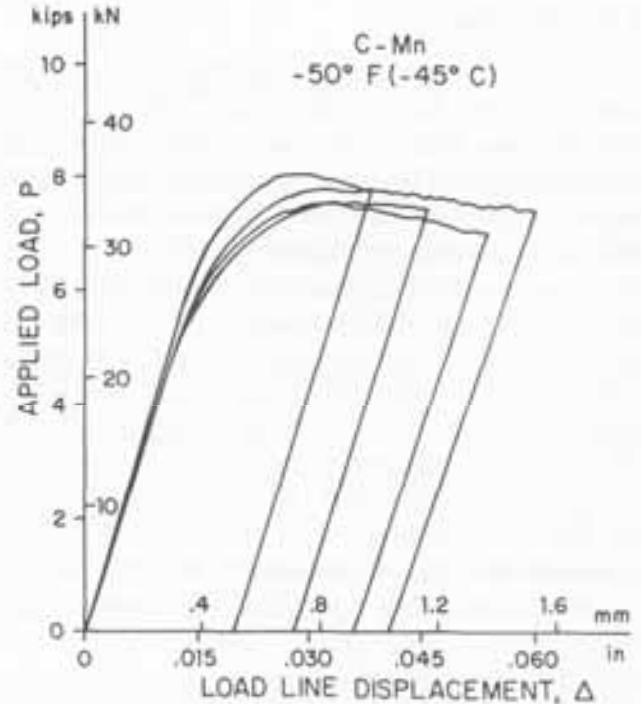


Figure 6.3. Load versus load line displacement for J_{IC} determination with C-Mn cast steel at -50°F (-45°C).

Four test conditions did not provide the stable crack extension shown in Figure 6.2. These were 0050A at room temperature and 0030, 0050A and 8630 steel at -50°F (-45°C). Load, P , versus load line displacement, Δ , test results are shown in Figure 6.4 for triplicate tests for each of the four non-valid J_{IC} test conditions. All test records in Figure 6.4 show that very limited displacement existed before an unstable brittle or cleavage fracture occurred. Only J_C ($J_{critical}$ or $J_{cleavage}$) values could be obtained for these four conditions. The different initial slopes are due to small variations in the initial crack lengths.

6.3 Test Data Reduction

The value of the J-integral for a given test specimen was calculated from

$$J = \frac{A}{Bb} f(a_0/w) \quad (6.2)$$

where

A = area (work) under the load, P, versus load line displacement Δ , curve

B = specimen thickness

b = initial uncracked ligament, w-a₀

w = specimen width

a₀ = original crack length, including the fatigue precrack

f(a₀/w) = Merkle-Corten dimensionless coefficient that corrects for the tensile load component (3)

The area A under the P- Δ curves were measured by a graphical integration method. This area is the work done on the specimen before and during stable crack extension. Four or more test specimens were used to obtain J_{IC} for a given cast steel and temperature. Values of the J-integral for each of these specimens were plotted versus stable physical crack extension, Δa_p , in Figure 6.5 to 6.8 for 0030, C-Mn, Mn-Mo and 8630 at room temperature respectively and in Figure 6.9 and 6.10 for C-Mn and Mn-Mo at -50°F (-45°C) respectively. Δa_p was measured from the fatigue crack tip at nine evenly spaced locations. These values were averaged according to ASTM E813 standard practice.

The crack tip blunting line is given by

$$J = (2\sigma_Y)\Delta a_p \quad (6.3)$$

where σ_Y is an effective tensile strength equal to the average of the monotonic yield and ultimate strengths for a given material and temperature as given in Table 1.5. This line is also plotted for each material/temperature condition in Figures 6.5 to 6.10. The blunting line approximates apparent crack advance due to crack tip blunting in the absence of slow-stable crack extension. Two dashed lines offset at .006 in (.15 mm) and .06 in (1.5 mm) are drawn parallel to the blunting line in Figures 6.5 to 6.10. The standard practice requires that at least four data points fall within these two extreme crack extension lines and at least one data point must be less than 1/3 of the horizontal distance from the blunting line to the data points of maximum Δa_p . A straight line was drawn through the J versus Δa_p data points for each test condition using a least square regression line of J on Δa_p . The intersection of this line with the blunting line gave J_{IC} if the following conditions were satisfied:

$$B \text{ or } b \geq 25 (J_{IC}/\sigma_Y) \quad (6.4)$$

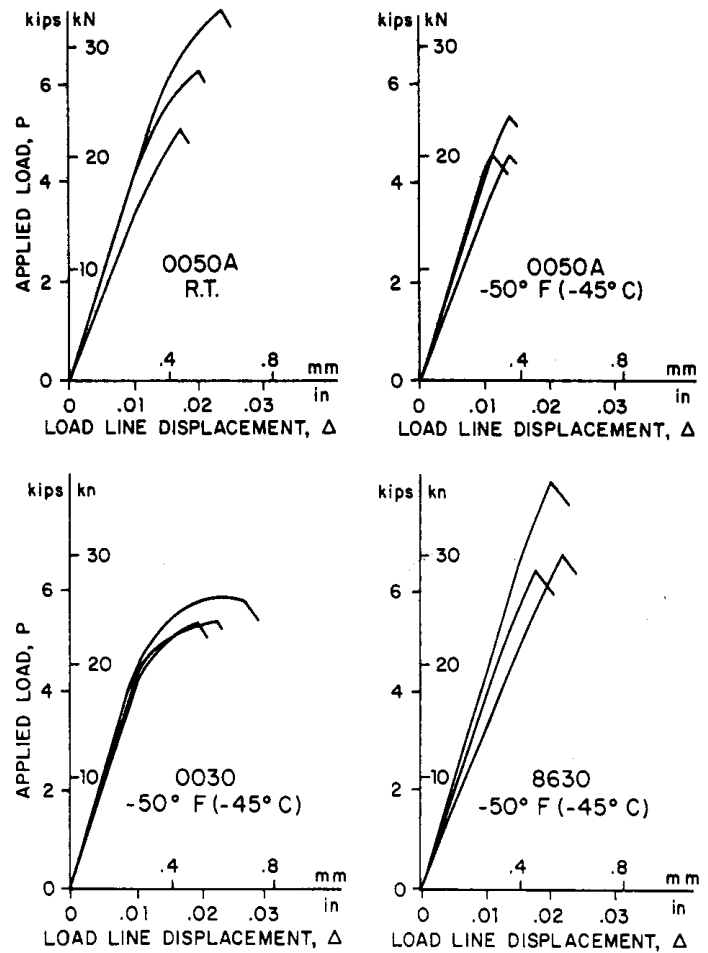


Figure 6.4. Load versus load line displacement for triplicated non-valid J_{IC} tests.

and each J data point

$$B \text{ or } b \geq 15 (J/\sigma_Y) \quad (6.5)$$

Both equations 6.4 and 6.5 were satisfied for each J_{IC} test condition.

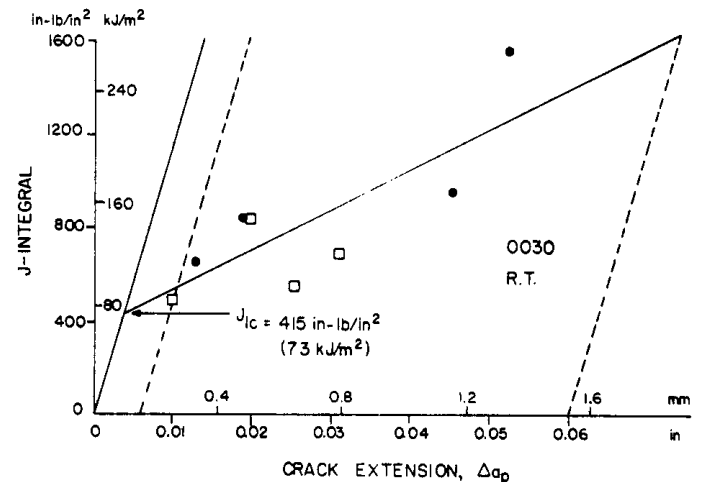


Figure 6.5. J_{IC} determination for 0030 cast steel at room temperature.

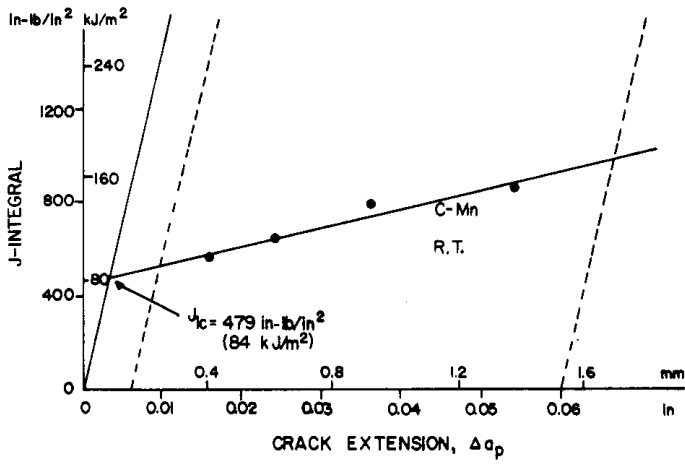


Figure 6.6. J_{IC} determination for C-Mn cast steel at room temperature.

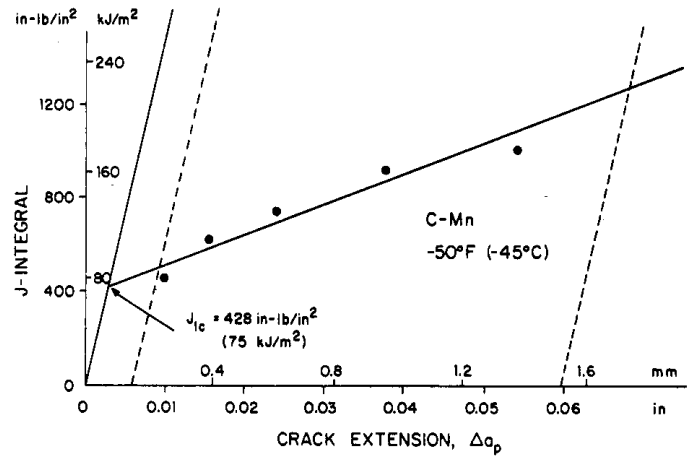


Figure 6.9. J_{IC} determination of C-Mn cast steel at -50°F (-45°C).

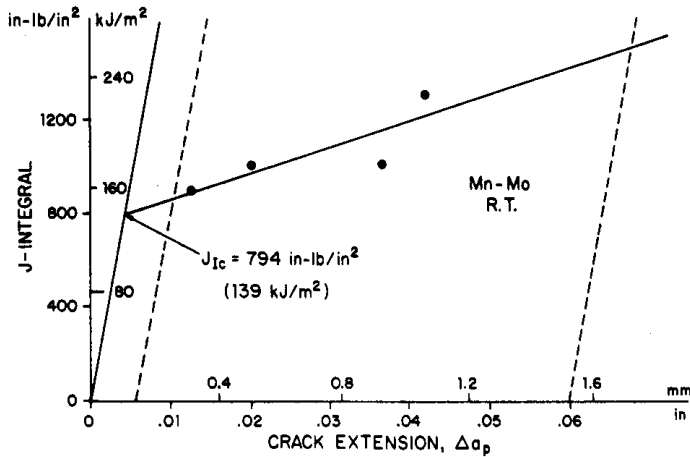


Figure 6.7. J_{IC} determination for Mn-Mo cast steel at room temperature.

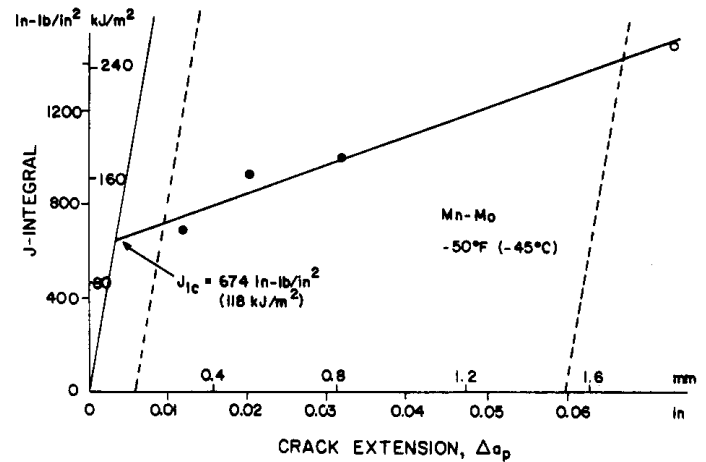


Figure 6.10. J_{IC} determination for Mn-Mo cast steel at -50°F (-45°C).

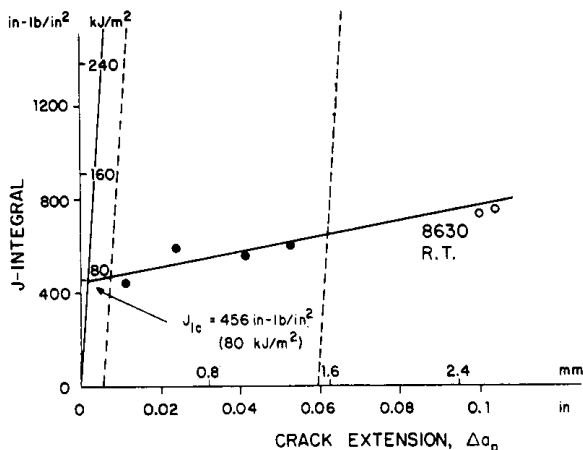


Figure 6.8. J_{IC} determination for 8630 cast steel at room temperature.

For 0030 cast steel at room temperature, Figure 6.5, the data from a previous investigation with this steel (4) were reanalyzed in accordance with the current ASTM test procedure and were incorporated with the current data. The previous data is shown as open squares in Figure 6.5. The scatter of data was not due to just incorporation of test results from two different investigators because each set of data has a fair amount of its own scatter.

In Figure 6.8, 8630 at room temperature has two data points beyond the maximum crack extension line as shown by open circles. These two data points were not included in the least square regression line but they still fall very close to the regression line. In Figure 6.10, Mn-Mo at -50°F (-45°C) has

Table 6.1. Fracture toughness values for five cast steels at room temperature and -50°F (-45°C)

Material	Room Temperature				-50°F (-45°C)				Percent Decrease
	J _{IC}	J _C	K _{IC}	K _C	J _{IC}	J _C	K _{IC}	K _C	
	$\frac{\text{in-lb}}{\text{in}^2} \left(\frac{\text{kJ}}{\text{m}^2} \right)$	$\frac{\text{in-lb}}{\text{in}^2} \left(\frac{\text{kJ}}{\text{m}^2} \right)$	ksi√in (MPa√in)	ksi√in (MPa√in)	$\frac{\text{in-lb}}{\text{in}^2} \left(\frac{\text{kJ}}{\text{m}^2} \right)$	$\frac{\text{in-lb}}{\text{in}^2} \left(\frac{\text{kJ}}{\text{m}^2} \right)$	ksi√in (MPa√in)	ksi√in (MPa√in)	
0030	415 (73)		118 (130)			*282 (49) + 215 (44)		*98 (108) + 85 (93)	32 40
0050A		*209 (37) + 145 (25)		*84 (92) + 70 (77)		*95 (17) + 78 (14)		*56 (61) + 51 (56)	55 46
C-Mn	479 (84)		126 (139)		428 (75)		120 (132)		11
Mn-Mo	794 (139)		163 (179)		674 (118)		151 (166)		15
8630	456 (80)		123 (135)			*218 (38) + 174 (30)		*86 (95) + 77 (85)	52 62

*average value
+ lowest value

the fourth data point slightly beyond the maximum crack extension line. This data point was included in the regression line calculation based upon only a slight violation of the standard practice and the closeness of fit for invalid tests in Figure 6.8 for 8630 at room temperature. Valid values for J_{IC} for six test conditions are given in Figures 6.5 to 6.10 and in Table 6.1. Values of J_C, both lowest and average, for the invalid J_{IC} test of Figure 6.4 are also given in Table 6.1. J_C values were obtained from P-Δ curves and equation 6.2. Values of K_{IC} and K_C given in Table 6.1 were obtained from J_{IC} and J_C values using equation 6.1 with ν = 1/3 for all steels.

6.4 Discussion of Results

6.4.1 J_{IC}, J_C, K_{IC}, K_C

Valid values of J_{IC}, and hence conservative estimates of K_{IC}, were obtained for four of the cast steels at room temperature (0030, C-Mn, Mn-Mo and 8630) and two of the cast steels at -50°F (-45°C) (C-Mn and Mn-Mo). Only J_C (J_{cleavage} or J_{critical}) and hence estimates of K_C, could be obtained for the other material/temperature conditions. Since brittle fracture occurred with all the J_C test results, a K_{IC} indirect analysis using ASTM E399 (1) restrictions was done with these tests using a crack opening displacement correction (5). None of these tests satisfied E399 due to not satisfying either or both

$$P_{\max}/P_Q \leq 1.1 \quad (6.6)$$

$$B \text{ and } b \geq 2.5 \frac{K_{IC}^2}{S_y} \quad (6.7)$$

Also, a/w was between .6 and .65 while ASTM E399 recommends a/w be between .45 and .55. Two additional tests with 0050A at -50°F (-45°C) using ASTM E399 procedures did not quite satisfy equation 6.7. Thus only six valid J_{IC} or K_{IC} estimates were obtained.

Those test conditions that did not result in valid J_{IC} values were in the CVN transition temperature energy region (Figure 1.5). Landes et al. (6) using A471 wrought steel showed that J_C fracture toughness values obtained in this region from small J-integral test specimens had substantial scatter and that the lower limit of this J_C scatter band was similar to that of equivalent toughness measured on larger specimens. Therefore, Landes et al. suggested that the lower bound value of the J_C scatter band may be reasonable to use for conservative design criteria in the CVN transition temperature region. Both the lower and average values of J_C are given in Table 6.1 for comparison. The difference between the upper and lower J_C values for a given test condition was between 40 and 90 percent. Thus appreciable scatter in J_C was present in these four cast steel/temperature conditions.

As shown in Table 6.1, Mn-Mo cast steel exhibited the highest fracture toughness (J_{IC} or K_{IC}) at both room temperature and -50°F (-45°C), while 0050A cast steel showed the lowest fracture toughness (J_C or K_C) at both temperatures. The three martensitic cast steels (C-Mn, Mn-Mo and 8630) had better

fracture toughness at room temperature compared to the two ferritic-pearlitic cast steels (0030 and 0050A). However, at -50°F (-45°C) 8630 had J_c less than 0030. In fact, 8630 cast steel had the largest decrease in fracture toughness at -50°F (-45°C) compared to room temperature. Between only 10 and 15 percent reduction in J_{Ic} or K_{Ic} occurred for C-Mn and Mn-Mo steels at -50°F (-45°C) compared to room temperature. C-Mn and Mn-Mo steels had ductile stable crack growth and the highest J_{Ic} values at both room temperature and -50°F (-45°C), and hence based upon J-integral tests they were the best steels at both temperatures.

Calculations of approximate thickness needed to perform valid K_{Ic} tests using ASTM E399 procedures rather than the J-integral were made using equation 6.7 and the K_{Ic} or K_c values from Table 6.1. These approximations ranged from 3 in (76 mm) to 18 in (460 mm) at room temperature and 1.1 in (28 mm) to 9 in (230 mm) at low temperature.

6.4.2 Correlation Between K_{Ic} and Upper Shelf CVN Energy

Several different empirical equations (7) were analysed in order to formulate a general relationship for the cast steels involving the upper shelf Charpy V notch impact energy, CVN, .2% yield strength, S_y , and conservative values of K_{Ic} obtained from J_{Ic} . The best correlation for the cast steels at room temperature was in the form of a Rolfe-Novak-Barsom equation (8). However, the specific constants of their results for principally high strength martensitic wrought steels (equation 6.8 for British units) were not satisfied with the cast steel data.

$$\left(\frac{K_{Ic}}{S_y}\right)^2 = 5\left(\frac{CVN}{S_y} - .05\right) \quad (6.8)$$

This should be expected due to the usual lower CVN data for cast steels compared to equivalent yield strength wrought steels and the higher strengths used to formulate equation 6.8.

The room temperature data for the four cast steels which had valid J_{Ic} results are plotted in Figure 6.11. Of the four cast steels used in obtaining equations 6.9 and 6.10, three were martensitic and one was ferritic-pearlitic with values of S_y ranging from 44 to 115 ksi (303 to 796 Mpa), CVN ranging from 34 to 44 ft-lbs. (47 to 60 Joules) and K_{Ic} ranging from 118 to 163 ksi \sqrt{in} (130 to 179 MPa). A least square computer program was applied to determine the two coefficients. The correlation equations between K_{Ic} , S_y and CVN for British and SI

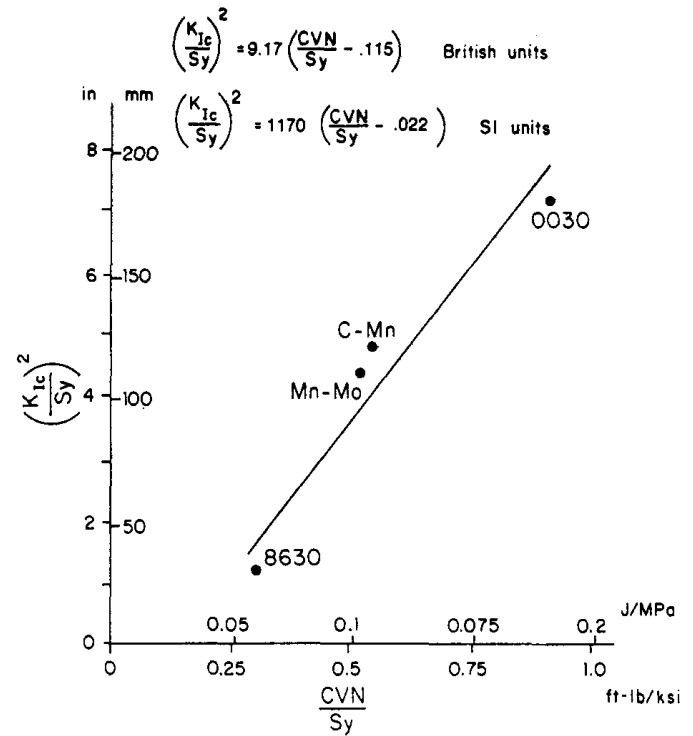


Figure 6.11. Correlation between room temperature K_{Ic} , S_y and upper shelf CVN energy for four cast steels.

units respectively follows:

$$\left(\frac{K_{Ic}}{S_y}\right)^2 = 9.17\left(\frac{CVN}{S_y} - .115\right) \quad \text{British units} \quad (6.9)$$

$$\left(\frac{K_{Ic}}{S_y}\right)^2 = 1170\left(\frac{CVN}{S_y} - .022\right) \quad \text{SI units} \quad (6.10)$$

where K_{Ic} is in ksi \sqrt{in} (MPa \sqrt{in})
 S_y is in ksi (MPa)
 CVN is in Ft-lbs (Joules)

These equations represent a reasonable starting approximation between the three parameters for cast steels. A better correlation can be obtained when substantial additional cast steel K_{Ic} data become available.

Similar correlations were attempted with the five cast steels at -50°F (-45°C) using K_{Ic} values or estimated K_c values obtained from lower J_c values as suggested by Landes et al. (6). -50°F (-45°C) is in the middle transition to lower shelf CVN energy region and no correlation was found for these data.

6.4.3 Valid J_{Ic} Determination in the CVN Transition Temperature Region

Of the six valid J_{Ic} tests, four were at room

temperature which was in the upper shelf CVN temperature region. The other two valid J_{Ic} values were at -50°F (-45°C) which was in the middle or lower CVN energy region (based on the y or energy axis) as shown in Figure 1.5. The four tests in which only J_c (J_{cleavage} or J_{criteria}) was obtained due to brittle or cleavage fracture were in the transition or lower shelf CVN temperature region. Thus it is not clear if prior whether J_{Ic} or J_c will exist in the CVN transition region.

Due to the sigmoidal shape of the CVN transition temperature region, the mid-point based upon upper and lower shelf energy values (y axis) is not the same as the mid-point based on temperatures which define the beginning of the two shelf regions (x axis). It was found that when the temperature of the above tests were greater than the approximate transition mid-point based on x axis calculations that valid J_{Ic} tests occurred. When the temperature was below this transition temperature region mid-point, J_c existed. Therefore it may be true for other cast steels too, that test temperatures greater than this defined mid-point will yield valid J_{Ic} results. Below this mid-point temperature, researchers would be wise to consider the normal ASTM E399 standard of test to determine K_{Ic} for cast steels.

6.5 Summary and Conclusions

1) Valid J_{Ic} values using 1 in (25.4 mm) thick compact specimens were obtained for 0030, C-Mn, Mn-Mo and 8630 cast steels at room temperature and for C-Mn and Mn-Mo cast steels at -50°F (-45°C). Only J_c (J_{cleavage} or J_{critical}) could be obtained for 0050A at room temperature and 0030, 0050A and 8630 at -50°F (-45°C) due to brittle or cleavage fracture. Values of J_{Ic} and J_c were converted to conservative values of K_{Ic} and K_{Ic} .

2) Higher fracture toughness, J_{Ic} or K_{Ic} , occurred with the three martensitic cast steels (C-Mn, Mn-Mo and 8630) compared to the two ferritic-pearlitic cast steels (0030 and 0050A) at room temperature. Mn-Mo had the highest values at both room temperature and -50°F (-45°C) while 0030, 0050A and 8630 cast steels had between 30 and 60 percent decreases in fracture toughness based upon J_{Ic} and/or J_c at -50°F (-45°C) relative to room

temperature. Based on both room and low temperatures, Mn-Mo and C-Mn had the best plane strain fracture toughness values of the five cast steels.

3) A correlation between K_{Ic} and S_y at room temperature with the upper shelf CVN energy resulted in the following empirical expressions for British and SI units respectively, where K_{Ic} is in $\text{ksi} \sqrt{\text{in}}$ ($\text{MPa} \sqrt{\text{in}}$), S_y in ksi (MPa) and CVN in Ft-lb (Joules).

$$\left(\frac{K_{Ic}}{S_y}\right)^2 = 9.17 \left(\frac{\text{CVN}}{S_y} - .115\right) \quad \text{British units}$$

$$\left(\frac{K_{Ic}}{S_y}\right)^2 = 1170 \left(\frac{\text{CVN}}{S_y} - .022\right) \quad \text{SI units}$$

These equations were obtained with just four data points and additional data is needed for a more general relationship.

4) This research suggests that valid J_{Ic} testing for cast steel is possible if the test temperature is above the mid-point transition region as measured along the temperature axis.

Chapter 6 References

1. "Standard Test Method for Plane-Strain Fracture Toughness of Metallic Material", Annual Book of ASTM Standards, Part 10, E399, 1981.
2. J.R. Rice, "A Path Independent Integral and the Approximate Analysis of Strain Concentration by Notches and Cracks", Journal of Applied Mechanics, Vol. 35, June, 1968, p. 379.
3. "Standard Test for J_{Ic} , A Measure for Fracture Toughness", Annual Book of ASTM Standards, Part 10, E813, 1981.
4. R.I. Stephens, G. Mauritzson, P.H. Benner and D.R. Galliard, "Fatigue and Fracture Toughness of SAE 0030 Cast Steel and Comparison with SAE 1020 Wrought Steel", Journal of Steel Castings Research, No. 83, July, 1978, p. 1.
5. E. Roberts Jr., "Elastic Crack-Edge Displacements for the Compact Tension Specimen", Materials Research and Standards, Vol. 9, Feb., 1969, p. 27.
6. J.D. Landes and D.H. Shaffer, "Statistical Characteristics of Fracture in the Transition Region", in Fracture Mechanics, ASTM STP 700, p. 368.
7. R.W. Hertzberg, Deformation and Fracture Mechanics of Engineering Materials, John Wiley and Sons, New York, 1976.
8. S.T. Folfe and J.M. Barsom, Fracture and Fatigue Control in Structures-Applications in Fracture Mechanics, Prentice-Hall Inc., Englewood Cliffs, New Jersey, 1977.

Background on Low Cycle Fatigue, ϵ -N

In a notched component or specimen subjected to cyclic external loads, the behavior of material at the root of the notch is best considered in terms of strain. As long as there is elastic constraint surrounding a local plastic zone at the notch the strains can be calculated more easily than the stress. This concept has motivated a finite fatigue life design philosophy based on relating the fatigue life of notched parts to the life of small unnotched specimens that are cycles to the same strains as the material at the notch root. This is called strain control. Reasonable expected fatigue life, based on the initiation or formation of small macrocracks can then be determined knowing the local strain-time history at a notch in a component and the unnotched strain-life fatigue properties of the material and assuming a reasonable cumulative damage theory. The SAE Fatigue Design and Evaluation Committee has recently completed an extensive interlaboratory test and evaluation program that included evaluation this technique [4]. The results were very encouraging. The remaining fatigue crack growth life of a component can be analyzed using fracture mechanics concepts.

Substantial strain-life fatigue data needed for the above procedure have been accumulated and published in the form of simplified fatigue material properties [21]. Some of these data are included in Table A.2 for selected engineering alloys. These properties are obtained from small, polished, unnotched axial fatigue specimens similar to those in Figures 5.6c and 5.6d. Tests are performed under constant amplitude fully reversed cycles of strain, as shown in Figure 3.10. Steady-state hysteresis loops can predominate through most of the fatigue life, and these can be reduced to elastic and plastic strain ranges or amplitudes. Cycles to failure can involve from about 10 to 10^6 cycles and frequencies range from about 0.2 to 5 Hz. Beyond 10^6 cycles, load or stress controlled higher frequency tests can be run, because of the small plastic strains and the greater time of failure. The strain-life curves are often called low cycle fatigue data because much of the data are for less than about 10^5 cycles.

Strain-life fatigue curves plotted on log-log scales are shown schematically in Figure 5.15, where N or $2N$ is the number of cycles or reversals to failure, respectively. Failure criteria for strain-life curves have not been consistently defined in that failure may be the life to a small detectable crack, life to a certain percentage decrease in load amplitude, or life to fracture. Differences in fatigue life depending on these three criteria may be small or appreciable. Crack lengths at these failure criteria are discussed later in this section.

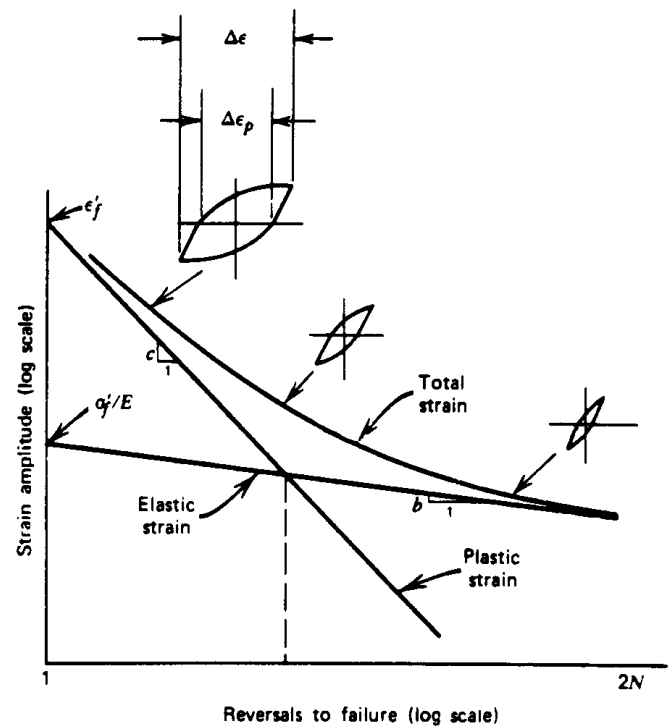


Figure 5.15. Strain-life curves showing total elastic and plastic strain components.

The total strain amplitude in Figure 5.15 has been resolved into elastic and plastic strain components from the steady-state hysteresis loops. At a given life N , the total strain is the sum of the elastic and plastic strains. Both the elastic and plastic curves can be approximated as straight lines. At large

strains or short lives, the plastic strain component is predominant, and at small strains or longer lives the elastic strain component is predominant. This is indicated by the straight line curves and the hysteresis loop sizes in Figure 5.15. The intercepts of the two straight lines at $2N = 1$ are ϵ_f' for the plastic component and σ_f'/E for the elastic component. The slopes are c and b , respectively. This provides the following equation for strain-life data of small smooth axial specimens:

$$\frac{\Delta\epsilon}{2} = \frac{\Delta\epsilon_e}{2} + \frac{\Delta\epsilon_p}{2} = \frac{\sigma_f'}{E}(2N)^b + \epsilon_f'(2N)^c$$

- where $\Delta\epsilon/2$ = total strain amplitude
 $\Delta\epsilon_e/2$ = elastic strain amplitude
 $= \Delta\sigma/2E = \sigma_a/E$
 $\Delta\epsilon_p/2$ = plastic strain amplitude
 $= \Delta\epsilon/2 - \Delta\epsilon_e/2$
 ϵ_f' = fatigue ductility coefficient
 c = fatigue ductility exponent
 σ_f' = fatigue strength coefficient
 b = fatigue strength exponent
 E = modulus of elasticity
 $\Delta\sigma/2 = \sigma_a =$ stress amplitude

The straight line elastic behavior can be transformed to

$$\frac{\Delta\sigma}{2} = \sigma_e = \sigma_f'(2N)^b \quad (5.11)$$

which is Basquin's equation proposed in 1910 [22]. The relation between plastic strain and life is

$$\frac{\Delta\epsilon_p}{2} = \epsilon_f'(2N)^c \quad (5.12)$$

which is the Manson-Coffin relationship first proposed in the early 1960s [23,24]. The exponent c ranges from about -0.5 to -0.7, with -0.6 as a representative value. The exponent b ranges from about -0.06 to -0.14, with -0.1 as a representative value. The term ϵ_f' is somewhat related to the true fracture strain, ϵ_f , in a monotonic tensile test and in most cases ranges from about 0.35 to 1.0 times ϵ_f . The coefficient σ_f' is somewhat related to the true fracture stress, σ_f , in a monotonic tensile test. Sometimes ϵ_f' and σ_f' may be taken as ϵ_f and σ_f , respectively, as a rough first approximation. A typical complete strain-life curve with data points is shown in Figure 5.16 for 4340 steel [25]. Eleven test specimens were used to form these strain-life curves.

Manson [26] has simplified Eq. 5.10 even further with his method of university slopes where

$$\Delta\epsilon = 3.5 \frac{S_u}{E} (N)^{-0.12} + \epsilon_f^{0.6} (N)^{-0.6} \quad (5.13)$$

S_u , E , and ϵ_f are all obtained from a monotonic tensile test. He assumes the two exponents are fixed for all materials and only S_u , E , and ϵ_f control the

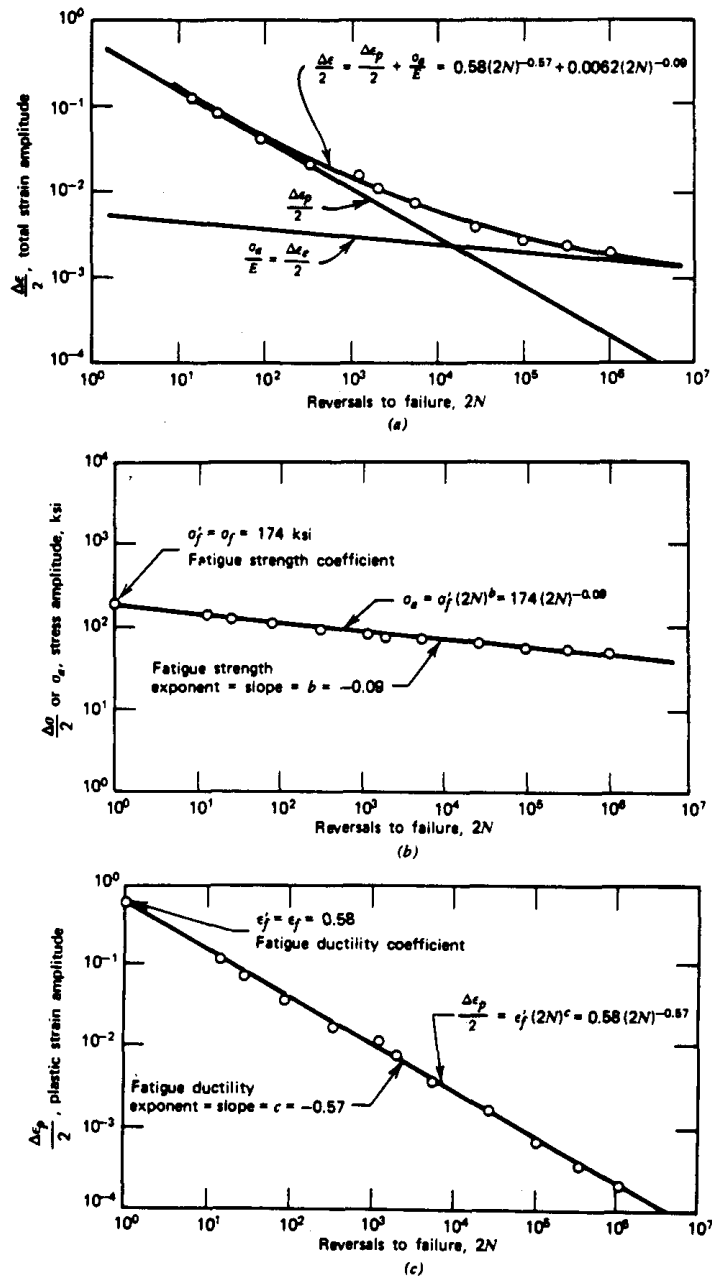


Figure 5.16. Low cycle fatigue behavior of annealed 4340 steel [25] (reprinted with permission of the Society of Automotive Engineers). (a) Total strain amplitude. (b) Elastic strain amplitude x E. (c) Plastic strain amplitude.

fatigue behavior. Figure 5.17 indicates good agreement between unnotched smooth specimen experimental data and the universal slopes method. Thus the universal slopes method can be a first approximation for the fully reversed strain-life curve for unnotched smooth specimens, based on monotonic tensile properties.

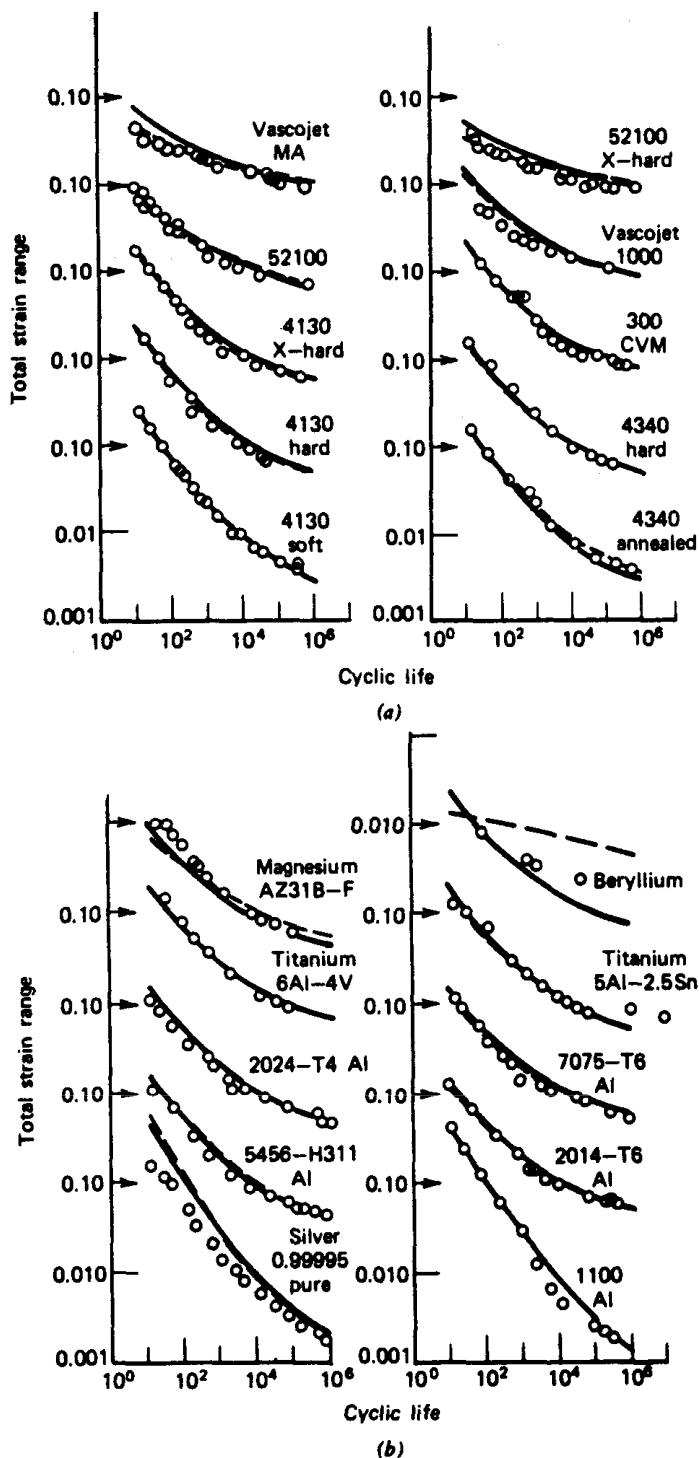


Figure 5.17. Comparison of predicted and experimental axial fatigue life using the method of universal slopes [26] (reprinted with permission of the Society for Experimental Stress Analysis). (a) Steels. (b) Nonferrous metals. (O) Experimental; (---) predicted by four-point correlation; (—) predicted by universal slopes. Note shift in strain scales.

The general differences of metals under strain-controlled tests are shown in Figure 5.18. Many materials have about the same life at a total strain amplitude of 0.01. At larger strains, increased life of unnotched smooth test specimens is dependent more on ductility, while at smaller strains better life is obtained from stronger materials. Life here refers to the initiation of a small detectable crack, a percentage decrease in the load amplitude that is caused by crack initiation and growth, or final fracture. For the final fracture criterion, the crack would grow to about 10 to 70 percent of the test specimen cross section. Since strain-life test specimens are usually between about 3 and 6 mm (1/8 and 1/4 in.), this implies the strain-life fracture criteria are based on cracks growing to a depth of about 0.25 to 5 mm (0.01 to 0.2 in.). The actual value depends on the strain amplitude, modulus of elasticity, and the material's fracture toughness. The other two criteria are based on life to cracks, which would be smaller than those at fracture. In general, cracks less than 0.25 mm (0.01 in.) would not be readily observed in these tests and would probably not cause sufficient decrease in the load amplitude to terminate a test. Thus a reasonable important conclusion concerning failure criteria in strain-life testing of unnotched smooth specimens is that the life to failure means life to fatigue crack lengths of between 0.25 to 5 mm (0.01 to 0.2 in.). This criterion is dependent on strain amplitude, modulus of elasticity, and fracture toughness.

Low cycle strain-life fatigue data in Table A.2 and in reference 21 were obtained under the above conditions. Both monotonic tensile properties and strain-life material properties are included for com-

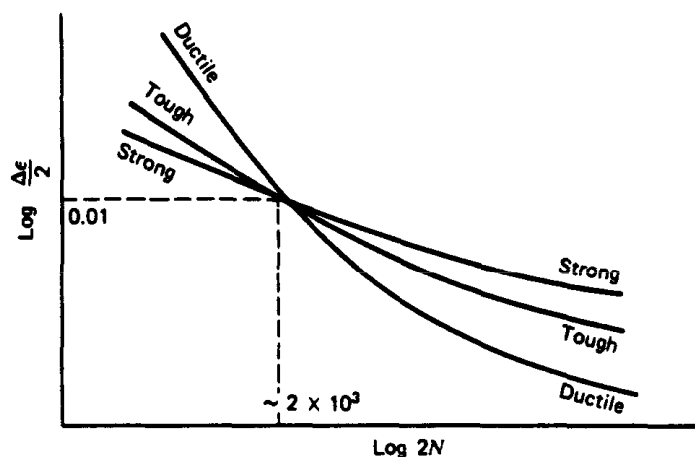


Figure 5.18. Schematic of strain-life curves for different materials.

pleteness in both SI and American/British units. Terms in Table A.2 are described earlier. Data for the last two columns, S_f and S_f/S_u , were obtained by substituting the proper material constants and $2N = 10^7$ cycles into Eq. 5.10 to obtain S_f . This value is an approximation of reasonable long-life unnotched smooth axial fatigue strengths and should be somewhat compatible with values of S_f in Table A.1. Values in Table A.2 should be about 10 to 25 percent lower than those in Table A.1 for a given material, because of the difference between bending and axial long-life fatigue strengths. The fatigue ratio, S_f/S_u (last column), does have values lower than those given in Figure 5.8. Material properties in Table A.2 also omit influences of surface finish, size, stress concentration, temperature, and corrosion. These must be included in fatigue design, and thus values in Table A.2 do not represent final fatigue design properties.

The inclusion of mean stress or mean strain effects in fatigue life prediction methods involving strain-life data is very complex. One method is to replace σ'_f with $\sigma'_f - \sigma_m$ in Eq. 5.10 [25], where σ_m is the mean stress, such that

$$\frac{\Delta \epsilon}{2} = \frac{(\sigma'_f - \sigma_m)(2N)^b}{E} + \epsilon'_f(2N)^c \quad (5.14)$$

here σ_m is taken positive for tensile values and negative for compression values. Another equation suggested by Smith et al. [27], based on strain-life

test data at fracture obtained with various mean stresses, is

$$\sigma_{\max} \epsilon_a E = (\sigma'_f)^2 (2N)^{2b} + \sigma'_f \epsilon'_f E (2N)^{b+c} \quad (5.15)$$

where $\sigma_{\max} = \sigma_m + \sigma_a$ and ϵ_a is the alternating strain. If σ_{\max} is zero, Eq. 5.15 predicts infinite life, which implies that tension must be present for fatigue fractures to occur. Both Eqs. 5.14 and 5.15 have been used to handle mean stress effects [4,25].

Appendix A References

4. R.M. Wetzel, Ed., *Fatigue Under Complex Loading: Analysis and Experiments*, SAE, 1977.
21. "Technical Report on Fatigue Properties", SAE J1099, 1975.
22. O.H. Basquin, "The Exponential Law of Endurance Tests", *Proc. ASTM*, Vol. 10, Part II 1910, p. 625.
23. J.F. Tavernelli and L.F. Coffin, Jr., "Experimental Support for Generalized Equation Predicting Low Cycle Fatigue", *Trans. ASME, J. Basic Eng.*, Vol. 84, No. 4, Dec. 1962, p. 533.
24. S.S. Manson, discussion of reference 23, *Trans. ASME J. Basic Eng.*, Vol. 84, No. 4, Dec. 1962, p. 537.
25. J.A. Graham, Ed., *Fatigue Design Handbook*, SAE, 1968.
26. S.S. Manson, "Fatigue: A Complex Subject-Some Simple Approximations", *Exp. Mech.*, Vol. 5, No. 7, July 1965, p. 193.
27. K.N. Smith, P. Watson, and T.H. Topper, "A Stress-Strain Function for the Fatigue of Metals", *J. Mater.*, Vol. 5, No. 4, Dec. 1970, p.767.

Appendix B

Fundamentals of LEFM for Application to Fatigue Crack Growth and Fracture

The importance of fatigue crack propagation and fracture was brought out in the preceding chapter. This chapter deals with the quantitative methods of handling crack propagation and final fracture. This requires the use of fracture mechanics concepts, with linear elastic fracture mechanics (LEFM) concepts being the most successful. The stress intensity factor K and the stress intensity factor range ΔK are used extensively. Their units are stress times square root of length. We bring out the need for LEFM in the discussion below.

Figure 4.1. shows schematically three crack length versus applied cycles curves for three identical test specimens subjected to different repeated stress levels with $S_1 > S_2 > S_3$. All specimens contained the same initial small crack length, and in each test the minimum stress was zero. We see that with higher stresses in crack propagation rates are higher and the fatigue life is shorter. The crack lengths at fracture were shorter at the higher stress levels. Therefore, total life to fracture depended on the initial crack length, the stress magnitude, and the final fracture resistance of the material. We must ask ourselves, How can fatigue crack growth data, such as that in Figure 4.1, be used in fatigue design? The format of Figure 4.1 is not applicable to fatigue design except under the exact same conditions used in obtaining the data. Thus the need arises to apply LEFM concepts to reduce Figure 4.1 data to a format useful in fatigue design. This involves obtaining crack growth rate, da/dN , versus the applied stress intensity factor range, ΔK , as shown schematically in Figure 4.2. This sigmoidal shaped curve is essentially independent of initial crack lengths. Stress range, ΔS , and crack length, a , are included in ΔK . Thus, using the proper stress intensity factor for a given component and crack, integration of the sigmoidal shaped curve can provide fatigue crack growth life for components subjected to different stress levels and different initial crack sizes. Crack length at fracture can be estimated from critical stress intensity values K_{Ic} or K_{Ic} , called fracture toughness. Complex interac-

tion or sequence effects can be considered by analyzing plastic zone sizes at the crack tip along with crack closure models.

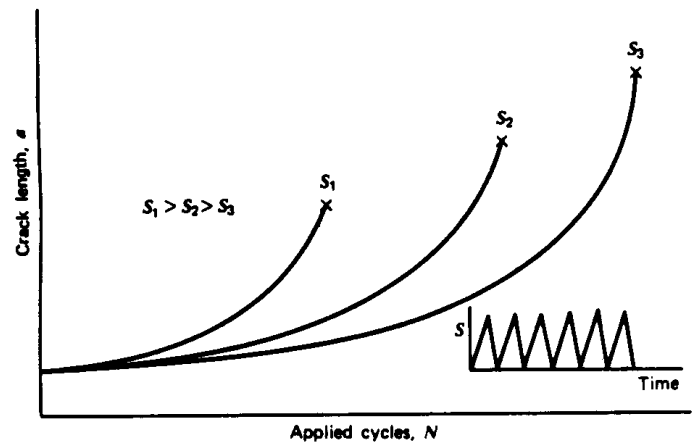


Figure 4.1. Fatigue crack length versus applied cycles. Fracture is indicated by x.

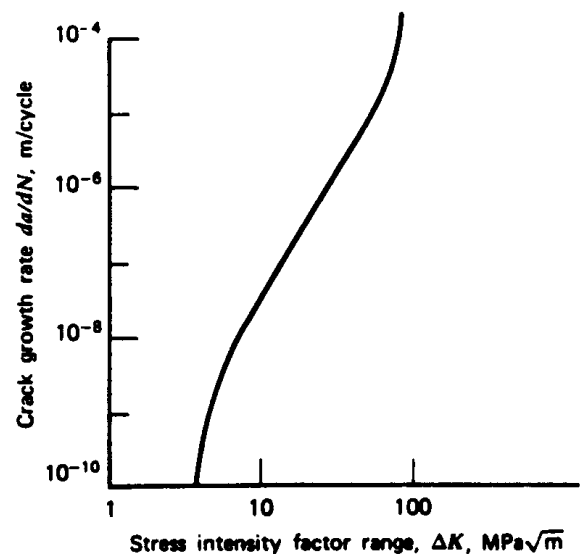


Figure 4.2. Schematic sigmoidal behavior of fatigue crack growth rate versus stress intensity factor range.

This chapter provides an introduction to the important aspects of linear elastic fracture mechanics, which is used in later chapters to describe and predict fatigue crack growth and final fracture. This chapter does not contain the mathematics used to develop the theory but does provide the background fracture mechanics concepts and numerical tools needed for fatigue design involving fatigue crack growth and final fracture. Several excellent textbooks on final fracture mechanics can be referred to for greater rigor and detail [1-4]. Fracture mechanics uses the stress intensity factor K , the strain energy release rate G , and the J -integral J , along with critical or limiting values of these terms. We are involved exclusively with the stress intensity factor K and its critical or limiting values K_c , K_{Ic} , and ΔK_{th} . Fracture mechanics has been used heavily in the aerospace, nuclear, and ship industries with only a recent extension to the ground vehicle industry. The chapter is divided into three sections, dealing first with the stress intensity factor K , then plastic zone sizes f_y , followed by fracture toughness K_c and K_{Ic} .

4.1 Stress Intensity Factor K

Figure 4.3 shows three modes in which a crack can extend. Mode I is the opening mode, which is the most common, particularly in fatigue, and has received the greatest amount of investigation. Mode II is the shearing or sliding mode, and mode III is the tearing or antiplane mode. Combinations of these crack extension modes can also occur,

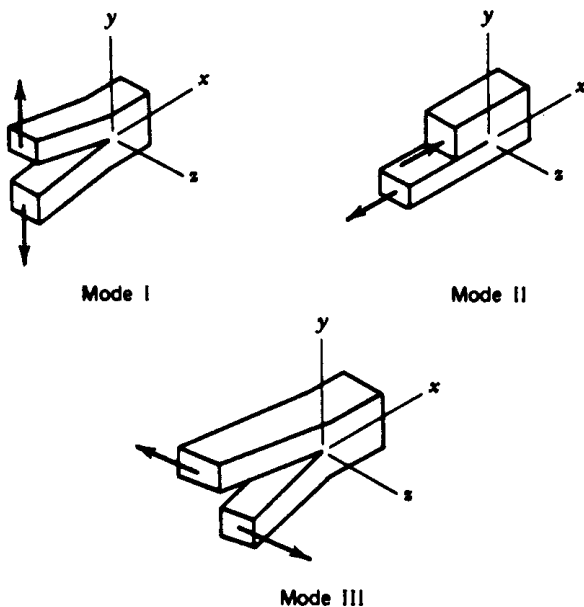
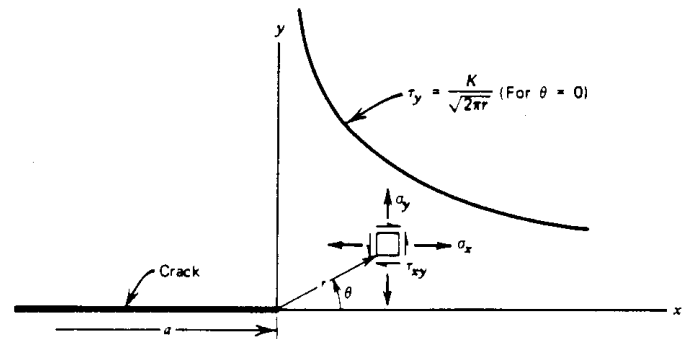


Figure 4.3. Three modes of crack extension.

particularly modes I and III as shown in Figure 3.5. Now let us consider a through thickness sharp crack in a linear elastic isotropic body subjected to Mode I loading. Such a two-dimensional crack is shown schematically in Figure 4.4. An arbitrary stress element in the vicinity of the crack tip with coordinates r and θ relative to the crack tip and crack plane is also shown. Using the mathematical theory of linear elasticity and the Westergaard stress function in complex form, the stresses at any point near the crack tip can be derived [5]. These stresses are given in Figure 4.4. Higher order terms exist, but these are negligible in the vicinity of the crack tip. It should be noted that by definition the normal and shear stresses involving the z direction (perpendicular to the x - y plane) are zero for plane stress, while the normal and shear strains (and shear stresses) involving the z direction are zero for plane strain.

Figure 4.4 shows that elastic normal and elastic shear stresses in the vicinity of the crack tip are dependent on r , θ , and K only. The magnitudes of these stresses at a given point are thus dependent entirely on K . For this reason, K is called a stress field parameter, or stress intensity factor. K is not to be confused with the elastic stress concentration factor K_t , which is the ratio of the maximum stress at a notch to the nominal stress at the notch. The value of the stress intensity factor, K , depends on



$$\sigma_y = \frac{K}{\sqrt{2\pi r}} \cos \frac{\theta}{2} \left[1 + \sin \frac{\theta}{2} \sin 3 \frac{\theta}{2} \right]$$

$$\sigma_x = \frac{K}{\sqrt{2\pi r}} \cos \frac{\theta}{2} \left[1 - \sin \frac{\theta}{2} \sin 3 \frac{\theta}{2} \right]$$

$$\tau_{xy} = \frac{K}{\sqrt{2\pi r}} \cos \frac{\theta}{2} \sin \frac{\theta}{2} \cos 3 \frac{\theta}{2}$$

$$\sigma_z = \tau_{xz} = \tau_{yz} = 0 \quad \text{for plane stress}$$

$$\sigma_z = \mu [\sigma_x + \sigma_y] \quad \left. \begin{array}{l} \text{for plane strain} \\ \tau_{xz} = \tau_{yz} = 0 \end{array} \right\}$$

Figure 4.4. Elastic stresses near the crack tip ($r/a < 1$).

the loading, body configuration, crack shape, and mode of crack displacement. K used without a mode subscript I, II, or III normally refers to mode I.

The elastic stress distribution in the y direction for $\theta = 0$ is shown in Figure 4.4. As r approaches zero, the stress at the crack tip approaches infinity, and thus a stress singularity exists at $r = 0$. Since infinite stresses cannot exist in a physical body, the elastic solution must be modified to account for crack tip plasticity. If, however, the plastic zone size r_p at the crack tip is small relative to local geometry (for example, r_p/t and $r_p/a < 0.1$ where t is thickness), little or no modification to the stress intensity factor, K , is needed. Thus an important restriction to the use of linear elastic fracture mechanics is that the plastic zone size at the crack tip must be small relative to the geometrical dimensions of the specimen or part. A definite limiting condition for linear elastic fracture mechanics is that nominal stresses in the crack plane must be less than the yield strengths. In actual usage the nominal stress in the crack plane should be less than 0.8 times the yield strength [6].

Values of K for various loadings and configurations can be calculated using the theory of elasticity involving both analytical and numerical calculations along with experimental methods. The most common reference value of K is for a two-dimensional center crack of length $2a$ in an infinite sheet subjected to a uniform tensile stress s . For the infinite sheet, K is:

$$K = S\sqrt{\pi a} \approx 1.77 S\sqrt{a} \quad (4.1)$$

Units of K are $\text{Mpa} \sqrt{\text{m}}$ and $\text{ksi} \sqrt{\text{in.}}$, where $1 \text{ MPa} \sqrt{\text{m}} = 0.91 \text{ ksi} \sqrt{\text{in.}}$

The stress intensity factor for other crack geometries, configurations, and loadings are usually modifications of Eq. 4.1, such that

$$K = S\sqrt{\pi a} \alpha \quad \text{or} \quad S\sqrt{\pi a} f\left(\frac{a}{w}\right) \\ \text{or} \quad S\sqrt{a} Y \quad (4.2)$$

where α , $f(a/w)$, and Y are dimensionless parameters, w is a width dimension, and S is the nominal stress, assuming the crack did not exist. For central cracks, the crack length is taken as $2a$ (or $2c$) and for edge cracks the crack length used is just a (or c). Opening mode I stress intensity expressions in the form of dimensionless curves are given in Figure 4.5 for several common configura-

tions of thickness B [2,7]. In each case it is evident that K depends on the crack length to width ratio, a/w . These tabulations were obtained from analytical or numerical solutions, often in the form of polynomials. The actual mathematical expression is of greater importance in fatigue crack growth since numerical integration is usually required. Several of these common mathematical expressions are given in Table 4.1. For the single or double edge crack in a semiinfinite plate ($a/w \rightarrow 0$)

$$K = 1.12 S\sqrt{\pi a} \approx 2S\sqrt{a} \quad (4.3)$$

where 1.12 is the free edge correction. Additional stress intensity factor expressions for all three modes, K_I , K_{II} , and K_{III} can be found in references 1 to 10. Superposition of K expressions can also be used for each separate mode.

The elliptical crack approximates many cracks found in engineering components and structures and has received widespread analytical, numerical, and experimental analysis. Common circular and elliptical embedded and surface cracks are shown in Figure 4.6. The general reference specimen is the embedded elliptical crack in an infinite body subjected to uniform tension S at infinity (Figure

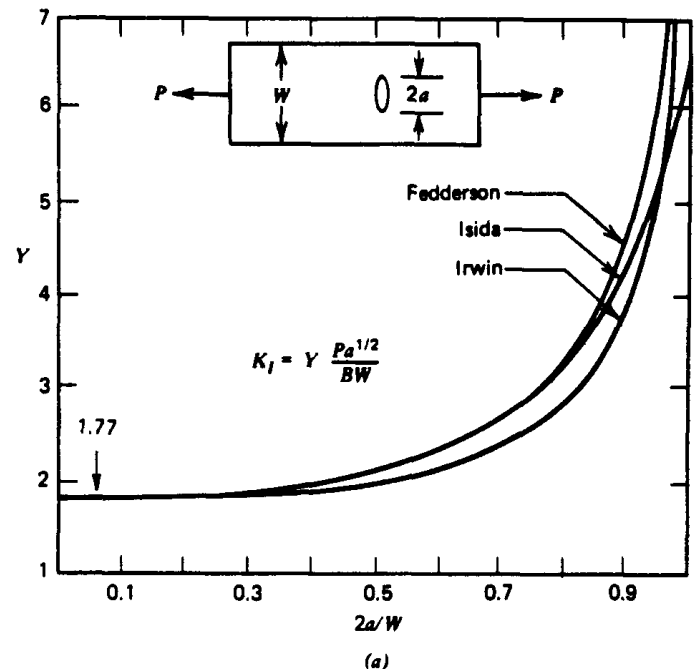


Figure 4.5 K_I for common configurations [2,7] (reprinted by permission of Noordhoff International Publishing Co. and the American Society of Testing and Materials). (a) Center cracked plate in tension [2].

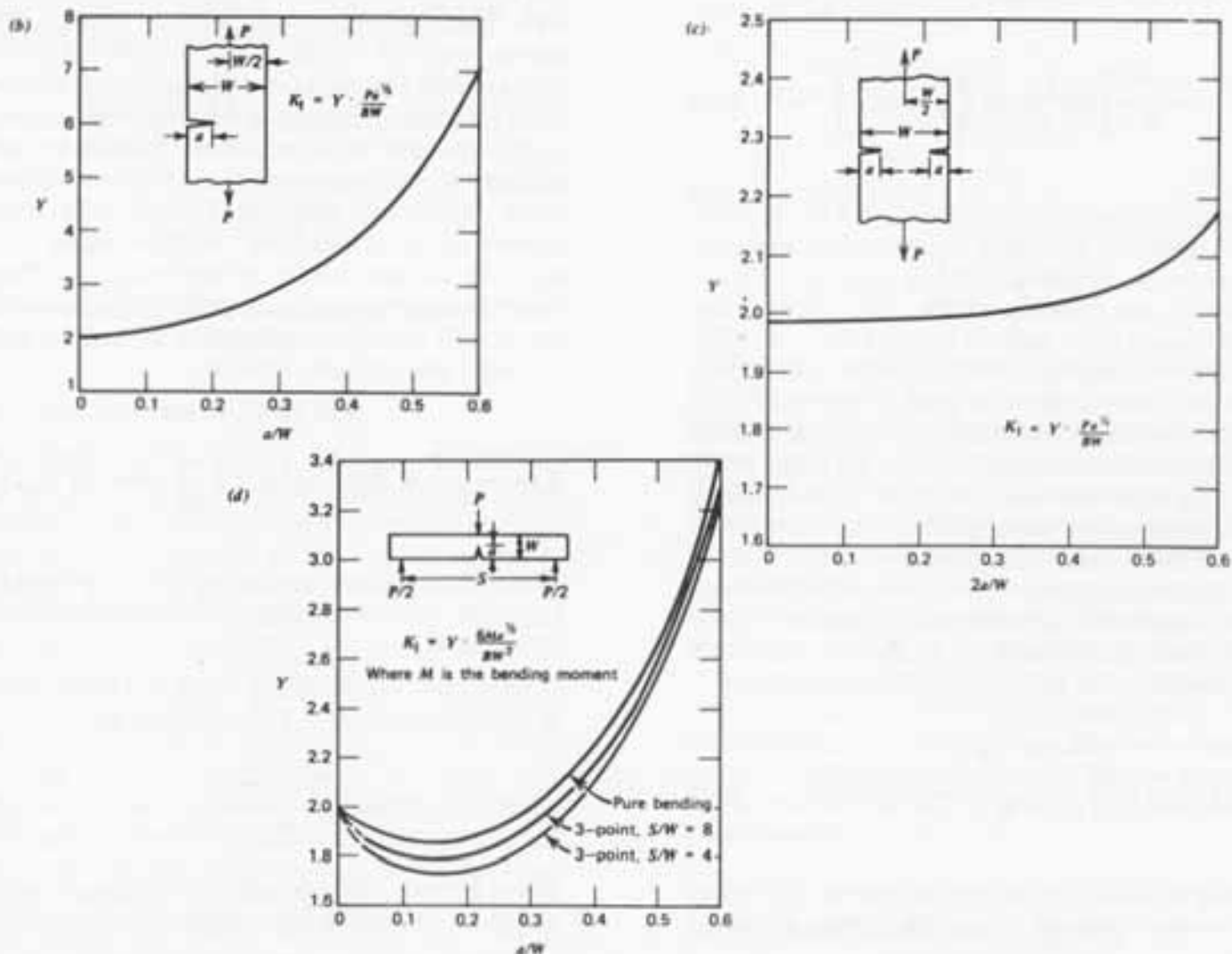


Figure 4.5 (continued). K_I for common configurations [2,7] (reprinted by permission of Noordhoff International Publishing Co. and the American Society for Testing and Materials). (b) Single edge crack in tension [7]. (c) Double edge crack in tension [7]. (d) Single edge crack in bending [7].

Table 4.1. K Expressions for Figure 4.5.

a. Center cracked plate in tension

Fedderson:

$$K_I = S\sqrt{\pi a} \left[\sec \frac{\pi a}{w} \right]^{1/2}$$

Irwin:

$$K_I = S\sqrt{\pi a} \left[\frac{w}{\pi a} \tan \frac{\pi a}{w} \right]^{1/2}$$

b. Single-edge crack in tension

$$K_I = S\sqrt{a} \left[1.99 - 0.41 \left(\frac{a}{w} \right) + 18.7 \left(\frac{a}{w} \right)^2 - 38.48 \left(\frac{a}{w} \right)^3 + 53.85 \left(\frac{a}{w} \right)^4 \right]$$

where

$$1.12\sqrt{\pi} = 1.99$$

$$S = P/Bw$$

c. Double-edge crack in tension

$$K_I = S\sqrt{a} \left[1.98 + 0.36 \left(\frac{2a}{w} \right) - 2.12 \left(\frac{2a}{w} \right)^2 + 3.42 \left(\frac{2a}{w} \right)^3 \right]$$

where

$$S = P/Bw$$

d. Pure bending of a beam

$$K_I = \frac{6M\sqrt{a}}{Bw^3} \left[1.99 - 2.47 \left(\frac{a}{w} \right) + 12.97 \left(\frac{a}{w} \right)^2 - 23.17 \left(\frac{a}{w} \right)^3 + 24.8 \left(\frac{a}{w} \right)^4 \right]$$

4.6c). For this embedded configuration K is:

$$K = \frac{S\sqrt{\pi a}}{\Phi} \left[\sin^2 \beta + \left(\frac{a}{c}\right)^2 \cos^2 \beta \right]^{1/4} \quad (4.4)$$

where β is the angle shown in Figure 4.6g, $2a$ is the minor diameter, and $2c$ is the major diameter. The term θ is the complete elliptical integral of the second kind and depends on the crack aspect ratio a/c . Values of θ are given in Figure 4.6h, where it is seen that θ varies from 1.0 to 1.571 for a/c ranging from zero (very shallow ellipse) to one (circle). K varies along the elliptical crack tip according to the trigonometric expression involving the angle β (Eq. 4.4). The maximum value of K for the embedded crack exists at the minor axis and the minimum is at the major axis. Since fatigue crack growth depends principally on K , the embedded elliptical crack subjected to uniform tension tends to grow to a circle with a uniform K at all points on the crack tip perimeter. For the circular embedded crack

$$K = S\sqrt{\pi a} \left(\frac{2}{\pi}\right) = 2S\sqrt{\frac{a}{\pi}} \approx 1.13 S\sqrt{a} \quad (4.5)$$

Surface elliptical cracks tend to grow to other elliptical shapes because of the free surface effect.

The surface semicircular or semielliptical crack in a finite thickness solid (Figs. 4.6d to 4.6f and the quarter-elliptical corner crack (Figures 4.6e and 4.6f are very common in fatigue and are extremely more complex compared to the embedded crack in an infinite solid. K at the surface intersection and around the crack tip perimeter has been estimated using numerical methods [11-14] and three-dimensional photoelasticity [15]. References 1 to 6 and 8 to 10 also contain K estimations for these three dimensional cracks. A general expression for the mode I semielliptical surface crack in a finite thickness plate (Figure 4.6d) is

$$K = \frac{S\sqrt{\pi a}}{\Phi} M_f M_b \left[\sin^2 \beta + \left(\frac{a}{c}\right)^2 \cos^2 \beta \right]^{1/4} \quad (4.6)$$

where M_f is a front face correction factor and M_b is a back face correction factor. M_f and M_b are functions of β

For a surface semielliptical crack in a thick plate K at the deepest point is approximated as:

$$K \approx \frac{1.12 S\sqrt{\pi a}}{\Phi} \quad (4.7)$$

where $M_f \cong 1.12$ is analogous to the free edge correction of the single edge crack. For the quarter-

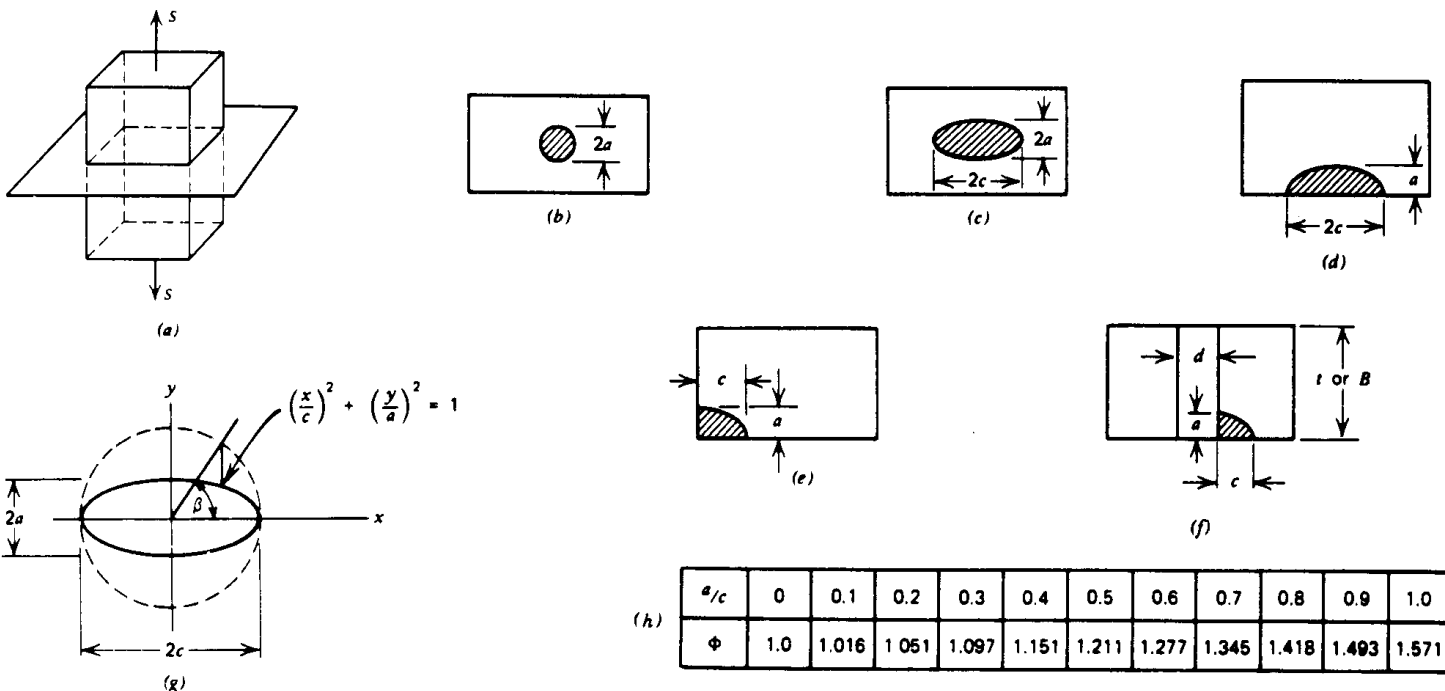


Figure 4.6. Elliptical and circular cracks. (a) Tensile loading and crack plane. (b) Embedded circular crack. (c) Embedded elliptical crack. (d) Surface half-elliptical crack. (e) Quarter-elliptical corner crack. (f) Quarter-elliptical corner crack emanating from a hole. (g) Elliptical crack parameters. (h) Values of Φ .

circular corner crack ($a/c = 1$) in Figure 4.6e, with two free edges, K is approximated as:

$$K = \frac{(1.12)^2 S \sqrt{\pi a}}{\Phi} \approx (1.12)^2 2S \sqrt{\frac{a}{\pi}} \quad (4.8)$$

$$\approx 2.5 S \sqrt{\frac{a}{\pi}} \approx 1.41 S \sqrt{a}$$

These simple approximations agree quite well with more complex calculations.

4.2 Crack Tip Plastic Zone Size

Whether a fracture occurs in a ductile or brittle manner, or a fatigue crack grows under cyclic loading, the local plasticity at the crack tip controls both fracture and crack growth. It is possible to calculate a plastic zone size at the crack tip as a function of stress intensity factor, K , and yield strength, S_y , by using the stress equations in Figure 4.4 and the von Mises or maximum shear stress yield criteria. The resultant monotonic plastic zone shape for mode I using the von Mises criterion is shown schematically in Figure 4.7.

For plane stress conditions, a much larger plastic zone exists compared to plane strain conditions, as indicated in the lower right corner. This is due to σ_z having a different value for plane stress than for plane strain as given in Figure 4.4., which decreases the magnitude of two of the three principal shear stresses. Now let us assume a through crack exists in a thick plate. The plate's free surfaces have zero normal and shear stresses, and therefore the free surfaces must be in a plane stress condition. However, the interior region of the plate near the crack tip is closer to plane strain conditions as a result of elastic constraint away from the crack. Thus the plastic zone along the crack tip varies similarly to that shown schematically in Figure 4.7. The actual stress-strain distribution within the plastic zone is difficult to obtain; however, this is not significant for the use of linear elastic fracture mechanics in design.

It is seen in Figure 4.7 that the plastic zone is proportional to the square of the ratio of the stress intensity factor to the yield strength. Because of plastic relaxation of the stress field in the plastic zone, the actual plane stress plastic zone size is approximately twice the value shown in Figure 4.7. The plane strain plastic zone size in the plane of the crack is usually taken as one-third the plane stress value. Thus, under monotonic loading, the plane stress plastic zone size, $2r_y$, at the crack tip, in the

plane of the crack, is:

$$2r_y = 2 \left[\frac{1}{2\pi} \left(\frac{K}{S_y} \right)^2 \right] = \frac{1}{\pi} \left(\frac{K}{S_y} \right)^2 \quad (4.9)$$

and for plane strain

$$2r_y = \frac{1}{3\pi} \left(\frac{K}{S_y} \right)^2 \quad (4.10)$$

Additional models for plastic zone size and shape, which have also received wide spread use, have been formulated by Dugdale [16] and Hahn and Rosenfield [17]. Under cyclic loading, a reversed plastic zone occurs when the tensile load is removed. Rice [18] showed that it is much smaller than the peak monotonic values given by Eq. 4.9 or 4.10. For example, the size of the reversed plastic zone after unloading to zero load is only one-quarter of that which existed at the peak tensile load. Then the stresses in the plastic zone are compressive, while outside the plastic zone they change from compression to tension. Fatigue load sequence effects are caused by these plastic zones containing compressive or tensile stresses, as is discussed in later chapters.

4.3 Fracture Toughness - K_c , K_{Ic}

Quantitative monotonic fracture toughness can be obtained for brittle materials from tests using

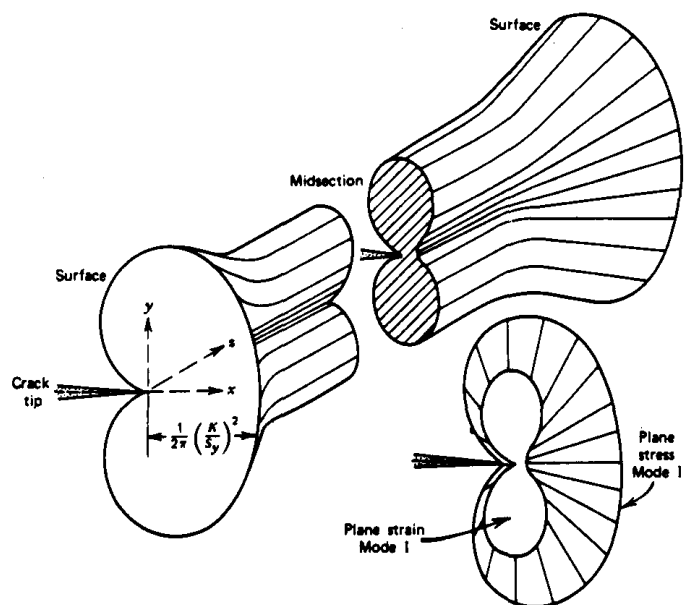


Figure 4.7. Plastic zone size at the tip of a through thickness crack.

specimens with fatigue cracks with known K expressions such as those in Figure 4.5 and Table 4.1. Critical values of K refer to the condition when a crack extends in a rapid (unstable) manner without an increase in load or applied energy. Critical values of K are denoted with a subscript c as follows:

$$K_c = S_c \sqrt{\pi a_c} f \left(\frac{a_c}{w} \right) \quad (4.11)$$

where S_c is the applied nominal stress at crack instability and a_c is the crack length at instability; K_c is called fracture toughness and depends on the material, temperature, strain rate, environment, thickness, and to a lesser extent, crack length. If K_c is known for a given material and thickness, and K is known for a given component and loading, a quantitative design criteria to prevent brittle fracture exists involving applied stress and crack size. Since K_c also represents the stress intensity factor at the last cycle of a fatigue fracture, it can be used to obtain critical crack sizes for fracture under cyclic loading. In 1920 Griffith [19], using elastic energy balance equations and experimentation with brittle glass, was the first to produce a quantitative relationship for brittle fracture of cracked bodies.

The general relationship between fracture toughness, K_c , and thickness is shown in Figure 4.8. The fracture appearance accompanying the different thicknesses is also shown schematically for single-edge notch specimens. The beach markings at the crack tip represent fatigue precracking at low cyclic stress intensity factor range to assure a sharp crack tip. The fracture toughness values would be higher for dull, or notch type, crack fronts. It is seen that thin parts have a high value of K_c accompanied by appreciable “shear lips” or slant fracture. As the thickness is increased, the percentage of “shear lips” or slant fracture decreases, as does K_c . This type of fracture appearance is called mixed mode. For thick parts, essentially the entire fracture surface is flat and K_c approaches an asymptotic minimum value. Further increase in thickness does not decrease the fracture toughness, nor does it alter the fracture appearance. The minimum value of fracture toughness is called the “plane strain fracture toughness” K_{Ic} . The subscript I refers to the fact that these fractures occur almost entirely by mode I crack opening. The term “plane strain” is incorporated here since flat fractures best approach a true plane strain constraint throughout most of the crack tip region. For thin sections where ap-

preciable “shear lips” occur, the crack tip region most closely experiences a plane stress situation. Thus plastic zone sizes at fracture are much larger in thin parts as compared to thick parts. Plane strain fracture toughness K_{Ic} is considered a true material property because it is independent of thickness. Approximate thickness required for steels and aluminums to obtain valid K_{Ic} values are given in Table 4.2. Low strength, ductile materials are subject to plane strain fracture at room temperature only if they are very thick. Therefore, most K_{Ic} data have been obtained for the medium and higher strength materials or for the lower strength materials at low temperatures.

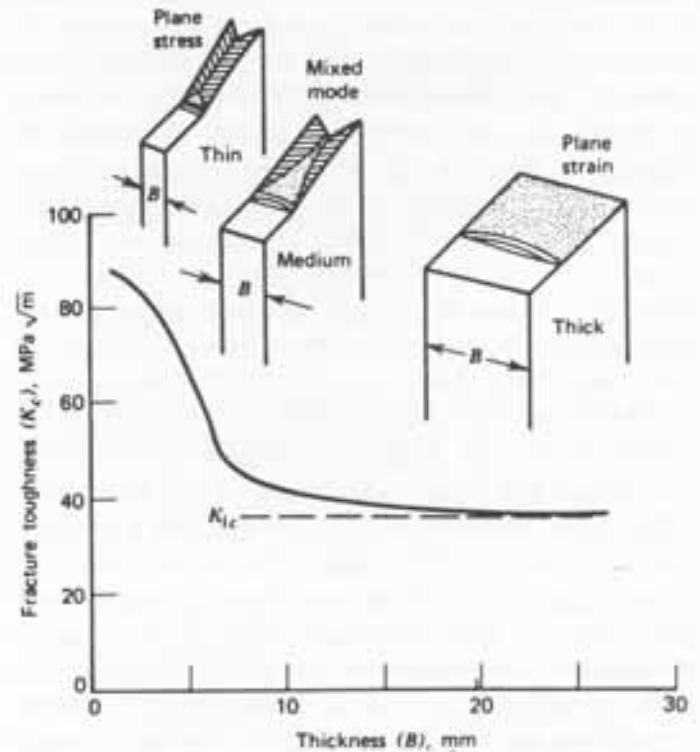


Figure 4.8. Effect of specimen thickness on fracture toughness.

Table 4.2. Approximate Thickness Required for Valid K_{Ic} Tests.

Steel S_y MPa (ksi)	Aluminum S_y MPa (ksi)	Thickness, mm (in.)
690 (100)	275 (40)	> 76 (3)
1030 (150)	345 (50)	76 (3)
1380 (200)	448 (65)	45 (1- $\frac{1}{2}$)
1720 (250)	550 (80)	19 ($\frac{3}{4}$)
2070 (300)	620 (90)	6 ($\frac{1}{4}$)

A general trend of K_{Ic} at room temperature, as a function of yield strength for three major base alloys, aluminum, titanium, and steel, is given in Figure 4.9 [20]. As can be seen, a wide range of K_{Ic} can be obtained for a given base alloy. However, a higher yield or ultimate strength generally produces a decrease in K_{Ic} for all materials, and thus a greater susceptibility for catastrophic fracture. This is an important conclusion that too many engineers overlook. Figure 4.9 does not provide K_{Ic} data for all levels of yield strength because of the large thickness required for low strength materials. The use of linear elastic fracture mechanics is not suitable for these low strength materials under monotonic loading because of the extensive plastic zones occurring at the crack tip. Exceptions occur, however, at very low temperatures, in the presence of corrosive environments, and under fatigue conditions where only small scale yielding occurs near the crack tip. Appreciable K_{Ic} data for specific materials can be found in reference 21 and some representative K_{Ic} values are given in Table A.3. Much variability, however, occurs for a given yield strength, depending on the type and quality of the material. This is best illustrated for steels in Figure 4.9, where vacuum-induction melting (VIM) plus vacuum-arc melting (VAR) of the base material produce greater K_{Ic} for a given yield strength than just single vacuum-arc remelting or air melting of steels (AIR). Thus low impurity materials provide better fracture toughness.

Fracture toughness K_{Ic} of metals is also dependent on temperature, strain rate, and corrosive environment. Figure 4.10 shows typical temperature results for a low alloy steel [22]. As the temperature

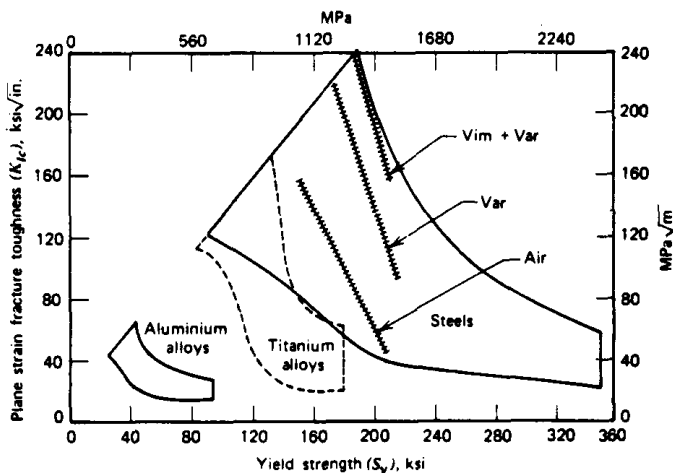


Figure 4.9. Locus of plane strain fracture toughness versus yield strength [20].

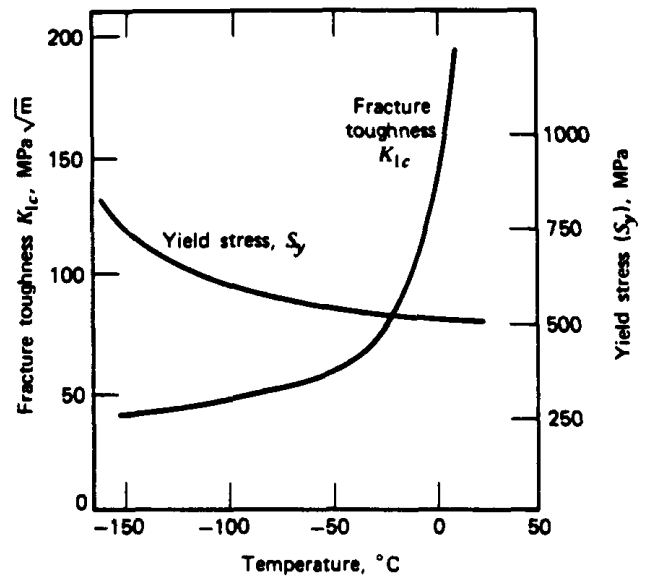


Figure 4.10. Variation of K_{Ic} with temperature for low alloy nuclear pressure vessel steel A533B [22] (reprinted with permission of E.T. Wessel).

decreases, K_{Ic} usually decreases, while the yield strength increases. Thus even though unnotched or uncracked tensile strength increases with decreasing temperature, the flaw or crack resistance can be drastically reduced. Increased strain rate tends to cause changes in K_{Ic} similar to that of decreasing the temperature. That is, higher strain rates often produce lower fracture toughness, and hence, greater crack sensitivity. Corrosive environmental influence on short term fracture toughness may show small or large changes. However, corrosive environments can cause appreciable decreases in crack tolerance under long term stress corrosion cracking and fatigue crack growth conditions. Environmental considerations are covered in Chapter 11.

A general schematic drawing of how changes in fracture toughness influence the relationship between allowable nominal stress and allowable crack size is shown in Figure 4.11, which is a plot of

$$S = \frac{K_{Ic}}{\sqrt{\pi a}} \quad (4.12)$$

This equation comes from equating the stress intensity factor K for a center crack in a wide plate to the fracture toughness K_{Ic} . The allowable stress in the presence of a given crack size is directly proportional to the fracture toughness, while the allowable crack size for a given stress is proportional to the square of the fracture toughness. Thus

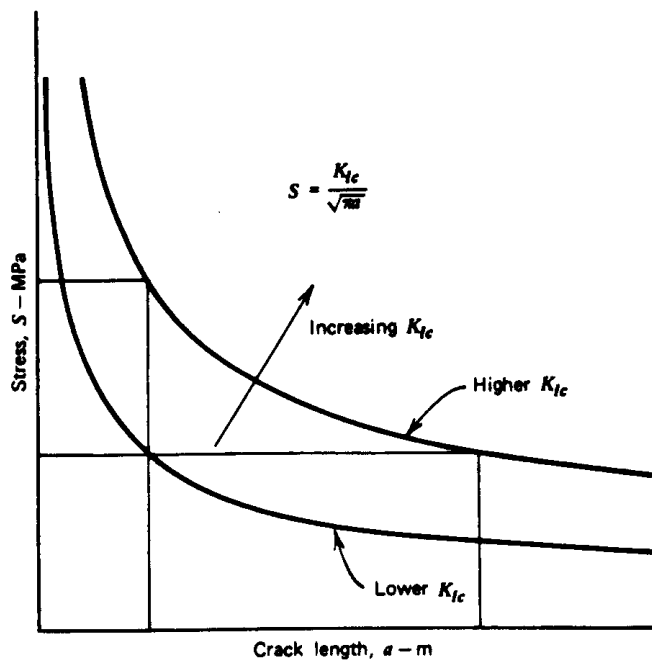


Figure 4.11. Influence of fracture toughness on allowable stress or crack size.

increasing K_{Ic} has a much larger influence on allowable crack size than on allowable stress. For monotonic loading of components containing cracks, a higher fracture toughness results in larger allowable crack sizes or larger allowable stresses at fracture.

Appendix B References

1. J.F. Knott, *Fundamentals of Fracture Mechanics*, Halsted Press, John Wiley and Sons, New York, 1973.
2. D. Broek, *Elementary Engineering Fracture Mechanics*, Noordhoff International Publishing Co., Leyden, The Netherlands, 1974.
3. S.T. Rolfe and J.M. Barsom, *Fracture and Fatigue Control in Structures - Applications of Fracture Mechanics*, Prentice-Hall, Englewood Cliffs, NJ, 1977.
4. R.W. Hertzberg, *Deformation and Fracture Mechanics of Engineering Materials*, John Wiley and Sons, New York, 1976.
5. V Weiss and S. Yukawa, "Critical Appraisal of Fracture Mechanics", *Fracture Toughness Testing and Its Applications*, ASTM STP 381, 1965, p. 1.
6. *Fracture Toughness Testing and Its Application*, ASTM STP 381, 1965.
7. W.F. Brown, Jr. and J.E. Srawley, *Plane Strain Crack Toughness Testing of High Strength Metallic Materials*, ASTM STP 410, 1966, p. 1.
8. H. Tada, P.C. Paris, and G.R. Irwin, *The Stress Analysis of Cracks Handbook*, Del Research Corp., Hellertown, PA, 1973.
9. G.C. Sih, *Handbook of Stress Intensity Factors*, Institute of Fracture and Solid Mechanics, Lehigh University, Bethlehem, PA, 1973.
10. D.P. Rooke and D.J. Cartwright, *Compendium of Stress Intensity Factors*, Her Majesty's Stationery Office, London, 1976.
11. R.C. Shah and A.S. Kobayashi, "Stress Intensity Factors for an Elliptical Crack Approaching the Surface of a Semi-Infinite Solid", *Int. J. Fract.*, Vol. 9, No. 2, 1973, p. 133.
12. F.W. Smith and D.R. Sorenson, "The Semi-Elliptical Surface Crack-A Solution by the Alternating Method", *Int. J. Fract.*, Vol. 12, No. 1, 1976, p. 47.
13. T.A. Cruse and G.J. Meyers, "Three-Dimensional Fracture Mechanics Analysis", *J. Struct. Div. ASCE*, Vol. 103, No. ST2, Feb. 1977, D. 309.
14. D.M. Tracy, "3-D Elastic Singularity Element of Evaluation of K along an Arbitrary Crack Front", Vol. 9, No. 3, 1973, p. 340.
15. C.W. Smith, "Fracture Mechanics", *Experimental Techniques in Fracture Mechanics*, Vol. 2, AS. Kobayashi, Ed., The Iowa State University Press, 1975, p. 3.
16. D.S. Dugdale, "Yielding of Steel Sheets Containing Slits", *J. Mech. Phys. Solids*, Vol. 8, 1960, p. 100.
17. G.T. Hahn and A.R. Rosenfield, "Local Yielding and Extension of a Crack under Plane Stress", *Acta Metall.*, Vol. 13, No. 3, 1965, p. 293.
18. J.R. Rice, "Mechanics of Crack Tip Deformation and Extension by Fatigue", *Fatigue Crack Propagation*, ASTM STP 41 5, 1967, p. 247.
19. A.A. Griffith, "The Phenomena of Rupture and Flow in Solids", *Philos. Trans., R. Soc. Lond., Ser. A*, Vol. 221, 1920, p. 163.
20. W.S. Pellini, "Criteria for Fracture Control Plans", *NRL Report 7406*, May, 1972.
21. *Damage Tolerant Design Handbook, A Compilation of Fracture and Crack Growth Data for High Strength Alloys*, MCIC-HB-01, Metals and Ceramics Information Center, Battelle, Columbus, OH.
22. E.T. Wessel, "Variation of K_{Ic} with Temperature for Low Alloy Nuclear Pressure Vessel Steel A533B", *Practical Fracture Mechanics for Structural Steel*, Chapman and Hall, 1969.

Fatigue Crack Growth $da/dN = \Delta K$

Linear elastic fracture mechanics (LEFM) concepts are most useful to correlate fatigue crack growth behavior, as is shown in Chapter 4. The form of this correlation for constant amplitude loading is usually a log-log plot of fatigue crack growth rate, da/dN , in m/cycle (in./cycle), versus the opening mode stress intensity factor range ΔK_I (or ΔK), in $\text{MPa}\sqrt{\text{m}}$ ($\text{ksi}\sqrt{\text{in.}}$), where ΔK_I is defined as:

$$\Delta K_I = \Delta K = K_{\max} - K_{\min} = S_{\max} \sqrt{\pi a} \alpha - S_{\min} \sqrt{\pi a} \alpha \quad (5.16)$$

Since the stress intensity factor $K_I = S\sqrt{\pi a} \alpha$ is undefined in compression, K_{\min} is taken as zero if S_{\min} is compression.

The elastic stress intensity factor is applicable to fatigue crack growth even in low strength, high ductility materials because K_I values needed to cause fatigue crack growth are quite low. Thus plastic zone sizes at the crack tip are often small enough to allow an LEFM approach. At very high crack growth rates some difficulties can occur, as a result of large plastic zone sizes, but this is often not a problem because very little fatigue life may be involved.

5.5.1 Sigmoidal Shaped da/dN - ΔK Curve

Many fatigue crack growth data have been obtained under constant load amplitude test conditions using sharp notched fatigue cracked specimens similar to those in Figures 5.6g through 5.6j. Mode I fatigue crack growth has received the greatest attention, because this is the predominant mode of macroscopic fatigue crack growth. KII and KIII usually have only second order effects on both crack direction and crack growth rates. Crack growth is usually measured with optical, compliance, ultrasonic, eddy current, electrical potential, or acoustic emission techniques. Figure 4.1 shows typical crack length versus applied cycles for constant amplitude tests. Crack growth rates, da/dN , as a function of ΔK_I , can be obtained at consecutive positions along these curves using

graphical or numerical methods. A typical complete log-log plot of da/dN versus ΔK_I is shown schematically in Figure 4.2 and 5.19. This curve has a sigmoidal shape that can be divided into three major regions, as shown in Figure 5.19.

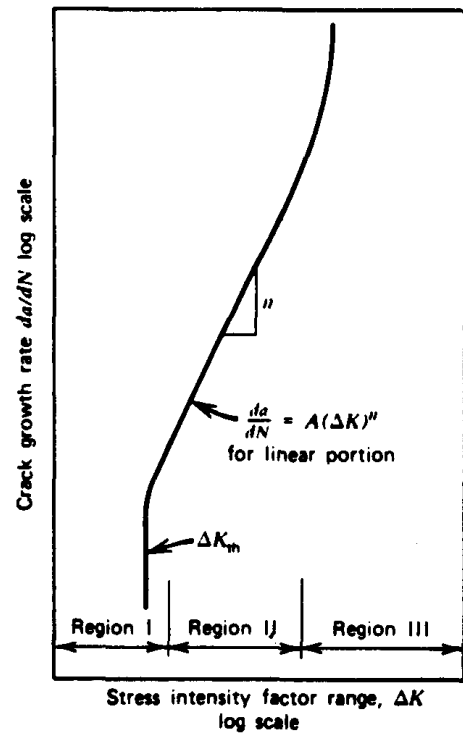


Figure 5.19. Schematic sigmoidal behavior of fatigue crack growth rate versus ΔK .

Region I indicates a threshold value ΔK_{th} , below which there is no observable crack growth. This threshold occurs at crack growth rates on the order of 2.5×10^{-10} m/cycle (10^{-8} in./cycle) or less. Below ΔK_{th} , fatigue cracks behave as non-propagating cracks. Region II shows essentially a linear relationship between $\log da/dN$ and $\log \Delta K_I$, which corresponds to the formula

$$\frac{da}{dN} = A(\Delta K_I)^n \quad (5.17)$$

first suggested by Paris [28]. Here n is the slope

of the curve and A is the coefficient found by extending the straight line to $\Delta K_I = 1 \text{ MPa}\sqrt{\text{m}}$ ($\text{ksi}\sqrt{\text{in.}}$). In region III the crack growth rates are very high and little fatigue crack growth life is involved. Region III may have the least importance in most fatigue situations. This region is controlled primarily by fracture toughness K_{Ic} or K_{Ic} .

The fatigue crack growth behavior shown in Figure 5.19 is essentially the same for different specimens or components taken from a given material, because the stress intensity factor range is the principal controlling factor in fatigue crack growth. This allows fatigue crack growth rate versus ΔK_I data obtained under constant amplitude conditions with simple specimen configurations to be used in design situations. Knowing the stress intensity factor expression, K_I , for a given component and loading, the fatigue crack growth life of the component can be obtained by integrating Eq. 5.17 between limits of initial crack size and final crack size. The greatest usage of Figure 5.19 data has been in fail-safe design of aircraft and nuclear energy systems along with fractographic failure analysis. Crack growth rate behavior has also become important in material selection and comparative prototype designs. However, as with all constant amplitude material fatigue properties, these data do not provide information on fatigue crack growth interaction or sequence effects, which are covered in Chapter 10.

5.5.2 da/dN - ΔK for $R = 0$

Conventional S-N or ϵ -N fatigue behavior is usually referenced to the fully reversed stress or strain conditions ($R = -1$). Fatigue crack growth data, however, are usually referenced to the pulsating tension condition with $R = 0$ or approximately zero. This is based on the concept that during compression loading the crack is closed and hence no stress intensity factor, K , can exist. The compression loads should thus have little influence on constant amplitude fatigue crack growth behavior. In general, this is fairly realistic, but under variable amplitude loading, compression cycles can be important to fatigue crack growth, as is seen in later chapters.

Regions II and III of the sigmoidal curve have received the widest attention. A standard ASTM practice exists for obtaining crack growth experimental data above rates of 10^{-8} m/cycle ($4 \times 10^{-7} \text{ in./cycle}$). Many mathematical equations depicting fatigue crack growth above threshold levels have been formulated. Hoepfner and Krupp [29] list 33 empirical equations. However, the Paris

equation seems to be the most popular equation for $R = 0$ loading. Substantial constant amplitude data can be found in the Damage Tolerant Handbook for common aircraft alloys [30].

Barsom [31] has evaluated Eq. 5.17 for a wide variety of steels varying in yield strength from 250 to 2070 MPa (36 to 300 ksi). He shows that the fatigue crack growth rate scatter band for a given ΔK_I , with many ferritic-pearlitic steels, varies by a factor of about 2. Partial results from Barsom [31] are shown in Figure 5.20. He also found a similar scatter band width for martensitic steels, as shown in Figure 5.21. He suggested that conservative values of the upper boundaries of these scatter bands could be used in design situations if actual data could not be obtained. These suggested conservative equations are:

for ferritic-pearlitic steels

$$\frac{da}{dN} \text{ (m/cycle)} = 6.9 \times 10^{-12} (\Delta K \text{ MPa}\sqrt{\text{m}})^{3.0} \quad (5.18)$$

$$\frac{da}{dN} \text{ (in./cycle)} = 3.6 \times 10^{-10} (\Delta K \text{ ksi}\sqrt{\text{in.}})^{3.0}$$

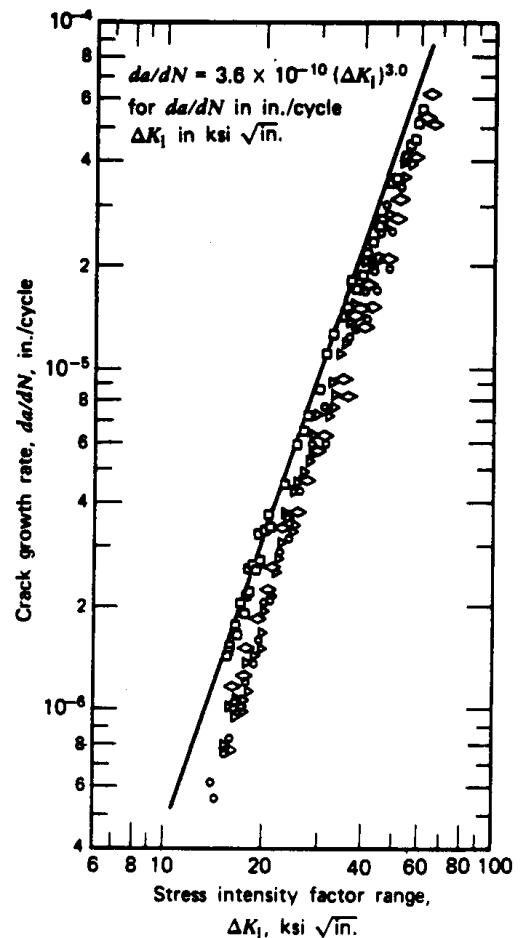


Figure 5.20. Summary of fatigue crack growth rate data for ferritic-pearlitic steels [31] (reprinted with permission of the American Society of Mechanical Engineers). (Δ) A36, (\circ) A302-B, (\square) A537-A.

for martensitic steels

$$\frac{da}{dN} \text{ (m/cycle)} = 1.35 \times 10^{-10} (\Delta K \text{ MPa}\sqrt{\text{m}})^{2.25} \quad (5.19)$$

$$\frac{da}{dN} \text{ (in./cycle)} = 6.6 \times 10^{-9} (\Delta K \text{ ksi}\sqrt{\text{in.}})^{2.25}$$

and for austenitic stainless steels

$$\frac{da}{dN} \text{ (m/cycle)} = 5.6 \times 10^{-12} (\Delta K \text{ MPa}\sqrt{\text{m}})^{3.25} \quad (5.20)$$

$$\frac{da}{dN} \text{ (in./cycle)} = 3.0 \times 10^{-10} (\Delta K \text{ ksi}\sqrt{\text{in.}})^{3.25}$$

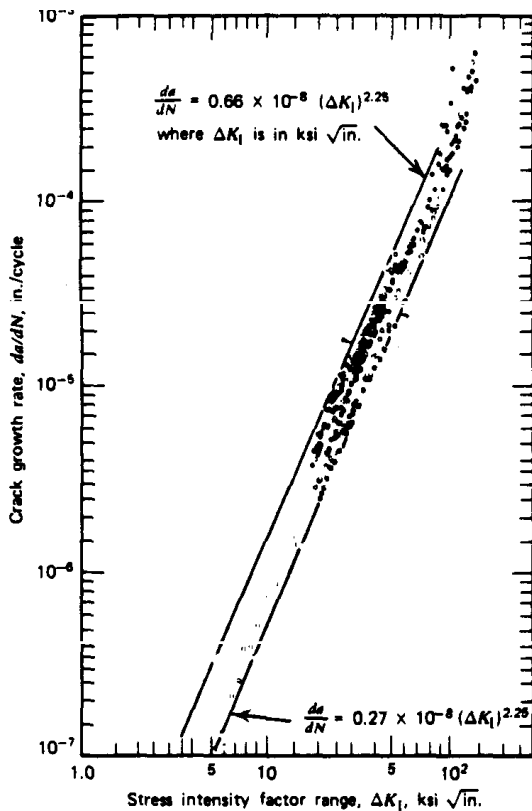


Figure 5.21. Summary of fatigue crack growth rate data for martensitic steels [31] reprinted with permission of the American Society of Mechanical Engineers. (○) 12 Ni steel, (□) 10 Ni steel, (●) Hy-130 steel, (■) Hy-80 steel.

Superposition of these three equations indicates in general that the ferritic-pearlitic steels have better region II fatigue crack growth properties than the martensitic steels or the austenitic stainless steels. The narrowness of the region II scatter bands for the different classifications of steels suggests that large changes in constant amplitude fatigue crack growth life may not be obtained by choosing a

slightly different steel. However, this does not take into consideration behavior near or at threshold levels, which does show greater variations as a function of microstructure. An approximate schematic sigmoidal shaped scatter band for steels with Barsom's scatter bands superimposed is shown in Figure 5.22. It is clear that Barsom's results do not take into consideration complete crack growth rate behavior. Also, despite the numerous tests and materials used to obtain Eqs. 5.18 to 5.20, there are many exceptions. Values of the exponent n have ranged from about 2 to 7. For different aluminum alloys, the fatigue crack growth rates for a given ΔK_I in region II vary much more. The width of the scatter band for different aluminum alloys corresponds to a factor of about 10.

Frequency, wave shape, and thickness effects on constant amplitude fatigue crack growth rates are secondary compared to environmental effects

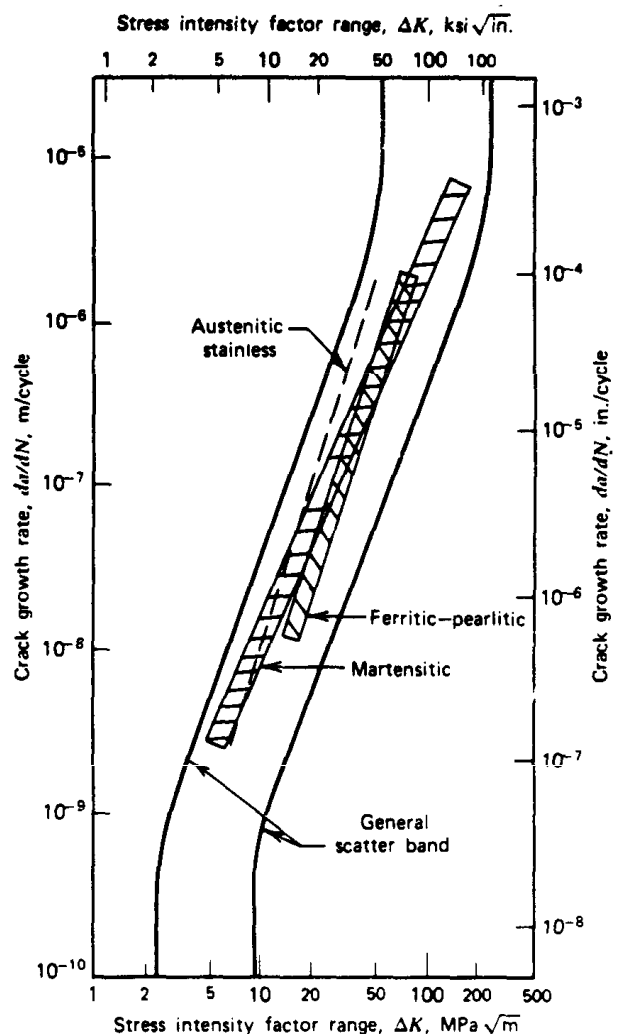


Figure 5.22. Superposition of Barsom's scatter bands on the general fatigue crack growth scatter band for steels.

such as corrosion and temperature. They can have influence, but this often is less than that due to different heats or use of different manufacturers.

The largest influence comes from variable amplitude loading in various environments. The thickness influence can be greatest in region III because of the inverse relationship between fracture toughness and thickness, as shown in Figure 4.8, which affects the allowable crack size at fracture. A high fracture toughness is desirable because of the longer final crack size at fracture, which allows easier and less frequent inspection and, therefore, safer components or structures.

Threshold stress intensity factor ranges, ΔK_{th} , are given in Table A.4 for selected engineering alloys. These values are usually less than $9 \text{ MPa}\sqrt{\text{m}}$ ($8 \text{ ksi}\sqrt{\text{in.}}$) for steels and less than $4 \text{ MPa}\sqrt{\text{m}}$ ($3.5 \text{ ksi}\sqrt{\text{in.}}$) for aluminum alloys. Values of ΔK_{th} are substantially less than K_{Ic} values given in Figure 4.9 and Table A.3. In fact, ΔK_{th} can be as low as just several percent of K_{Ic} . The threshold stress intensity factor, ΔK_{th} , has often been considered analogous to the unnotched fatigue limit, S_f , since an applied stress intensity factor range below ΔK_{th} does not cause crack growth. Figure 5.23 shows the use of ΔK_{th} as a design parameter for no crack growth using a single-edge cracked infinitely wide plate subjected to $R = 0$ loading as shown. In Figure 5.23, any combination of ΔS and crack length, a , that falls below the curve [assume $\Delta K_{th} = 5.5 \text{ MPa}\sqrt{\text{m}}$ ($5 \text{ ksi}\sqrt{\text{in.}}$)] does not cause fatigue crack growth. This criterion comes from setting ΔK_I in Eq. 5.16 equal to ΔK_{th} and using the proper stress intensity factor, K_I , from Figure 4.5b. It should be noted from Figure 5.23 that for crack lengths greater than about 2.5 mm (0.1 in.), ΔS_{th} is about 55 MPa (8 ksi) or less. Thus to keep cracks from propagating, the tensile stress must be kept very small. Nonpropagating cracks are considered in more detail in later chapters.

5.5.3 Mean Stress Effects

The general influence of mean stress on fatigue crack growth behavior is shown schematically in Figure 5.24. The stress ratio $R = K_{min}/K_{max} = S_{min}/S_{max}$ is used as the principal parameter. Most mean stress effects on crack growth have been obtained with only tensile stressing, that is, $R \geq 0$. Figure 5.24 indicates that increasing the R ratio (which means increasing both S_{max} and S_{min}) has a tendency to increase the crack growth rates in all portions of the sigmoidal curve. The increase in region II, however, may be small. In region III, where fracture toughness K_c or K_{Ic} con-

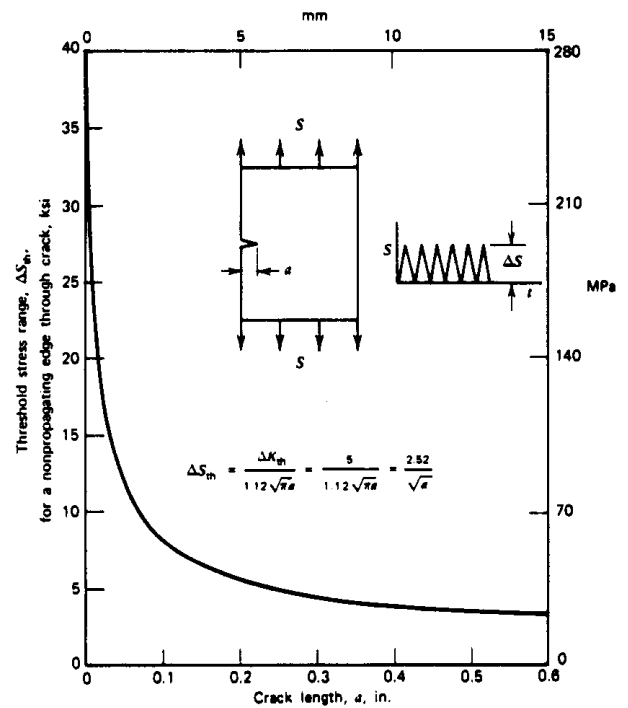


Figure 5.23. Threshold stress range for nonpropagating edge through cracks in wide plates, $R = 0$, $\Delta K_{th} = 5.5 \text{ MPa}\sqrt{\text{m}}$ ($5 \text{ ksi}\sqrt{\text{in.}}$)

trols, substantial differences in crack growth rates occur for different R ratios. The upper transition regions on the curves are shifted to lower ΔK_I values as R , and hence K_{max} , increases. The most commonly used equation depicting mean stress ef-

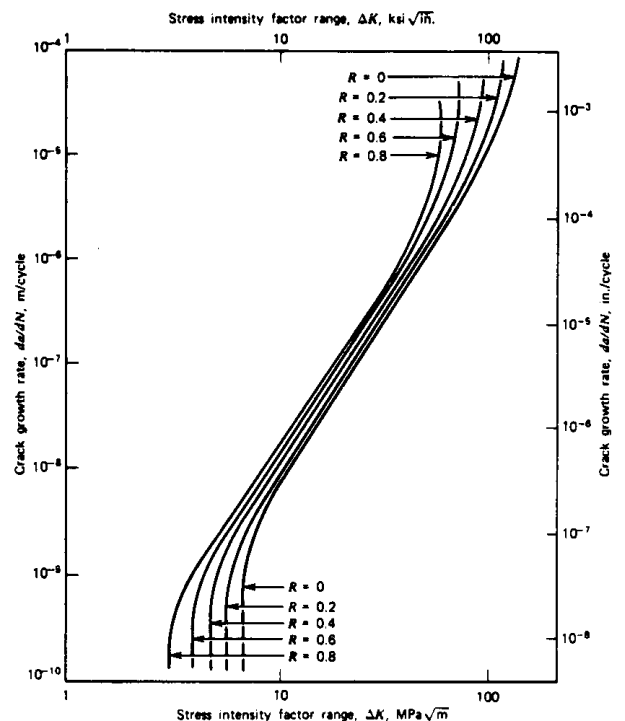


Figure 5.24. Schematic mean stress influence on fatigue crack growth rates.

fects in regions II and III is the Forman equation [32]:

$$\frac{da}{dN} = \frac{A(\Delta K)^n}{(1-R)K_c - \Delta K} \quad (5.21)$$

where A and n are empirical fatigue material constants and K_c is the applicable fracture toughness for the material and thickness. The Forman equation is a modification of the Paris equation.

The effect of mean stress on ΔK_{th} can be substantial, as is indicated in Figure 5.24 and Table A.4. ΔK_{th} for nine materials with different positive R ratios are included in Table A.4. For R increasing from zero to about 0.8, the threshold ΔK_{th} decreases by a factor of about 1.5 to 2.5. This has the effect of shifting the curve in Figure 5.23 toward the abscissa by these same factors, which reduces ΔS_{th} for a given crack length by the same factors.

The effect of negative R ratios, which includes compression in the cycle, has not been sufficiently investigated, particularly at the threshold levels. Stephens et al. [33] obtained da/dN versus ΔK for regions II and III for Man-Ten steel as shown in Figure 5.25, with R ranging from +0.5 to -2.0. The scatter band is small except for R = -2 at lower crack growth rates. Here, the R = -2 curve reversed, because of high crack growth rates immediately following precracking with R = 0. The results of many negative R ratio tests on wrought and cast steels, cast irons, and aluminum alloys subjected to constant amplitude conditions in regions II and III indicate crack growth rates on ΔK values (which neglect compressive nominal stresses) are similar to R = 0 results, or are increased by not more than a factor of 2 [33-35].

5.5.4 Crack Growth Life Integration Example

Let us assume a very wide SAE 1020 cold-rolled plate is subjected to constant amplitude uniaxial cyclic loads that produce nominal stresses varying from $S_{max} = 200$ MPa (29 ksi) to $S_{min} = -50$ MPa (-7.3 ksi). The monotonic properties for this steel are $S_y = 630$ MPa (91 ksi), $S_u = 670$ MPa (97 ksi). $E = 207$ GPa (30×10^6 psi), and $K_c = 104$ MPa \sqrt{m} (95 ksi $\sqrt{in.}$). What fatigue life would be attained if an initial through the thickness edge crack were no greater than 0.5 mm (0.02 in.) in length?

Before we can solve this problem, several questions must be answered. Namely, what is the applicable stress intensity factor expression for this component and loading? What crack growth rate

equation should be used? How do we integrate this equation? What value of ΔK will cause fracture? Does corrosion or temperature play an important part?

In solving this problem let us assume a corrosive environment is not involved and that room temperature prevails. The Paris crack growth rate equation (Eq. 5.17) is often a reasonable expression for region II, and even region III, crack growth behavior. Integration of the Paris equation involves numerical methods unless α from Eq. 5.16 is independent of crack length a. Since K_I for an infinite plate with a single edge crack has a equal to a constant of 1.12 from Table 4.1b or Figure 4.5b, it would be desirable to assume the infinite plate K_I solution. This is a very reasonable assumption as long as the crack length does not exceed about 10 percent of the width (see Figure 4.5b), Direct integration is preferable for the illustration and hence the infinite plate is assumed. K_{max} initial with $S = 200$ MPa and $a_i = 0.5$ mm is

$$1.12 S \sqrt{\pi a} = (1.12)(200 \text{ MPa}) \sqrt{\pi(0.0005)} = 9 \text{ MPa}\sqrt{m}$$

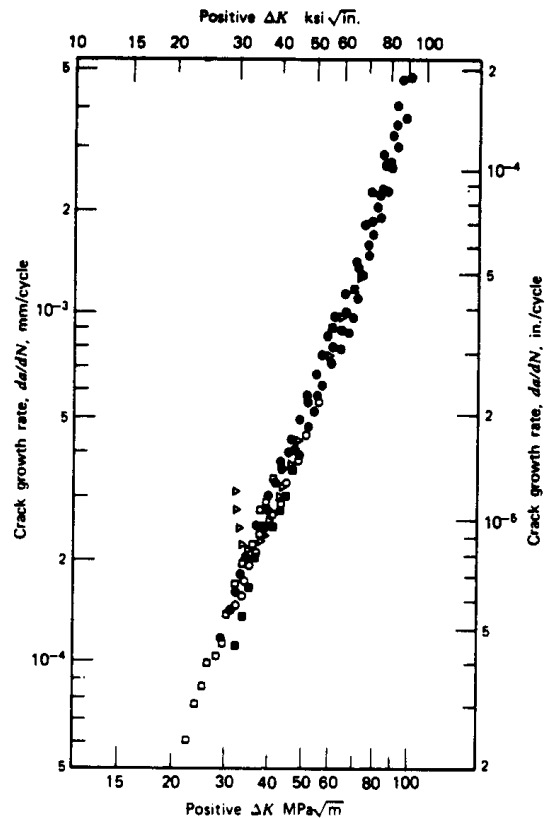


Figure 5.25. Positive stress intensity factor range versus crack growth rate with negative R ratios, Man-Ten steel [33] (reprinted by permission of the American Society for Testing and Materials.) (□) R = +0.5, (●) R = 0, (○) R = -0.5, (■) R = -1, (△) R = -2.

which is above threshold levels and hence the Paris equation is applicable. The final crack length a_f (or a_c is also commonly used) can be obtained from setting K_{max} at fracture equal to K_c .

Thus the following equations apply:

$$\Delta K = \Delta S \sqrt{\pi a} \alpha \quad (5.22a)$$

$$\frac{da}{dN} = A(\Delta K)^n = A(\Delta S \sqrt{\pi a} \alpha)^n$$

$$= A(\Delta S)^n (\pi a)^{n/2} \alpha^n \quad (5.22b)$$

$$a_f = \frac{1}{\pi} \left(\frac{K_c}{S_{max} \alpha} \right)^2 \quad (5.22c)$$

Integrating Eq. 5.22b,

$$N_f = \int_0^{N_f} dN = \int_{a_i}^{a_f} \frac{da}{A(\Delta S)^n (\pi a)^{n/2} \alpha^n} \quad (5.22d)$$

$$= \frac{1}{A(\Delta S)^n (\pi)^{n/2} \alpha^n} \int_{a_i}^{a_f} \frac{da}{a^{n/2}}$$

If $n \neq 2$

$$\int_{a_i}^{a_f} \frac{da}{a^{n/2}} = \left[\frac{a^{-(n/2)+1}}{-n/2+1} \right]_{a_i}^{a_f} = \frac{a_f^{-(n/2)+1} - a_i^{-(n/2)+1}}{-n/2+1} \quad (5.22e)$$

Therefore,

$$N_f = \frac{a_f^{-(n/2)+1} - a_i^{-(n/2)+1}}{(-n/2+1)A(\Delta S)^n (\pi)^{n/2} \alpha^n} \quad (5.22f)$$

Equation 5.22f is the general integration of the Paris equation when a_i is independent of crack length a and when n is not equal to 2. This equation is not correct if a_i is a function of a , which is the usual case.

Since specific crack growth rate data were not given for the SAE 1020 cold-rolled steel, a reasonable first approximation could use the conservative empirical equation 5.1 8 for ferritic-pearlitic steels suggested by Barsom [31]. Although this equation was developed for $R = 0$, the small compressive stress, 50 MPa, will not have much effect on crack growth and can be neglected and thus $\Delta S = 200 - 0 = 200$ MPa is very reasonable. From Eq. 5.22c

$$a_f = \frac{1}{\pi} \left(\frac{K_c}{S_{max} \alpha} \right)^2 = \frac{1}{\pi} \left(\frac{104}{200 \times 1.12} \right)^2$$

$$= 0.068 \text{ m} = 68 \text{ mm} = 2.7 \text{ in.} \quad (5.22g)$$

Substitution of the appropriate values into Eq. 5.22f results in

$$N_f = \frac{(0.068)^{-(3/2)+1} - (0.0005)^{-(3/2)+1}}{(-3/2+1)(6.9 \times 10^{-13})(200)^3 (\pi)^{3/2} (1.12)^3}$$

$$= \frac{(0.068)^{-0.5} - (0.0005)^{-0.5}}{-2.16 \times 10^{-4}} = 189,000 \text{ cycles}$$

Now let us assume the fracture toughness, K_c , was incorrect by a factor of ± 2 , that is, $K_c = 208$ MPa $\sqrt{\text{m}}$ (180 ksi $\sqrt{\text{in.}}$) or 52 MPa $\sqrt{\text{m}}$ (425 ksi $\sqrt{\text{in.}}$). The final fracture length from Eq. 5.22c would result in $a_f = 270$ mm (10.8 in.) and 17 mm (0.68 in.), respectively. The final life, N_f from Eq. 5.22f would be 198,000 and 171,000 cycles, respectively. Thus increasing or decreasing the fracture toughness by a factor of 2 caused increases or decreases in the final crack length by a factor of 4, respectively. However, changes in fatigue crack growth life were less than 10 percent, which are very small differences. If the initial crack length a_i were 2.5 mm (0.1 in.), the life would have been only 75,000 cycles instead of 189,000 cycles for the original problem with a_i equal to 0.5 mm (0.02 in.). This illustrates the importance of minimizing initial flaw or crack lengths to obtain long fatigue life and that appreciable changes in fracture toughness will alter final crack lengths but may not have appreciable effects on fatigue life. High fracture toughness in fatigue design, however, is still very desirable because of the randomness of many load histories and the larger crack lengths before fracture, which permits much better inspection success.

Appendix C References

28. P.C. Paris and F. Erdogan, "A Critical Analysis of Crack Propagation Laws", Trans. ASME, J. Basic Eng., Vol. 85, No. 4, 1963, p. 528.
29. D.W. Hoepfner and W.E. Krupp, "Prediction of Component Life by Application of Fatigue Crack Growth Knowledge", Eng. Fract. Mech., Vol. 6, 1974, p. 47.
30. Damage Tolerant Design Handbook, Metals and Ceramics Information Center, Battelle Labs, Columbus, OH, 1975.
31. J.M. Barsom, "Fatigue-Crack Propagation in Steels of Various Yield Strengths", Trans. ASME, J. Eng. Ind., Ser. B, No. 4, Nov. 1971, p. 1190.
32. R.G. Forman, V.E. Kearney, and R.M. Engle, "Numerical Analysis of Crack Propagation in Cyclic-Loaded Structures", Trans. ASME, J. Basic Eng., Vol. 89, No. 3, 1967, p. 459.
33. R.I. Stephens, E.C. Sheets, and G.O. Njus, "Fatigue Crack Growth and Life Predictions in Man-Ten Steel Subjected to Single and Intermittent Tensile Overloads", Cyclic Stress-Strain and Plastic Deformation Aspects of fatigue Crack Growth, ASTM STP 637, 1977, p. 176.
34. R.I. Stephens, "Fatigue Crack Growth Retardation: Fact and Fiction", Proceed. 9th ICAF Symp. Darmstadt, Ger., 1977, p. 5.5/1.
35. R.I. Stephens, P.H. Benner, G. Mauritzson, and G.W. Tindall, "Constant and Variable Amplitude Fatigue Behavior of Eight Steels", J. Test. Eval., Vol. 7, No. 2, March 1979, p. 68.

Low Temperature Fatigue Behavior of Steels - A Review

Fatigue behavior at low temperatures has received much less attention than that at room temperature and elevated temperatures. This is apparently due to the beneficial effects from low temperature unnotched and notched constant amplitude fatigue behavior found from S-N curves. Textbooks on fatigue of metals published between 1959 and 1974 usually have just several pages or less devoted to low temperature fatigue (1-8).^{*} Excerpts such as the following taken from fatigue textbooks based upon constant amplitude fatigue tests tend to imply that fatigue is not a problem at low temperatures. Forrest (1) states

Almost without exception fatigue strengths of both plain and notched pieces are increased by reduction of temperature. It is probably because of this that there are relatively few fatigue data at low temperatures, for it is possible to design for air temperature conditions and feel confident that fatigue failures will not result from operation at lower temperatures.

Mann (2) states

The fatigue strengths of most metallic materials increase as the temperature is reduced below normal . . . It appears the rate of increase in notched fatigue properties of plain carbon steels with decreasing temperature may be less than that of the unnotched properties . . . Inasmuch as the actual fatigue strengths of most materials at low temperatures do not appear to be less than those at room temperature, reduced temperatures should not introduce any additional general problems from the fatigue viewpoint.

Dolan and Sines and Waisman (3) states

Fortunately, . . . all metals show improved fatigue properties at low temperatures, . . . no correlation exists between the notched-bar impact tests for a given metal and its notch

sensitivity in fatigue; the fatigue strength of notched specimens is improved by lowering the temperature.

Osgood (4) states,

For notched specimens the proportionate increase in fatigue strength is lower than for the unnotched because the notch sensitivity of all alloys generally rises with decreasing temperature.

Frost, Marsh and Pook (5) state,

. . . the fatigue strength of a material increases as the temperature decreases, for example, the ratio of the fatigue limit at liquid air temperature to that at room temperature is in the range 1.5-2.5 for most metallic alloys (1), softer materials generally giving higher values of this ratio than harder materials. Thus, a design based on room-temperature fatigue data will be safe for use at lower temperatures, although, of course, any increased susceptibility to brittle fracture under the applied loadings must be taken into account.

Grove (6) states

In general, the ratio of fatigue limit (under fully-reversed stressing) to the tensile ultimate will also be as high or higher than at room temperature. While there are some data on fatigue-notch sensitivity at low temperatures, these are rather inadequate to provide confidence in design.

The present knowledge about fatigue behavior at low temperatures can be summarized as follows. Enough surveys have been made to indicate the general presence of fatigue phenomena at temperatures down as low as -423 °F. Studies have shown no particularly alarming trends. However, in anticipation of more concern with this environ-

ment in the near future, much more study will be needed.

Munse and Grover (7) state,

However, since many structural steels become susceptible to brittle fracture at low temperatures the possibility should not be overlooked of a brittle fracture starting from a small fatigue crack which might otherwise require a much longer time for propagation.

Yen in Madayag (8) states,

From a macroscopic point of view it should be noted that higher temperatures often hasten crack initiation but may sometimes retard crack propagation and increase critical crack length. Lower temperatures, on the contrary, often retard crack initiation, hasten crack propagation, and reduce critical crack length.

The last three excerpts seem to imply that there should be concern about fatigue failures at low temperatures. This is especially true since all the above ideas on low temperature fatigue were primarily based upon constant amplitude S-N tests. No influence of strain-life low cycle fatigue results, fatigue crack propagation rates, interaction influences from real-life variable amplitude loading and residual stress were apparently considered. The implication that low temperature fatigue behavior is at least no worse than room temperature fatigue behavior motivated the authors of this paper to make a comprehensive literature review of low temperature fatigue behavior. Hopefully this would provide S-N, strain-life low cycle fatigue, and crack propagation data under both constant and variable amplitude loading which would either substantiate or refute the general implication of low temperature fatigue. Unfortunately no variable amplitude low temperature fatigue data were found, although we are sure some exists. Thus interaction influences at low temperature can only be hypothesized by the authors. Very little strain-life low cycle fatigue data were found. Most of the research prior to the 1970's involved S-N diagrams, while most of the research in the 1970's involved fatigue crack growth rates, da/dN versus stress intensity range, ΔK , for crack growth rates primarily higher than 2.5×10^{-8} m/cycle (10^{-6} in./cycle).

Monotonic Behavior at Low Temperature

In general, the unnotched ultimate tensile strength

and yield strength increase at lower temperatures with the ratio of the ultimate strength to the yield strength approaching a value of one at lower temperatures. The ductility as measured by the percent elongation or reduction in area at fracture usually decreases with lower temperatures while the modulus of elasticity usually has a small increase. The total strain energy or toughness at fracture decreases at lower temperatures as measured by the area under the stress-strain curve. Under notched conditions, toughness and ductility decrease even further. This is true for both low and high strain rates. Impact energy as measured from the Charpy impact (CVN), pre-cracked Charpy (K_{I_d}) or dynamic tear (DT) test can show substantial decreases as shown schematically in Figure 1 for low, medium and high strength steels. An upper and lower shelf and transition region usually exists for the low and medium strength steels. Higher strength steels have a more continuous low energy curve as shown. Both plane stress fracture toughness, K_{Ic} , and plane strain fracture toughness, K_{IIc} , along with JIc often decrease with lower temperatures similar to the impact energy properties. Substantiated research has attempted to correlate K_{Ic} with CVN or DT data (9,10). The nil-ductility temperature, DNT, as measured from the drop weight test using a brittle weld-bead with a machined notch has varied from above room temperature to almost absolute zero temperature for steels. Thus it is quite well known that impact energy absorbing capabilities of notched or cracked components can be drastically reduced at lower temperatures depending upon microstructure. This implies greater notch and

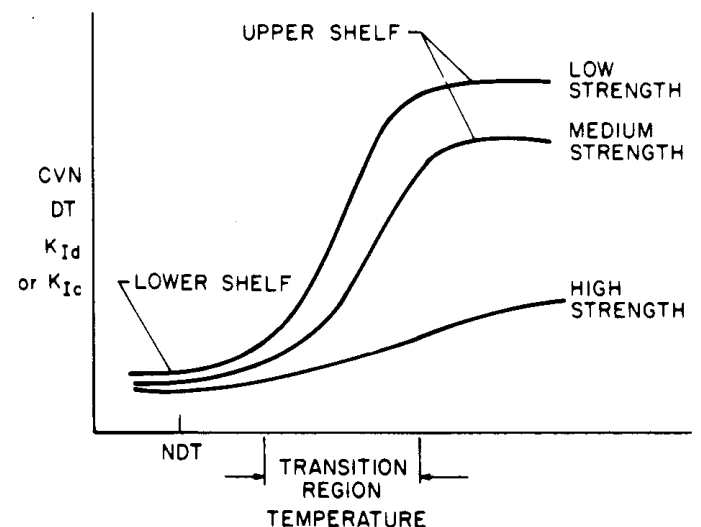


Figure 1. Schematic CVN, DT, K_{Ic} and K_{I_d} properties for steels as a function of temperature.

crack sensitivity exists at lower temperatures. Final fatigue crack lengths at fracture can then be drastically reduced at lower temperatures. The lower fracture toughness, lower ductility and higher unnotched tensile strength do not, however, provide sufficient information as to the mechanisms of how cracks will initiate and propagate in components under variable amplitude real-life load histories at low temperatures.

SN Fatigue Behavior

Comprehensive summaries of S-N fatigue behavior at low temperature have been made by Teed (1) in 1950 and by Forrest (1) in 1962. A tabular summary by Forrest for carbon steels, alloy steels and cast steels is shown in Figure 2. Here the average of long-life fully-reversed fatigue strengths at low temperature divided by the fully-reversed fatigue strengths at room temperature are shown for unnotched and notched specimens. No effort was made to correlate strength levels nor stress concentration factors. The goal was to provide a general trend for long-life fatigue strengths at low temperatures compared to room temperature. The number of materials is given at the bottom of each column. The carbon steels have lower tensile strengths than the alloy steels while showing better

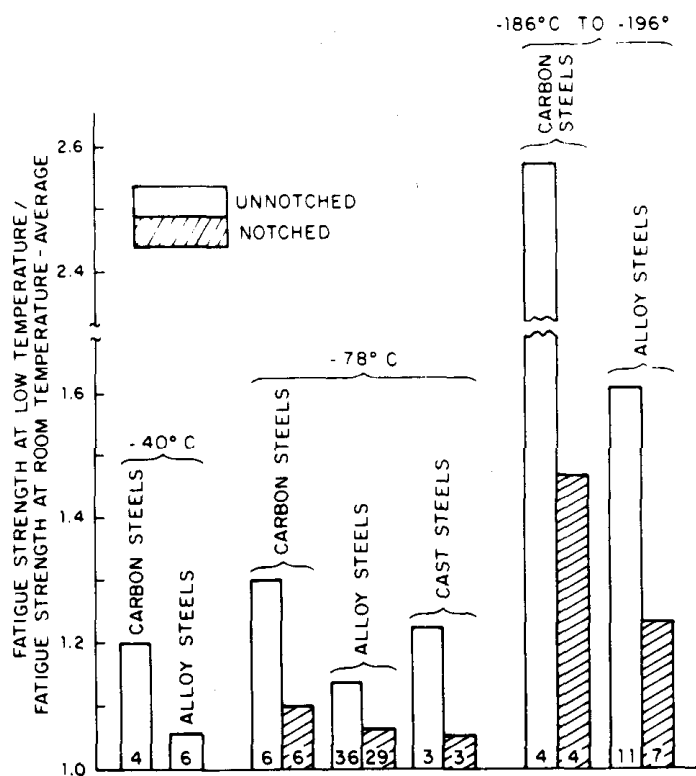


Figure 2. Comparison of average fatigue strengths at low temperatures and room temperature for unnotched and notched steels (1).

low temperature properties for both unnotched and notched specimens compared to the higher strength alloy steels. The cast steel data is more limited, but shows beneficial effects. From a design engineering standpoint, the most important aspect of Figure 2 is the substantially smaller increases in fatigue strength in the notched specimens. The average values at -78°C showed only 5 to 10% increases over room temperature. At -186°C to -196°C the average increases were 22 to 47 percent. It seems that these smaller notched increases are overshadowed by the larger unnotched increases yet it is the notched component that is of greater concern in engineering design.

Figure 2 does not give an indication of the complete S-N behavior for steels at low temperature relative to room temperature. Excerpts of typical S-N diagrams taken from three papers (12-14) of many reviewed are shown in Figures 3-7. Only steels with both unnotched and notched data are included. Materials include yield strengths from 420 MPa (60 ksi) to 1580 MPa (230 ksi). In all cases except Figure 6 the S-N curves for unnotched specimens are higher at low temperatures than for room temperature. This indicates that unnotched fatigue strengths at shorter lives are also generally better at lower temperature. This was a general trend in most unnotched S-N data analyzed with cycles to failure greater than about 10^3 . No specific data trends existed for less than 10^3 cycles.

Figures 3-5 obtained by Spretnak, Fontana and Brooks (12) had $K_t = 2.5$ for the notched reversed bending tests. These are high strength steels and it is seen that mixed results occur with the notched specimens. In Figure 3, 4340 steel with $\sigma_u = 1585$

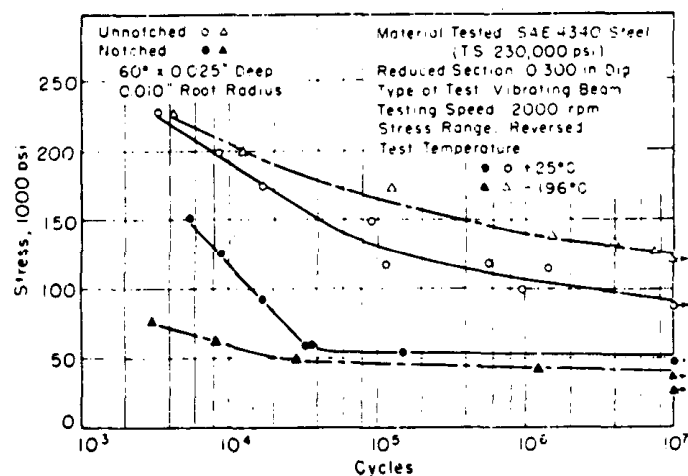


Figure 3. S-N behavior of 4340 steel at 25°C and -196°C (12).

MPa (230 ksi) has low temperature (-196°C) notched S-N behavior slightly poorer than at room temperature. In Figures 4 and 5 for 18-8 stainless with $\sigma_u = 1450$ MPa (210 ksi) and 8630 steel with $\sigma_u = 1030$ MPa (150 ksi) the notched S-N curves intersect such that slight improvements occur at long-life for low temperature (-196 °C) while at short lives the cold temperature is detrimental. Figure 6, obtained by Nachtigall (13) with very sharp notches ($k_t \approx 18$) under axial loading, shows similar notched S-N behavior at room temperature (294 K) and 77 K, however, at 4 K the short life notched S-N curve is inferior. Figures 3-6 indicate that short life notched S-N fatigue behavior can be detrimental at low temperatures for these high strength steels.

Figure 7, obtained by Troshchenko et al. (14) shows smooth and notched S-N data for 420 MPa (60 ksi) yield strength steel four temperatures. Lives vary

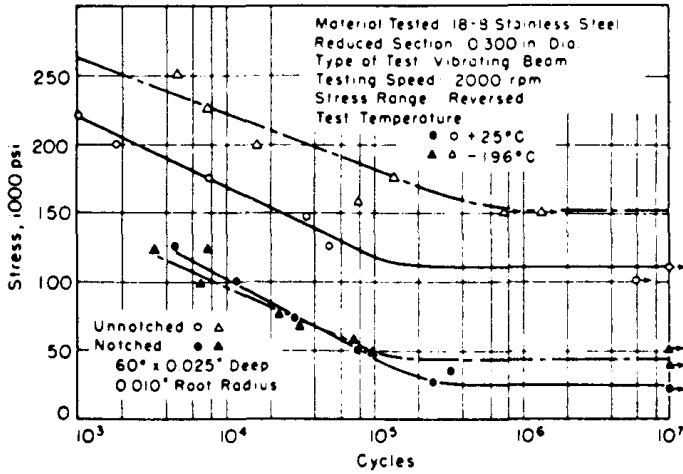


Figure 4. S-N behavior of 18-8 stainless steel at 25°C and -196°C (12).

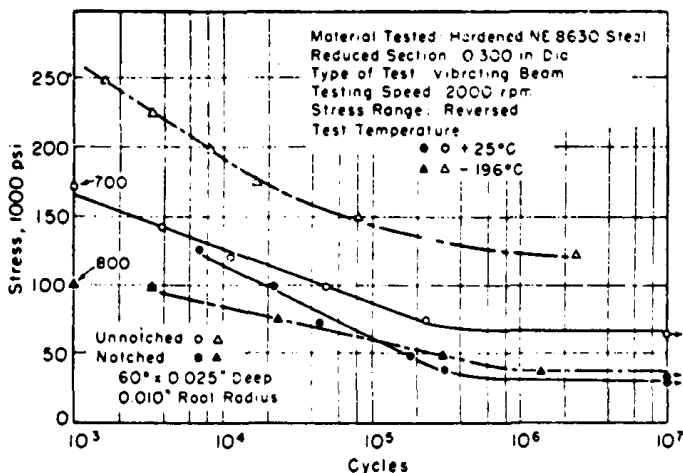


Figure 5. S-N behavior of 8630 steel at 25°C and -196°C (12).

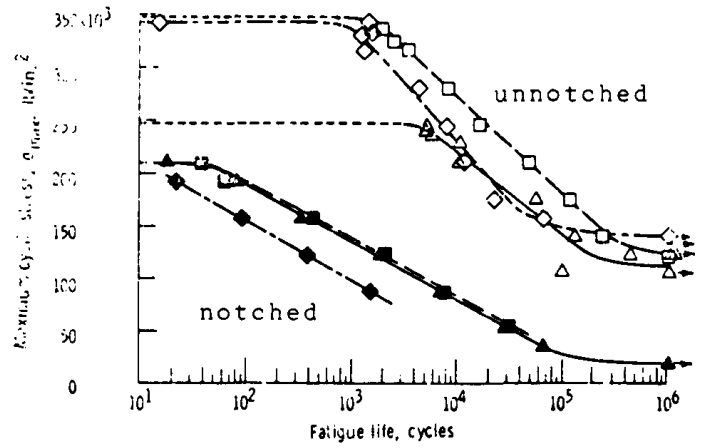


Figure 6. S-N behavior of 301 stainless steel at 294 K, 77 K and 4 K (13).

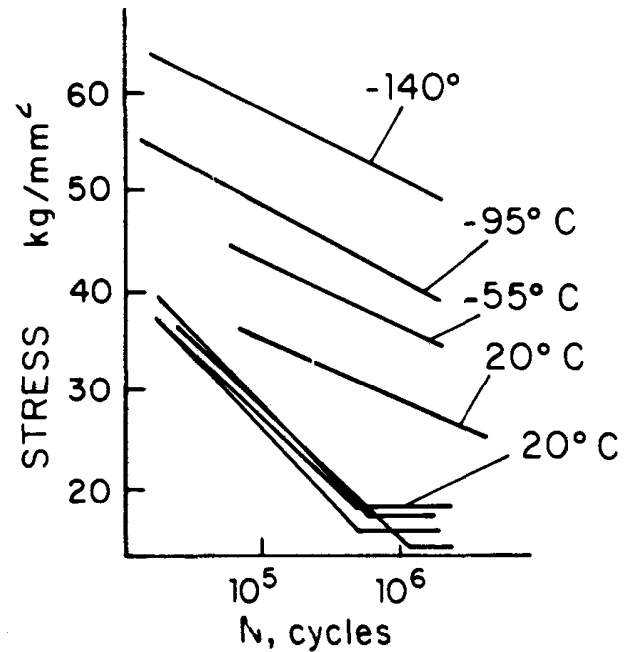


Figure 7. S-N behavior 15G2AFDps steel [$S_y = 420$ MPa (60 ksi)] -55°C, -95°C and -140°C (14).

from 2×10^4 to 2×10^6 cycles. It is evident that all unnotched fatigue strengths increase substantially as the temperature is lowered. At 2×10^6 cycles, the fatigue strengths differed by 250 MPa (36 ksi) or a factor of two. Notched data are for two types of notched specimens. One with a deep circular groove and another with a shallow circular scratch. Both notched specimens had $K_t \approx 3$. With the notches and the four temperatures, fatigue strengths at 2×10^6 cycles differed by about 40 MPa (6 ksi) or 25 percent. At 2×10^4 cycles the notched fatigue strengths also different by about 40 MPa (6 ksi) or 15 percent. The notched curves overlap and intersect which may be due to the limited test points

obtained. At 2×10^6 cycles the low temperature notched fatigue strengths were poorer than those at room temperature. At 2×10^4 cycles mixed results occurred with very little differences.

Kudryavtsev et al. (15) showed that notched fatigue lives ($N \approx 7 \times 10^3$ cycles) at room temperature for two structural steels were similar under a given pulsating bending load. However at lower temperatures fatigue life decreased substantially for one steel and decreased and then increased for the other steel as shown in Figure 8. Fatigue crack lengths at fracture decreased with temperature for both steels. Thus differences in life were due primarily to changes in crack initiation and crack growth rates at the different temperatures.

A summary of the S-N behavior found for steels indicates unnotched fatigue strengths at lives greater than say 10^4 cycles are better at lower temperatures. The larger increases occurred in the lower strength steels and larger increases also occurred at the lower temperatures. Notched fatigue strengths at long lives of say 10^6 cycles or more, however, are usually slightly better or similar to values at lower temperatures. Some small detrimental effects, however, were also found. The abrupt Charpy, DT or K_{Ic} transition temperatures found in monotonic tests apparently do not have similar effects on the long-life unnotched or notched fatigue strengths. At short lives, greater mixed results were found and low temperatures can be noticeably beneficial, detrimental or have little influence.

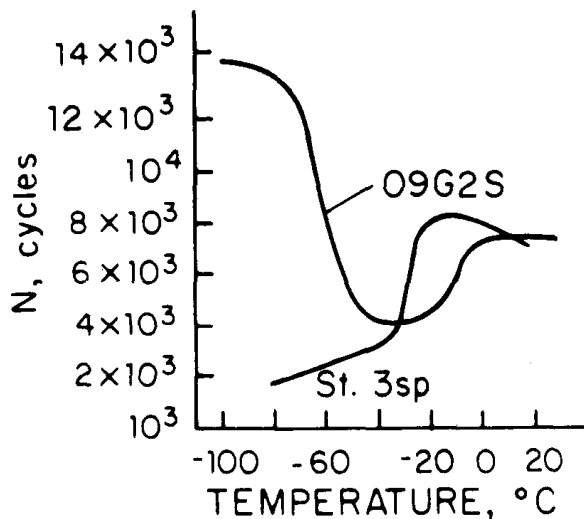


Figure 8. Notched fatigue life of two structural steels at low temperatures (15).

Low Cycle Fatigue ϵ -N Behavior

Very little low cycle, ϵ -N, fatigue behavior was found for steels at low temperature. Nachtigall (16) determined low cycle fatigue behavior of ten different materials using unnotched specimens at room temperature (300 K) and two cryogenic temperatures of 78 K (liquid nitrogen) and 4 K (liquid helium). He determined fatigue lives from about 50 cycles to 2×10^5 cycles for most of the ten materials. Three of these materials were steels, namely 18-Ni maraging, 304 L stainless, and 310 stainless. In all ten cases, at high-cyclic fatigue lives, where the elastic strain range component is dominant, the fatigue resistance increased at the cryogenic temperatures. Conversely, at low-cyclic lives, where the plastic strain range component is dominant, the fatigue resistance generally decreased with decreasing temperature. Only one nickel base alloy, Inconel 718, showed increased fatigue resistance over the entire life range at the cryogenic temperatures.

The strain-life curves for the three steels from Nachtigall are shown in Figure 9(a). Here it is seen that for a given material at the three different

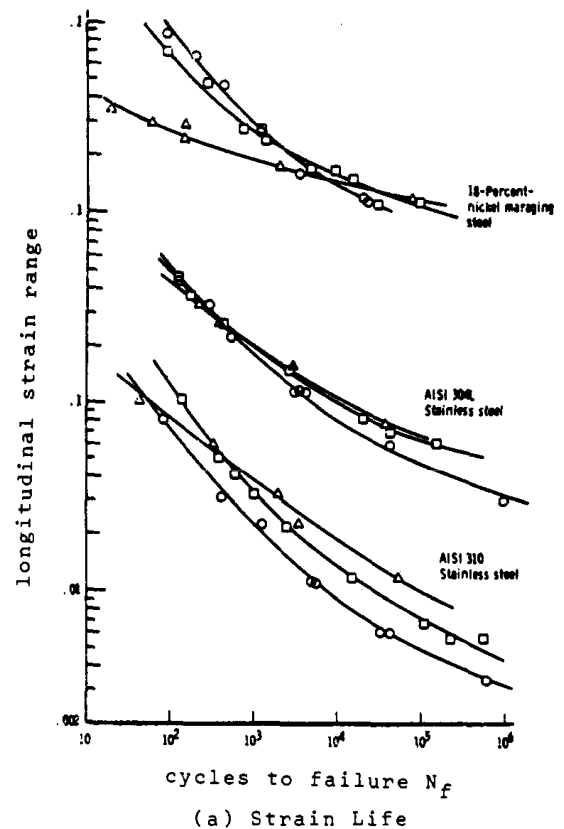
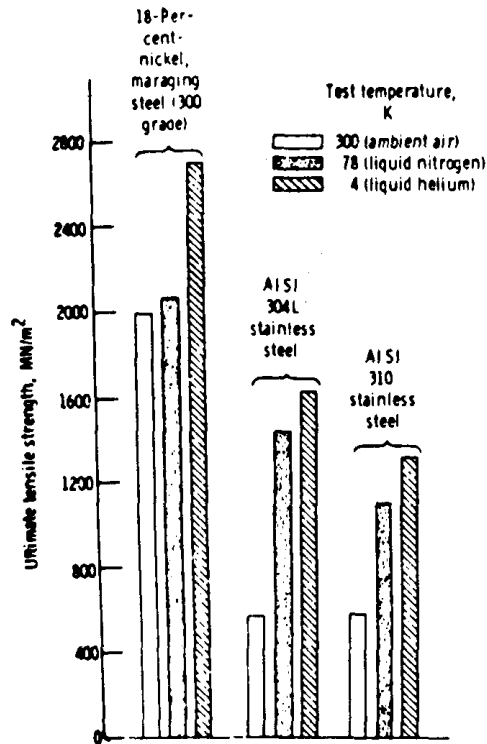


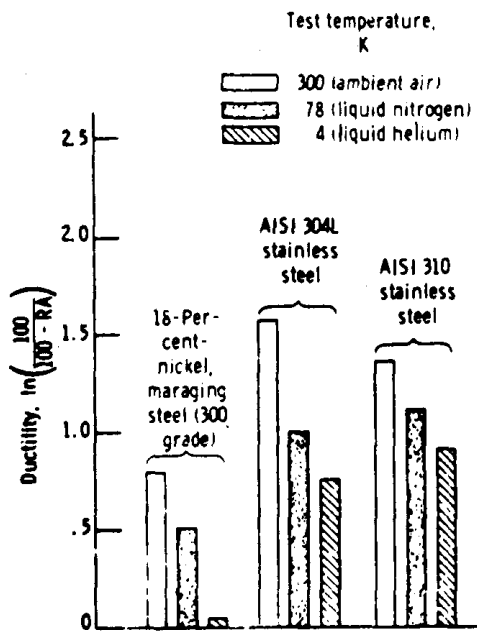
Figure 9. Effect of cryogenic temperatures on low cycle fatigue, ultimate tensile strength and ductility of three steels (16).

temperatures, the strain-life curves either intersect or converge at short lives. Very little difference exists in 304 L stainless steel at short lives while a substantial decrease in fatigue resistance for the maraging

steels exists in short lives. Figures 9(b) and 9(c) show the ultimate strength and ductility (true fracture strain) for the three steels at the three temperatures. In all cases the ultimate strength increased at lower temperatures and the ductility increased. It should be noted that a drastic reduction in ductility exists in the maraging steel at 4 K. This great loss in ductility explains the substantial decrease in fatigue resistance at short lives where the plastic strain range is predominant.



(b) ultimate strength



(c) ductility

Nachtigall used the Manson method of universal slopes to predict the strain-cycling fatigue behavior of the ten materials at cryogenic temperatures with a degree of accuracy similar to that obtained for room temperature results. He concluded that low cycle fatigue behavior of these materials can be predicted for cryogenic temperatures by using material tensile properties obtained at the same temperatures.

Polak and Klesnil (17) obtained similar intersections of strain-life curves with mild steel for 295 K, 213 K and 148 K. Their data were obtained between about 200 cycles and 10^5 cycles to failure. They contributed the deleterious effect of low temperature on low-life fatigue resistance to very short fatigue cracks and brittle fracture. They found that the plastic range-life curves (Manson-Coffin curves) for the three temperatures were about the same and that the differences in life could be attributed to the different elastic strain range-life curves. These latter curves tended to converge at low life and showed increases in elastic strain range at long lives with decreasing temperature. Kikukawa (18) showed that the Manson-Coffin plastic strain range-life curves between about 5 and 10^3 cycles tend to be lower at lower temperatures thus indicating a detrimental effect at low temperatures. They showed this for both a low and medium strength steel.

A summary of the unnotched strain-life low cycle fatigue behavior indicates that long-life fatigue resistance is increased at lower temperatures while the short-life fatigue resistance may be decreased due to low ductility and low fracture toughness. At short lives, ductility is a principal parameter in strain-control behavior while at longer lives strength is more of a controlling factor.

Fatigue Crack Growth Behavior

Fatigue crack growth rates, da/dN , are usually analyzed using linear elastic fracture mechanics

Figure 9 (continued). Effect of cryogenic temperatures on low cycle fatigue, ultimate tensile strength and ductility of three steels (16).

and the stress intensity range ΔK where

$$\Delta K = K_{\max} - K_{\min} \quad (1)$$

$$= \sigma_{\max} \sqrt{\pi a} - \sigma_{\min} \sqrt{\pi a} \quad (2)$$

K is the stress intensity, σ is the nominal stress, a is the crack length and α is a non-dimensional function dependent upon specimen or component geometry, loading and type of crack. A complete schematic representation of da/dN versus ΔK for a given stress ratio, R , is shown in Figure 10. The complete curve is sigmoidal in shape and involves crack growth rates from about 10^{-10} m/cycle (4×10^{-9} in./cycle) to 10^{-3} m/cycle (4×10^{-2} in./cycle). Regions I, II and III are indicated in Figure 10.

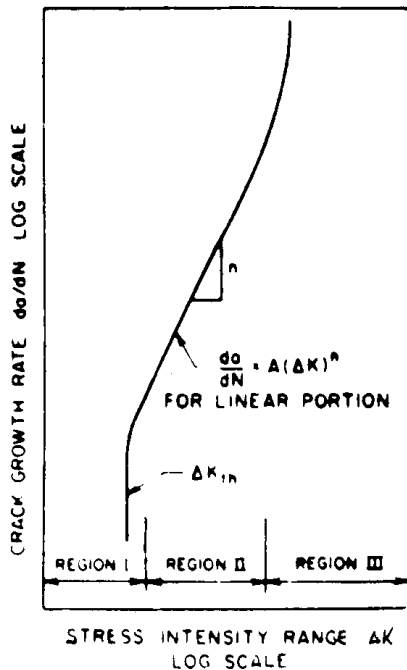


Figure 10. Schematic sigmoidal representation of fatigue crack growth behavior.

In order to make a complete analysis of fatigue crack growth behavior under constant amplitude conditions, the complete sigmoidal curve with the three regions must be considered. However, most low temperature and even room temperature fatigue crack growth data have been obtained in regions II and III with crack growth rates greater than 10^{-8} m/cycle (4×10^{-7} in./cycle). Any conclusions related to fatigue crack growth rate are only valid for the specific range of investigation. Extrapolation of curves to the threshold region I is not correct. However, it is the lower part of region II and also region I that accounts for most of the

fatigue crack growth life in many components and structures. Thus a complete picture of fatigue crack growth behavior at low temperatures has not been sufficiently determined.

Original data obtained from fatigue crack growth tests are usually in the form of crack length versus applied cycles N . Figures 11 and 12 show such data for various temperatures (19,20). Kawasaki (19) used compact specimens made of low-alloy steel with a yield strength of 755 MPa (110 ksi) under constant amplitude load conditions with $R = 0.08$. All specimens were tested under the same load conditions while temperature was varied from 20°C to -180°C . It is seen from Figure 11 that

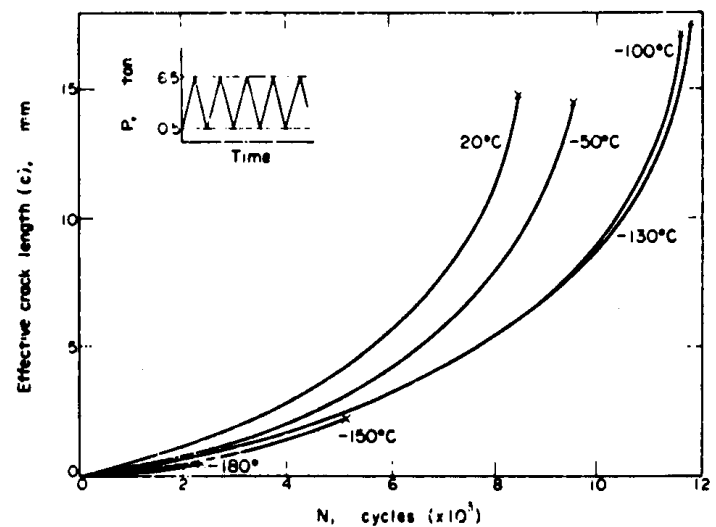


Figure 11. Effect of temperature on fatigue crack growth behavior (19).

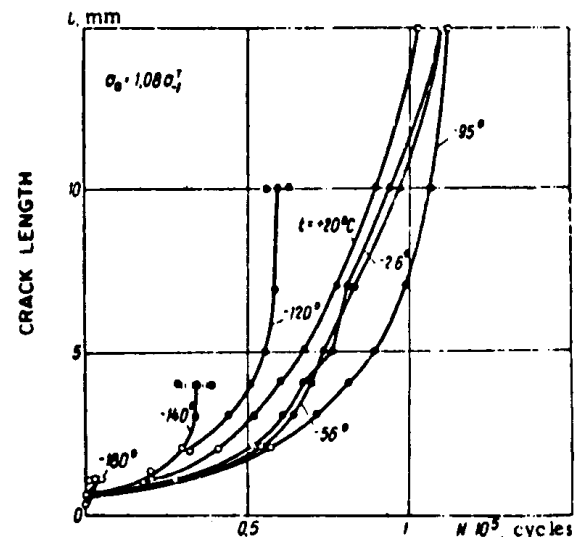


Figure 12. Effect of temperature on fatigue crack growth behavior (20).

fatigue crack growth rates (slope) decreased as the temperature decreased. The life to fracture increased for lower temperatures down to -130°C , however, below -130°C both life and crack length at fracture decreased substantially. It should be noted that these data cover a short range of fatigue crack growth rates between 5×10^{-7} m/cycle and 10^{-5} m/cycle which is principally region II and III of the sigmoidal curve of Figure 10.

Slightly different results were obtained by Troshchenko et al. (20-22) in low-alloy steel with a tensile yield strength of 420 MPa (60 ksi) as shown in Figure 12. They used round specimens under rotating bending conditions ($R = -1$) subjected to the same alternating stress with temperatures ranging from 20°C to -180°C . The crack lengths were measured on the surface of the specimens giving a peripheral crack length. It is seen in Figure 12 that fatigue crack growth rates decreased with lower temperatures until -95°C . Below this temperature the crack growth rate increased with a simultaneous reduction in crack length at fracture and fatigue life. The -95°C temperature was found to be a transition temperature from ductile to brittle fracture obtained from fracture toughness tests (21). Fatigue crack growth rates in Figure 12 ranged from about 10^{-8} m/cycle to 10^{-5} m/cycle which represents primarily region II and III of the sigmoidal curve. Figures 11 and 12 indicate that low temperatures can be beneficial or detrimental to region II and III fatigue crack growth rates and total fatigue crack growth life.

The complete sigmoidal da/dN versus ΔK curves at 20°C and -160°C were obtained by Yarema et al. (23,24) using a low carbon steel with $\sigma_Y = 300$ MPa (43 ksi) and an alloy steel with $\sigma_Y = 890$ MPa (130 ksi). The specimens were flat circular disks with a central crack as shown in Figure 13. All tests were performed under constant amplitude loading with $R = 0$. The results for the low carbon steel are shown in Figure 13. Similar behavior existed for the alloy steel. Figure 13 shows that the effect of low temperature depends upon the crack growth rates or stress intensity range investigated. At lower crack growth rates (region I and the lower part of region II), the low temperature was quite beneficial with approximately a 100 percent increase in the threshold stress intensity range, ΔK_{th} . However at higher crack growth rates the low temperature was detrimental. Similar fatigue crack growth behavior was found by Broek and Rice (25) for regions II and III using 1080 rail steel with $\sigma_Y = 550$ MPa (80 ksi) at room temperature and -40°C . Their results were

obtained from compact specimens with R equal to zero and 0.5 and are shown in Figure 14. Similar trends existed for the two R ratios.

Gerberich and Moody (26) reviewed substantial fatigue crack growth behavior for a variety of

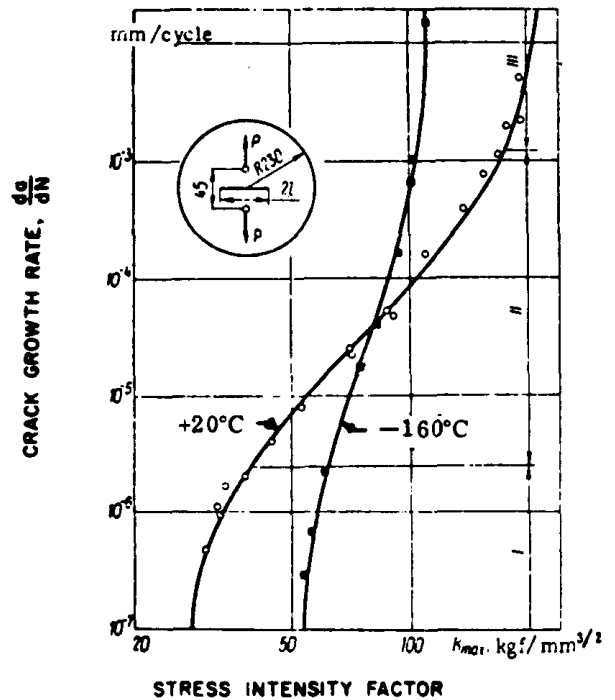


Figure 13. Fatigue crack growth rate versus ΔK in low carbon steel at 20°C and -160°C (23).

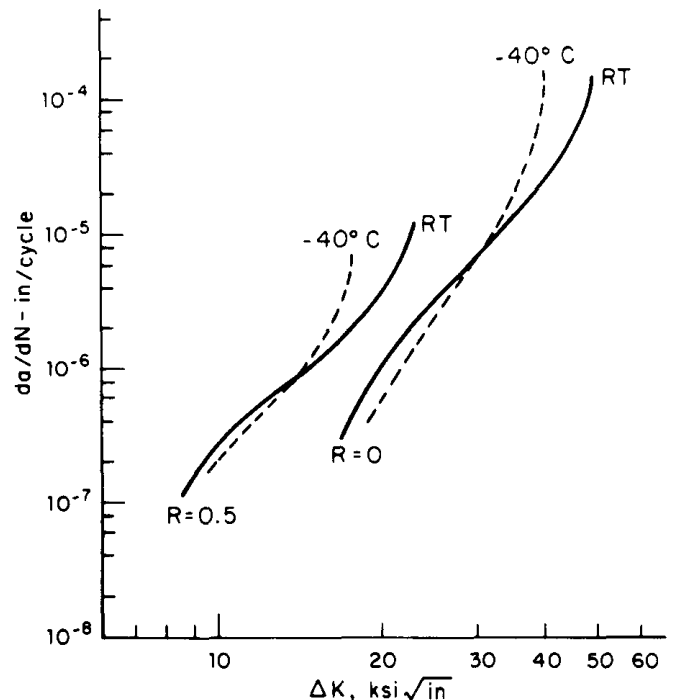


Figure 14. Fatigue crack growth rate versus ΔK in 1080 railroad rail steel at room temperature and -40°C (25).

materials. They indicated many alternate fatigue crack growth fracture processes existed in metals at various low temperatures and they emphasized the importance of microstructure on fatigue behavior. They showed that region II fatigue crack growth rates could be substantially altered at different low temperatures. For example, Figure 15 shows constant amplitude results for a Fe-2.4% Si with $\sigma_Y = 200$ MPa (29 ksi) at four different temperatures using compact specimens. When the temperature was decreased from 296 K (room temperature) to 233 K substantial decreases in da/dN occurred. As the temperature was further decreased to 173 K and then to 123 K the crack growth rates increased for a given stress intensity range with some higher crack growth data becoming inferior to room temperature data. Thus a reversal in region II fatigue crack growth behavior occurred at about 233 K. Similar behavior is shown in Figure 16 for Fe-2.5% Ni with $\sigma_Y = 160$ MPa (23 ksi) where all low temperature crack growth rates are lower than room temperature rates, but a reversal in trends occurred at about 173 K for this alloy. After the reversal, the slope of the $da/dN - \Delta K$

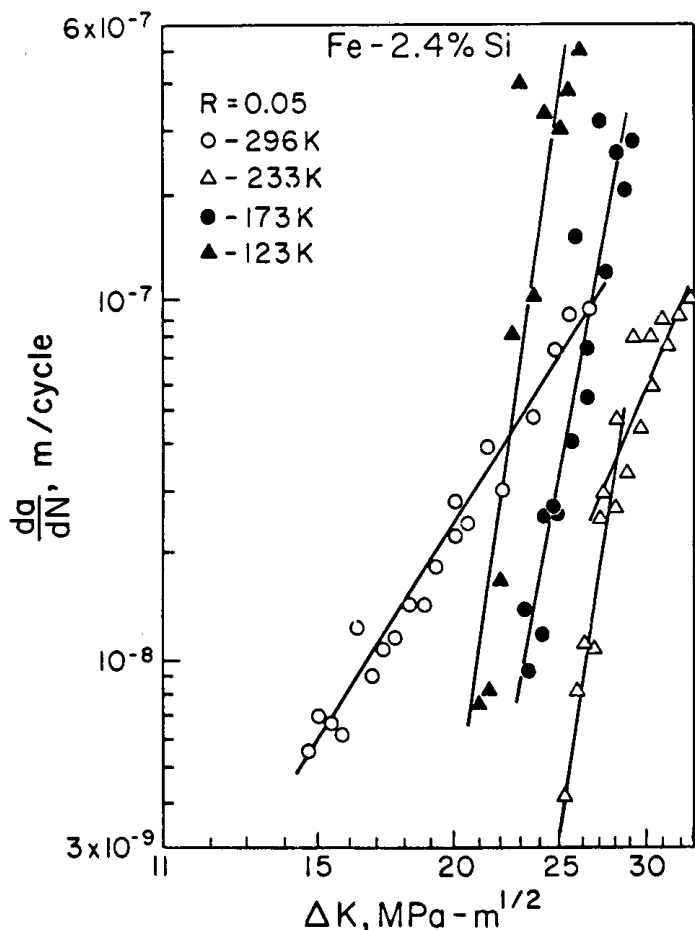


Figure 15. Fatigue crack growth rate versus ΔK in Fe-2.4% Si at room and low temperatures (26).

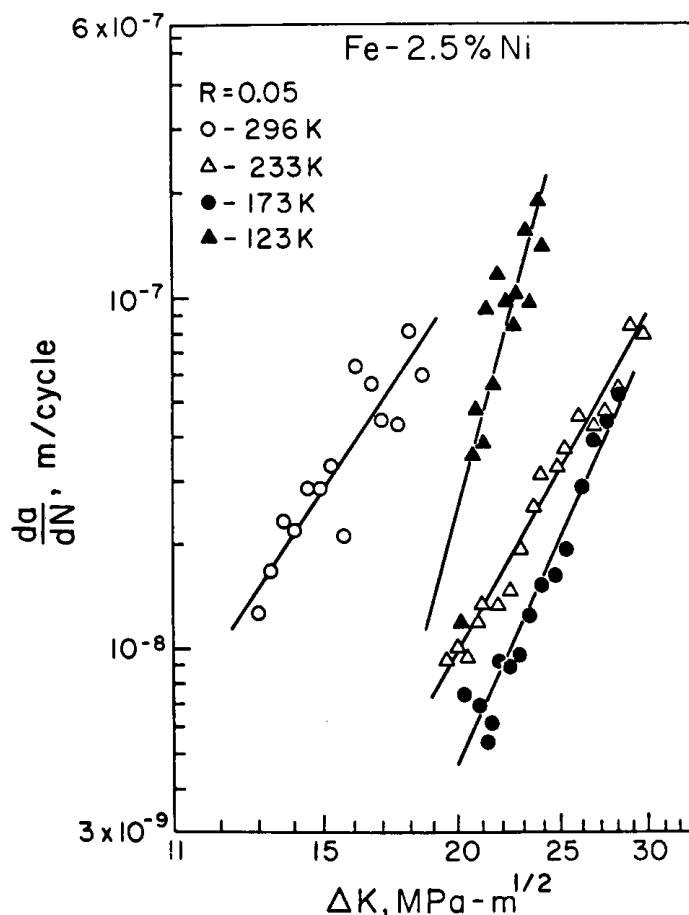


Figure 16. Fatigue crack growth rate versus ΔK in Fe-2.5% Ni at room and low temperatures (26).

curves increased. Electron fractographs revealed that cyclic cleavage became the predominant mode of fatigue crack growth at temperatures below where the reversal in behavior occurred. Thus a ductile-brittle fatigue transition temperature (FTT) exists for these steels. Gerberich and Moody showed that region II slopes could increase sharply for many steels at low temperatures except for some of the Fe-Ni steels. These steels show a very low impact ductile-brittle transition temperature and high fracture toughness at these low temperatures. Thus, they suggest a parallel exists between a ductile-brittle fatigue transition temperature with the monotonic ductile-brittle transition temperatures. Comparing the Fe-2.4% Si steel with the Fe-2.5% Ni the fatigue ductile-brittle transition temperature was lower for the Fe-2.5% Ni steel which was in agreement with lower NDT and CVN transition temperature.

The Cryogenics Division, National Bureau of Standards, Boulder, Colorado has obtained region II and III fatigue crack growth rate data for many cryogenic materials at temperatures between 294

K and 4 K (27,28). Tests were performed on compact specimens with constant load amplitude and $R = 0.1$. Ferritic-pearlitic steels exhibited behavior similar to that reported by Gerberich and Moody. That is, constant amplitude fatigue crack growth rates are usually reduced at lower temperatures until a fatigue transition temperature is reached at which drastic increases in crack growth rates can begin. Some of these rates can exceed room temperature values. Tobler and Reed (27) showed that Fe-Ni alloys provided similar or lower crack growth rate properties as long as the temperature remained in the "upper shelf" range which was defined as the region where dimpled rupture or fibrous fractures occur during static fracture toughness tests. These steels exhibited abrupt transitions to low fracture toughness involving cleavage at temperatures primarily determined by the nickel content. Cleavage cracking also led to drastic acceleration of fatigue crack growth rates at temperatures below the transition region.

Tobler and Reed (27) found that stable austenitic alloy steels exhibited improved region II and III constant amplitude fatigue crack growth resistance at cryogenic temperatures as compared to room temperature behavior.

Metastable austenitic steels can undergo a significant martensitic phase transformation during fatigue tests at cryogenic temperatures. Tobler and Reed found evidence of martensite in the crack-tip plastic zones and assumed that transformations preceded the crack growth and that the cracks propagated through partially transformed austenite at cryogenic temperatures. They felt it was difficult to generalize on the trends for metastable austenitic alloys since beneficial, detrimental and temperature-insensitivity were found depending upon alloy composition. Most data, however, showed cryogenic temperatures were not detrimental to fatigue crack growth rates in these alloys.

Stonesifer (29) attempted to obtain region II and III fatigue crack growth rates in quenched and tempered A533 B steel at room temperature and 77 K as a function of grain size using compact specimens with $R = 0.1$. Both room temperature and 77 K CVN data were at the lower shelf energy. Thus any effects would be independent of the normal impact transition temperature range. The room temperature region II fatigue crack growth data were essentially the same for ASTM grain sizes 8.5, 4 and 00. In region III, however, the coarser grain sizes had higher rates with lower ΔK values as frac-

ture was approached. This was attributed to the lower room temperature fracture toughness of the coarser grained steel. The testing methods used at room temperature were unsuccessful at 77 K. A specimen pre-cracked at room temperature and then tested at 77 K would withstand many thousand load cycles and then fracture without any apparent subcritical crack growth. At a slightly higher ΔK the specimen would fracture after only a few cycles, again without apparent subcritical crack growth. Electron fractographic analysis, however, did reveal small bands of subcritical crack growth. These bands were analyzed and da/dN versus ΔK was obtained. The crack growth rate curve had a slope of almost infinity which explained the experimental difficulty in obtaining measurable subcritical crack growth behavior at 77 K. It appeared that the 77 K data were reasonably in agreement with room temperature data for the very low crack growth rates of about 10^{-8} m/cycle (4×10^{-7} in./cycle). Above this rate the low temperature crack growth resistance was negligible.

Stonesifer's research indicates an important aspect of how low temperatures can reduce fracture toughness to a level where very little fatigue crack growth may occur. This was also shown in Figures 11 and 12. Crack initiation life may then constitute the entire low temperature fatigue life. His work also indicates that CVN brittle-ductile transition temperature mechanisms can be completely different than ductile-brittle transition temperature fatigue crack growth mechanisms.

Kawasaki et al. (19) found a fatigue transition temperature (FTT) based upon the maximum stress intensity existing at fatigue fracture (K_{fc}) in a high strength low carbon tempered martensitic steel with $S_y = 760$ MPa (110 ksi) as shown previously in Figure 11. A plot of K_{fc} and K_c is shown in Figure 17 where excellent agreement exists for the temperature transition involving K_{fc} and K_c at -150°C . The FTT transition is substantially below the NDT and CVN transitions. The authors emphasized the importance of operating above the FTT point for a given material and component. Consequently the research group carried out an additional investigation of fracture toughness and fatigue crack growth in a 5.5% Ni steel at low temperatures (30). Figure 18 shows discontinuities at 123 K for K_{fc} , number of cycles of crack growth N_f , crack growth rate da/dN and the slope of the da/dN versus ΔK curve (δ) as a function of temperature. These four fatigue parameters indicate the FTT for this steel is 123 K. These tests,

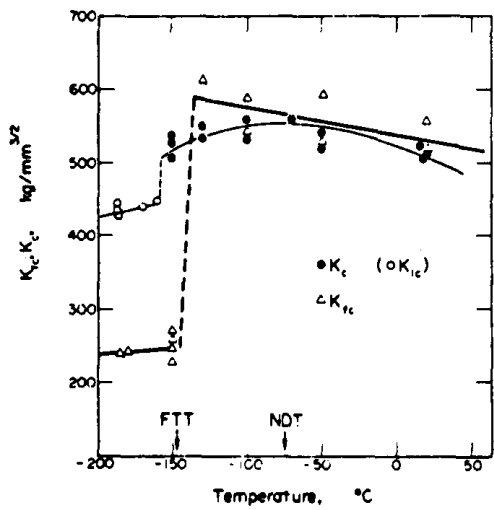


Figure 17. Fracture toughness and fatigue fracture toughness in low carbon high strength steel versus temperature (19).

however, were carried out at quite high ΔK values placing most of the results in the upper region II and region III. Similar da/dN transitions occurred at 123 K for ΔK equal to 80,90,100 and 110 $MPa\sqrt{m}$. The fracture toughness K_{Ic} did not show an appreciable discontinuity at any temperature and no correlation of FTT was made with CVN data.

A summary of fatigue crack growth behavior under constant amplitude conditions reveals insufficient region I cold temperature data exists. The

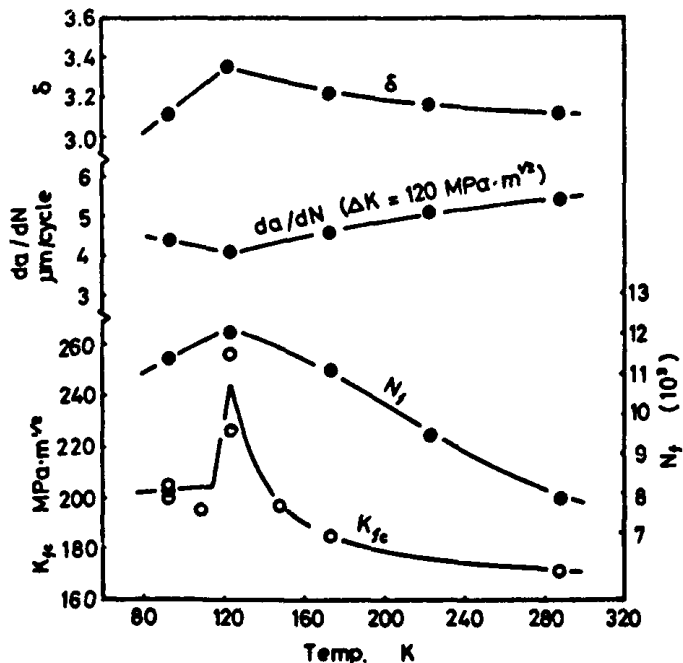


Figure 18. Fatigue crack growth parameters in 5.5% Ni steel versus temperature (30).

sigmoidal $da/dN - \Delta K$ curves may intersect and at high ΔK values the low temperatures can be detrimental. Reduced fracture toughness K_{Ic} or K_{Ic}^c at lower temperatures can substantially reduce critical crack lengths which can reduce total fatigue life. This also contributes to increased difficulty of nondestructive inspection of components and structures. Many crack growth tests showed increased fatigue resistance as the temperature was lowered and then a reversal in this trend. A ductile-brittle fatigue transition temperature (FTT) thus existed. The FTT value was suggested to be related to microstructure which changed from ductile to brittle fatigue crack growth mechanisms. This transition was often below NDT values and CVN transition values. Lower NDT and CVN transition values seemed to have accompanying lower FTT values.

Summary and Conclusions

Fatigue behavior at low temperatures has been determined primarily under constant amplitude conditions. Conclusions can only be drawn then for constant amplitude conditions since it is well established that even at room temperature constant amplitude comparisons can provide quite different results from real-life variable amplitude situations. Interaction and sequence effects at low temperature can only be hypothesized at this point. For example, residual stresses formed prior or during real-life loading which can greatly alter both crack initiation and propagation have not been quantified at low temperatures. Thus even though we may know quite a bit about constant amplitude low temperature fatigue, substantial research is still needed to understand low temperature load history effects. General constant amplitude low temperature fatigue conclusions for steels follow:

- 1) Unnotched long-life fatigue strengths have consistently increased at low temperatures. Increases may be small such as a few percent or can be substantial such as several hundred percent.
- 2) Notched long-life fatigue strengths have substantially smaller increases at low temperature. In some cases small decreases were found. The design engineer should think more in terms of the smaller notched effects rather than the larger unnotched increases.
- 3) At short lives under both stress or strain controlled conditions, low temperature fatigue unnotched and notched resistance can be increased,

decreased or have little change. However, a sufficient amount of research indicates detrimental or small changes may exist. Low ductility and low fracture toughness contribute to this behavior.

4) Fatigue crack growth behavior in regions II and III indicate many steels showed increased fatigue crack growth resistance as the temperature was lowered, followed by a reversal in this trend due to ductile-brittle fatigue transition temperature mechanisms. Insufficient region I data exists, however, the data found indicates threshold stress intensity levels, ΔK_{th} , can be increased at lower temperatures.

5) Large reductions in fracture toughness and ductility at low temperatures may result in very small critical crack lengths and hence the majority of fatigue life may be primarily crack initiation life for these conditions.

6) The NDT or CVN transition temperature range is generally different from the fatigue transition temperature range. The FTT may be similar or substantially lower. Lower NDT and CVN transition temperatures appear to be accompanied with lower FTT values.

7) Each material and loading situation needs to be considered independently since low temperatures can be beneficial, detrimental or have little influence on total constant amplitude fatigue life.

Acknowledgment

The authors would like to thank the many researchers who so kindly responded to our request for low temperature fatigue behavior.

Appendix D References

1. P.G. Forrest, "Fatigue of Metals". New York: Pergamon Press, 1962.
2. J.Y. Mann, "Fatigue of Materials". Australia: Melbourne University Press, 1967.
3. G. Sines and J.L. Waisman, "Metal Fatigue". New York: McGrawHill Book Co., 1959.
4. C.C. Osgood, "Fatigue Design". New York: Wiley Interscience, 1970.
5. N.E. Frost, K.J. Marsh and L.P. Pook, "Metal Fatigue". London: Oxford University Press, 1974.
6. H.C. Grover, "Fatigue of Aircraft Structures". Naval Air Systems Command, 1966.
7. W.W. Munse and L. Grover, "Fatigue of Welded Structures". Welding Research Council, New York, 1964.
8. A.F. Madaayag, "Metal Fatigue: Theory and Design". New York: John Wiley and Sons, 1969.
9. S.T. Rolfe and J.M. Barsom, "Fracture and Fatigue Control in Structures - Applications of Fracture Mechanics". Englewood Cliffs, New Jersey: Prentice-Hall, 1977.
10. W.S. Pellini, "Integration of Analytical Procedures for Fracture - Safe Design of Metal Structures". NRL Report 7251, March, 1971.
11. P.L. Teed, "The Properties of Metallic Materials at Low Temperatures". Chapman and Hall, 1950.
12. J.W. Spretnak, M.G. Fontana and H.E. Brooks, "Notched and Unnotched Tensile and Fatigue Properties of Ten Alloys at 25 and -196°C". Transactions ASM, Vol. 43, 1951, p. 547.
13. A.J. Nachtigall, S.J. Klima and J.C. Freche, "Fatigue of Liquid Rocket Engine Metals at Cryogenic Temperatures to -452°F (4°K)". NASA TN D-4274, 1967.
14. V.T. Troshchenko, V.V. Pokrovskii and A.V. Prokopenko, "Effect of a Stress Raiser on the Conditions Governing the Transition from Fatigue to Brittle Fracture in 15G2AFDp- Steel at Low Temperatures". Strength of Materials, Vol. 8, No. 2, 1976, p. 136.
15. I. V. Kudryavtsev, A.D. Chudnovskii and I.M. Rafalovich, "Low Temperature Fatigue Strength of Structural Steels". Strength of Materials, Vol. 8, No. 1, 1976, p. 5.
16. A.J. Nachtigall, "Strain-Cycling Fatigue Behavior of Ten Structural Metals Tested in Liquid Helium (4 K), in Liquid Nitrogen (78 K) and in Ambient Air (300 K)". NASA TN D-7532, February, 1974.
17. J. Polak and M. Klesnil, "The Dynamics of Cyclic Plastic Deformation and Fatigue Life of Low Carbon Steel at Low Temperatures". Materials Science Engineering, Vol. 26, No. 2, December, 1976, p. 157.
18. M. Kikukawa, M. Jono, T. Kamato and T. Nakano, "Low Cycle Fatigue Properties of Steels at Low Temperatures". Proceedings 13th Japan Congress on Materials Research, 1970, p. 69.
19. T. Kawasaki, S. Nakanishi, Y. Sawaki and T. Yokobori, "Fracture Toughness and Fatigue Crack Propagation in High Strength Steel from Room Temperature to -180°C". Engineering Fracture Mechanics, Vol. 7, 1975, p. 465.
20. B.T. Troshchenko, "A Study of Low Temperature Effect on Fatigue Crack Growth in Steel 15G2AFDps". Probiemy Prochnosti, No. 10, 1975, p. 8, (In Russian).
21. T.T. Troshchenko and V.V. Pokrovskii, "Methods of Investigating Laws of Fatigue Fracture of Metals under Harmonic and Complex Loads at Low Temperatures". Strength of Materials, Vol. 5, No. 2, 1973, p. 166.
22. B.T. Troshchenko and V.V. Pokrovskii, "Mechanisms of Fatigue and Brittle Failure in 15G2AFDps Steel at Low Temperatures". Strength of Materials, Vol. 5, No. 3, 1973, p. 274.
23. S. Ya Yarema, "Growth of Fatigue Crack in Low Carbon Steel Under Room and Low Temperatures". Problemy Prochnosti, No. 3, 1977, p. 21, (In Russian).
24. S. Ya Yarema and O.P. Ostosh, "A Study of Fatigue Crack Growth in Low Temperatures". Fiz-khim. Mekh. Mater., No. 2, 1977, p. 48, (In Russian).
25. D. Broek and R.C. Rice, "Prediction of Fatigue - Crack Growth in Railroad Rails". Battelle Columbus Laboratories, 1978.
26. W.W. Gerberich and N.R. Moody, "A Review of Fatigue Fracture Topology Effects on Threshold and Kinetic Mechanism". Symposium on Fatigue Mechanisms, ASTM, STP to be published 1979.
27. R.L. Tobler and R.P. Reed, "Fatigue Crack Growth Resistance of Structural Alloys at Cryogenic Temperatures".

- Presented at the Cryogenic Engineering Conference/International Cryogenic Materials Conference, University of Boulder, Colorado, August, 1977.
28. R.L. Tobler, R.P. Mikesell and R.P. Reed, "Cryogenic Effects on the Fracture Mechanics Parameters of Ferritic Nickel Alloy Steels". Cryogenic Division, National Bureau of Standards, Boulder, Colorado.
 29. F.R. Stonesifer, "Effect of Grain Size and Temperature on Fatigue Crack Propagation in A533 B Steel". Engineering Fracture Mechanics, Vol. 10, 1978, p. 305.
 30. T. Kawasaki, T. Yokobori, Y. Sawaki, S. Nakanishi and H. Izumi, "Fatigue Fracture Toughness and Fatigue Crack Propagation in 5.5% Ni Steel at Low Temperatures". Fracture 1977, ICF-4, Vol. 3, Waterloo, Canada, June, 1977.